Nonlinear Losses in Single Crystalline and Ceramic Yb:YAG Thin-Disk Lasers

Dissertation

zur Erlangung des Doktorgrades
des Department Physik
der Universität Hamburg

vorgelegt von

Susanne T. Fredrich-Thornton

aus Rellingen

Hamburg
2010

Gutachter der Dissertation:	Prof. Dr. G. Huber Prof. Dr. K. Ueda
Gutachter der Disputation:	Prof. Dr. G. Huber Priv. -Doz. Dr. V. M. Baev
Datum der Disputation:	26.08.2010
Vorsitzender des Promotionsausschusses:	Prof. Dr. J. Bartels
Dekan der Fakultät für Mathematik, Informatik und Naturwissenschaften:	Prof. Dr. H. Graener

"But diagrams somehow have a penchant for becoming pedagogical and interpretational aids as well as memory aids, and a poor diagram is often definitely harmful."

Lyman G. Parratt

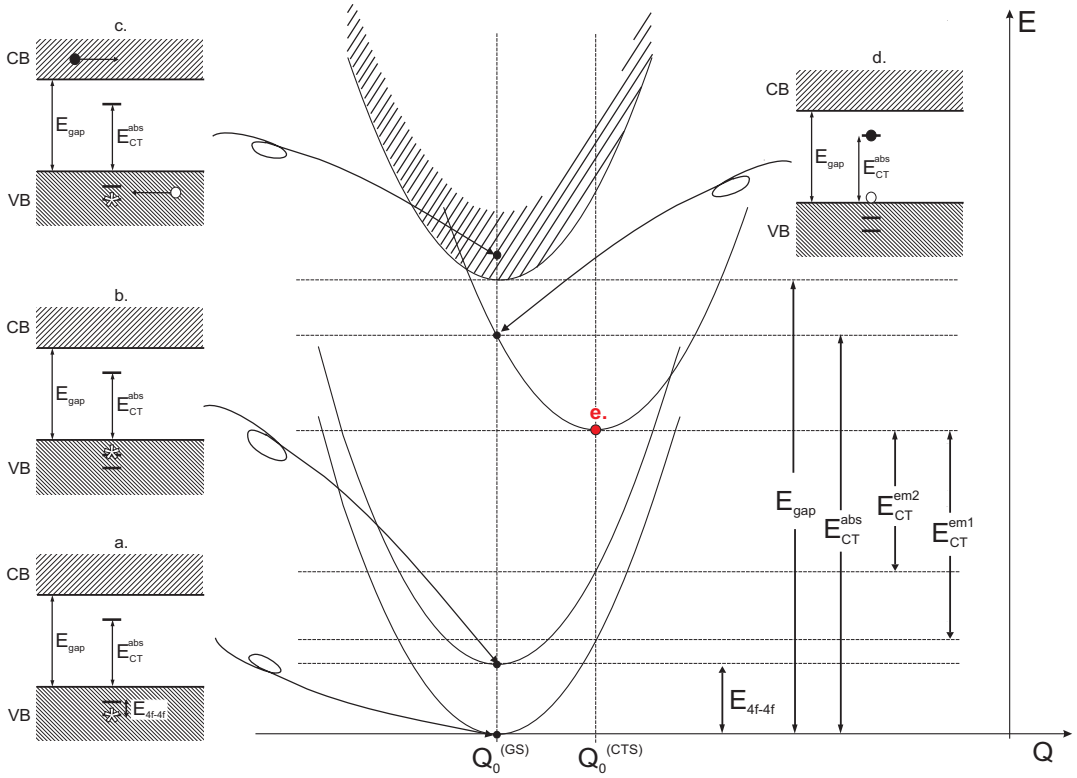

An attempt to link the configurational coordinate diagram (CCD) with the one-electron jump diagram for trivalent Yb in an isolator, e.g. YAG, after Shinozuka (Jpn. J. Appl. Phys. Vol. 32 (1993) pp. 4560-4570). VB denotes the valence band and CB the conduction band. Open circles represent holes, filled circles electrons and the open stars indicate the actual $4f$ configuration of the Yb-ion. The arrows point to the positions in the CCD to which the corresponding one-electron jump diagrams (labelled with lower case alphabet) belong to. The one-electron jump diagram corresponding to *e*. does not exist. One might also argue that in configurational coordinates a parabola is not an accurate representation for an electron in the conduction band as depicted in *c*. It should also be noted that strictly speaking the utilisation of configurational coordinates for the description of electron exchange processes is not justifiable.

Abstract

S. T. Fredrich-Thornton: *Nonlinear Losses in Single Crystalline and Ceramic Yb:YAG Thin-Disk Lasers*

The subject of this thesis is the investigation of the laser properties of highly ytterbium-doped $Y_3Al_5O_{12}$ (Yb:YAG) laser gain materials at high inversion densities with regard to their applications in high power thin-disk lasers. In this context, Yb:YAG single crystalline and ceramic samples are compared concerning their spectroscopic properties and thin-disk laser characteristics.

The examinations focus on laser losses observed at high densities of Yb^{3+}-excitations, which currently limit the Yb-doping concentrations of efficient thin-disk lasers to below 15%. These losses are found to increase nonlinearly with the transmission rate of the outcoupling mirror leading to significant heat generation in the laser medium. Based on the analysis of the data obtained from the thin-disk laser experiments, the participation of an ensemble of two to four excited Yb^{3+}-ions in the loss process is proposed. As an involvement of the host valence and conduction band states is assumed, a comprehensive energy level scheme of the trivalent and divalent Yb-ion local states with respect to the host energy bands is compiled and discussed. Furthermore, photoconductivity measurements at 940 nm excitation have been implemented, which revealed the creation of free carriers in Yb:YAG under Yb^{3+}-excitation. Photocurrents of almost 80 nA have been detected for Yb:YAG crystals, whereas in silicon-codoped Yb:YAG samples, even larger photocurrents of several microamperes have been found. The results of the photoconductivity measurements also indicate a high order process with the participation of two to three excited Yb^{3+}-ions in the current generating process. Thus, a cooperative upconversion mechanism is proposed for the creation of free carriers. A hopping mechanism involving the Yb^{3+}/Yb^{2+} charge transfer (CT) states is discussed as a possible charge transport model.

A connection between the nonlinear losses observed in thin-disk lasers at high inversion densities and the photoconductivity of Yb:YAG found at 940 nm irradiation is strongly suggested. It is assumed that the major impact of the photoconductivity phenomenon on the laser efficiency lies in the presumably high heat generation at the recombination of the carriers. Spectroscopic investigations have been carried out with particular regard to possible defect centres and impurities, which could act as quenching centres to the Yb:YAG laser. Spectroscopical investigations did not confirm the existence of an impurity band formed by Yb^{3+}/Yb^{2+} CT states in the band gap of YAG. It is concluded that it might not be possible to populate the current carrying states by optical excitation at wavelengths corresponding to the energy of two to three Yb^{3+}-excitations due to the Franck-Condon principle. Thin-disk laser operation using ceramic Yb:YAG gain media has been achieved for the first time. The highest efficiency of the ceramic samples investigated has been obtained for a 15.0%Yb:YAG ceramic sample, with which slope efficiencies of up to 67% have been achieved, a value comparable to commercial single crystalline Yb:YAG thin-disk lasers. The evaluation of the experimental data also suggests that ceramic Yb:YAG gain materials are less prone to the nonlinear loss processes compared to their single crystalline counterparts.

Zusammenfassung

S. T. Fredrich-Thornton: *Nichtlineare Verlustprozesse in einkristallinen und keramischen Yb:YAG Scheibenlasern*

Gegenstand dieser Arbeit ist die Untersuchung Ytterbium-dotierter $Y_3Al_5O_{12}$ (Yb:YAG) Lasermaterialien bei hohen Anregungsdichten hinsichtlich ihrer Lasereigenschaften im Scheibenlaser. Hierzu werden sowohl die spektroskopischen Eigenschaften als auch die Leistungsparameter im Scheibenlaserbetrieb von Yb:YAG Einkristallen und Keramiken unterschiedlicher Dotierungskonzentration miteinander verglichen.

Der Schwerpunkt liegt auf der Untersuchung von Verlustprozessen, die in Scheibenlasern bei hohen Inversionsdichten zu einer erheblichen Verminderung der Effizienz führen. Es wird aufgezeigt, dass diese Verluste mit steigendem Auskoppelgrad in nichtlinearer Weise zunehmen und zu einer starken Wärmeentwicklung im Lasermedium führen, die den Laserbetrieb unterbindet. Die Analyse der Scheibenlaserexperimente lässt die Beteiligung eines Ensembles aus zwei bis vier angeregten Yb^{3+}-Ionen für den Verlustprozess vermuten. Da angenommen wird, dass Leitungsband- und Valenzbandzustände in den Verlustprozess involviert sind, wird ein umfassendes Energieniveauschema erstellt, welches die lokalen Energieniveaus sowohl von Yb^{3+}- als auch von Yb^{2+}-Ionen relativ zu den Wirtsbändern zeigt. Des Weiteren wird in Photoleitungsexperimenten durch die Messung von Photoströmen von bis zu 80 nA in Yb:YAG Kristallen die Erzeugung von freien Ladungsträgern bei Yb^{3+}-Anregung unter 940 nm Pumpstrahlung nachgewiesen. Bei Silizium-Kodotierung beträgt der maximale Photostrom sogar mehrere Mikroampere. Die Messungen weisen auf einen Prozess höherer Ordnung als Ursache für den Photostroms hin, in den zwei bis drei Yb^{3+}-Anregungen involviert sind. Aus diesem Grund wird ein kooperativer Energietransferprozess als Mechanismus für die Erzeugung freier Ladungen vorgeschlagen. Außerdem werden die Beteiligung von Yb^{3+}/Yb^{2+} Charge-Transfer Zuständen in einem Hopping-Mechanismus als ein mögliches Model für den Ladungstransport und ein Zusammenhang zwischen den nichtlinearen Laserverlusten und der Photoleitfähigkeit von Yb:YAG untersucht. Hieraus ergibt sich, dass der Haupteinfluss der Photoleitungseigenschaft von Yb:YAG in einer mutmaßlich hohen Wärmeerzeugung bei dem Rücktransferprozess der Ladungsträger besteht.

Spektroskopische Untersuchungen konzentrieren sich auf die Detektion und Identifikation möglicher Defektzentren und Verunreinigungen, die den Laserbetrieb beeinträchtigen. Ein Nachweis für die Existenz eines Störstellenbandes in der YAG Bandlücke, das durch zwei bis drei Yb^{3+}-Anregungen besetzt werden könnte, kann durch spektroskopische Untersuchungen jedoch nicht gefunden werden. Eine mögliche Erklärung dafür ist, dass eine direkte optische Anregung eines solchen Bandes durch Licht mit einer Energie entsprechend zwei bis drei Yb^{3+}-Anregungen aufgrund des Franck-Condon Prinzips nicht stattfindet. Im Rahmen der Untersuchungen wird erstmals Lasertätigkeit im Scheibenlaseraufbau mit keramischen Yb:YAG Materialien realisiert. Dabei weist die effizienteste Probe, eine 15.0%Yb:YAG Keramik, einen differentiellen Wirkungsgrad von bis zu 67% auf, eine Effizienz die vergleichbar mit kommerziellen einkristallinen Yb:YAG Scheibenlasern ist. Diese Ergebnisse weisen daraufhin, dass keramische Yb:YAG Lasermaterialien weniger von den nichtlinearen Verlustprozessen beeinflusst werden als Einkristalle vergleichbarer Spezifikation.

Contents

List of Figures

List of Tables

1. Introduction

1.1. Motivation

The pursuit of efficient high power lasers with high beam quality has led to the development of the thin-disk laser design by Giesen and coworkers in 1994 [Gie94]. In this setup, the gain medium has the geometry of a thin disk, with the thickness of the disk being considerably smaller than the pump spot diameter. A dielectric coating is applied on the backside of the disk, which is highly reflective for both the laser wavelength and the pump wavelength. The disk is mounted with its end face onto the heat sink allowing for highly efficient removal of the excess heat generated during laser operation. In this way, almost one-dimensional heat flow parallel to the propagation direction of the laser radiation is accomplished so that thermal lensing due to radial heat flow is significantly reduced. Thus, high beam quality is maintained even at very high output powers. High optical-to-optical efficiencies are achieved by using a multi-pass pump arrangement, which allows for sufficient absorption despite the thin active medium .

There are many requirements for a laser material to be suitable for the use in commercial highly efficient high power thin-disk laser applications: broad and high absorption bands, matching the spectral characteristics of available high power pump laser diodes are needed. To reduce excess heat generation, a low quantum defect between the pump and the laser wavelength is desirable. For high laser gain efficiency a high σ_{em}-τ product, i.e. the product of the laser emission cross-section and the upper laser level lifetime, is of advantage. To achieve sufficient absorption within the thin disk, high doping concentrations should be possible. Good thermo-mechanical properties such as hardness for easy handling and high thermal conductivities are favourable. Furthermore, for commercial use the availability in large quantities and good qualities is essential. Ytterbium doped oxides are an attractive choice of medium, which fulfill most of the above requirements. The main advantage over neodymium for laser operation in the 1 µm spectral region is the quasi-three-level nature of the ytterbium laser, which ensures a very low quantum defect. In addition, the simple energy level structure with only two $4f$ manifolds suggests that even at high doping concentrations quenching processes like cross-relaxation and upconversion should not be observed. In the last years, thin-disk laser operation has been demonstrated for ytterbium in various oxide host materials, e.g. Lu_2O_3 and Sc_2O_3 [Pet09], $Lu_3Al_5O_{12}$ [Bei08], $LaSc_3(BO_{34})$, $Ca_4YO(BO_3)_3$, YVO_4 and $LuVO_4$ [Krä08], $NaGd(WO_4)_2$ [Pet08], $KGd(WO_4)_2$ and $KY(WO_4)_2$ [Gie07]. However, for high average power thin-disk laser operation so far only ytterbium doped $Y_3Al_5O_{12}$ (Yb:YAG) single crystals are of industrial importance. This is mainly due to the optimal balance between favourable spectroscopic characteristics and good thermo-mechanical properties together with the easy crystal growth of large boules by the Czochralski method, which ensures high availability for this material. So far, up to 500 W of output power with a nearly diffraction limited beam quality have

been obtained from a single Yb:YAG disk [Men09]. In multi mode operation with one disk more than 5.3 kW of average output power with optical-to-optical efficiencies of up to 65% has been achieved [Kil08]. However, Yb:YAG thin-disk lasers suffer from decay processes, which are known to be dependent on the density of excited Yb^{3+}-states, resulting in suppression of laser operation for crystals with a doping concentration of 15% and greater [Lar05]. It is assumed that these losses are based on an energy transfer process involving pairs or even ensembles of more than two excited neighbouring Yb^{3+}-ions. Today, commercially available high quality Yb:YAG crystals are usually of high purity so that also a loss process intrinsic to Yb:YAG at high inversion densities has to be considered.

1.2. Outline

The aim of this research is to identify the loss processes that occur in Yb:YAG thin-disk lasers at high densities of Yb^{3+}-excitations. For power scaling in the thin-disk laser setup, high doping concentrations are generally desirable as this allows to use even thinner disks which further minimise thermal effects thus allowing for higher pump power densities. Currently, the doping concentration for efficient thin-disk laser operation seems to be limited to below 15% for Yb:YAG. It is thus of particular interest to find the origin of the losses observed as well as to find possible solutions. In this context, the laser properties of highly Yb-doped YAG single crystals are investigated and reassessed. These investigations are extended to Yb:YAG ceramics with different Yb-concentrations, to determine whether ceramics suffer the same problems as those of single crystal thin-disk lasers. This work gives a comprehensive overview of the current state of knowledge regarding single crystalline and ceramic Yb:YAG as gain media in high power thin-disk lasers.

In chapter 2, at first the theoretical foundations necessary to understand the interaction of light and matter, as well as basic quasi-three level laser theory are summarised. The configurational coordinate diagram and the one-electron jump diagram are introduced as two different models for the description of processes in optical materials. In chapter 3, the laser material Yb:YAG is introduced with particular focus on the energy level positions of the trivalent and also divalent Yb-ions with respect to the host valence and conduction bands. The crystal growth and the fabrication technique for single crystals and ceramics are also presented together with some crystallographic properties of these materials. The state of the art regarding charge transfer characteristics of Yb:YAG and the laser losses observed in Yb:YAG thin-disk lasers is summarised at the end of this chapter. The results of the spectroscopic investigations on Yb:YAG single crystals and ceramics are presented in chapter 4. The fifth chapter deals with the thin-disk laser experiments performed within the framework of this research. The investigations focus particularly on the dependence between laser performance and inversion density. The laser results obtained for the single crystals and ceramics are compared and discussed. In chapter 6, the phenomenon of photoconductivity found in Yb:YAG under 940 nm irradiation is presented. Some possible models for the current generating process and the charge transport mechanism are suggested. At the end of this chapter, the connection between the observed laser losses and photoconductivity is discussed. This work closes with a summary and an outlook for further possible experiments.

2. Theoretical Foundations

For interpretation of the spectroscopic investigations of Yb:YAG presented in chapter 4, and evaluation of the photoconductivity measurements in chapter 6, a basic understanding of the energetic constitution of the Yb^{3+}- as well as the Yb^{2+}-ion in a crystalline matrix is necessary. Similarly, comprehension of the laser results presented in chapter 5 demands knowledge of the underlying interactions between light and matter. In this chapter the general principles are briefly summarised and the consequences for the Yb-ion discussed. Detailed descriptions can be found in textbooks, e.g. [Hen89, Gör96] and [Sve93].

2.1. The Lanthanoid Series

The lanthanoid series, previously also referred to as the lanthanides, comprises of the elements with atomic numbers $Z = 57$ (lanthanum) to $Z = 71$ (lutetium). Some chemists differentiate between lanthanides and lanthanoids in the way that lanthanoids are the lanthanum-similar elements excluding lanthanum whereas the term lanthanides includes it. Together with the actinides, the lanthanides belong to the f-block of the periodic table (also known as the inner transition metals), where the highest energy-electrons of the ground state occupy f-orbitals[1]. This block follows periods of similar atomic numbers rather than groups of similar electron configuration. In the case of the lanthanides the $4f$ shell is partially filled, thus the general electronic configuration of the lanthanides is $[Xe]4f^n5d^m6s^2$, where [Xe] represents the filled electronic layers of the xenon rare gas. With increasing atomic number the number of electrons in the $4f$ shell increases from lanthanum, with $n = 0$, up to lutetium, which has a completely filled $4f$ shell with the electronic configuration $[Xe]4f^{14}5d^16s^2$. At this, the $5d$ shell does not necessarily have to be occupied. More precisely, for cerium ($n = 1$)[2], gadolinium ($n = 7$), and lutetium ($n = 14$) $m = 1$, whereas $m = 0$ for all others. Figure 2.1 displays the periodic table, accentuating the chemical similarity of the lanthanides.

Due to their specific electronic configurations, lanthanide atoms, when incorporated into a crystalline matrix, tend to lose three electrons, usually the $5d^1$ and $6s^2$ electrons, to attain their most stable oxidation state as trivalent ions. In order to obtain the divalent state, the lanthanide ion needs to be reduced. Divalent europium, ytterbium, samarium and, with some limitations, thulium can already be obtained in significant amounts during crystal growth by using suitable lattices containing divalent cation sites, appropriate co-dopants for charge compensation, and a

[1] From this definition lanthanum, gadolinium and lutetium would not belong to the f-block.

[2] In the case of the cerium ground state, two different configurations can be found in different textbooks: $[Xe]4f^15d^16s^2$ [Hou07] and $[Xe]4f^26s^2$ [Rie96].

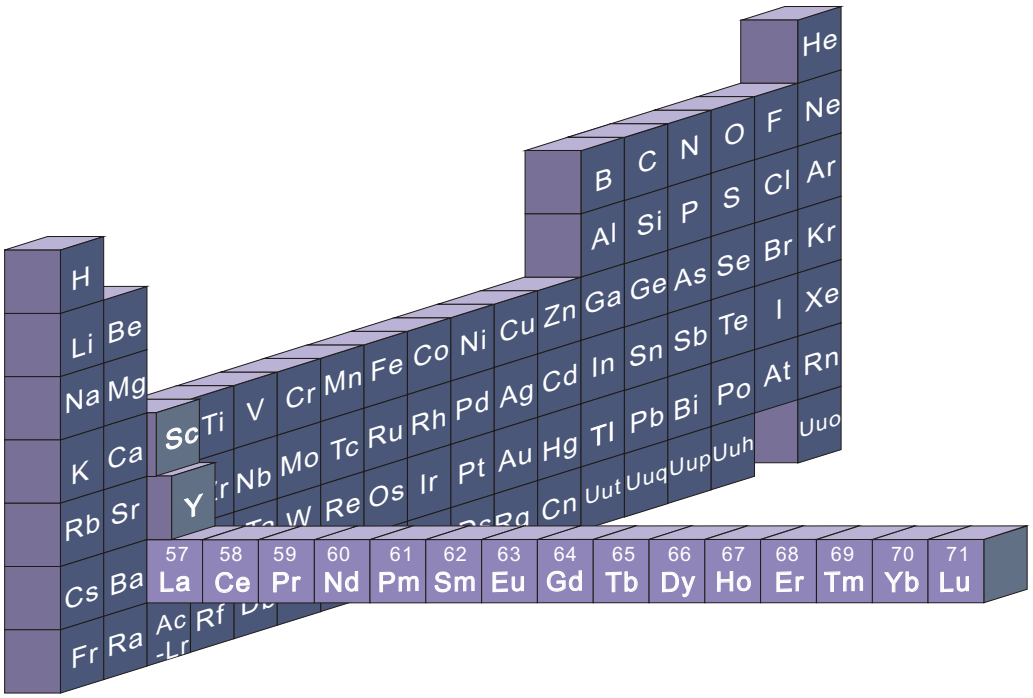

Figure 2.1.: The periodic table of the elements with the rare earths accentuated.

reducing atmosphere. The other divalent lanthanides are difficult to obtain in crystals; usually special growth conditions as well as pre- and post-treatment is necessary.

The $4f$ orbitals lay inside the ion, shielded by the closed $5s$ and $5p$ orbitals. Therefore, their energy states are only slightly influenced by the ligands and behave to a large extent like those of a free ion. The crystal field can thus be treated as a weak distortion to the free ion case and basic perturbation theory can be applied to calculate the respective energy states. Perturbation by the crystal field leads to mixing of states so that the initially parity forbidden intraconfigurational electric-dipole transitions between $4f$ states become weakly allowed in non-centrosymmetric crystal fields. As a consequence of the small crystal field perturbation, lanthanides exhibit low variation of the $4f$ states in different local environments and rather narrow transition linewidth for $4f \rightarrow 4f$ transitions. In contrast, interconfigurational transitions between $4f$ and the less shielded $5d$ states are subjected to strong influence of the ligands and as a result the emission and absorption bands are considerably broadened in comparison to $4f \rightarrow 4f$ transitions. The main objects of study in lanthanide spectroscopy are the trivalent ions from Ce^{3+} ($4f^1$) to Yb^{3+} ($4f^{13}$), as these ions have partly filled $4f$ shells and can interact with electromagnetic radiation. La^{3+}- and Lu^{3+}-ions are not optically active because they have empty and filled $4f$ shells, respectively. Therefore, the term lanthanoid is favoured over the term lanthanide in this work and will be used in the following chapters.

The ionic radii of the lanthanoids decrease through the period, the so-called lanthanide contraction [Gol25], which results from poor shielding of nuclear charge by the $4f$ electrons. The ionic radius in eightfold coordination drops from 1.14 Å for Ce^{3+} to 0.98 Å for Lu^{3+} [Hou07]. Since the outer shells of the lanthanoids do not change within the group, their chemical be-

haviour is very similar. However, the differing atomic and ionic radii do affect their chemistry. Without the lanthanide contraction, a chemical separation of lanthanoids would be difficult. Table 2.1 lists the ground state electronic configuration of the neutral, divalent, trivalent and tetravalent lanthanoids and lanthanum, together with the atomic radius and the ionic radius for the trivalent ion in eightfold coordination according to [Hou07]. For clarity reasons, the number of electrons occupying the $4f$ shell are always given, even in cases were the actual number is zero. In the following, the simpler and more common notation is used, where empty shells and the occupation number 1 for singly occupied shells are omitted.

Together with the transition metals with atomic numbers $Z = 21$ (scandium) and $Z = 39$ (yttrium) and lanthanum the 14 lanthanoids form the collection of the rare earth elements (RE).

Element Name	Symbol	Z	Ground State Electronic Configuration				Radius [Å]	
			Ln	Ln^{2+}	Ln^{3+}	Ln^{4+}	Ln	Ln^{3+}
Lanthanum	La	57	[Xe]$5d^1 6s^2$	[Xe]$5d^1$	[Xe]$4f^0$		1.88	1.16
Cerium	Ce	58	[Xe]$4f^1 5d^1 6s^2$	[Xe]$4f^2$	[Xe]$4f^1$	[Xe]$4f^0$	1.83	1.14
Praseodymium	Pr	59	[Xe]$4f^3 6s^2$	[Xe]$4f^3$	[Xe]$4f^2$	[Xe]$4f^1$	1.82	1.13
Neodymium	Nd	60	[Xe]$4f^4 6s^2$	[Xe]$4f^4$	[Xe]$4f^3$		1.81	1.11
Promethium	Pm	61	[Xe]$4f^5 6s^2$	[Xe]$4f^5$	[Xe]$4f^4$		1.81	1.09
Samarium	Sm	62	[Xe]$4f^6 6s^2$	[Xe]$4f^6$	[Xe]$4f^5$		1.80	1.08
Europium	Eu	63	[Xe]$4f^7 6s^2$	[Xe]$4f^7$	[Xe]$4f^6$		1.99	1.07
Gadolinium	Gd	64	[Xe]$4f^7 5d^1 6s^2$	[Xe]$4f^7 5d^1$	[Xe]$4f^7$		1.80	1.05
Terbium	Tb	65	[Xe]$4f^9 6s^2$	[Xe]$4f^9$	[Xe]$4f^8$	[Xe]$4f^7$	1.78	1.04
Dysprosium	Dy	66	[Xe]$4f^{10} 6s^2$	[Xe]$4f^{10}$	[Xe]$4f^9$	[Xe]$4f^8$	1.77	1.03
Holmium	Ho	67	[Xe]$4f^{11} 6s^2$	[Xe]$4f^{11}$	[Xe]$4f^{10}$		1.76	1.02
Erbium	Er	68	[Xe]$4f^{12} 6s^2$	[Xe]$4f^{12}$	[Xe]$4f^{11}$		1.75	1.00
Thulium	Tm	69	[Xe]$4f^{13} 6s^2$	[Xe]$4f^{13}$	[Xe]$4f^{12}$		1.74	0.99
Ytterbium	Yb	70	[Xe]$4f^{14} 6s^2$	[Xe]$4f^{14}$	[Xe]$4f^{13}$		1.94	0.99
Lutetium	Lu	71	[Xe]$4f^{14} 5d^1 6s^2$	[Xe]$4f^{14} 5d^1$	[Xe]$4f^{14}$		1.73	0.98

Table 2.1.: The electronic configuration for the ground states of neutral, divalent, trivalent and tetravalent lanthanoids and lanthanum, together with the atomic and the trivalent ionic radius for eightfold coordination according to [Hou07]. Ln is used as a general symbol for the lanthanoids.

2.1.1. The Energy Level Structure of the Lanthanoids

The energy level structure of atoms, or as in this case that of a lanthanoid ion, arises from the successive interaction of different Hamiltonians of the optically active electron wave function, which gradually removes the degeneracy. The first simple step in the conventional approach of atomic energy level calculation has been to diagonalise energy matrices concerning only single electron configurations. The development of a complete Hamiltonian for $4f^n$ configurations is performed in two stages. First, the fundamental interactions, including electrostatic Coulomb interactions and the spin-orbit coupling have to be dealt with. In this way, the energy level structure for the free ion case is obtained. In a second step the crystal field interaction that arises when the ion is incorporated into a solid matrix has to be taken into account. To reproduce more accurately the energy level structures observed in experiments, often additional

Type of Interaction	ΔEnergy [cm^{-1}]	Optical Probe
Configuration Splitting ($4f^n$ - $4f^{n-1}5d$)	10^5	UV and VUV spectroscopy
Splitting within a $4f^n$ configuration		
Non-central electrostatic field	10^4	Absorption, fluorescence
Spin-orbit interaction	10^3	or
Crystal field interaction	10^2	excitation spectroscopy
Ion-ion interaction induced band structure	10^{-2}-10	
Hyperfine Splitting	10^{-3}-10^{-1}	Selective and nonlinear
Superhyperfine splitting	10^{-4}-10^{-2}	laser spectroscopy
(ion-ligand hyperfine interaction)		

Table 2.2.: Orders of magnitude for the energy level for the different interactions for lanthanoid ions in crystalline matrices together with the means for optical probing [Liu05].

effective operators dealing with higher order free ion interactions and corrective crystal field interactions are introduced. The theoretical framework, thus utilises well established theories in two conventional fields: The quantum theory of atomic spectroscopy which is the foundation for establishing the free ion energy level structure and the point group theory which facilitates the determination of crystal field splittings according to the symmetry properties of a crystalline lattice.

Table 2.2 lists the orders of magnitude for the electronic energy level splitting resulting from different electronic interactions. Due to the shielding of the $4f$ shell, the scale of crystal field splitting is smaller than that of the free ion splitting and the hyperfine energy level structures are even smaller, so that it is legitimate to apply perturbation theory for their calculation.

The Free Ion Hamiltonian

The lanthanoid ion is a many-body systems with N electrons and the atomic number Z. The Hamiltonian of such an ion constitutes of the kinetic and the potential energy felt by the electron, the Coulomb interaction between the electrons and all other interactions, which act on the electron:

$$\mathcal{H} = \sum_{i=1}^{N} \left(-\frac{\hbar^2}{2m_e}\Delta_{\overrightarrow{r_i}} - \frac{Ze^2}{4\pi\varepsilon_0 r_i} \right) + \sum_{i<j=1}^{N} \frac{e^2}{4\pi\varepsilon_0 r_{ij}} + ..., \tag{2.1}$$

where r_i is the distance between the nucleus and the electron i, $r_{ij} = |\overrightarrow{r_i} - \overrightarrow{r_j}|$ is the distance between electron i and electron j, $\hbar$ is the reduced Planck constant, m_e is the electron mass, e is the electron charge and ε_0 is the electric constant. Due to the last term the corresponding Schrödinger equation cannot be separated into N one-body problems and therefore cannot be solved analytically. The traditional approach is to use the central field approximation and the Hartree-Fock method. In the central field approximation, each electron is supposed to move independently in a spherically symmetric potential due to the nucleus and the other electrons.

Thus, the exact Hamiltonian of equation 2.1 is replaced by the much simpler central field Hamiltonian:

$$\mathcal{H}_{ef} = \sum_{i=1}^{N} \left(-\frac{\hbar^2}{2m_e}\Delta_{\vec{r_i}} - \frac{Ze^2}{4\pi\varepsilon_0 r_i} + u_i(r) \right), \tag{2.2}$$

with the central field potential $U(r) = \sum_i u_i(r)$. This Hamiltonian contains only one-electron spherically symmetric terms and can now be separated into a radial and an angular part. The eigenfunctions Ψ_0 of the central field Schrödinger equation

$$\mathcal{H}_{ef}\Psi_0 = E_{ef}\Psi_0 \tag{2.3}$$

are the determinantal products of the one-electron functions

$$\Psi_0 = \prod_i \mid n_i l_i m_{li} m_{si} \rangle, \tag{2.4}$$

where n is the principle quantum number, l is the angular momentum quantum number, m_{li} is the magnetic quantum number and m_{si} is the spin projection quantum number. The eigenvalues of the central field equation are themselves sums of the single electron eigenvalues and are only dependent on the principle and the angular momentum quantum numbers. The central field eigenvalues are highly degenerate and each eigenvalue may be said to determine the energy of a particular "configuration" in the zeroth approximation. The obtained eigenfunctions may be used to construct a suitable set of antisymmetrised basis functions which can be then used to construct the energy matrix for the residual interactions.

After first having considered the outer electrons as completely independent, their electrostatic repulsion and their spin-orbit interactions have to be taken into account. The exact free-ion Hamiltonian of a system can be written as

$$\mathcal{H}_{free\ ion} = \mathcal{H}_0 + V. \tag{2.5}$$

The operator $\mathcal{H}_0$ is chosen in such a way as to describe a simple zero-order representation of the system[3] and the operator V is to be considered a perturbation on this. Now, only the outer electrons are considered, i.e. the outer $4f$ electrons are regarded to be in a central field provided by the nucleus screened by the 54 electrons of the completed xenon-like shell. In this one-electron approximation electron correlations are neglected and all $4f$ electrons are considered equivalent. Treating the inter-electron Coulomb interactions and the spin-orbit interactions as perturbations, equation 2.5 becomes

$$\mathcal{H}_{free\ ion} = \mathcal{H}_0 + \mathcal{H}_{ee} + \mathcal{H}_{so}, \tag{2.6}$$

with the Hamiltonian

$$\mathcal{H}_{ee} = -\sum_{i=1}^{n} u_i(r) + \sum_{i<j=1}^{n} \frac{e^2}{4\pi\varepsilon_0 r_{ij}} \tag{2.7}$$

accounting for the inter-electron Coulomb interaction and the Hamiltonian

$$\mathcal{H}_{so} = \sum_{i=1}^{n} \zeta(r_i)\vec{l}_i \cdot \vec{s}_i, \tag{2.8}$$

[3] $\mathcal{H}_0$ is thus almost the same as $\mathcal{H}_{ef}$.

accounting for the spin-orbit interactions as perturbation potentials. Here, ζ is the spin-orbit coupling constant and $\vec{l}$ and $\vec{s}$ is the orbital and spin angular momentum. The summation is done over the n outer electrons, i.e. only for the $4f$ electrons in the case of the trivalent and most of the divalent lanthanoids.

To construct wave functions for a multi-electron ion on the basis of the central field approximation, one needs to choose a coupling scheme of momentum summation. There are two coupling schemes that are commonly used for two extreme cases. In lighter atoms the spin-orbit interaction tends to be small compared to the electrostatic interactions between electrons ($\mathcal{H}_{ee} > \mathcal{H}_{so}$) and L and S are approximately good quantum numbers. Therefore, the so-called Russell-Saunders or LS coupling scheme is an appropriate choice [Rus25]. With increasing Z number, electrostatic interactions decrease and spin-orbit interactions become more important. In the heavier ions, spin-orbit interactions become much stronger than Coulomb interactions ($\mathcal{H}_{so} > \mathcal{H}_{ee}$) and one should consider the j-j coupling scheme. In lanthanoid ions the Coulomb electrostatic interactions and spin-orbit interactions have the same orders of magnitude. Therefore, neither coupling scheme is appropriate and an intermediate coupling scheme, which is developed from the LS scheme, is applied. In the LS coupling scheme, orbital momentum and spin momentum of individual electrons are summed separately, where

$$\vec{L} = \sum_{i=1}^{n} \vec{l}_i\,, \qquad \vec{S} = \sum_{i=1}^{n} \vec{s}_i \tag{2.9}$$

are the total orbital and total spin momentum operator respectively, and

$$\vec{J} = \vec{L} + \vec{S} \tag{2.10}$$

is the total angular momentum operator. With this, the effective Hamiltonian $\mathcal{H}_{free\ ion}$, which accounts for the different electric and magnetic interactions experienced by an individual $4f$ electron can be expressed as

$$\mathcal{H}_{free\ ion} = -\sum_{i=1}^{n} \frac{\hbar^2}{2m_e}\Delta_{\vec{r_i}} - \sum_{i=1}^{n} \frac{Ze^2}{4\pi\varepsilon_0 r_i} + \sum_{i<j=1}^{n} \frac{e^2}{4\pi\varepsilon_0 r_{ij}} + \sum_{i=1}^{n} \zeta(r_i)\vec{l}_i \cdot \vec{s}_i. \tag{2.11}$$

The first two terms are spherically symmetric and do not remove any degeneracy within the $4f^n$ configuration. The next interaction, for n equal to or greater than 2, gives rise to the terms which degeneracy is removed by the magnetic moment coupling between the spin and the orbital momentum of the $4f$ electron. The resulting degenerate J levels are characteristic of the free ion energy.

Usually, the free ion state or multiplet is named according to the LS coupling scheme by the symbol $^{2S+1}L_J$, where S and J are specified with numbers (0, $\frac{1}{2}$, 1, ...) and L is traditionally specified with letters[4] $S, P, D, F, G, H, \ldots$ for $L = 0, 1, 2, 3, 4, 5, \ldots$. The energetic ground state of a multi-electron system is in accordance with the LS coupling scheme determined by Hund's rules:

[4]The first four letters are taken from the naming of the orbitals: sharp, principal, diffuse and fundamental. The naming for $L > 3$ follows the alphabet.

Ln^{2+}	Ln^{3+}	n	Ground State	$4f^n$	$4f^{n-1}5d$	$4f^{n-1}6s$	$4f^{n-1}6p$	Sum
-	La	0	$^1S_0$	1	-	-	-	1
La	Ce	1	$^2F_{5/2}$	2	2	1	2	7
Ce	Pr	2	$^3H_4$	13	20	4	12	49
Pr	Nd	3	$^4I_{9/2}$	41	107	24	69	241
Nd	Pm	4	$^5I_4$	107	386	82	242	817
Pm	Sm	5	$^6H_{5/2}$	198	977	208	611	1994
Sm	Eu	6	$^7F_0$	295	1878	396	1168	3737
Eu	Gd	7	$^8S_{7/2}$	327	2725	576	1095	4723
Gd	Tb	8	$^7F_6$	295	3006	654	1928	5883
Tb	Dy	9	$^6H_{15/2}$	198	2725	576	1095	4594
Dy	Ho	10	$^4I_8$	107	2878	396	1168	3549
Ho	Er	11	$^4I_{15/2}$	41	977	208	611	1837
Er	Tm	12	$^3H_6$	13	386	82	242	723
Tm	Yb	13	$^2F_{7/2}$	2	107	24	69	202
Yb	Lu	14	$^1S_0$	1	20	4	12	37

Table 2.3.: The number of energy levels for the four lowest configurations of the free-ion (degeneracy $2J+1$) trivalent and divalent lanthanoids [Die63].

1. For a given electron configuration, the term with maximum multiplicity $2S+1$, i.e. with maximum S has the lowest energy.
2. For a given multiplicity, the term with the largest value of L has the lowest energy.
3. For a given term, in an ion with the outer subshell half-filled or less, the level with the lowest value of J has lowest energy. For more than half-filled outer shells, the level with the highest J value is lowest in energy.

The number of energy levels for the trivalent and divalent lanthanoids are listed together with their ground state notations in table 2.3. The eigenfunctions of the intermediate coupling scheme describe the energy states of the Hamiltonian including Coulomb and spin-orbit interactions and are obtained from mixing all LS terms with the same J in a given $4f^n$ configuration. Due to this mixing labelling a multiplet as $^{2S+1}L_J$ is incomplete in the intermediate coupling scheme. In most cases the nominal labelling of a free ion state in this way only indicates that this multiplet has a leading component from the pure LS basis $\mid LSJ\rangle$. In the early 1960s, Dieke and Crosswhite presented the energy level schemes for the free-ion trivalent and divalent lanthanoids obtained from preliminary empirical data and approximate calculations using two parameters, i.e. the spin-orbit coupling parameter and a scaling parameter determined by the effective charge [Die63]. The results are plotted in figure 2.2. The electrostatic and spin-orbit interactions give the right order of magnitude for the energy level splitting of the $4f^n$ configurations. Although these two interactions are by far the most important terms in the Hamiltonian, often discrepancies of several hundred cm^{-1} between experimental and calculated levels are found. This is because two fitting parameters cannot absorb all the effects of additional mechanisms such as relativistic effects and configuration interactions, i.e. the spin-independent interaction between configurations of equal parity. For n equal or greater than 3, three-body electrostatic configuration interaction has also to be introduced. To overcome the arising difficulties of calculation, the

parametric approach which treats all the radial dependencies as adjustable parameters is often adopted. Following this concept, the matrix elements of effective Hamiltonians describing the different interactions can be rewritten as products of angular and radial integrals. In total, 20 parameters, which are listed in table 2.4 together with the respective Hamiltonian, are required to reproduce the energy level structure of the free ion lanthanoid. These are all phenomenological parameters which are determined through least-squares fitting procedure to experimental data. Thus, an effective-operator Hamiltonian is developed, which has been used as the most comprehensive free-ion Hamiltonian in several spectroscopic analyses of lanthanoid ions in solids.

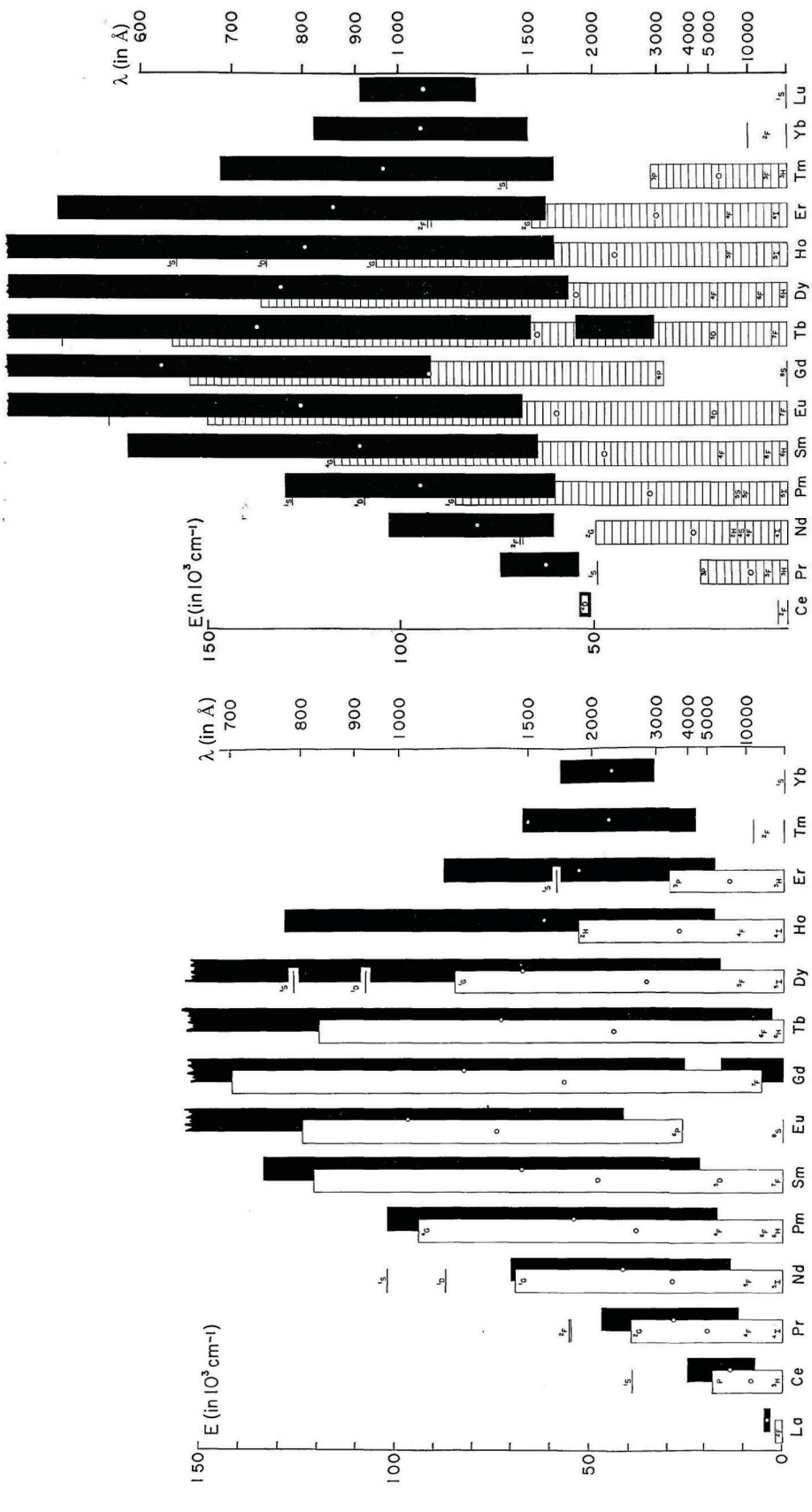

Figure 2.2.: Schematic diagram of the $4f^n$ (white) and $4f^{n-1}5d$ (black) configurations of the divalent (left) and trivalent (right) lanthanoid ions [Die63]. The positions of the $4f^{n-1}5d$ energy levels in the case of the divalent lanthanoids are comparable to those in [Dor03b]. In the case of the trivalent lanthanoids the $4f^{n-1}5d$ levels are at least of the same magnitude as those presented in [Dor00].

The Crystal Field

When the lanthanoid ion is incorporated into a crystalline matrix, it experiences a static electric field due to the charge distribution around the metallic ion which distorts the free space isotropy. The interaction of the ligand field acts strongly on the angular part of the $4f$ wave function and removes partially or totally the degeneracy of the free ion J levels, depending on the degree of symmetry of the site, which the ion occupies. This splitting and shifting of levels, the latter also known as the centroid shift, in the presence of an external static electric field is referred to as the Stark effect [Sta14].

The total Hamiltonian of the lanthanoid ion in a solid is the sum of the free ion and crystal field Hamiltonians:

$$\mathcal{H}_{total} = \mathcal{H}_{free\ ion} + \mathcal{H}_{CF}. \tag{2.12}$$

The crystal field potential is usually expanded in a series of tensor operators that transform like spherical harmonics following the formalism developed by Rajnak and Wybourne [Raj64]. Thus, the Hamiltonian accounting for the single particle crystal field interaction is written as

$$\mathcal{H}_{CF} = \sum_{k,q,i} B_q^k C_q^{(k)}(i), \tag{2.13}$$

where B_q^k are crystal field parameters comprising the radial part and $C_q^{(k)}$ are tensor operators for the angular part of the crystal field matrix elements. k is the rank of the tensor operator and q is the relevant component of this operator limited by the point group symmetry, i.e. by the requirement that the crystal field potential is invariant under the operations of the point group of the lattice site that the ion occupies in the crystal. The coefficients B_q^k are generally treated as crystal field parameters to be determined by a least squares fit to experimental data. In the single independent electron model, these crystal field parameters absorb a variety of combined effects. These are treated as phenomenological parameters that take into account different electrostatic contributions to the general potential generated by the central ion and the ligands. In fact, as they may vary drastically from compound to compound depending on the chemical bonding, they cannot be only described by pure electrostatic interactions and covalent contributions should also be accounted for. Consequently, ab initio crystal field parameter calculations or extrapolation procedures between ions even in the same environment are always a delicate problem. Newman introduced the superposition model to the crystal field theory [New71]. According to his approach, the global potential is the sum of potentials generated by individual ligands. Calculations show that overlap and covalency can be considered as major components which contribute significantly to the crystal potential.

It should be pointed out that due to the time reversal invariance of electric fields, energy levels of systems with an odd number of electrons remain at least doubly degenerate in the presence of purely electric fields. This theorem is referred to as Kramers degeneracy theorem after its discoverer Hendrik Anthony Kramers [Kra30].

The effect of the crystal field is not only the splitting of the $^{2S+1}L_J$ multiplets, but the crystal field operators can also induce J mixing. For this reason, both J and M are no longer considered good quantum numbers. The crystal quantum number μ is introduced to characterise classes of non-interacting sets of states and the total Hamiltonian is diagonalised simultaneously.

	Interaction	Hamiltonian	Parameters	Label	Quantum numbers
Dominant interactions free ion Hamiltonian	Core potential	$\mathcal{H}_0 = \sum_i^n \frac{\hbar^2}{2m_e}\Delta_{r_i}$		Configuration	n, l
	Electronic repulsion ($n \geq 2$)	$\mathcal{H}_{ie} = \sum_{k=0}^{6} f_k F^k$ (k even)	F^0, F^2 F^4, F^6	Terms	L, S
	Spin-orbit	$\mathcal{H}_{so} = A_{so}\zeta_{4f}$	ζ_{4f}	J levels (free ion)	L, S, J
Higher-order corrections free ion Hamiltonian	Two-body configuration interaction	$\mathcal{H}_1 = \alpha L(L+1) + \beta G(G_2) + \gamma G(R_7)$	α, β, γ		
	Three-body configuration interaction ($n \geq 3$)	$\mathcal{H}_2 = \sum_k t_k T^k$	T^k ($k = 2,3,4,6,7,8$)		
	Magnetic effect due to electrostatic configuration interaction	$\mathcal{H}_3 = \sum_k p_k P^k$	P^k ($k = 2,4,6$)		
	Spin-spin and spin-other orbit interaction	$\mathcal{H}_4 = \sum_k m_k M^k$	M^k ($k = 0,2,4$)		
Ion in solid state	Crystal field interaction	$\mathcal{H}_{CF} = \sum_{k,q,i} B_q^k C_q^{(k)}(i)$	B_q^k k, q depend on site symmetry	Crystal field levels	μ

Table 2.4.: List of parameters commonly used in the calculation of energy levels of lanthanoid ions in solids [Cro84, Kru95].

For further, more extensive details about the theoretical considerations just outlined here, one can refer to textbooks and a number of publications, e.g. [Raj64, Jud66, Jud68, New71, Car89, Liu05]. Parameter sets for each lanthanoid ion calculated from mean values from the different free ion parameters available in the literature can be found in [Gör96].

The $4f^{n-1}5d$ Configuration

After only having considered single configuration in the theoretical model for the modelling of the $4f^n$ energy structure of the lanthanoids, the theory needs to be extended, if other configurations are to be taken into account. The number of energy levels in the four lowest configurations of the free-ion trivalent and divalent lanthanoids are summarised in table 2.3. In particular, the $4f^{n-1}5d$ configurations are of interest. These are excited states of ions with $4f^n$ ground configuration, reached by interconfigurational transition, which promotes one $4f$ electron into the $5d$-orbitals. Due to the extended nature of the $5d$ wave functions, there is a displacement of the equilibrium positions of the ligands in the $4f^{n-1}5d$ states. Furthermore, the $4f^{n-1}5d$ configuration has usually[5] a higher average energy than the $4f^n$ configuration, the energy difference containing contributions from several sources such as kinetic energy, Coulomb and crystal field effects. To give a sense for the orders of magnitude, the $4f^n$ and $4f^{n-1}5d$ energy level posi-

[5]The ground state of Gd^{2+} has a $4f^7 5d$ configuration, the $4f^8$ configuration has higher energy.

tions of the divalent and trivalent free-ion lanthanoids relative to the respective ground states are shown in figure 2.2. These were calculated by Dieke and Crosswhite using only two parameters [Die63], however the positions of the $4f^{n-1}5d$ energy levels in the case of the divalent lanthanoids correspond well to the ones given in [Dor03b]. In the case of the trivalent ions, the $4f^{n-1}5d$ levels are at least of the same magnitude as those in [Dor00].

For the calculation of the $4f^{n-1}5d$ energy levels in a crystalline matrix it is necessary to include the splitting of the $5d$ state due to the crystal field and the spin-orbit coupling as well as the interaction between the $4f^{n-1}$ and $5d$ configurations in the cases where $n > 1$. The additions[6] to the free ion Hamiltonian can be described by

$$\mathcal{A}(fd) = \sum_k F^k(fd) f_k(fd) + \sum_j G^j(fd) g_j(fd) + \zeta(dd) A_{SO}(dd), \tag{2.14}$$

with $k = 2,4$ and $j = 1,3,5$ and where the letters in brackets indicate the type of the electron involved in the interaction. The $F^k(fd)$ and $G^j(fd)$ are parameters for the Coulomb interaction between the $4f$ and $5d$ electrons. The $\zeta(dd)$ parameter is associated with the spin-orbit interaction of the $5d$ electron. Due to the extended nature and the therefore weaker shielding by the $5s$ and $5p$ orbitals, the $5d$ shell will be perturbed much more by the host lattice than the $4f$ orbitals. However, the parameters $F^k(fd)$, $G^j(fd)$ and $\zeta(dd)$ are largely determined by the part of the $5d$ orbitals close to the nucleus and therefore, it is expected that these parameters will not significantly differ from the free ion values when incorporated into a crystalline lattice. The influence of the crystal field on the $5d$ electron is given by

$$\mathcal{H}_{CF}(dd) = \sum_{kq} B^k_q(dd) C^{(k)}_q(dd), \tag{2.15}$$

with $k = 2,4$ and the same restrictions for q as for the $4f^n$ configuration. In contrast to the $4f^n$ configuration, where the crystal field is considered a small perturbation, the $5d$ crystal field interactions dominate the splitting of the $4f^{n-1}5d$ configuration. The crystal field parameters associated with the $5d$ electron of the $4f^{n-1}5d$ configuration are large, typically 10 to 20 times the parameters for the $4f$ electrons. In contrast to the energy of the electronic levels of the well shielded $4f^n$ energy levels, which remain constant within several $100\,\mathrm{cm}^{-1}$ in different matrices, the position of the $4f^{n-1}5d$ levels depends strongly on the crystalline environment and may change by tens of thousand cm^{-1} from compound to compound.

In the free ion, since the $4f^n$ and $4f^{n-1}5d$ configurations have opposite parity, there is no electrostatic configuration interaction between them [Hen00]. However, when incorporated into a solid, the odd parity crystal field interaction can lead to coupling of the configurations, the contribution to the Hamiltonian of which is

$$\mathcal{H}_{CF}(fd) = \sum_{kq} B^k_q(fd) C^{(k)}_q(fd), \tag{2.16}$$

where $k = 1,3,5$. This mixing of $4f$ states with opposite parity configurations is of essential importance for the spectroscopical properties of lanthanoids in solids. These admixtures give rise to the originally parity forbidden electric dipole transitions within the $4f$ shell [Ofe62,

[6] The $4f^{n-1}$ core can be treated as to experience the same interactions as the $4f^n$ configuration.

Jud62]. However, calculations showed that this coupling of configurations has only a small effect on the energy levels of either configuration. Detailed descriptions of the theory and comparisons to experiments can be found in, e.g. [Rei00, Rei02, Pie02].

In 2000, Dorenbos showed that once the position of the lowest $4f^{n-1}5d$ level of a trivalent lanthanoid in a compound is known, the lowest $4f^{n-1}5d$ levels of all other trivalent lanthanoids in that same compound can be predicted with an accuracy of $\pm 600\,\mathrm{cm}^{-1}$ [Dor00][7]. An empirical expression which relates the energy difference between the $4f^n$ and the lowest $4f^{n-1}5d$ states $E(Ln,A)$ in units of cm^{-1} was introduced:

$$E(Ln,A) = 49\,340\,\mathrm{cm}^{-1} - D(A) + \Delta E^{Ln,Ce}, \tag{2.17}$$

with $49\,340\,\mathrm{cm}^{-1}$ being the energy of the first transition between the $4f^1$ and the $5d^1$ states of the free Ce^{3+}-ion, $D(A)$ being the so-called crystal field depression and $\Delta E^{Ln,Ce}$, which is defined as the difference between the lowest $4f^{n-1}5d$ level of Ln^{3+} and that of Ce^{3+}. The crystal field depression is the lowering of the energy of the first interconfigurational transition when the lanthanoid ion is incorporated into a compound. The magnitude of this red shift in a certain material appears, in first approximation, the same for all lanthanoids. In contrast, $\Delta E^{Ln,Ce}$ is in first approximation independent of the type of compound and can therefore be regarded as an intrinsic property of the lanthanoid ion. Tables listing the $\Delta E^{Ln,Ce}$ values for the different trivalent lanthanoids and $D(A)$ values for different compounds can be found in [Dor00].

[7] A similar dependency is suggested also for the divalent lanthanoids [Dor03b]. The crystal field depression of divalent lanthanoids $D(2+,A)$ on trivalent sites is usually not available, however the empirical relationship $D(2+,A) = 0.64D(3+,A) - 0.233\,\mathrm{eV}$ is a good estimate [Dor03c].

2.2. The Interaction of Light and Matter

Regarding the interaction of light and matter one distinguishes between intraionic, interionic and electron exchange processes such as charge transfer and ionisation. In the following these three different types of processes will be introduced and examined regarding their specific properties. The selection rules for the respective optical transitions are also discussed.

2.2.1. Intraionic Processes

As described in section 2.1, electrons bound to an ion only occupy a series of discrete states, with electromagnetically induced transitions among these states giving rise to the ion's optical spectrum. Intraionic refers to those processes which occur within the energy levels of just one ion.

Through energy deposition into a lanthanoid-doped solid material it is possible to shift the lanthanoid ion into an excited state. This process is referred to as absorption. The excited ion can relax to a lower lying energy level or back to its ground state by stimulated or spontaneous emission. The principles of these three most basic mechanisms of interaction between light and matter were first described by Albert Einstein back in 1916 [Ein16].

Absorption and Stimulated Emission

Between two energy states E_1 and E_2 of an ion, where $E_1 < E_2$ and E_1 is the initial state, a photon of frequency ν can be resonantly absorbed if $\Delta E = E_2 - E_1 = E_\gamma = h\nu$, with h being Planck's constant. The population density N_1 of the initial state changes as

$$\frac{dN_1}{dt} = -W_{12}N_1 = -\sigma_{12}FN_1, \tag{2.18}$$

where $W_{12} = \sigma_{12}F$ is the rate of absorption dependent on the photon flux F and the absorption cross-section σ_{12}, which is defined as the probability of an absorption transition per second per unit photon flux per ion in the starting level. A schematic visualising this process is given on the left of figure 2.3.

Stimulated emission occurs when an ion in its excited state E_2 is irradiated with photons of energy $h\nu$ resonant to the energy difference ΔE. The excited ion is stimulated to relax down to the state E_1 thereby emitting a photon which is identical to the stimulating photon in frequency, phase, polarisation and propagation direction. The process of stimulated emission can be described as

$$\frac{dN_2}{dt} = -W_{21}N_2 = -\sigma_{21}FN_2, \tag{2.19}$$

with the stimulated emission cross-section σ_{21} and the initial state E_2 having the population density N_2. This process is schematically depicted in the middle of figure 2.3. These processes

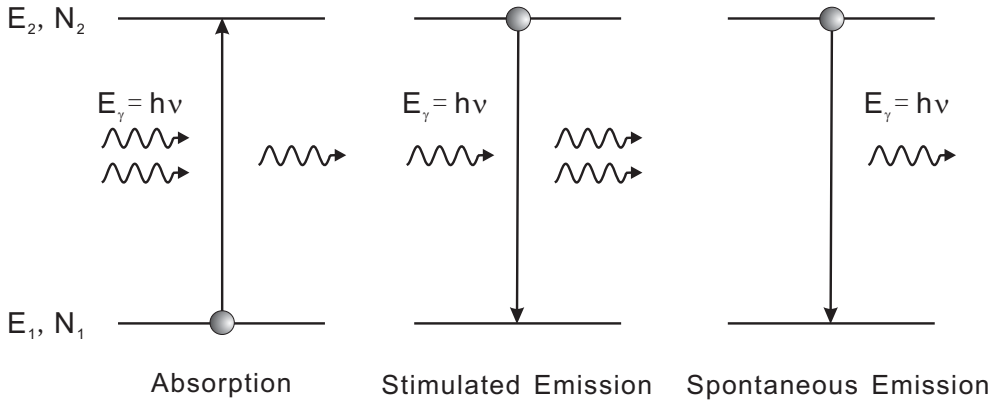

Figure 2.3.: The three most basic processes of interaction between light and matter are the intraionic processes of absorption (left), stimulated emission (middle) and spontaneous emission (right).

of absorption and stimulated emission are physically symmetric and for levels of same degeneracy the probability of both events is the same. For states i with degeneracy g_i, the atomic cross-sections for absorption and stimulated emission have the following relationship

$$g_1 \cdot \sigma_{12} = g_2 \cdot \sigma_{21}. \tag{2.20}$$

If an optically active medium of length z is irradiated with electromagnetic radiation of frequency ν, resonant to the energy difference of the active ion's excited state E_2 and the ground state E_1 with population densities N_2 and N_1 respectively, the change of the photon flux F is given by

$$dF = (\sigma_{21} F N_2 - \sigma_{12} F N_1)\, dz = \sigma_{21} F \left(N_2 - \frac{g_2}{g_1} N_1 \right) dz. \tag{2.21}$$

Gain, i.e. the amplification of photon flux, can only be achieved if $\frac{dF}{dz}$ is positive, for which the condition

$$N_2 > \frac{g_2}{g_1} N_1 \tag{2.22}$$

needs to be satisfied. This condition is referred to as population inversion and can e.g. be achieved by optical excitation also referred to as optical pumping of the active medium. In a classical two level system inversion cannot be realised as the absorption and the stimulated emission cross-sections are equal and at $N_2 = N_1$ both processes will compensate for each other. Inversion is needed for the realisation of a laser and therefore the involvement of at least three or four energy levels is a requirement.

Equation 2.21 also gives rise to the Beer-Lambert law. If stimulated emission can be neglected, due to absorption incident light of intensity I with resonant frequency is only partly transmitted when travelling through a medium of length z

$$dI = -\sigma_{12} I N_1 dz. \tag{2.23}$$

The solution is obtained by integration and yields an exponential relationship between the intensity of the incident light I_0 and that of the transmitted light I

$$I = I_0 \exp(-\alpha z) \tag{2.24}$$

with $\alpha = N_1\sigma_{12}$ being the absorption coefficient of the material.

If the initial state of an absorption process is not the ground state level of the optically active ion but an excited state, this process is referred to as excited state absorption (ESA). ESA can be a major loss process in laser materials if the process is resonant to the pump or laser radiation. However, it is also possible to take advantage of ESA and populate high lying excited states, using a multi-step absorption process, in which ions are excited from the ground state to an excited state and from there again into another excited state.

Spontaneous Emission

An ion in an excited state E_2 may decay to a lower lying state or ground state E_1 spontaneously by emitting a photon with the frequency ν, where $\Delta E = E_\gamma = h\nu$ (figure 2.3, right). The phase of the emitted photon is random as is the direction the photon propagates in. The spontaneous emission follows the same probability law as radioactive decay. If no other processes are involved, the change in population density of the excited level is given by

$$\frac{dN_2}{dt} = -A_{21}N_2, \tag{2.25}$$

where the rate of spontaneous emission A_{21}, also referred to as the Einstein A coefficient is with $A_{21} = \frac{1}{\tau_{rad}}$ the inverse of the radiative lifetime τ_{rad}. With this the solution of equation 2.25 can be written as

$$N_2(t) = N_{2,0}\exp\left(-\frac{t}{\tau_{rad}}\right) \tag{2.26}$$

with $N_{2,0}$ being the initial density of excited states at time 0. In general, an excited state E_j can relax into more than one lower lying level. The total rate of the spontaneous emission A_j is then described by

$$A_j = \sum_{i<j} A_{ji} = \sum_{i<j} \frac{1}{\tau_{ji}}, \tag{2.27}$$

where the summation is done over all possible final states of the decay i. The radiative lifetime $\tau_{rad,j}$ of state j is then given by

$$\tau_{rad,j} = \frac{1}{A_j}. \tag{2.28}$$

The branching ratio β_{jl} gives the fraction of excited states j which decay by an individual decay channel to the final state l with respect to the total number of excited states j which decay

$$\beta_{jl} = \frac{A_{jl}}{\sum_{i<l<j} A_{ji}}. \tag{2.29}$$

The spontaneous emission can be treated as a stimulated emission into the vacuum fluctuations of the photon field. To explain the reasons for spontaneous transitions to occur, quantum electrodynamics is needed. More information can be found in text books such as [Gol95].

Einstein Coefficients

At equilibrium the net change in the density of excited states is zero being balanced by decay and gain due to all processes.

$$0 = A_{21}N_2 + B_{21}\rho(\nu)N_2 - B_{12}\rho(\nu)N_1, \tag{2.30}$$

with $B_{ij} \cdot \rho(\nu) = W_{ij}$, where $\rho(\nu)$ is the radiation density of the radiation field at the frequency of the transition and B_{ij} are the Einstein B coefficients, which determine the probability for the transition between the states i and j, per second, per unit spectral radiance of the radiation field. Following the Boltzmann distribution for the fractional number of ions occupying a set of states i possessing energy E_i

$$\frac{N_i}{N} = \frac{g_i \exp(-E_i/k_BT)}{Z(T)}, \tag{2.31}$$

where $N = \sum_i N_i$ is the total number of optically active ions, g_i is the degeneracy, k_B is the Boltzmann constant, T is the temperature and $Z(T) = \sum_i g_i \exp(-E_i/k_BT)$ is the partition function. The ratio of the populations of level 1 and 2 is thus obtained as

$$\frac{N_2}{N_1} = \frac{g_2}{g_1} \exp\left(-\frac{E_2 - E_1}{k_BT}\right). \tag{2.32}$$

Substituting this expression into equation 2.30 and using the relation $E_2 - E_1 = h\nu$ yields

$$\rho(\nu) = \frac{A_{21}}{B_{12}\frac{g_1}{g_2}\exp(h\nu/k_BT) - B_{21}}. \tag{2.33}$$

By identifying equation 2.33 with Planck's law

$$\rho(\nu) = \frac{8\pi h\nu^3}{c^3} \frac{1}{\exp(h\nu/k_BT) - 1} \tag{2.34}$$

the relationship between the Einstein A and B coefficients can be written as

$$\frac{A_{21}}{B_{21}} = \frac{8\pi h\nu^3}{c^3} \tag{2.35}$$

and

$$\frac{B_{21}}{B_{12}} = \frac{g_1}{g_2}. \tag{2.36}$$

The stimulated transition rates W_{ij} are obtained by a semiclassical approximation in which the ion is treated quantum mechanically with the Schrödinger equation while the electromagnetic radiation is described classically by Maxwell's equations. For incident electromagnetic radiation of the form $\overrightarrow{E} = \overrightarrow{E_0}\sin(2\pi\nu t)$ with amplitude $\overrightarrow{E_0}$, the frequency ν close to the resonant frequency $\nu_0 = (E_2 - E_1)/h$ and a wavelength much larger than the ionic radius, the transition rate can be obtained using time dependent perturbation theory

$$W_{ij} = \frac{\pi^2}{3h^2} |\overrightarrow{\mu_{ij}}|^2 \overrightarrow{E_0}^2 \delta(\nu - \nu_0) \tag{2.37}$$

with the transition dipole moment $\overrightarrow{\mu_{ij}}$, which is given by the relevant off-diagonal element of the dipole matrix calculated from an integral taken over the product of the wave functions Ψ_i, the initial, and Ψ_j, the final states of the transition, and the dipole moment operator $\widehat{d}$

$$\overrightarrow{\mu_{ij}} = \int \Psi_i^* \widehat{d} \Psi_j dV. \tag{2.38}$$

Effective Cross-Sections

Often, the lanthanoid energy levels participating in optical transitions are different components of Stark split $4f$ manifolds. As the crystal field splitting is usually in the range of some $100\,\mathrm{cm}^{-1}$ [Liu05], the different Stark levels of a manifold are thermally coupled. Thermalisation within a manifold is reached on very short time scales, i.e. usually within picoseconds or less [Gay86].

The relative probability of a Stark level i of a multiplet m being occupied at thermal equilibrium is given by the Boltzmann factor

$$f_{m,i} = g_{m,i} \exp\left(-\frac{E_{m,i} - E_{m,0}}{k_B T}\right), \tag{2.39}$$

where $g_{m,i}$ is the degeneracy and $E_{m,i}$ is the energy of Stark level i, $E_{m,0}$ is the lowest Stark level of multiplet m, k_B is the Boltzmann constant and T is the temperature. The ratio of the probabilities of two states is given by the ratio of their Boltzmann factors. Normalising the Boltzmann factor with the partition function

$$Z_m = \sum_j g_{m,j} \exp\left(-\frac{E_{m,j} - E_{m,0}}{k_B T}\right), \tag{2.40}$$

which is the sum of all Boltzmann factors for all Stark levels of the manifold m, gives the Boltzmann distribution, which describes the fractional number of ions in state i relative to the total number of ions occupying the multiplet m

$$\frac{N_{m,i}}{N_m} = \frac{g_{m,i} \exp\left(-\frac{E_{m,i} - E_{m,0}}{k_B T}\right)}{Z_m}. \tag{2.41}$$

The atomic cross-sections introduced in equations 2.18 and 2.19 are defined for certain electronic energy levels. For transitions between Stark split manifolds this concept cannot easily be applied, since the different combinations of sublevel transitions overlap spectrally and are therefore difficult to distinguish. Depending on the wavelength, transitions between different Stark levels contribute with varying degrees. Temperature dependent broadening mechanisms further complicates the assignments. Also, often the exact energetic positions of the Stark levels are not known. Therefore, it is more convenient to use the so called effective cross-sections, which are related to the averages of the cross-sections of different sublevel transitions, with weight factors depending on population densities in thermal equilibrium.

The effective cross-sections of the absorption and emission processes arising from the upper and lower manifolds u and l with the Stark levels j and k characterised by the energies E_j and E_k and the degeneracies g_j and g_k, respectively, can be described as a summation of the individual atomic cross-sections σ_{jk} and σ_{kj} between the Stark levels as follows [Pay92]:

$$\begin{aligned} \sigma_{abs}(\lambda) &= \sum_{jk} \frac{N_{l,j}}{N_l} \sigma_{jk}(\lambda) g_k \\ \sigma_{em}(\lambda) &= \sum_{jk} \frac{N_{u,k}}{N_u} \sigma_{kj}(\lambda) g_j. \end{aligned} \tag{2.42}$$

These effective transition cross-sections can directly be obtained from spectroscopic measurements without resolving the different sublevel transitions. It should be pointed out that effective cross-sections are strongly temperature dependent as temperature directly affects the relative occupation probabilities within the sublevels.

Saturation of the Ground State Absorption

The efficiency of pump absorption can be reduced by bleaching of the ground state population of the optically active ions. This effect is in the first instance dependent on the intensity of the incident radiation. The higher the population density of the excited state the lower is the population density of the ground state and consequently the probability for ground state absorption. In extreme cases the ground state depletion can lead to total bleaching of the absorption and the material becomes transparent. The magnitude of this ground state depletion depends predominantly on the absorption cross-section σ_{abs} and the radiative emission lifetime τ_{rad}.

Consider two Stark level manifolds E_1 and E_2 with E_1 being the ground state of the system. Pumping the system with light of energy $E_2 - E_1 = h\nu$ leads to population of level E_2 as described in section above. Taking into account the processes of absorption, stimulated emission and spontaneous decay, the change in population of E_2 with time is given by

$$\frac{dN_2}{dt} = (\sigma_{abs} N_1 - \sigma_{em} N_2) \frac{S_p}{h\nu} - \frac{1}{\tau_{rad}} N_2, \tag{2.43}$$

where the product of the pump power density S_p and the photon energy is the pump photon flux, $h\nu \frac{S_p}{h\nu} = F$. If no other energy level is involved $N_t = N_1 + N_2$ is the total doping concentration of the optically active ions. For steady state condition, i.e. for $\frac{dN_2}{dt} = 0$, the excited state population can be expressed as

$$N_2 = \frac{\sigma_{abs}\tau_{rad}}{h\nu} N_t \cdot \frac{S_p}{1 + \frac{S_p}{S_p^{sat}}} \tag{2.44}$$

with $S_p^{sat} = \frac{h\nu}{\tau_{rad}(\sigma_{abs}+\sigma_{em})}$ being the pump power saturation density. This expression for the excited state population can be approximated for two cases. If $S_p \ll S_p^{sat}$,

$$N_2 \approx \frac{\sigma_{abs}\tau_{rad}}{h\nu} N_t \cdot S_p \tag{2.45}$$

and the excited state population is directly proportional to the pump power. If, $S_p \gg S_p^{sat}$,

$$N_2 \approx \frac{\sigma_{abs}\tau_{rad}}{h\nu} N_t \cdot S_p^{sat} = \frac{\sigma_{abs}}{\sigma_{abs} + \sigma_{em}} N_t \tag{2.46}$$

and saturation is reached. It is obvious that for a true two level system, where $\sigma_{abs} = \sigma_{em}$, no population inversion can be achieved as N_2 cannot exceed $\frac{N_t}{2}$.

Accordingly, the absorption coefficient is modified. The absorption coefficient α for a given frequency ν at high pump power densities is given by:

$$\alpha(\nu) = \sigma_{abs} N_1 - \sigma_{em} N_2 = \frac{\alpha_0}{1 + \frac{S_p}{S_p^{sat}}}, \tag{2.47}$$

where $\alpha_0 = \sigma_{abs} N_t$ is the unsaturated or small signal absorption coefficient, which applies in the case of low optical intensities.

The Influence of Phonons

The interaction of the $4f$ electrons with their surroundings is well known to be weak due to the shielding by the outer $5s^2$ and $5p^6$ electrons. This shielding gives the optical spectra of the lanthanoid ions their characteristic appearance with sharp transition lines, which resemble atomic spectra. Still electron-phonon coupling is present and this interaction is responsible for important processes, e.g multiphonon relaxation, vibronic transitions, line broadening, and phonon-assisted energy transfer. Some of these phenomena are discussed in the following paragraphs.

Vibronic Transitions

An optical centre in a solid interacts with its surroundings (the ligands) by participating in the vibrational motion of the host lattice, which affects the optical properties of the centre. The literature contains many terms to indicate this interaction, e.g. electron-lattice interaction, electron-phonon interaction or vibrational-electronic interaction. Following the latter notation, in this work optical transitions, which involve simultaneous changes in the electronic and in the vibrational states of the system are called vibrational-electronic transitions or abbreviated, vibronic transitions.

The environment of a dopant ion in a host lattice is not static, i.e. the surrounding ions vibrate about some average positions, so that the crystalline field varies. If the vibronic interaction is weak, the spectra will be dominated by sharp lines, especially at low temperatures. If the interaction is strong, structureless bands are observed.

When discussing optical transitions this vibronic interaction needs to be taken into account. Optical transitions can take place if the energy of the photon corresponds to the purely electronic transition energy or to the purely electronic transition energy plus the energy of one or more lattice phonons. The involved states are described by so-called Born-Oppenheimer-wave functions $\Psi = \psi\chi$ which are based on the Born-Oppenheimer approximation [Bor27]. This approximation, also known as the adiabatic approximation, implies gradual (adiabatic) adjustment of the electronic states to the slowly varying ionic positions, which applies as the electron motion is several orders of magnitudes faster than the ionic motion. The Born-Oppenheimer approximation thus allows the separation of the wave function into a product of purely electronic

wave functions ψ and purely vibrational wave functions χ. Considering a vibronic transition between two states $\Psi(a,n)$ and $\Psi(b,n')$ where a and b are the initial and final electronic states and n and n' are the initial and final vibrational states, respectively. The transition matrix element $\overrightarrow{\mu}$ in equation 2.38 is then given by

$$\overrightarrow{\mu} = \int \Psi^*(b,n')\widehat{d}\Psi(a,n)dV = \int \psi^*(b)\chi_b^*(n')\widehat{d}\psi(a)\chi_a(n)dV. \tag{2.48}$$

At low temperatures only the $n = 0$ vibrational level of the initial electronic state a will be occupied. The transition from $n = 0$ to $n' = 0$ is purely electronic since no vibrational change is involved. These so-called zero-phonon transitions usually occur in spectra as very sharp lines. At higher temperatures also vibrational levels with $n > 0$ are occupied in the initial electronic state a. As a consequence the vibronic intensities are temperature dependent. By using the Condon approximation, i.e. the assumption that the electronic wave functions are independent of nuclear coordinates [Con26], equation 2.48 can be simplified to

$$\overrightarrow{\mu} = \int \Psi^*(b,n')\widehat{d}\Psi(a,n)dV = \int \psi^*(b)\widehat{d}\psi(a)dV \int \chi_b^*(n')\chi_a(n)dV. \tag{2.49}$$

Equation 2.49 is the mathematical expression of the so-called Franck-Condon principle [Fra26, Con26]. This principle states that during an optical transition between two vibronic states, a change from one vibrational energy level to another will be more likely if there is a large overlap between the two vibrational wave functions.

The most simple model which accounts for the interaction between the electronic states of the dopant ion and the vibrating lattice is the single configurational coordinate model [Hip36, Sei39]. In this model, only one vibrational mode is considered, the so-called breathing or stretching mode in which the surrounding lattice pulsates in and out around the optically active ion. This model is assumed to be described by the harmonic oscillator model. The configurational coordinate Q represents the distance from the central ion to the first shell of the neighbouring ions and is the variable of the lattice state, which oscillates about its equilibrium value Q_0. Usually, the effect of lattice distortion on the electronic energy and the interionic potential energy are summarised by a Morse potential. In the harmonic approximation the Morse potential is replaced by a harmonic potential $V(Q)$ and the ionic energy potentials, i.e. the electronic states appear as parabolas when plotted against the configurational coordinate Q. The ionic potential energy of an electronic state a is written as

$$E^{(a)}(Q) = E_0^{(a)} + V^{(a)}(Q), \tag{2.50}$$

where $E_0^{(a)} = E^{(a)}(Q_0)$ represents the average energy in the equilibrium distance of state a. The harmonic potential is given by

$$V^{(a)}(Q) = \frac{1}{2}M\omega^2(Q - Q_0^{(a)})^2 \tag{2.51}$$

with M being an effective ligand mass and ω being the frequency of the breathing mode. In general, two states (a) and (b) of one system have different equilibrium distances as well as different breathing modes, i.e. the two states experience different electron-phonon coupling. In

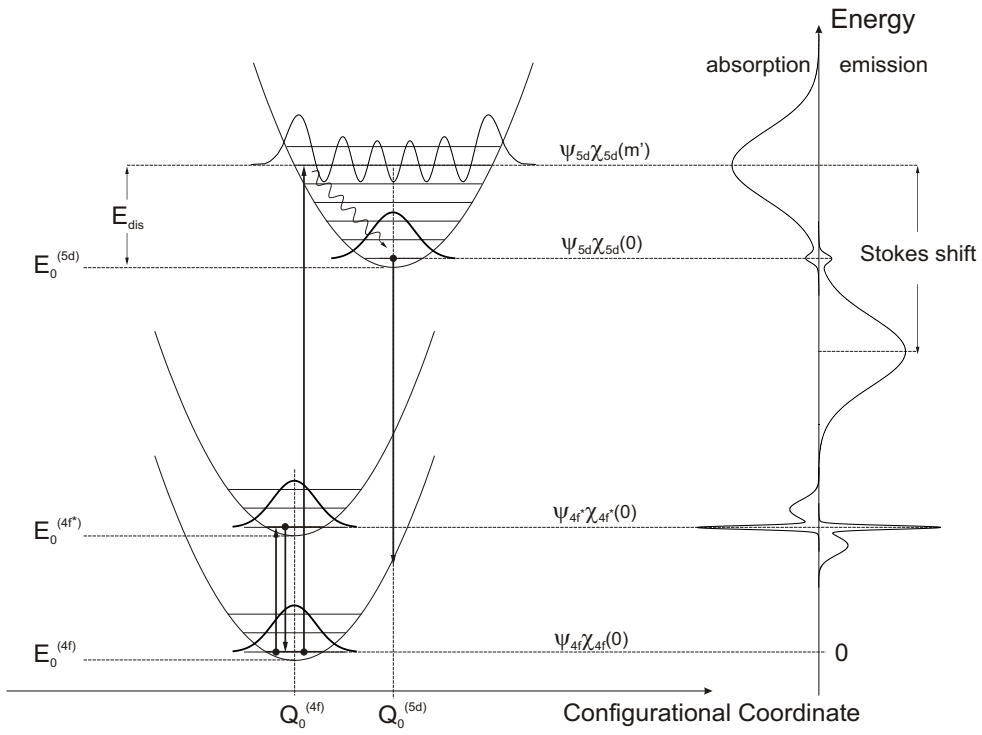

Figure 2.4.: Configurational coordinate diagram in the harmonic approximation for an electronic ground state of the $4f^n$ configuration with two excited states $4f^*$ and $5d$ of the $4f^n$ and the $4f^{n-1}5d$ configuration, respectively.

the configurational coordinate diagram the difference in electron-phonon coupling of two states therefore manifests itself in a lateral displacement of the equilibrium distances and parabolas of different widths. Usually, an electron in the excited state is weaker bound than in the ground state which suggests lower frequencies for the breathing mode[8]. For the following discussion the common simplifying assumption that the vibrational frequency is the same for both electronic states is adopted. Therefore, the parabolas in figure 2.4 have all the same curvature.

Figure 2.4 schematically shows the configurational coordinate diagram for an arbitrary lanthanoid ion with an electronic ground state $4f$ and the two excited states $4f^*$ and $5d$, where the ground state and the first excited state $4f^*$ are both of $4f^n$ configuration and the state $5d$ of $4f^{n-1}5d$ configuration. The ground state energy $E_0^{(4f)}$ is treated as the zero of energy. The vibrational levels for each of the electronic states are indicated by equidistant horizontal lines. The amplitudes of the harmonic oscillator wave function $\chi_{5d}(m')$ as well as those of the ground state harmonic oscillator wave functions $\chi_a(0)$ are also shown. The wave function of the lowest vibrational state $\chi_a(0)$ is Gaussian, which means the most likely value of Q is Q_0. For higher vibrational states however, the probability distribution of the ligand position has the greatest amplitude at the turn around points just as for the classical oscillator. The turn around points correspond to positions where the potential energy of the oscillator reaches its maximum value,

[8]Usually, excitation leads to a more extended probability density which in turn leads to an increase in the ionic radius. For this reason the lattice in the surroundings of the excited ion is distorted and the bond length is changed. The binding energy decreases resulting in the decrease of the breathing mode's frequency. The energy of the excited state then depends less on the configurational coordinate, i.e. the potential curve has less curvature [Nak06].

i.e. the most probable values of Q lie very close to the parabolas. Optical transitions between levels of $4f^n$ configuration belong to the weak interaction case. Actually, the interaction is usually assumed to be vanishing due to the shielding by the outer $5s$ and $5p$ electrons. Therefore, the two parabolas for states $4f$ and $4f^*$ have the same equilibrium distance $Q_0^{(4f)}$. The situation is different for the $4f^{n-1}5d$ configuration, as the $5d$ orbitals are more extended compared to $4f$ orbitals and therefore less shielded. The $5d$ level thus has a different equilibrium distance $Q_0^{(b)}$. According to the Franck-Condon principle equation 2.49, the value of Q does not change instantaneously during transitions between states so that the transition energies are described by vertical distances and optical transitions are indicated by vertical arrows in figure 2.4. For the intraconfigurational transition between the ground state and the excited state $4f^*$ at low temperatures, the highest overlap for the vibrational wave functions is found for the $\psi_{4f}\chi_{4f}(0)$ and $\psi_{4f^*}\chi_{4f^*}(0)$ states. Consequently, the most probable optical transitions between $4f^n$ states are sharp zero phonon transitions. The spectra are therefore dominated by strong zero phonon lines accompanied by weak one-phonon sidebands as indicated on the right side of figure 2.4. In case of interconfigurational optical transitions, e.g. from the $4f$ ground state to the excited state $5d$ with different equilibrium distances, the transition leaves the upper electronic state in a highly excited vibrational level $\chi_{5d}(m')$ that may subsequently relax through multiphonon emission as indicated by the curled arrow in figure 2.4. This relaxation can be understood as lattice relaxation of the whole system, to the equilibrium configuration of the excited state, i.e. the adjustment of the excited ion's surroundings to the new situation, which usually implies changes in ionic radii, Coulomb forces, nearest neighbour distances, bond strength, etc. At this point, the energy of the system is reduced by $E_{dis} = \frac{1}{2}M\omega^2(Q_0^{(5d)} - Q_0^{(4f)})$. This energy is dissipated into the lattice and therefore also often referred to as lattice relaxation energy. The difference in the equilibrium distances leads to high electron-phonon couplings for the interconfigurational transitions. The band peaks in the optical spectra occur at the energies given by the lengths of the vertical arrows. The optical emission from the $5d$ state to the ground state thus occurs at lower energy. This shift in energy between the emission and the absorption peaks is known as the Stokes shift. Other than for the intraconfigurational transitions between $4f^n$ states, for the interconfigurational transition most of the intensity is in the phonon sidebands and the zero phonon line is less pronounced. As the excited state parabolas and the ground state parabola in this representation are all identical, the emission and absorption band shapes indicated on the right side of figure 2.4 are mirror images of each other.

The strength of electron-phonon coupling for an optical transition between two states a and b is often described by the so-called Huang-Rhys parameter [Hua50]

$$S = \frac{1}{2}\frac{M\omega^2}{\hbar\omega}\left(Q_0^{(a)} - Q_0^{(b)}\right)^2 = \frac{E_{dis}}{\hbar\omega}, \tag{2.52}$$

which represents the number of phonons created during lattice relaxation . The S value can vary from $S = 0$ for vanishing coupling to $S \sim 20 - 40$ for very strong coupling. One speaks of intermediate coupling if $1 < S < 5$, which is the case for most interconfigurational transitions between $4f^n$ and $4f^{n-1}5d$ states [Bla92]. As stated above, intraconfigurational transitions between $4f^n$ states belong to the weak coupling case with $S < 1$ [Hen89].

The theory of vibronic transitions is well developed and has been described in many textbooks, e.g. [Hen89].

Line Broadening

In equation 2.37 the linewidth of the optical transition was assumed to be a Dirac δ-function. For a number of reasons this is not true. However, equation 2.37 remains valid if the δ-function is replaced by the normalised line shape function $g(\nu - \nu_0)$, which depends on the particular broadening mechanisms involved. The linewidth, i.e. the full width at half maximum (FWHM), of a zero phonon line is bounded from below by the spontaneous emission lifetime of the states involved in the transition. This affects all ions of the same type in the same way and therefore belongs to the homogeneous broadening mechanisms. The natural linewidth is thus described by a Lorentzian line. In terms of line broadening however, as the radiative lifetimes of lanthanoid $4f$ states are typically in the order of 10^{-2}-10^{-6} s, ($\Delta\nu_{nat} = (2\pi\tau_{sp})^{-1}$), natural line broadening can usually be considered negligible [Yen64]. At the lowest temperatures, the transition linewidths of optically active ions incorporated into solids exhibit measurable breadth, which can be accounted to random variations of the active ions' surroundings. These local field variations lead to inhomogeneous line broadening and the line shape function is given by a Gaussian function. At 4.2K, typical inhomogeneous linewidths for optical transitions in lanthanoid ions are of the order of $0.1\,\mathrm{cm}^{-1}$ in high quality single crystals [Yen64] and up to some $100\,\mathrm{cm}^{-1}$ in glasses [Ber86]. While inhomogeneous line broadening dominates at low temperatures, with increasing temperature the contribution of phonons increases and so do the widths of the lines. The total linewidth of a transition $\Delta E(T)$ (in cm^{-1}) is given by

$$\Delta E(T) = E^{Inh} + E^{Rad} + E^{D}(T) + E^{R}(T) + E^{Orb}(T) + E^{MR}(T), \tag{2.53}$$

where E^{Inh} and E^{Rad} are the temperature independent contributions due to inhomogeneous linebroadening and radiative relaxation, respectively. The one-phonon process ($E^{D}(T)$), the Raman two-phonon process ($E^{R}(T)$), the Orbach two-phonon process ($E^{Orb}(T)$), and the multiphonon relaxation ($E^{MR}(T)$) are the temperature dependent contributions. As stated above, natural line broadening can usually be neglected. The same holds for the multi-phonon process, where the energy difference between two states is bridged by the simultaneous emission or absorption of more than one phonon [Yen64, Ris67]. The Orbach two-phonon process is a resonant two-phonon process. In terms of line broadening it is usually only considered to be effective in the case of relaxation between Zeeman split, Kramers degenerate energy levels, where one-phonon as well as Raman processes are of minor importance. The remaining contributions are thus due to the inhomogeneous linewidth, the one-phonon process and the Raman two-phonon process.

The one-phonon process is a direct process, where the energy difference ΔE_{ij} between two states i and j, which e.g. can be the different components of a Stark split multiplet, is bridged by one single phonon. This contribution is described by

$$E^{D}(T) = E^{D}_{em}(T) + E^{D}_{abs}(T) = \sum_{j<i} \beta_{ij}(n+1) + \sum_{j>i} \beta_{ij}(n), \tag{2.54}$$

where E^{D}_{em} and E^{D}_{abs} are the contributions of emission and absorption, respectively. n is the phonon occupation number given by

$$n = \frac{1}{\exp(\Delta E_{ij}/k_B T) - 1}, \tag{2.55}$$

and β_{ij} is a parameter describing the electron-phonon coupling strength for the direct process. The direct process is often neglected, e.g. in [Kus69], however its contribution can be significant, see e.g. [Yen64] .

The Raman two-phonon process $\Delta E^R(T)$ is a non-resonant process. The energy level i absorbs one phonon, which bridges the gap to a virtual level j', that subsequently decays to the level j with $E_j > E_i$ through the emission of another phonon. In this case, the energy differences between the levels i and j' as well as j and j' are assumed to be large compared to the energy difference between levels i and j. If the phonons that are absorbed and emitted are of the same energy, the process is called intrinsic Raman two-phonon process [Hen89]. The temperature-dependent contribution to the linewidth due to the Raman process is described by

$$E^R(T) = \overline{\alpha}\left(\frac{T}{\Theta_D}\right)^7 \int_0^{\Theta_D/T} \frac{x^6 \exp(x)}{(\exp(x)-1)^2} dx. \tag{2.56}$$

In this equation $\overline{\alpha}$ describes the electron-phonon coupling strength for the Raman process, Θ_D is the Debye temperature and $x = \hbar\omega/k_B T$. In terms of line broadening, usually the contribution from the Raman two-phonon process becomes dominant at room temperature [Ell97b].

All phonon based contributions to the line broadening give rise to homogeneous line broadening and thus the associated line shape function is described by a Lorentzian. If homogeneous and inhomogeneous contributions are of the same order, the total line shape function is given by the convolution of the Gaussian and the Lorentzian function, the so-called Voigt profile.

Nonradiative Decay and Multiphonon Relaxation

The excited state of an ion can relax to a lower lying level not only through the spontaneous emission of a photon, as described in section 2.2.1, but also the relaxation process to the next lowest level can occur nonradiatively through multiphonon emission. In this case, the energy ΔE between the two states participating in the transition is emitted to the lattice as phonons. Usually, several phonons are involved, i.e. the process is of higher order. Assuming reasonably low temperatures and neglecting other decay channels, as e.g. nonradiative energy transfer processes, the spontaneous nonradiative decay rate $W_{nr,0}$ has an exponential dependence on the energy gap between levels [Ris68, Miy70]:

$$W_{nr,0} = C \cdot \exp(-\alpha \cdot \Delta E), \tag{2.57}$$

where C, associated to the relaxation rate extrapolated to zero gap, and α are constants which are characteristic of the particular crystal. With increasing temperature, induced phonon emission becomes important and then the transition probability is given by [Ris67, Web68]

$$W_{nr}(T) = W_{nr,0} \cdot (1 - \exp(-\hbar\omega/k_B T))^{-p}, \tag{2.58}$$

where the order of the process p is given by the number of the phonons of equal energy emitted, the sum of which is equal to the total relaxation energy

$$p = \frac{\Delta E}{\hbar\omega_{eff}}. \tag{2.59}$$

In this treatment, the different lattice phonons participating in the transition are summarised to one effective phonon of the energy $\hbar\omega_{eff}$. However, Riseberg *et al.* found that the multiphonon decay is dominated by processes involving the most energetic phonons available, i.e. multiphonon relaxation is primarily due to those processes that can occur in lowest order. As a rule of thumb, the multiphonon relaxation rate becomes equal to radiative rates if the energy gap ΔE to the next lowest level corresponds to four or five times the energy of the most energetic phonon [Ris67].

If interionic energy transfer processes are absent, the fluorescence lifetime τ_{flu} of an excited state is thus given by

$$\frac{1}{\tau_{flu}} = W_{nr}(T) + A \tag{2.60}$$

with $A = \frac{1}{\tau_{rad}}$ being the radiative transition rate (see section 2.2.1). The ratio between fluorescence lifetime and radiative lifetime gives the quantum efficiency of the system:

$$\eta_q = \frac{\tau_{flu}}{\tau_{rad}}. \tag{2.61}$$

The Electron-Phonon Coupling Strength through the Lanthanoid Series

The question whether there is a systematic variation of the electron-phonon coupling strength through the lanthanoid series has been the subject of study for many years. There exist many different approaches with different conclusions which will be briefly summarised in the following paragraphs.

The energy-gap law for multiphonon relaxation for instance, assumes that the multiphonon relaxation transition probability depends only on the required number of phonons to bridge the energy gap between the two energy levels in question. Thus, in the simple energy-gap law no differences in electron-phonon coupling strength are considered for the different lanthanoid ions. On the other hand, measurements on vibronic transitions in Pr^{3+} and Gd^{3+} suggest that the vibronic transition probability for the former is one order of magnitude larger than that for the latter. This was explained by the lanthanide contraction [Gol25], which is assumed to lead to a decrease in overlap of $4f$ and ligand wave functions[9]. Differences in the admixture of the $4f^{n-1}5d$ states have also been discussed in this context [Mei94]. Based on these findings a gradual decrease in electron-phonon coupling strength with increasing atomic numbers would be expected through the lanthanoid series. In contrast, it has been found that vibronic transition probabilities of Tm^{3+} are of the same order of magnitude as those of Pr^{3+} and are significantly larger than those of Gd^{3+} in the same compounds. This suggests that the electron-phonon coupling strength is strong at the beginning and end of the lanthanoid series, and weak in the middle [Ell96]. This symmetric behaviour was proposed earlier by Hellwege [Hel41] and also by Krupke [Kru66].

[9]Usually, the overlap between the well shielded lanthanoid $4f$ and the ligand wave functions is said to be negligible. However, the role of the $4f$ orbitals in chemical bonds is a topic often discussed in the literature, e.g. [Hub80, Kot92, Dol96, Str99, Cho02, Mak04].

In 1997, Ellens and coworkers presented their systematic study on the variation of electron-phonon coupling strength through the lanthanoid series. Temperature dependent measurements of transition linewidths and vibronic sidebands of different lanthanoid ions incorporated into $LiYF_4$ have been performed and proven to be a useful method to probe electron-phonon coupling strengths [Ell97b, Ell97a]. The symmetric behaviour with strong electron-phonon-coupling strengths at the beginning and the end of the lanthanoid series and weak coupling strength in the middle was confirmed in these measurements. To qualitatively explain the observed trend, the contribution of two opposing effects has been suggested. The lanthanide contraction leads to a decrease in the average quadratic distance between the $4f$ electrons and the nucleus through the series. As stated above, this is assumed to cause a decrease in overlap of the $4f$ wave functions with the wave functions of the ligands, which leads to a decrease in electron-phonon coupling strength through the lanthanoid series. On the other hand, according to e.g. Blok and Shirley, there is a gradual decrease of the shielding of the $4f$ electrons by the outer $5s$ and $5p$ electrons from Ce^{3+} to Yb^{3+} [Blo66]. This again implies an increase of electron-phonon coupling strength through the series. It is the sum of these two opposing effects which most likely results in the symmetric behaviour found.

However, this variation in electron-phonon coupling strength has not been observed in data obtained from measurements of multiphonon relaxation in [Ell97a]. Ellens *et al.* explain this with the difficulty in finding the variation of electron-phonon strengths on the logarithmic scale of the multiphonon relaxation probabilities.

2.2.2. Interionic Processes

In contrast to the intraionic processes, interionic processes refer to processes which occur between at least two ions. Strictly speaking, only processes which involve the direct transfer of excitation energy between two or more ions without absorption or emission of photons are counted as interionic processes. In these cases the ions are coupled through multipolar, exchange, or superexchange interaction. However, in this section cooperative emission and absorption processes, which do not imply energy transfer from one ion to another as well as reabsorption, which involves real photons, are also listed as interionic processes since more than one ion is needed.

Interionic Energy Transfer Processes

In general, non radiative transitions of excitation energy from an excited Donor ion D^* to an acceptor ion A are referred to as interionic energy transfer processes. The involved transitions in both ions need to be of similar energy, where the energy transfer can be phonon-assisted. These processes can lead to reduction of the radiative transition rate and thus to significant heating of a laser material due to non radiative decay of the final state, especially in cases where the transfer occurs between different types of ion:

$$D^* + A \rightarrow D + A^* + \Delta E. \tag{2.62}$$

However, it is also possible to take advantage of these processes and e.g. use suitable donor ions with high absorption cross-sections as sensitisers for less absorbing laser ions.

The non radiative energy transfer processes between two ions can be characterized by transfer rates W such as $\exp(-Wt)$ expressing the probability for the donor excited state staying populated in the presence of an acceptor. The transfer rates are determined by the type of interaction between the ions involved in the transfer. These can be comprised of both multipolar and exchange contributions, which show characteristic dependencies on the donor-acceptor distance.

A thorough investigation of the quantum mechanical description of interionic energy transfer processes based on multipolar interactions was carried out by Förster for electric dipole transitions in liquids [För48] and has been extended to processes based on higher order as well as exchange interactions by Dexter for solids [Dex53]. Following their models, the rate of energy transfer between a donor and an acceptor separated by the distance R based on multipolar interaction can be described by

$$W_{DA} = \frac{C_{DA}^{(s)}}{R_{DA}^{s}}, \tag{2.63}$$

with the exponent s in the denominator taking the values 6, 8 or 10 depending on the type of interaction, i.e. dipole-dipole, dipole-quadrupole and quadrupole-quadrupole interactions, respectively. The type of interaction is determined by the character of the transitions in D and A involved in the energy transfer. The strong dependence on the inverse distance between the two interacting ions is obvious. The closer the ions involved are situated in the laser medium, the higher the probability of the energy transfer to occur. Thus, the probability of the energy transfer increases with the concentration of the ions. The microparameter $C_{DA}^{(s)}$, where (s) is just an index, characterises the strength of the interaction and depends on the spectral properties of the ions such as the overlap integral of the donor emission and the acceptor absorption, the spontaneous emission lifetime of the donor excited state in absence of an acceptor and the matrix elements of the interactions that determine the electronic transitions involved in the energy transfer. Following Dexter [Dex53], the $C_{DA}^{(s)}$ for dipole-dipole interaction[10] becomes

$$C_{DA}^{dd} = \frac{3\hbar^4 c_0^4 Q_A}{4\pi n(\lambda)^4 \tau_{sp}^{D}} \int \frac{f_D(E) F_A(E)}{E^4} dE, \tag{2.64}$$

where c_0 is the speed of light in a vacuum and $n(\lambda)$ is the refractive index of the laser material at wavelength λ. $F_A(E)$ and $f_D(E)$ are the normalised line-shape functions of the acceptor absorption and the donor emission cross-sections respectively, such that e.g. $\sigma_{abs}^{A}(E) = Q_A F_A$, where $\int F_A(E)dE = 1$ and $Q_A = \int \sigma_{abs}^{A}(E)dE$ is the area under the acceptor absorption cross-section. The integral in equation 2.64 is the overlapping ratio of these spectra, that is to say the probability of the transfer is highly dependent on the overlap between the donor emission and the acceptor absorption spectrum. Furthermore, the rate of the energy transfer depends also on the fluorescence lifetime of the donor excited state τ_{sp}^{D}. Typical dipole-dipole energy transfer ranges from 4.5 Åto 30 Å[Auz94]. From equation 2.63 it is evident that the effective reach is even smaller for higher order multipolar interactions. Therefore, it is common practice to attribute the dipole-dipole type interaction to the energy transfer among optically active ions in

[10] In this expression, the absorption parameter of the donor ion and thus back transfer is not considered.

a laser medium and neglect higher order mechanisms. However, higher order terms may be of importance at high concentrations and short distances, particularly in cases where the electronic transitions involved in the transfer are electric quadrupole permitted [Sou02].

Energy transfer can also occur through pure quantum mechanical exchange interaction if the wave functions of the donor and the acceptor ions are significantly overlapped. The transfer rate W_{ex} is then given by

$$W_{ex} = \frac{1}{\tau_{sp}^{D}} \exp\left[\gamma\left(1 - \frac{R_{DA}}{R_0}\right)\right] \tag{2.65}$$

with

$$\gamma = 2R_0 L^{-1}, \tag{2.66}$$

where R_0 is the distance at which the exchange rate equals the rate of intrinsic spontaneous emission of the donor excited state and L is the effective Bohr radius. The transfer rate in case of exchange interaction shows a strong dependence on distance as well, but is also influenced by the nature, number and geometric configuration of the ions in question. In general, typical transfer times for nearest neighbour sites are in the order of 10^{-10} s to 10^{-11} s and thus the exchange mechanism is slightly less efficient than energy transfer based on dipole-quadrupole interaction [Dex53]. If the energy is transferred indirectly, i.e. by exchange interaction involving the ligands, this effect is also referred to as superexchange interaction.

Magnetic multipolar interactions and the resulting energy transfer processes occur with the same dependency on the donor-acceptor distance as the electric multipolar interactions. However these transfer processes are of several orders of magnitude lower probability compared to purely electric multipolar interactions so that these have only to be considered in very exceptional cases.

The occurrence of such energy transfer processes may result in fluorescence decay curves which significantly deviate from single exponential decay behaviour. In the presence of acceptor ions these act as traps, making the energy transfer process entirely or at least partially irreversible and the excitation energy is in most cases lost for the donor ions resulting in shortening of the donors' fluorescence lifetime. In that case, the fluorescence lifetime of the donor excited state is said to be quenched and the acceptor ion is referred to as a quenching centre. Therefore, studies of energy transfer often involve examination of the donor fluorescence lifetimes as a function of donor and acceptor concentrations. Especially the time evolution of the donor fluorescence decay provides distinguishing features helpful in identifying the dominant relaxation mechanism. If the donor and acceptor ions are randomly distributed in the host and direct donor-acceptor energy transfer is dominant, the temporal evolution of the donor's excited state population follows the Inokuti-Hirayama equation [Ino65].

There are different types of energy transfer processes based on these interactions, which depend on the energy level structure of the participating ions. In the following these processes will be shortly introduced:

Energy Migration

In the first instance, energy migration refers to donor-donor interaction, i.e. interaction between same types of ions as shown on the left of figure 2.5, that does not cause loss but merely displace

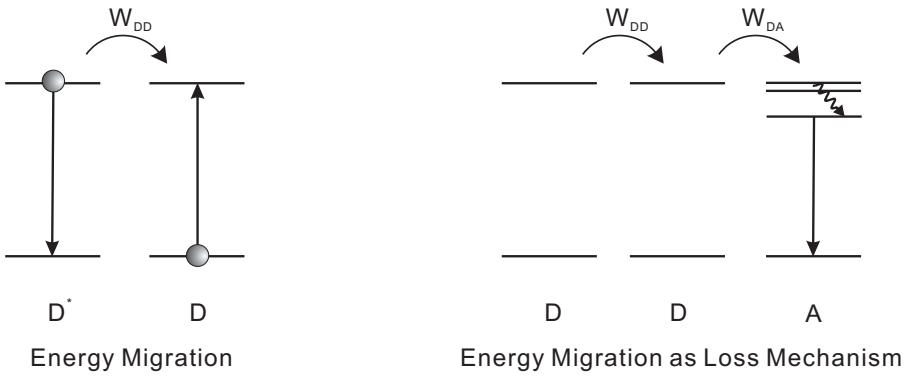

Figure 2.5.: An excited donor ion D^* transfers its energy with transfer rate W_{DD} to a nearby ion D of the same type which is initially in its ground state (left). In this way the excitation energy can be rapidly transported through the sample until an acceptor ion of different type A is reached, which acts as an energy sink (right).

the excitation energy in space. In this way, the excitation energy is transported quickly through the active medium and thus the probability for all kinds of transfer processes increases. As displayed on the right of figure 2.5, the excitation energy may also be easily transported into the vicinity of impurities or lattice imperfections which act as quenching centres. If the intrinsic decay of the excited state is so slow that the excitation energy can be transferred to an other donor prior to the decay, eventually an acceptor centre will be reached where the quenching rate is much higher than that of the initial donor. For this process, even a very low number of acceptors is sufficient to reduce significantly the donor's fluorescence lifetime. The higher the donor concentration the faster this process. As quenching thus increases most notably with donor concentration, the effect of migration with subsequent energy transfer to acceptor centres is often also referred to as concentration quenching.

As stated above, energy transfer processes modulate the decay characteristics of the donor fluorescence and so does energy migration. There are two approaches to the treatment of energy migration, where one is based on the physical picture of excitation hopping among donors [Bur72] and the other on the description of energy delocalisation by diffusion [Yok67]. In the limit of many steps both approaches are equivalent [Cho80]. Based on these approaches, different models have been developed to describe the effects of energy migration on the characteristics of the donor relaxation. Yokota and Tanimoto obtained a simple expression for the temporal evolution of excited donors by considering energy migration as a diffusion process. This expression is limited to strong donor-acceptor interaction with weak migration, i.e. only for the diffusion limited regime, and is restricted to energy transfer processes with dipole-dipole interaction among the participating ions. The Yokota-Tanimoto model was extended and generalised by Martin *et al.* so that any kind of multipole interactions can be considered [Mar99]. On the other hand, when the average donor separation is small and the probability for resonant energy transfer between donors is large, energy diffusion can be very rapid, leading to a spatial equilibrium within the donor system. This case is referred to as the fast diffusion or super-migration regime and the limiting step for the donor relaxation is then the donor-acceptor transfer rate or the acceptor relaxation rate [Cho80]. Reviews on the kinetics of energy transfer

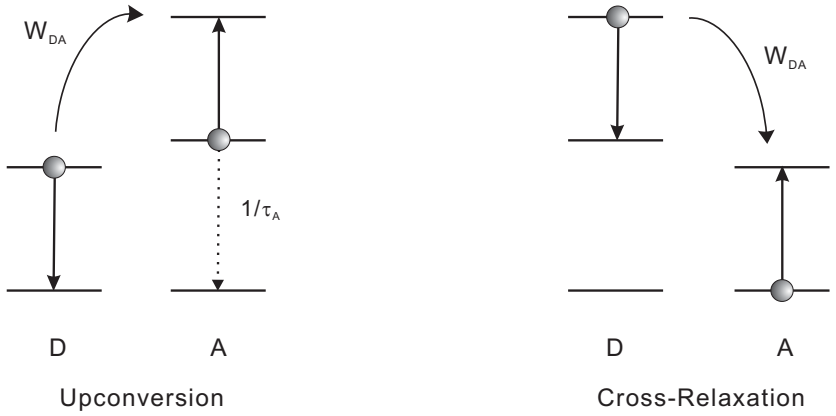

Figure 2.6.: Left side: Example of upconversion type energy transfer. The initial donor excited state is lower in energy than the final acceptor excited state. The transfer rate W_{DA} is required to be greater than the spontaneous decay rate τ_A^{-1} of the acceptor initial state. Right side: Example of cross-relaxation type energy transfer. The donor initial state is higher in energy than the acceptor final state. Both processes are non radiative processes and can occur in same type of ions or as displayed here in different type of ions. Upconversion is the reverse process of cross-relaxation.

are given in e.g. [Web71, Bur85]. A table listing and comparing the commonly used phenomenological models of energy transfer together with the physical situations in which each model is valid can be found in [Cho80].

Upconversion and Cross-Relaxation

Upconversion and cross-relaxation are special cases of energy transfer. In case of upconversion, the final state of the acceptor ion is in an higher excited state than the initial state of the donor ion (see figure 2.6, left). Upconversion requires that the transfer probability is faster than radiative and non-radiative decay from the initial excited state of the acceptor ion, i.e. $W_{DA} \geq \tau_A^{-1}$. If the final state of the acceptor ion is in a lower excited state than the initial state of the donor ion, one speaks of cross-relaxation (see figure 2.6, right). Cross-relaxation is thus the reverse process of upconversion. For both these processes as for all energy transfer processes, energy states with similar energetic differences are needed in neighbouring donor and acceptor ions. At this donor and acceptor ion do not necessarily need to be of the same type.

As all energy transfer processes, upconversion and cross-relaxation can be unwanted loss mechanisms, where especially upconversion might be further deleterious as it is often connected with additional heating of the medium. Nevertheless, both mechanisms can also be used to reach energy levels that are otherwise not directly excitable and in the case of cross-relaxation even to increase pump quantum efficiency [Fan87].

Cooperative Processes

Cooperative processes just as all interionic processes in the classical sense require the presence of two optically active ions at near by lattice sites.

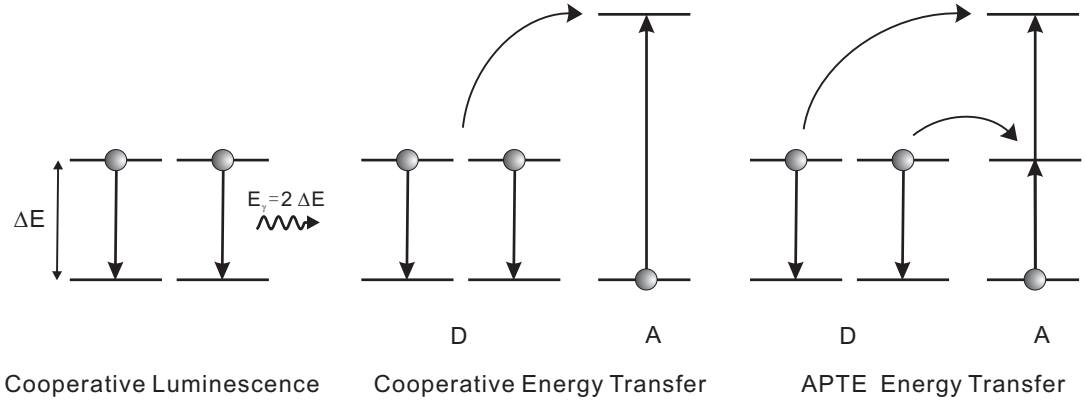

Figure 2.7.: Left: Cooperative emission. Two excited ions on neighbouring sites relax simultaneously and a photon with the added energy differences of the two single ions is emitted. The reverse process is referred to as cooperative absorption. Middle: Cooperative energy transfer to and acceptor *A*. The energy of two excited neighbouring ions is transferred to an acceptor ion, which is excited to an energy state with the added energy differences of the two single ions. In this case, the two single ions act together as the donor so that they are considered a pair, dimer or molecule. Right: APTE type energy transfer process. The two excited ions act each as a donor and the energy is transferred stepwise to the acceptor.

Cooperative optical transitions manifest themselves in additional lines in the absorption and emission spectra, which are due to the simultaneous absorption and emission of one photon by two coupled ions respectively (see figure 2.7, left). The additional lines are therefore found at the added energy differences of the two single ions. As all second-order events, the dependence on excitation intensity is quadratic for cooperative processes. Therefore, the decay rate of cooperative fluorescence is twice the rate of the corresponding first-order transition. The fluorescence spectrum of cooperative luminescence is mathematically obtained by self-convolution of the single ion emission spectrum.

Nonradiative, cooperative energy transfer processes also exist. In this case, two or more excited ions act as the donor and thus at least three interacting partners are necessary. Two different approaches have been followed in the development of a model describing the process. Auzel proposed a mechanism based on a successive excitation transfer, which is referred to as APTE (Addition de Photons par Transferts d'Energie) upconversion [Auz66]. Here, as shown on the right side of figure 2.7, the two donor ions would each transfer their energy to one acceptor, which would stepwise reach its final state. In the truest sense this mechanism would not be a cooperative transfer but rather a multi-ion upconversion process as the term cooperative implies the simultaneity of a process. A model based on the truly simultaneous energy transfer from two donor ions to an acceptor ion, which subsequently emits a photon of the sum of the two donor excitation energies was proposed by Feofilov and Ovsyankin [Feo67]. In this case, the donor constitutes of two single ions which are treated as one pair, dimer or molecule. A schematic for the cooperative energy transfer process is given in the middle of figure 2.7. This process is also often referred to as cooperative upconversion, although the initial state of the donor as a whole is most often not lower in energy than the final state of the acceptor. Which of the two competing processes dominates, depends mainly on whether a real intermediate energy state exists in the acceptor ion, which can act as the intermediate state after the first step of the

APTE type upconversion. Only for cases were APTE upconversion is not possible, cooperative energy transfer needs to be considered [Miy70, Auz94].

Theoretical treatment of cooperative processes is commonly based on a concept by Dexter which states that cooperative transitions are only possible because of the perturbation induced by the electronic Coulomb interaction on the initial and final levels [Dex62]. Otherwise, a single-electron operator has a vanishing matrix element for a two-centre multipole type transition, providing no overlap between the interacting ions. Other works suggest superexchange type interaction as the mechanism underlying cooperative processes [Sch75, Ish05]. Experimental observations on Yb^{3+}-doped samples indicate that covalency of the metal-ligand bonding has an influence on the efficiency of cooperative processes [Weg95], which also points to cooperative transitions occurring via superexchange interaction.

Reabsorption

If an emitted photon is again absorbed by another ion before it can leave the sample, one speaks of a reabsorption process. Thus, reabsorption can be understood as two subsequently occurring intraionic processes. The probability of a reabsorption event depends exponentially on the distance the emitted light has to travel in the sample. Other factors are the reabsorption cross-section, the ion density, the luminescence quantum yield and the physical dimensions of the sample [Heh97]. Especially photons emitted at transitions to the ground state are often subject to reabsorption.

In general, if the reabsorbing ion is of the same type as the emitting ion, reabsorption is not a real loss mechanism, as the excitation energy is not lost to the optically active ions. However, presence of reabsorption on the lasing wavelength does have influences on the behaviour of a laser [Ris88] as will be discussed later in section 2.3.1. For this reason, in the context of laser performance the term reabsorption loss is often used.

Reabsorption also affects and complicates the measurement of spectroscopical characteristics of a luminescent system, which are key factors for the determination of the performance of a solid-state laser material. The effect is particularly pronounced for fluorescence lifetime measurements of excited states with unity branching ratio. After the initial emission occurs from the sample each subsequent reabsorption event acts as a time reset on the relaxation of this excitation and after a series of reabsorption and reemission processes, the result is an overall lengthening of the observed excited state decay. If care is not taken, the measured fluorescence spectrum will also be distorted and together with an overestimate of the excited state lifetime, subsequent errors have to be expected in derived quantities such as the stimulated emission cross-section. Details concerning these problems and possibilities to avoid errors based on reabsorption will be presented in chapter 4.

2.2.3. Electron Exchange Processes

Just as photons may induce transitions between the different electronic states of an ion, transitions may be induced between the bands of the host lattice and the dopant ions. These molecular transitions correspond to the transfer of electrons from bonding orbitals (valence band) to

non-bonding orbitals (e.g. f-orbitals of lanthanoid ions), referred to as charge transfer (CT) transitions, and to excitation of electrons from non-bonding orbitals to anti-bonding orbitals (conduction band), which equates to photoionisation. In laser crystals doped with lanthanoids the CT process can be understood as a charge exchange process between the lanthanoid central ion ("metal") and the ligands, where the lanthanoid ion acts as an electron acceptor whereas for photoionisation processes it acts as an electron donor. Therefore, the CT and the photoionisation processes are also often referred to as Ligand to Metal Charge Transfer (LMCT) and Metal to Ligand Charge Transfer (MLCT), respectively. The actual electron transfer occurs between the lanthanoid ion and one of its direct ligands, which in case of a lanthanoid-doped oxide crystal is an oxygen ion. The transfer occurs locally. However, while the electronic energy level structure of the shielded $4f$ states is described by almost unperturbed localised energy states, the energy states of the oxygen valence electrons are described by delocalised Bloch states.

The energies of the lowest CT absorption transitions σ can be estimated by a simple empirical relationship developed by Christian Klixbüll Jørgensen [Jør70].

$$\sigma = (30\,000\,\mathrm{cm}^{-1})\,[\chi_{opt}(X) - \chi_{opt}(M)]\,, \tag{2.67}$$

where $\chi_{opt}(X)$ and $\chi_{opt}(M)$ are the optical electronegativities of the ligand ion X and the central ion M, respectively. Electronegativity is a chemical property introduced by Linus Pauling [Pau32] that describes an ion's ability to attract the binding electrons in a chemical bond. The higher the electronegativity of an atom, the more the electrons in a chemical bond are attracted towards it. Jørgensen developed the concept of optical electronegativity values originally for halides, where the value is connected with the change of the LMCT transition energy in the F, Cl, Br, I series. The shifts in the energies are proportional to the differences in the Pauling electronegativities if one optical electronegativity unit is put equal to $30\,000\,\mathrm{cm}^{-1}$ [Jør62]. From equation 2.67 it can be deduced that the CT energy is lower for metals and ligands with similar electronegativities, i.e. CT processes are higher in probability for metals and ligands with chemical bonds that are covalent in character rather than ionic. However, the energy determined by equation 2.67 is only an estimate and the actual energy involved in CT depends further on the distance between the ligands and the central ion as well as the electron affinity of the latter [Kru95].

Model Descriptions for Electron Exchange Processes

These electron transfer processes are nontrivial to study since they often occur in the far UV spectral region. But the major difficulty lies in their model description as these transitions occur between delocalised initial and localised final states or vice versa and involve a change in valency of the localised lanthanoid ion, changing its electronic level structure as well as the local lattice environment due to different Coulomb forces and different ionic radii. Therefore, a thorough understanding of the total host-dopant system is required, that involves both the dopant electronic states and the extended electronic states of the host lattice, i.e. the delocalised energy bands. There are various approaches each having different advantages and disadvantages. These are briefly summarised and discussed for the concept of the configuration coordinate diagram introduced in section 2.2.1 and the concept of the one-electron band scheme in the following paragraph.

In configuration coordinate diagrams, the adiabatic potential of the system is presented as a function of the atomic configuration. The configuration coordinate diagram was first introduced to describe processes in localised electron systems, where the adiabatic potential is given by the sum of the electronic energy and the lattice potential energy (see equation 2.50 and the descriptions in the text of section 2.2.1 for details on the single configuration coordinate diagram). In order to apply this concept, the number of charge carriers needs to be conserved, which is not the case in electron exchange processes. Furthermore, in the discussed CT and ionisation processes, transition occurs between localised and delocalised states, so at first glance the utilisation of configuration coordinates is not justifiable. However, configuration coordinate diagrams have proven useful in visualising the lattice relaxation and thus explaining the large Stokes shifts observed in CT transitions [Nak78]. A major disadvantage is that the mobility of charge carriers cannot be made evident in this scheme. One-electron jump diagrams on the other hand, are widely used in solid state physics, particularly in semiconductor physics, to describe electronic processes in these systems [Par59]. Usually, the energy of a conduction electron increases upwards and that of a valence hole increases downwards. The abscissa is often interpreted as spatial coordinates. Several electrons and holes may be put into such a diagram at the same time and localised electrons and holes can be added to defects. This scheme describes well electronic processes in solids, except for the electron-lattice interaction. Lattice relaxation cannot be visualised. However, the mobility of charge carriers in the energy bands is evident.

Regardless of which picture is used, one should always bear in mind that these representations are just models which have their limitations, especially when processes involving both localised and delocalised states are shown in one picture. See section 3.4 for more details on the nature of localised and delocalised states. In section 6.3, an energy level diagram is developed for Yb:YAG, which attempts to link the configuration coordinate diagram with the one-electron jump diagram.

2.2.4. Selection Rules

Optical transitions are subject to selection rules, the existence of which can only be explained by a quantum mechanical treatment.

As shown in section 2.2.1, the probability for optical transition to occur is proportional to $|\overrightarrow{\mu_{ij}}|^2$. The transition dipole moment $\overrightarrow{\mu_{ij}}$ as defined in equation 2.38

$$\overrightarrow{\mu_{ij}} = \int \Psi_i^* \widehat{d} \Psi_j dV$$

determines the transitions allowed between atomic states and their strength. For electric dipole transitions $\widehat{d}$ represents the electric dipole moment operator of the system $\widehat{d} = \sum_i e\overrightarrow{r_i}$, with the electron charge e and the position vector $\overrightarrow{r_i}$ of the ith valence electron. In case of magnetic dipole transitions the dipole moment operator is given by $\widehat{d} = \sum_i (e/2m_e)(\overrightarrow{l_i} + 2\overrightarrow{s_i})$ with m_e being the electron mass and $\overrightarrow{l_i}$ and $\overrightarrow{s_i}$ being the orbital and the spin angular momentum respectively. The integral in equation 2.38 can thus be understood as the spatial overlap of the wave functions of the initial and the final states weighted with the acting dipole moment. The

evaluation of the extent of this overlap provides the probability that the transition will occur. Forbidden transitions are associated with states whose transition dipole moment is zero. From group theory and the Wigner-Eckart theorem [Wig27, Eck30] it can be deduced that an integral is non-zero only if the integrand is invariant under all symmetry transformations.

The wave functions for the various electronic states possess either even or odd symmetry with respect to an inversion centre. States with odd orbital angular momentum quantum numbers possess odd parity, while those with even quantum numbers possess even parity. When considering electric dipole coupling, the integral in equation 2.38 between the states Ψ_i and Ψ_f will have a non-zero value only if the two wave functions have opposite parity because the electric dipole moment operator introduces odd symmetry to the integral. This effect is reflected in the selection rules by requiring that $\Delta l = \pm 1$, which demands the electron involved in the transition to change parity. The energy level parity is given by the number of electrons having odd parity. An even number of odd parity electrons gives rise to an even parity energy level whereas an odd number of odd parity electrons leads to an odd parity energy level. As a consequence, having inversion symmetry, electric dipole transitions within a certain shell, e.g. within the $4f$ shell are forbidden. This selection rule is also referred to as the Laporte rule named after Otto Laporte [Lap25]. For magnetic dipole transitions the Laporte rule does not apply since the magnetic dipole moment operator has even parity. In this case the initial and the final state wave functions need to be of same parity.

Application of the Wigner-Eckart theorem considering other symmetry transformations yields selection rules for each contribution to the perturbation Hamiltonian developed in section 2.1.1 to approximate the atomic energy level structure. The relevant selection rules for electric dipole transitions are the following (see also table 2.4):

$\Delta l = \pm 1$		for the changing electron (change in parity)
$\Delta S = 0$		transitions between terms in *LS* coupling
$\Delta L = 0, \pm 1$	excluding $0 \longrightarrow 0$	
$\Delta J = 0, \pm 1$	excluding $0 \longrightarrow 0$	transition between *J* levels

Because of their rather strong spin-orbit coupling, the multiplicity selection rule $\Delta S = 0$ is a poor approximation for rare earth and heavy metal ions [Hen00]. Since the transition probabilities for electric dipole transitions is five or six orders of magnitude greater than for magnetic dipole and electric quadrupole transitions, the latter are generally only considered when the former are rigorously forbidden.

However, optical transitions which due to the selection rules are forbidden can still be observed, e.g. intraconfigurational transitions between lanthanoid $4f$ levels. The more complex the modifications and perturbations imposed by neighbouring bonds and electron-electron interactions in a solid, the more symmetry and thus the rigour of the selection rules is reduced. Configuration mixing of states with opposite parity by components of the crystal field which are odd under inversion leads to partially electric dipole allowed intraconfigurational transitions. Nevertheless, if the ion occupies a centrosymmetrical lattice site, the odd parity crystal

field components vanish and the ion is optically inactive. Parity mixing can be accomplished by both, odd components of the static crystal field and by odd modes of lattice vibration (see also section 2.2.1). Furthermore, the admixture of wave functions associated to ligands has also been discussed in connection with formation of mixed parity states [Hub80]. Interconfigurational transitions between lanthanoid $4f^n$ and $4f^{n-1}5d$ levels on the other hand are parity allowed and have therefore much higher transition cross-sections than intraconfigurational transitions. Of these interconfigurational transitions the spin allowed transitions have higher cross sections than the spin forbidden ones. Electron transfer processes such as charge transfer and ionisation are not based on dipole-dipole interaction and thus are fully allowed transitions, usually accompanied by intense spectral bands. The probabilities of these transitions strongly depend on the electro-chemical properties of the system. However, the strength of an optical transition is not only given by the selection rules. As stated above, the overlap of the wave functions of the initial and final states is decisive. For example, even though being fully allowed, transitions from the lanthanoid $4f^n$ levels to the conduction band (ionisation) are expected to be much weaker compared to those from the $4f^{n-1}5d$ levels due to the significantly smaller spatial overlap of the localised $4f$ wavefunctions with the delocalised Bloch wavefunctions of the conduction band [Sch98]. The orders of magnitude for the optical transition cross-sections of the different transition types are summarised in table 2.5.

Type of Transition	Typical Order of Magnitude for σ [cm^2]	Reference
Laporte-forbidden, spin-forbidden $4f^n \rightarrow 4f^n$	$<10^{-21}$	[Sve93, Hou07]
Laporte-forbidden, spin-allowed $4f^n \rightarrow 4f^n$	10^{-19}-10^{-21}	[Sve93, Hou07]
spin-forbidden $4f^n \rightarrow 4f^{n-1}5d$	10^{-18}-10^{-19}	[Sch98, Hen01]
spin-allowed $4f^n \rightarrow 4f^{n-1}5d$	10^{-17}-10^{-18}	[Hen01]
ligand to metal charge transfer	10^{-18}-10^{-17}	[Hou07]
$4f^{n-1}5d \rightarrow$ conduction band states (ionisation)	10^{-18}-10^{-17}	[Sch98]
$4f^n \rightarrow$ conduction band states (ionisation)	not observed	[Sch98]
free carrier absorption (innerband absorption)	10^{-15}-10^{-18}	[Sau98, Kek08]

Table 2.5.: Typical orders of magnitude for optical transition cross-sections σ for the different types of transitions involving lanthanoid ions in crystalline matrices.

2.3. Basic Laser Theory

The feasibility of amplification of photon flux in the presence of population inversion (see section 2.2.1), is crucial for the realisation of a laser (acronym for "light amplification by stimulated emission of radiation"). Aside from material specific properties, the amplification of the photon flux, also known as gain, is dependent on two quantities (see equation 2.21), the distance travelled by the electromagnetic wave through the active medium and the population inversion accomplished by pumping. Therefore, in order to maximise amplification it is reasonable to maximise path length and simultaneously reduce the number of possible frequencies and propagation directions of the electromagnetic waves. Optical resonators, also known as optical cavities serve this purpose of frequency and propagation direction selective feedback and thus ensure that stimulated emission outweighs spontaneous emission. The geometry of the chosen resonator defines the properties of the resonator eigenmodes, i.e. the radiation patterns that are reproduced on every round-trip of the light through the resonator. In the simplest case, an optical cavity is an arrangement of two mirrors that reflects the electromagnetic wave to be amplified back and forth through the active medium. Usually, one of the mirrors is partly transmittive for the amplified wavelength and thus allows outcoupling of the laser beam. In order to obtain positive net gain, amplification has to exceed the losses of the system. At threshold, i.e. just before the laser starts oscillating, light at the laser wavelength has zero round-trip net gain (see also equation 2.21)

$$2\gamma + 2\sigma_{21}\left(N_2 - \frac{g_2}{g_1}N_1\right)z = 0, \tag{2.68}$$

with $\gamma = \gamma_{int} + \frac{\gamma_1+\gamma_2}{2}$ being the total round-trip losses composed of internal losses $\gamma_{int} = -ln(1 - L_{int})$ due to imperfections of the laser medium, and the resonator losses $\frac{\gamma_1+\gamma_2}{2}$ including the intended outcoupling ($\gamma_2 = -ln(1-T_2)$, where $1-T_2 = R_2$ is the reflectivity of the outcoupling mirror on the lasing wavelength), N_2 and N_1 being the population density and g_2 and g_1 being the degeneracy of the upper and lower laser level, respectively, σ_{21} being the atomic transition cross-section between the two levels and z being the length of the laser active medium. Using the effective cross-sections introduced in section 2.2.1 for transitions between Stark split manifolds and exponentiating equation 2.68, the well known expression for the threshold condition is obtained:

$$R_1 R_2 (1 - L_{int})^2 \exp\left[\left(\sigma_{em}^{las} N_2 - \sigma_{abs}^{las} N_1\right) 2z\right] = 1. \tag{2.69}$$

It is evident that higher outcoupling, i.e. higher extraction of the laser beam, demands higher gain and thus higher inversion densities. If the resonator has a more complex design and the resonator consists of N mirrors and M_r passes through the active medium occur in a single round-trip, equation 2.69 can be generalised to

$$\prod_{i=1}^{N}(1 - T_i) \cdot (1 - L_{int})^{M_r} \exp\left[\left(\sigma_{em}^{las} N_2 - \sigma_{abs}^{las} N_1\right) M_r z\right] = 1. \tag{2.70}$$

To describe and model the relevant processes during laser operation, usually the dynamics of the energy level populations is examined using a set of rate equations. These are differential equations describing the temporal evolution of level populations taking into account optically

induced, spontaneous and nonradiative transitions as well as interionic processes as described in the preceding section 2.2. Depending on the number of energy levels participating in the laser process, different types of lasers can be distinguished. In the following, the rate equations for the so-called quasi-three-level laser will be introduced and discussed. For details on the classical four- and three-level-laser systems the reader is referred to textbooks, e.g. [Sve93].

2.3.1. The Quasi-Three-Level Laser

In a quasi-three-level system[11] the lower laser level is so close to the ground state that a non-negligible population is found in that level at the operating temperature. Usually, the lower laser level is a Stark component of the ground state. As a consequence, reabsorption on the laser wavelength occurs in the unpumped regions of the active medium (see also section 2.2.2) and transparency is only reached beyond a certain pump intensity. As a consequence, the threshold pump power required to start laser operation will always be higher compared to four-level lasers with comparable cross-sections. Also, the balance between stimulated emission and reabsorption and thus the spectral shape of the optical gain is highly dependent on excitation level. For low excitation levels the short wavelength net gain is particularly reduced as reabsorption is stronger at shorter wavelengths. Therefore, the laser wavelength obtained may strongly depend on the resonator losses. As stated above, higher losses require higher gain, and thus a higher inversion level so that a shorter wavelength of maximum gain can be reached.

Examples of quasi-three-level media are all kinds of Yb^{3+}-doped laser materials, Nd^{3+}-doped media that are operated on the ground state transition, Tm^{3+}-doped media for 2 µm emission as well as Er^{3+}-doped laser materials for 1.5 and 1.6 µm emission.

Rate Equations for the Quasi-Three-Level Laser

The number of rate equations to consider depends on the number of the manifolds involved in the occurring processes. If m manifolds are involved, $m-1$ rate equations are needed to describe the problem. Conservation of total doping concentration N_t gives

$$N_t = \sum_{i=1}^{m} N_i \tag{2.71}$$

with N_i being the population density in manifold i.

Assuming direct resonant pumping into the upper laser level E_2 in a system as schematically shown on the left of figure 2.8, several types of processes V changing the population N_2 have to be considered. Firstly, there are the processes connected to the pump light. If excited state absorption (ESA) on the pump wavelength is absent, just the ground state absorption needs to be considered. However, in an inband-pumped system as in figure 2.8, stimulated emission on the pump wavelength from the upper laser level has also to be taken into account:

$$V_{pump} = \left(\sigma_{abs}^{pump} N_1 - \sigma_{em}^{pump} N_2\right) \frac{S_{p,eff}}{h\nu_p}, \tag{2.72}$$

[11] It should be noted that Yb-lasers are also sometimes referred to as quasi-four-level laser, e.g. [Bru97].

where σ_{abs}^{pump} and σ_{em}^{pump} are the effective absorption and emission cross-sections for the pump wavelength respectively, $S_{p,eff}$ is the effective pump power density and $h\nu_p$ is the energy of a pump photon of frequency ν_p. Secondly, processes connected to the signal laser light, i.e. stimulated emission from level E_2 to the ground state, reabsorption and ESA into level E_3 as well as stimulated emission from level E_3 to level E_2 have to be considered:

$$V_{las} = \left(-\sigma_{em}^{las} N_2 + \sigma_{abs}^{las} N_1\right) \frac{S_{r,eff}}{h\nu_l} + \left(-\sigma_{abs}^{ESA,l} N_2 + \sigma_{em}^{ESA,l} N_3\right) \frac{S_{r,eff}}{h\nu_l}, \tag{2.73}$$

with σ_{abs}^{las} and σ_{em}^{las} being the effective absorption and emission cross-sections on the laser transition respectively, $S_{r,eff}$ being the effective resonator internal power density, $h\nu_l$ being the energy of one laser photon of frequency ν_l and $\sigma_{abs}^{ESA,l}$ and $\sigma_{em}^{ESA,l}$ being the effective absorption and emission cross-sections for the transition between levels E_2 and E_3, respectively. Thirdly, the interionic energy transfer process of upconversion[12] needs to be taken into account:

$$V_{UC} = -W_{UC} N_2^2 \tag{2.74}$$

with W_{UC} being the energy transfer rate for the upconversion process starting at level E_2. Fourth, radiative and nonradiative decay of the excited levels are addressed by the expressions:

$$\begin{aligned} V_{21} &= -\left(\frac{1}{\tau_{rad,21}} + W_{nr,21}\right) N_2 \\ V_{32} &= -\left(\frac{1}{\tau_{rad,32}} + W_{nr,32}\right) N_3 \\ V_{31} &= -\left(\frac{1}{\tau_{rad,31}}\right) N_3, \end{aligned} \tag{2.75}$$

with $\tau_{rad,ji}^{-1}$ and $W_{nr,ji}$ being the radiative and nonradiative decay rates for the transition from level j to level i, respectively.

Summing up these processes of population and decay for each manifold, the rate equations are set up:

$$\begin{aligned} \frac{dN_3}{dt} &= \left(\sigma_{abs}^{ESA,l} N_2 - \sigma_{em}^{ESA,l} N_3\right) \frac{S_{r,eff}}{h\nu_l} \\ &\quad + W_{UC} N_2^2 - \left(\frac{1}{\tau_{rad,32}} + W_{nr,32} + \frac{1}{\tau_{rad,31}}\right) N_3 \end{aligned} \tag{2.76}$$

$$\begin{aligned} \frac{dN_2}{dt} &= \left(\sigma_{abs}^{pump} N_1 - \sigma_{em}^{pump} N_2\right) \frac{S_{p,eff}}{h\nu_p} + \left(\sigma_{abs}^{las} N_1 - \sigma_{em}^{las} N_2\right) \frac{S_{r,eff}}{h\nu_l} \\ &\quad + \left(\sigma_{em}^{ESA,l} N_3 - \sigma_{abs}^{ESA,l} N_2\right) \frac{S_{r,eff}}{h\nu_l} \\ &\quad - 2 W_{UC} N_2^2 - \left(\frac{1}{\tau_{rad,21}} + W_{nr,21}\right) N_2 + \left(\frac{1}{\tau_{rad,32}} + W_{nr,32}\right) N_3 \end{aligned} \tag{2.77}$$

$$\frac{dN_1}{dt} = -\sum_{i}^{m-1} \frac{dN_i}{dt}. \tag{2.78}$$

[12]The process of cross-relaxation is neglected for simplicity reasons.

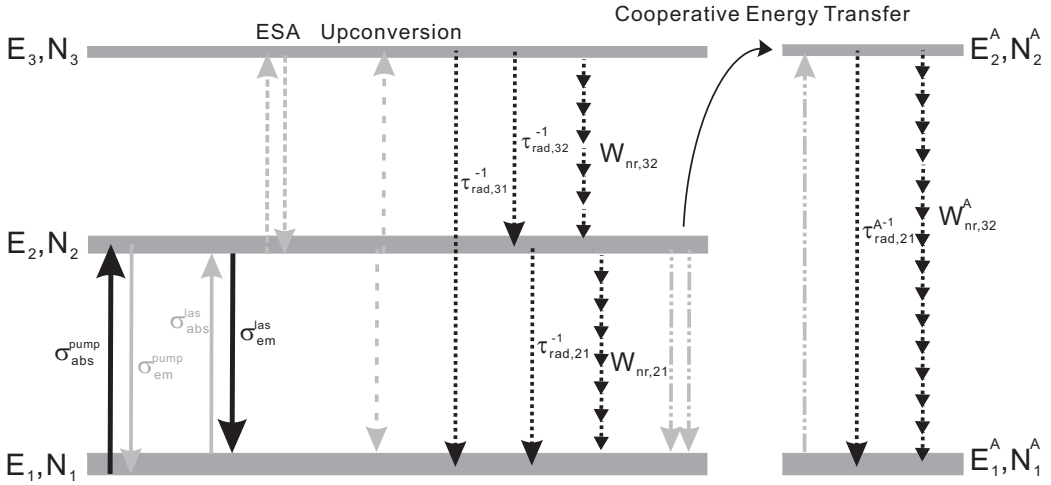

Figure 2.8.: Quasi-three-level system with three relevant Stark level manifolds (left) and an impurity acceptor ion with two relevant energy levels (right). Processes occurring when pumping the system into level E_2 are indicated by arrows. The solid black arrows indicate the intended transitions of pumping and stimulated emission. Solid grey arrows denote stimulated emission on the pump wavelength and reabsorption of the signal laser light. Narrow dashed and wide dashed arrows indicate possible ESA and upconversion mechanisms, respectively. Radiative spontaneous decay is schematically shown with dotted arrows while nonradiative decay through multiphonon emission is shown with multiarrows. A cooperative upconversion type energy transfer to the energy level E_2^A of an impurity acceptor ion is indicated by double-dot-dashed arrows.

If other types of ions, e.g. impurities with resonant energy levels exist in the active medium as schematically shown on the right of figure 2.8, these interactions also have to be considered. Higher order processes such as cooperative energy transfer processes are also possible. For example, to account for an acceptor ion which can be cooperatively excited from its ground state E_1^A to a level E_2^A, with $E_2^A - E_1^A = 2(E_2 - E_1)$, additionally the term $2W_{DA}{N_2}^2 N_1^A$, with W_{DA} being the energy transfer parameter for that process and N_1^A being the ground state population density of the acceptor ion, needs to be subtracted in equation 2.77. To that the two additional rate equations

$$\frac{dN_2^A}{dt} = W_{DA}{N_2}^2 N_1^A - \left(\frac{1}{\tau_{rad,21}^A} + W_{nr,21}^A\right) N_2^A \tag{2.79}$$

$$\frac{dN_1^A}{dt} = -\frac{dN_2^A}{dt} \tag{2.80}$$

for the population dynamics in the acceptor ion need to be considered.

Practically, the rate equations can be simplified by neglecting nonradiative transitions which bridge energy gaps of four to five times the energy of the most energetic phonon (see section 2.2.1) and high order processes because of their very low probability. The rate equations are solved for steady state laser condition by setting $\frac{dN_i}{dt} = 0$. Together with the expression for the threshold condition in equation 2.69, usually enough information is present to find dependencies with which threshold pump power, laser output power, laser efficiencies, etc. can be estimated. However, rate equations containing higher order processes like upconversion and cross-relaxation are in most cases not possible to solve analytically. Also, further information

from time resolved spectroscopical measurements is typically necessary to access the respective parameters. Often, thermal effects and, depending on the laser design, spatial effects need to be taken into account. To realistically model the laser properties of such a problem requires complex numerical simulations.

2.3.2. The Thin-Disk Laser

The thin-disk laser is a laser design developed by Giesen and coworkers which was introduced in 1994 [Gie94]. As the name states, the geometry of the active medium is a thin disk of some 100 µm thickness and a diameter of several millimetres or even centimetres. The thin disk has a dielectric coating on the backside, highly reflective for both the laser wavelength and the pump wavelength. The front side on the other hand is anti-reflection coated for both these wavelengths. The disk is soldered or glued with its backside onto a heat sink, which is water cooled. The concept of mounting one of the end faces to the heat sink is the basis for the excellent beam quality even at very high output powers of the thin-disk laser. This design using disks of much smaller thicknesses compared to the pump spot diameter allows very efficient removal of the excess heat generated during laser operation. The heat flow is almost one-dimensional and parallel to the propagation direction of the laser radiation. In a first approximation, the absence of radial heat flow eliminates the problem of thermal lensing and thus diffraction losses.

In the simplest case, the laser resonator consists of the highly reflection coated backside of the disk like active medium and an outcoupling mirror. In contrast, the pump setup is much more complex. To ensure enough absorption within the thin disk, the pump light is directed several times through the active medium. As schematically depicted in figure 2.9, the pump light from a fiber coupled diode laser is collimated by an incoupling unit, reflected and focussed by a parabolic mirror onto the thin disk, from which backside it is reflected to propagate again through the active medium. The non-absorbed part of the pump light again hits the parabolic mirror, now on another spot, where it is collimated and reflected towards a deflection prism. The prisms deflect the pump light so that another part on the parabolic mirror is hit and the pump light is again focussed onto the disk. Depending on the pump module used, up to 32 pump passes through the active medium can be realised. The thickness of the active medium is chosen according to the number of pump passes, the selected laser material, i.e. the absorption cross-section and the doping concentration. To prevent damage of the fiber end face due to back coupling of the pump light, at least 90% of the pump power should be absorbed. However, for highest efficiencies absorption rates of 98% and higher are desirable. The multiple pump passes also lead to a higher homogeneity of the pump spot and thus to a homogeneous excitation density within the pumped volume of the gain medium. In addition, the requirements for the beam quality of the pump light can be reduced. Scaling of the output power is achieved by increasing the pump spot diameter at constant pump power density. In this way, power scaling can be accomplished without approaching the fracture limit of the laser material. For more information on the setup and the concept of the thin-disk laser design, as well as details on mounting and the coatings used, the reader is referred to e.g. [Lar08, Krä08].

The thin-disk laser design is particularly profitable for quasi-three-level lasers. The multiple

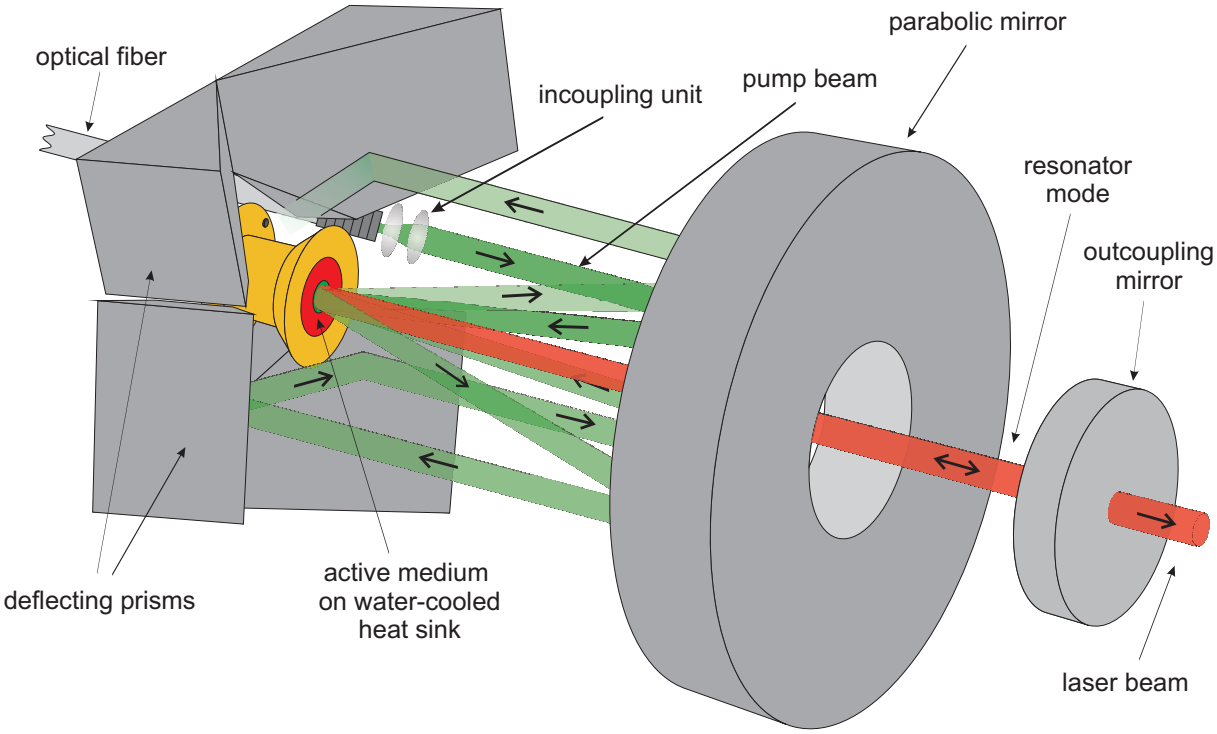

Figure 2.9.: Schematic representation of a thin-disk laser setup [Krä08].

pump passes allow for high pump power densities in the active medium, which due to the occurring reabsorption in quasi-three-level gain materials is needed to reach laser threshold. Furthermore, efficient heat removal keeps the population of the lower laser level small, resulting in lower laser thresholds.

The Zero-Dimensional Model for an Yb Thin-Disk Laser

The zero-dimensional model is an analytical model, which was first introduced by Voss [Vos02] and was further developed by Contag [Con02], is a simple analytical description for an Yb thin-disk laser based on the assumption of homogeneity of all laser relevant properties within the active medium.

Because of the rather simple energy level scheme of the Yb^{3+}-ion with only two $4f$ manifolds (see section 3.3.2), the basic rate equations for an Yb-laser can be easily obtained from equations 2.77 and 2.78 by neglecting all processes due to ESA and upconversion as well as the energy level E_3. With the ground state level E_1, the excited state E_2 and the respective populations N_1 and N_2, which are connected to the doping concentration N_t by $N_t = N_1 + N_2$, the fluorescence lifetime τ, which is the effective lifetime of the upper laser level possibly different

from the radiative lifetime due to non radiative decay (see section 2.2.1, Nonradiative Decay and Multiphonon Relaxation), the rate equations are given by

$$\begin{aligned}\frac{dN_2}{dt} &= \left(\sigma_{abs}^{pump}(N_t - N_2) - \sigma_{em}^{pump} N_2\right)\frac{S_p, eff}{h\nu_p} \\ &\quad + \left(\sigma_{abs}^{las}(N_t - N_2) - \sigma_{em}^{las} N_2\right)\frac{S_{r,eff}}{h\nu_l} - \frac{N_2}{\tau}\end{aligned} \tag{2.81}$$

and

$$\frac{dN_1}{dt} = -\frac{dN_2}{dt}, \tag{2.82}$$

where $S_{p,eff}$ and $S_{r,eff}$ are the effective pump power density and the effective resonator internal laser power density, respectively, ν_p and ν_l the frequencies of the pump and laser wavelength, σ_{abs}^{pump} and σ_{abs}^{las} are the absorption cross-sections and σ_{em}^{pump} and σ_{em}^{las} are the emission cross-sections on the pump and the laser wavelengths, respectively. The steady state solution for the upper level population is

$$N_2 = \frac{\frac{S_{p,eff}}{h\nu_p}\sigma_{abs}^{pump} + \frac{S_{r,eff}}{h\nu_l}\sigma_{abs}^{las}}{\frac{S_{p,eff}}{h\nu_p}(\sigma_{abs}^{pump} + \sigma_{em}^{pump}) + \frac{S_{r,eff}}{h\nu_l}(\sigma_{abs}^{las} + \sigma_{em}^{las}) + \frac{1}{\tau}} N_t, \tag{2.83}$$

where the unknown quantities are N_2 and $S_{r,eff}$. Due to the small thickness of the active medium, the amplification per pass can be considered small and therefore $S_{r,eff}$ can be approximated by the product of the number of laser beam passes M_r through the active medium per resonator round-trip and the single pass resonator internal power density S_r to

$$S_{r,eff} \approx M_r S_r. \tag{2.84}$$

Assuming homogeneous distribution of the pump power, the effective pump power density $S_{p,eff}$ can be expressed as the product of the incident pump power density S_p and the absorption efficiency η_{abs} distributed over the crystal length z in units of the absorption coefficient α

$$S_{p,eff} = \frac{S_p \eta_{abs}}{\alpha z}. \tag{2.85}$$

In section 2.2.1 the bleaching of the ground state absorption has been addressed. Modifying the expression for the absorption coefficient in equation 2.47 yields

$$\alpha(\nu) = \sigma_{abs}^{pump} N_1 - \sigma_{em}^{pump} N_2 = f_B \alpha_0, \tag{2.86}$$

with

$$f_B = 1 - \frac{\sigma_{abs}^{pump} + \sigma_{em}^{pump}}{\sigma_{abs}^{pump}} \frac{N_2}{N_t} \tag{2.87}$$

being the bleaching factor and $\alpha_0 = \sigma_{abs}^{pump} N_t$ being the unsaturated absorption coefficient. Using the Beer-Lambert law (see equation 2.24), for an initial launched intensity of I_0 the absorbed intensity I_{abs} is given as

$$I_{abs} = I_0\left(1 - \exp\left(-\alpha M_p z\right)\right) \tag{2.88}$$

and thus, using the obtained expression for α (equation 2.86) the absorption efficiency becomes

$$\eta_{abs} = 1 - \exp\left(-M_p \alpha z\right) = 1 - \exp\left(-f_B \sigma_{abs}^{pump} N_t M_p z\right) \tag{2.89}$$

where M_p is the number of pump passes through the active medium. With the above assumptions, the time evolution of the upper laser level in equation 2.81 can be simplified to

$$\frac{dN_2}{dt} = \frac{S_p}{h\nu_p}\frac{\eta_{abs}}{z} - \frac{N_2}{\tau} - M_r \frac{S_r}{h\nu_l}\left((\sigma_{em}^{las} + \sigma_{abs}^{las})N_2 - \sigma_{abs}^{las} N_t\right). \tag{2.90}$$

The steady state solution for the upper laser level population then becomes

$$N_2 = \frac{\frac{S_p}{h\nu_p}\frac{\eta_{abs}}{z} + M_r \frac{S_r}{h\nu_l}\sigma_{abs}^{las} N_t}{M_r \frac{S_r}{h\nu_l}(\sigma_{em}^{las} + \sigma_{abs}^{las}) + \frac{1}{\tau}}. \tag{2.91}$$

The small thickness of the laser material also suggests low internal losses per pass and for low outcoupling rates the expression for threshold condition given in equation 2.70 can be simplified to

$$T_{tot} + M_r L_{int} = ((\sigma_{em}^{las} + \sigma_{abs}^{las})N_2 - \sigma_{abs}^{las} N_t) M_r z, \tag{2.92}$$

where T_{tot} represents the total of losses on the resonator mirrors, which can usually be equated with the transmission rate T_{OC} of the outcoupling mirror. L_{int} represents the internal losses of the active medium per pass which are due to scattering or absorbing at imperfections as well as impurity centres. From this threshold condition the required population $N_{2,th}$ of the upper laser level for reaching the laser threshold can easily be determined to be

$$N_{2,th} = \frac{\sigma_{abs}^{las}}{\sigma_{em}^{las} + \sigma_{abs}^{las}} N_t + \frac{M_r L_{int} + T_{tot}}{M_r z(\sigma_{em}^{las} + \sigma_{abs}^{las})}. \tag{2.93}$$

The first term determines the threshold inversion for reaching transparency at the laser wavelength, which depends on the Yb-doped material and the total doping concentration. The second term describes the inversion needed to compensate for the resonator losses and the chosen outcoupling transmission rate. Neglecting any thermal effects, the inversion density is clamped to this threshold value during continuous wave operation, so that equation 2.91 and equation 2.93 can be equated to obtain an expression for the resonator internal power density:

$$S_r = \frac{\eta_{St}\eta_{abs}(S_p - S_{p,th})}{M_r L_{int} + T_{tot}}, \tag{2.94}$$

where $\eta_{St} = \frac{\nu_l}{\nu_p}$ is the Stokes efficiency given by the energy difference of the pump and laser photon. $S_{p,th}$ is the pump power density at threshold, which is obtained from equation 2.90 for $S_r = 0$, an assumption valid at threshold:

$$S_{p,th} = \frac{h\nu_p}{\tau\eta_{abs}} z N_{2,th}. \tag{2.95}$$

If the pump spot area A_p is known, with the expression for the threshold inversion density in equation 2.93 an estimate for the required threshold pump power can be made:

$$P_{th} = A_p \cdot S_{p,th} = \frac{A_p h\nu_p}{\tau\eta_{abs}} \frac{\sigma_{abs}^{las}}{\sigma_{abs}^{las} + \sigma_{em}^{las}} N_t z + \frac{A_p h\nu_p}{\tau\eta_{abs}} \frac{M_r L_{int} + T_{tot}}{M_r(\sigma_{abs}^{las} + \sigma_{em}^{las})}. \tag{2.96}$$

On the other hand, from the measured threshold pump powers the threshold inversion density can be estimated to be

$$N_{2,th} = \frac{P_{th}}{A_p} \frac{\tau \eta_{abs}}{z h \nu_p}. \tag{2.97}$$

In the zero dimensional model the cross section of the resonator mode is assumed to be the same as that of the pump mode. In this case, from equation 2.94 the actual laser power extracted using an outcoupling mirror of transmission rate T_{OC} can be estimated to be

$$P_{out} = T_{OC} \frac{S_r}{A_p} = \frac{T_{OC}}{M_r L_{int} + T_{tot}} \eta_{St} \eta_{abs} (P_{in} - P_{th}) \tag{2.98}$$

and with this the optical-to-optical efficiency becomes

$$\eta_{opt} = \frac{P_{out}}{P_{in}} = \eta_S \left(1 - \frac{P_{th}}{P_{in}} \right), \tag{2.99}$$

where

$$\eta_S = \frac{T_{OC}}{M_r L_{int} + T_{tot}} \eta_{St} \eta_{abs} \tag{2.100}$$

is the slope efficiency of the laser and P_{in} is the incident pump power.

3. The Laser Material Yb:YAG

This chapter deals primarily with the crystallographic properties of ytterbium-doped yttrium aluminium garnet (Yb:YAG). Other properties and aspects of Yb:YAG, which are considered important regarding its use as a laser material are also addressed. First, a brief overview of the historical background is given, followed by a crystallographic description of the host material YAG. The localised energy level schemes of the trivalent and divalent ytterbium ion are discussed, particularly their location in respect to the delocalised host energy bands. Next, single crystalline and ceramic Yb:YAG are introduced as two different classes of laser material that are investigated in the framework of this research. The techniques for crystal growth and fabrication of transparent ceramics are described and the crystals grown in the framework of this thesis are introduced, together with the ceramic samples used in this research. The Results of microscopy and microprobe analyses as well as thermal diffusivity measurements carried out on the different Yb:YAG samples are presented. The final section of this chapter summarises the current state of research. Some parameters of Yb:YAG important for laser operation are listed in table 3.4 at the end of section 3.5.

3.1. Historical Background

Yb:YAG was first spectroscopically investigated by Wood in the early sixties [Woo63], whose results were supplemented and improved by the works of Koningstein [Kon65], Buchanan [Buc67], Bogomolova [Bog76] and their coworkers in the mid-sixties to the mid-seventies.

Stimulated emission of Yb^{3+} in YAG was first observed by Johnson *et al.* in 1965 [Joh71], where the Yb:YAG crystal was cooled to 77 K and flash lamp pumped by a FT524 helical xenon lamp. However, the high threshold and low efficiency, primarily due to the lack of Yb^{3+} absorption bands, resulted in inefficient pumping with broadband flash lamps and discouraged further immediate interest. Therefore, and because of the quasi-three-level nature of the Yb^{3+}-ion at room temperature with about 4% of the population being in the terminal Stark level of the laser transition, development of ytterbium lasers has been rather slow compared to neodymium lasers. In 1971, Reinberg and coworkers presented the first resonantly pumped Yb:YAG laser using a Si:GaAs light-emitting-diode (LED) as a pump source. The efficiency of the system was significantly increased because of the superior spectral match of the LED emission to the single Yb^{3+} absorption band in Yb:YAG [Rei71]. Due to the limited brightness of the LED source used, this experiment also required cryogenic temperatures to overcome the laser threshold.

The potential of Yb:YAG as a useful laser material could only be realised when efficient InGaAs laser diodes became available in the late eighties to the early nineties [Kol88, Wu90, Cho90, Bou90]. The first room temperature diode-pumped continuous wave (CW) Yb:YAG

laser was developed by Lacovara and coworkers in 1991 using InGaAs strain-layer diode lasers emitting at 968 nm as a pump source in a simple end-pumped configuration [Lac91]. In 2000, room temperature laser action was also demonstrated in stoichiometric YbAG by Patel *et al.* [Pat01]. Much attention has been paid to the scaling of the output power of Yb:YAG lasers since the early nineties [Kru90, Fan92, Tai97]. In this attempt four main device architectures have been investigated, differentiated largely by the spatial orientation of the pump propagation direction relative to the geometric shape of the gain medium and to the direction of propagation of the output laser beam, as well as the directions in which waste heat is removed: The end-pumped rod design primarily investigated by Beach *et al.* [Bea00], the side-pumped rod architecture mainly developed by Bruesselbach *et al.* [Bru97], the edge-pumped slab primarily developed by the Byer-group [Rut00] and finally the thin-disk laser concept by Giesen *et al.* [Gie94]. An overview summarising the development of diode-pumped Yb solid-state lasers in the nineties is given by Krupke [Kru00].

3.2. The Host Material YAG

The spectroscopical properties of a laser ion are to a large extent determined by the choice of host material. Lattice symmetry as well as the distances to the neighbouring ions contribute to the crystal field and its influence on the laser ion. In addition, thermo-mechanical attributes such as hardness, cleavability and thermal conductivity are of great importance for a laser material. YAG is a synthetic, nonmagnetic garnet which was first fabricated by Yoder and Keith in 1951 [Yod51]. Due to its favourable properties YAG is one of the most established laser host materials finding widespread use in commercial solid-state lasers.

Garnets have the general formula $\{A_3\}[B_2](C_3)O_{12}$ with three structural cationic sites, where $\{\}$, [] and () denote D_2 dodecahedral (24(c) in Wyckoff notation), C_{3i} octahedral (16(a)) and S_4 tetrahedral (24(d)) coordination, respectively [Men25]. The structure has the cubic space group $Ia\bar{3}d$ (O_h^{10} in Schönflies notation) and all cation positions are fixed by symmetry. The anion occupies the general position (96(h)) and thus has three degrees of position freedom. This structure is visualised in figure 3.1 as a lattice formed by BO_6 octahedra and CO_4 tetrahedra. Each BO_6 octahedron is connected to another six octahedra through corner-sharing tetrahedra. Each CO_4 tetrahedron in turn, shares corners with four octahedra. The largest ions (A) occupy eight-coordination sites in the lattice interstices. Thus, in the case of YAG, site A is occupied by the Y^{3+}-ions, and sites B and C by the smaller Al^{3+}-ions forming the formula $Y_3Al_2Al_3O_{12}$, in shorter $Y_3Al_5O_{12}$. The unit cell contains eight formula units with 160 atoms, and the lattice constant at room temperature is 12.000 Å [Dob04].

A distortion of the garnet structure from the ideal cubic system has been reported for YAG single crystals obtained from the high temperature melt and has been attributed to substitution-type defects, so-called antisite defects, where some of the rare earth Y-ions localise at the C_{3i} octahedral instead of the D_2 dodecahedral sites [Ash77]. The concentration of these antisites has been estimated to be about 0.25% in YAG [Zor07] causing a shortening of the Y-O bond length [Kuk00]. It has been shown that antisites can localise the low-energy excitons due to the existence of a non-Coulomb potential arising from the substitution of the Al^{3+} by Y^{3+} core cations [Zor05].

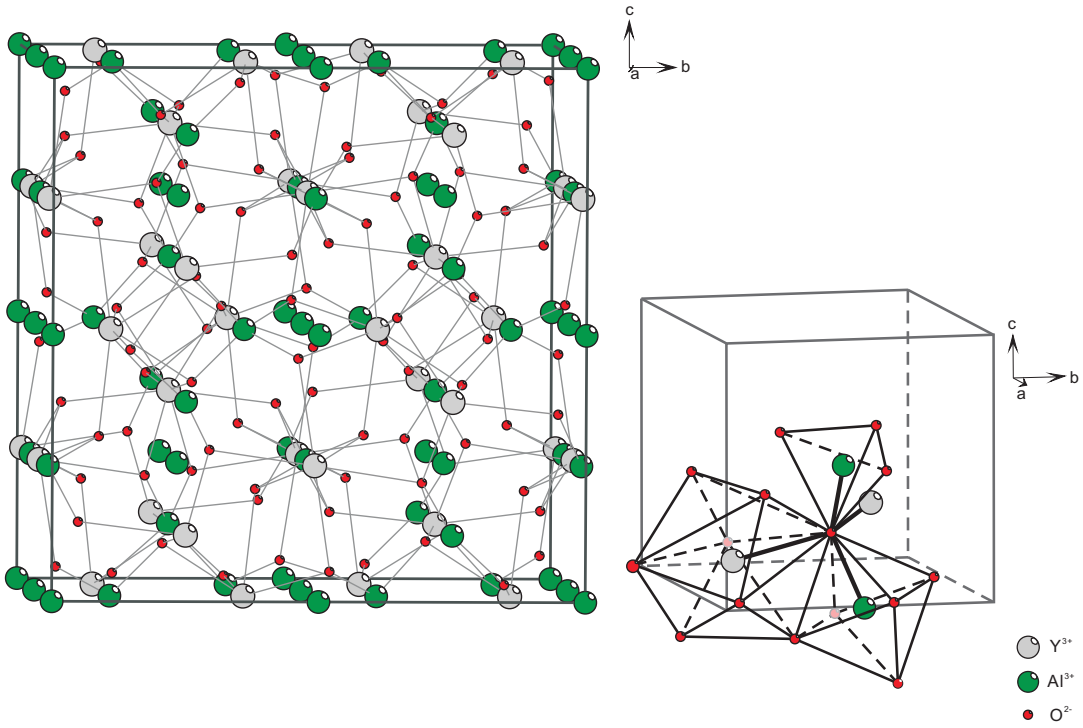

Figure 3.1.: Garnet structure. Left: Unit cell of YAG. Right: View of the three kinds of oxygen polyhedra; dodecahedral, octahedral and tetrahedral coordination depicted about an oxygen ion [Bel95].

The optical absorption of YAG displays a broad lattice phonon absorption region extending from about 100 µm to about 4.2 µm. The region between 100 µm and 11.6 µm has been assigned to one-phonon transitions while two- and three-phonon processes are found to dominate in the region between 11.6 µm and 4.2 µm [Sla69]. YAG has its band edge at around 190 nm [Thi01] [1] and is almost transparent throughout the visible and the near UV spectral range. The transparency range for an absorption coefficient $\alpha = 1\,\mathrm{cm}^{-1}$ is stated as 0.21 µm to 5.3 µm [Bas02] and 0.33 µm to 4.2 µm for $\alpha < 0.1\,\mathrm{cm}^{-1}$ [Sla69]. However, impurity and defect centres in the crystal lead to additional absorption bands which result in an extended absorption band edge. Known defects in single crystals grown from the melt are oxygen vacancies with either one or two trapped electron(s), denoted as F^+- and F-centres respectively, as well as impurity ions such as iron and nickel, which have their origin in the manufacturing process of the Ir-crucibles that are commonly used [Fag07]. The oxygen vacancy based colour centres are typical defects because of the inert or even reducing atmosphere during crystal growth. F^+-centres in the YAG host display absorption bands at 235 nm and 370 nm and under excitation within these bands, F^+ luminescence has been reported at about 400 nm. Evaluation of polarisation of this luminescence led to the proposal that F^+-centres might be perturbed by an adjacent antisite defect [Spr91]. Absorption bands at 240 nm and 200 nm were ascribed to F-centres; excitation within these bands yields a luminescence band centred at 460 nm [Puj01]. These oxygen vacancy related defects are completely eliminated by annealing the YAG crystal in air at about 1 000°C

[1] Different values for the band edge of YAG can be found in literature, e.g. [Sla69, Rot89b, Pie00]. For a discussion of this value see section 3.4.

for several hours. Optical and electron paramagnetic resonance (EPR) studies of Fe-impurities in YAG crystals confirmed Fe^{3+}-ions in tetrahedral and octahedral sites with their corresponding narrow absorption lines at around 407 nm and 415 nm, respectively. The absorption band centred at 255 nm was identified as a composite charge-transfer band made up of contributions from both of these symmetry sites [Sco74, Che88, Rot89b]. Iron can also be found in the divalent state, when charge compensated by other impurities or defects. The presence of divalent iron with tetrahedral coordination is revealed by a broad absorption band between 1 100 nm and 2 100 nm [Fag07]. Trivalent nickel located on octahedral sites displays an absorption peak at 420 nm which has been identified as being due to a charge transfer transition [Rot89a]. The divalent Ni^{2+}-ion is located in both tetrahedral and octahedral sites. The tetrahedrally coordinated Ni^{2+}-ion exhibits characteristic absorption bands at around 620 nm and 1035 nm [Koe90]. Other known impurities, usually in ppm range are silicon, gallium, sodium and other rare earth ions introduced by the raw materials [Fag07].

3.3. Ytterbium

The element ytterbium (Yb) has the atomic number $Z = 70$ and an atomic mass of 173.04 u, and is thus the second heaviest atom after lutetium in the lanthanoid series. Ytterbium was discovered in 1878 by the chemist de Marignac in the Swedish town Ytterby, after which the element is named. As all lanthanoid ions, in compounds ytterbium is mostly found in the oxidation state +III. Compared to the other lanthanoids, ytterbium as well as europium can also be found in the oxidation state +II due to relatively high ionisation energies of the third valence electron. This is also true for compounds in which only trivalent sites are available for substitution [Dic01]. Generally, the most stable oxidation state of an impurity in a certain compound depends on the Fermi energy of the material. The valence stability of the dopant Yb-ion in the different compounds is thus directly related to the location of its ground state energy level relative to the Fermi level of the undoped host material, which in insulators is located in the middle of the forbidden gap [Rob78]. Among the lanthanoids, relatively high electron-phonon coupling is found for the $4f$ states of the trivalent Yb-ion. This is commonly attributed to the gradual decrease in shielding of the $4f$ electrons by the $5s$ and $5p$ closed shells along the lanthanoid series [Ell97a] (see also section 2.2.1).

3.3.1. The Trivalent and Divalent Yb-Ion

The electronic configuration of the neutral Yb-atom is $[Xe]4f^{14}6s^2$. The ground states of trivalent and divalent ytterbium have a xenon closed shell and $4f^{13}$ and $4f^{14}$ valence configurations, respectively (see table 2.1).

Applying Hund's rules, the ground state of the Yb^{3+}-ion is denoted as $^2F_{7/2}$. The energy configuration with 13 electrons in the $4f$ shell is equivalent to a single hole and thus the case can be treated as formally identical to that of a single $4f$ electron. Therefore, all interactions involving two or more electrons in the $4f$ shell can be neglected. The number of free ion parameters is thus reduced to only two, i.e. $E_{AVE} \approx 4\,600\,\mathrm{cm}^{-1}$, which accounts for the spherically

symmetric part of the Hamiltonian and also incorporates the parameter F^0, and the spin-orbit coupling constant $\zeta_{4f} \approx 2\,900\,\mathrm{cm}^{-1}$ [Gör96][2]. Therefore, the Yb^{3+}-ion shows only two spin-orbit states ($J = 7/2$, 5/2) separated by about $10\,000\,\mathrm{cm}^{-1}$, each $2J+1$-fold degenerate. This number is too low to allow a precise determination of the B_q^k crystal field parameters describing the Stark levels, especially in case of low symmetry point sites where up to 27 parameters may be required [Gör96]. Therefore, to obtain the energy level structure of trivalent ytterbium in a certain compound, experimental data from the spectra and their correct interpretation are needed.

The 14 f electrons in the case of divalent ytterbium form a closed subshell and thus the ground state is a $^1S_0$ level. Therefore, intraconfigurational $4f$ transitions are not possible and optical excitation involves other configurations, the lowest configuration of the excited states being the $4f^{13}5d$ configuration, where one electron is raised into the $5d$ shell. The 13 electrons left in the $4f$ shell can be considered as a Yb^{3+}-ion configuration with the two manifolds $^2F_{7/2}$ and $^2F_{5/2}$. The spin of the $5d$ electron can either be parallel or antiparallel to that of the $4f^{13}$ core, thus the whole energy level scheme exists for singlet and for triplet states, from which, according to Hund's rules, the triplet states are energetically lower. The Russell-Saunders levels arising from this configuration are ^{1,3}(PDFGH) and the total degeneracy is 140 (35 singlet and 105 triplet states).

In 1965, Bryant presented the energy level structure of the free Yb^{2+}- and Yb^{3+}-ion deduced from measurements and calculations [Bry65]. An improved assignment of the Yb^{2+} free ion energy levels has been presented by Öberg and Lundberg in 2007 [Öbe07]. Figure 2.2 shows qualitatively the characteristics of the energy level schemes of the divalent and trivalent lanthanoids. From these it can be seen that both, the Yb^{2+}- and the Yb^{3+}-ion, display large energetic gaps between the $4f$ and the lowest $4f^{n-1}5d$ states, which lead to well separated interconfigurational and intraconfigurational transitions. In the free Yb^{3+}-ion, the first level of the $4f^{n-1}5d$ configuration has been measured to be $88\,195\,\mathrm{cm}^{-1}$ [Bry65], which is in good agreement with the predicted value of $87\,340 \pm 570\,\mathrm{cm}^{-1}$ [Dor00]. In case of the free Yb^{2+}-ion, the first level of the $4f^{n-1}5d$ configuration is located at about $E = 33\,400\,\mathrm{cm}^{-1}$ [Bry65, Dor03b, Öbe07].

3.3.2. The Trivalent and Divalent Yb-Ion in YAG

The Yb^{3+}-ion with an ionic radius of 0.985 Å in eightfold coordination predominantly substitutes the Y^{3+}-ion on the dodecahedral site, which has an ionic radius of 1.019 Å [Kam90]. The rather small differences in the ionic radii allow even full replacement of yttrium in the garnet structure so that any kind of doping concentration can be realised for Yb:YAG. As a consequence of the smaller ionic radius of Yb^{3+}, the unit cell length decreases with increasing doping level. The average unit cell parameters are linearly dependent on the concentration of the doping ions with the lattice constant decreasing from 12.000 Å to 11.928 Å from YAG to YbAG [Dob04]. In the same manner the nearest neighbour distances of the dodecahedral sites (four sites) change from 3.676 Å in YAG to 3.654 Å in YbAG [Mar04]. Although the ionic radii

[2] ζ_{4f} increases over the lanthanoid series from ca. $650\,\mathrm{cm}^{-1}$ for Ce^{3+} to $2\,900\,\mathrm{cm}^{-1}$ for Yb^{3+}[Car89]: In Yb^{3+} the spin-orbit coupling is so large that J is nearly a good quantum number.

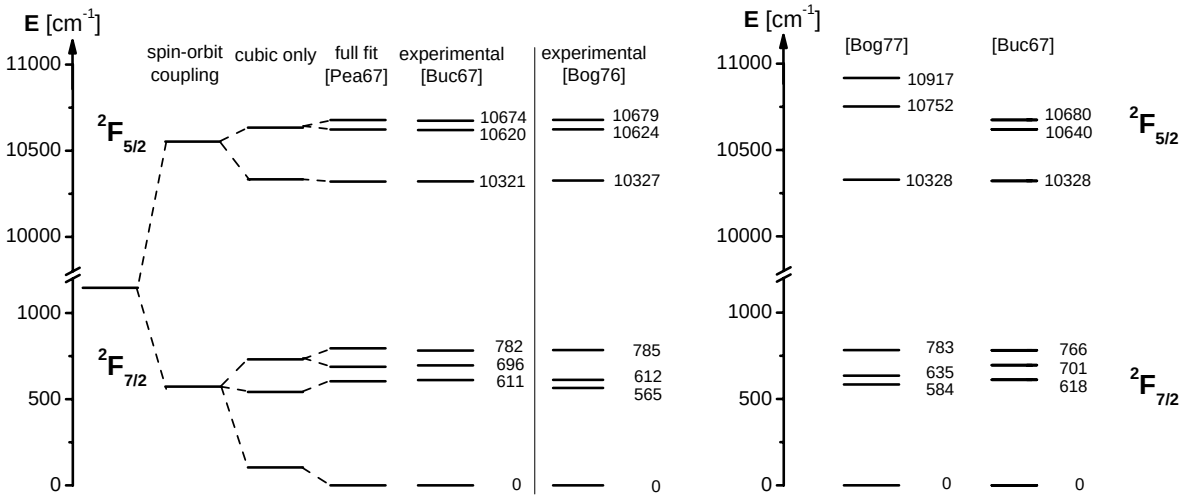

Figure 3.2.: The most cited values for the energy level structure of the Yb^{3+}-ion incorporated in YAG (left) [Buc67, Pea67, Bog76] and in the stoichiometric compound YbAG (right) [Bog77, Buc67]. The local site symmetry is D_2. "cubic only" and "full fit" refer to the crystal field parameters used in the calculations [Pea67]. See text for discussion.

of the Al-sites are much smaller compared to the dopant rare earth ions with 0.390 Å in tetrahedral and 0.535 Å in octahedral coordination, an antisite defect has been observed for small ions such as trivalent erbium, which in eightfold coordination has an ionic radius of 1.004 Å [Kam90]. In $Er_3Al_5O_{12}$ about 3% of the Er^{3+}-ions have been found to replace Al^{3+}-ions on the octahedral sites [Lup98]. This kind of deviation from stoichiometry results in different symmetry of the crystal environment of the cation sites yielding several types of spectra for rare earth ions inserted into such a host lattice. The antisite defect may thus be confirmed directly by spectra of rare earth ions occupying sites differing from D_2-symmetry. However, according to the Judd-Ofelt theory [Jud62, Ofe62] induced electric dipole transitions can only be observed if the point group of the site contains no centre of symmetry. The octahedral site with C_{3i}-symmetry belongs to a centrosymmetric point group which hinders the observation of such spectra. On the other hand, rare earth ions inserted into octahedral sites should also distort locally the environment of the adjacent dodecahedral sites removing the structural degeneracy of these sites. The spectral lines of lanthanoid ions located at the normal and distorted dodecahedral sites are thus inhomogeneously split.

Nonradiative decay of the upper laser level is a significant loss channel for a laser leading to shortening of the fluorescence lifetime (see also section 2.2.1). In YAG, assuming 860 cm^{-1} to be the energy of the most energetic optical phonon [Sla69], more than 10 phonons are needed to bridge the gap between the $^2F_{7/2}$ ground and the $^2F_{5/2}$ excited state of the Yb^{3+}-ion. A 10th order process is highly improbable and therefore multi-phonon relaxation can usually be neglected for Yb:YAG. On the other hand, the strong electron-phonon interaction of the Yb^{3+}-ion, which is causing the confusing phonon-assisted lines in the absorption and emission spectra has a positive benefit in that the intramanifold relaxation lifetimes (thermalisation) are very short. The small energy difference of $<800\,cm^{-1}$ between the levels are of the same order of

magnitude as the energy of the available phonons in YAG so that all intramanifold transitions are single phonon and therefore on a picosecond time scale [Bru97].

For Yb^{3+}-ion incorporated into YAG, several different energy level schemes can be found in the literature, among which the most cited are those of Buchanan and coworkers [Buc67, Pea67] and of Bogomolova *et al.* [Bog76]. Due to the difficulties in determining the relevant parameters and, owing to vibronics the rather complicated spectra of Yb:YAG (see also section 2.2.1), the identification of the Stark levels in both multiplets has been the focus of much research, e.g. [Bog77, Lup99a, Lup99b, Auz02]. In YAG the Yb-ion is incorporated on the dodecahedral site with an orthorhombic (D_2) local site symmetry (see section 3.2). In the crystal field, the $^2F_{7/2}$ ground state is split into four and the $^2F_{5/2}$ excited state is split into three Kramers-degenerate Stark levels. The energy level structure of the Yb^{3+}-ion in YAG as well as that in the stoichiometric compound YbAG are shown in figure 3.2. The left part of figure 3.2 displays the calculated and measured energy levels from [Buc67, Pea67]. The different columns show how the spin-orbit interaction and the crystal field act on the degeneracy of the energy levels. The terms "cubic only" and "full fit" refer to the used crystal field parameters in [Pea67]. The energy levels obtained experimentally in [Bog76] are also shown. While the agreement of the Stark level positions in [Buc67] and [Bog76] is very good for the $^2F_{5/2}$ excited state, the Stark levels of the $^2F_{7/2}$ ground state do not correspond well. The differences in interpretation are even more pronounced for the energy level structure of YbAG (figure 3.2, right). Here, the excited $^2F_{5/2}$ state also displays significant disagreements in the assignment. In the latest published data of Kaminskii for trivalent ytterbium in YAG, the Stark levels of the ground multiplet are given as 0, 565, 612, 785 cm^{-1} and those of the excited multiplet as 10 327, 10 624*, 10 679*, 10 912 cm^{-1}, where * implies nondefinite assignment [Kam90]. Lupei and coworkers reinterpreted the Yb:YAG spectra based on electron-phonon coupling theory and suggest the Stark level positions of the excited $^2F_{5/2}$ to be at 10 327, 10 646, and 10 914 cm^{-1} [Lup99b]. Auzel also questions the electronic energy level structure of the $^2F_{7/2}$ ground state multiplet and established a relationship between various crystal field parameters along the lanthanoid series versus the number of electrons in the $4f$ shell, which allows a prediction of the maximum splitting for the Yb^{3+} ground state if the maximum splitting of the $^4I_{9/2}$ ground state of the Nd^{3+}-ion is known for the same host [Auz02]. According to his work, the generally accepted value of 782 cm^{-1} [Buc67] for the highest Stark component of the $^2F_{7/2}$ ground state of the Yb^{3+}-ion is too low, and instead a value of 1 032 cm^{-1} is more appropriate. These discrepancies and disagreements in the literature show the difficulties in the calculations and interpretation of measurements for the evaluation of the energy level structure of the Yb^{3+}-ion incorporated into a host material. This results in a high level of uncertainty in the calculation of the emission cross sections of the Yb^{3+}-ion, which are necessary input values for the simulation of the laser performance of a material. Using the different available sets of Stark levels, the standard deviation for the emission cross sections of Yb:YAG obtained by the reciprocity principle was estimated to be about 20% [Mix99]. According to the empirical formula of Dorenbos [Dor00], the first $4f^{12}5d$ level of Yb^{3+} in YAG is expected to be at about 60 700 $\pm$ 570 cm^{-1} in the UV spectral range. The interconfigurational transition therefore overlaps the conduction band in oxide crystals, where the band gap is usually in the region of 50 000 cm^{-1}.

In the case of the Yb^{2+}-ion in YAG, some kind of charge compensation is needed to maintain charge neutrality and stabilise the divalent oxidation state at the trivalent D_2 lattice site. Usu-

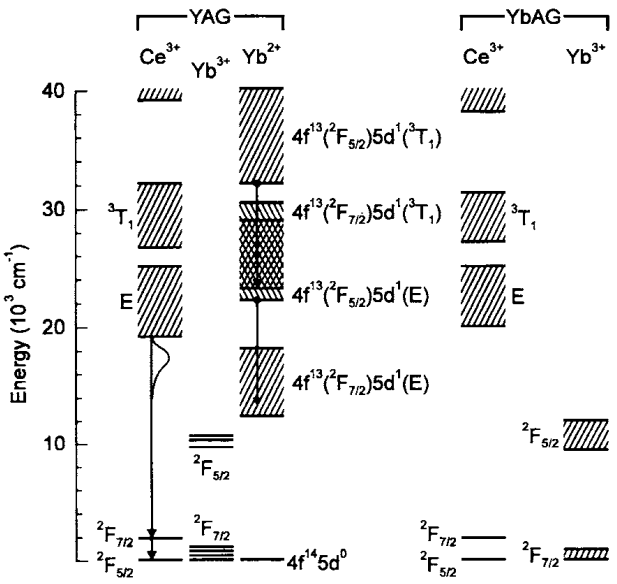

Figure 3.3.: The energy level scheme of Yb^{2+} in YAG according to [Kor96].

ally oxygen vacancies or codopants such as Si^{4+} or Zr^{4+} act as useful charge compensators. However, because of the energetically favourable condition of a complete $4f$ shell, ytterbium displays a very high ionisation energy for the third valence electron and thus, compared to other lanthanoid ions, is more commonly found in its divalent oxidation state. Valence stability of ytterbium has attracted much attention [Tem99, Thi03] and trivalent ytterbium has been extensively discussed as a charge carrier recombination centre (electron trap) [Dic01], particularly regarding its possible usage in scintillator materials [Woj96, Gue01]. Along with trivalent europium, the divalent oxidation state of which has a half filled $4f$ shell, trivalent ytterbium displays the lowest charge transfer (CT) energy among the trivalent lanthanoid ions, so that transient Yb^{2+}-ions might well be present in YAG under certain conditions. The 20 free ion levels associated with the excited $4f^{13}5d$ configuration decompose in a cubic field into a total of 58 levels [Pip67]. According to Loh, the $4f^{n-1}5d$ configuration of most of the divalent and trivalent lanthanoid ions in solids is known to be formed by weak interaction between the $5d$ orbitals, which are strongly split in the crystal field, with the $4f^{n-1}$ core [Loh73]. In a highly symmetric crystal field, the $5d$ orbitals of divalent ytterbium consists of t_{2g} ($d_{5/2}$) and e_g ($d_{3/2}$) components, resulting in the splitting of the $4f^{13}5d$ state into T_{2g} and E_g levels[3]. Assuming coupling of a crystal field split $5d$ electron ($d_{5/2}$, $d_{3/2}$) to a spin orbit split $4f^{13}$ core ($^2F_{7/2}$, $^2F_{5/2}$), at least four absorption peaks are expected for a Yb^{2+}-ion in a cubic crystal, which correspond to the final states $4f^{13}(^2F_{7/2}$ or $^2F_{5/2})$ $5d(T_{2g}$ or $E_g)$ [Loh73]. In YAG, due to reduction of symmetry from ideal cubic O_h to D_2, these states are further split. Furthermore, the $4f^{13}6s$ configuration is energetically close to the $4f^{13}5d$ states. Therefore, it may be the case that in some materials the $4f^{13}6s$ level is the lowest excited state. According to the em-

[3]The Mulliken Symmetry labels, developed for atomic and molecular orbitals, are often applied for energy states in a crystalline matrix. Lower case notation is used for orbitals and upper case for energy states. T_{2g}: Triply degenerate state, unsymmetric with respect to rotational axis C_2 and perpendicular to the principal axis C_n, and E_g: Doubly degenerate state. The subscript g indicates even (German: "gerade") parity.

pirical formula of Dorenbos the first $4f^{13}5d$ level of the Yb^{2+}-ion in YAG is located at about $18\,300 \pm 1\,700\,cm^{-1}$ [Dor03a, Dor05]. The only schematic of the Yb^{2+}-ion in (Fe-codoped) YAG, which could be found in the literature [Kor96], is shown in figure 3.3. In this diagram the lowest $4f^{13}5d$ state lies at about $12\,000\,cm^{-1}$, which is much lower located than the estimated value. This discrepancy will be discussed in detail in section 4.2.

3.4. Localised and Delocalised States

So far, only the electronic energy levels of the lanthanoid ions have been addressed. However, interactions between the localised electronic states of a dopant ion and the delocalised band states of the crystal lattice as described in section 2.2.3 can strongly effect the optical properties of laser materials. In particular photoionisation, which is closely linked to the position of the lanthanoids' $4f^{n-1}5d$ levels with respect to the host conduction band, and charge transfer between the dopant ions and the host can have negative effects such as elimination or reduction in quantum efficiency or the creation of colour centres that can be deleterious in laser applications. In contrast to the well studied $4f$ states, relatively little is known about the relationships between these two extremes of highly localised $4f$ electronic states of the lanthanoid ion and the delocalised one electron band states of the host.

3.4.1. The Host Energy Bands

The electronic states of the host can be qualitatively understood by extending the picture commonly used to describe bonding in molecules [Pet95]. The total energy of the molecular system is reduced by sharing the valence electrons among the participating atoms, where each atom retains its tightly bound core electrons. The shared valence electrons occupy new molecular orbitals, which are formed from combinations of the original atomic valence orbitals. The resulting molecular orbital with the lowest total energy corresponds to occupied bonding orbitals whereas the unoccupied combinations which increase the total energy are referred to as anti-bonding orbitals. The core orbitals of the atoms do not participate in the bonding and are therefore called non-bonding orbitals. Molecular orbitals are classified as ionic or covalent depending on whether the valence electrons are primarily localised on specific atoms or shared among all the atoms in the molecule, respectively. In an ionic material, the bonding orbitals are predominantly formed by the anion atom's valence orbitals while the anti-bonding orbitals are formed by cation orbitals. In a crystalline solid, the large number of valence orbitals, contributed by all of the atoms in the crystal, combines to produce extended electronic states known as Bloch states. These have the same translational symmetry as the crystal lattice to within a periodic phase factor. The Bloch states are equivalent to the atomic and molecular orbitals, where all valence electrons in the crystal are distributed among the different Bloch states and the total energy of the system is determined by the combination of the states occupied. Since the number of Bloch states is large, i.e. equal to the total number of valence orbitals contributed by all of the atoms in the crystal, the energies of the valence electrons in the crystal become distributed over a delocalised band of energies, the so-called valence band, and the unoccupied anti-bonding orbitals combine to form the so-called conduction band.

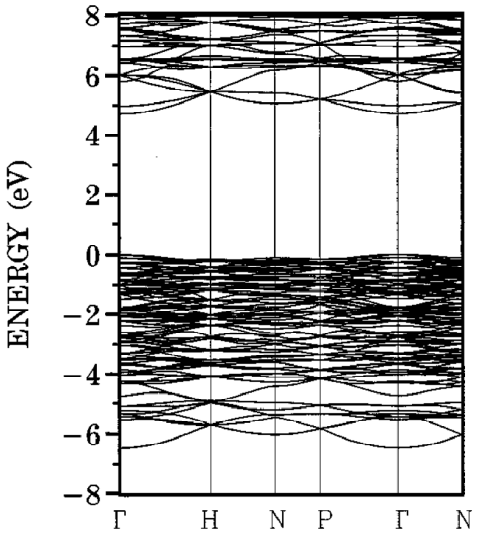

Figure 3.4.: The calculated YAG band structure along the symmetry lines of the cubic Brillouin zone [Xu99]. The band gap of 4.71 eV is direct at Γ. The band gap energy is an underestimation typical for the used approximations and is much smaller than actual measurements suggest.

Many of the properties of a solid are determined by the relative width of the Bloch bands relative to the mean separation of the bands. Typically, laser hosts are dielectrics, i.e. insulating materials. In these materials the separation of the energy bands is much greater than the combined widths so that there is an energy gap between the occupied and unoccupied band states. The width of this band gap, also known as the forbidden gap, is usually greater than 3 eV in insulating materials. For the band gap of YAG there exist many different values in the literature ranging between 6.5 eV [Thi01][4] and 6.97 eV [Pie00]. The precise determination and even the definition[5] of the band gap is not simple and the experimental values for this fundamental material property are uncertain. The interpretation of the experimental results is difficult due to broadening as well as additional features, mostly due to impurities or defects, that obscure the onset of the band to band transitions. The weak density of states and strong momentum dependency typical of the conduction band minimum in optical materials further complicates the determination. This is particularly important for indirect band gap materials where the valence band maximum and the conduction band minimum do not have the same value of crystal momentum. In these materials, the optical band gap measured from absorption may be larger than the minimum thermodynamic band gap because of the momentum selection rules for op-

[4]The value of 6.5 eV is stated in many publications and the paper of Slack *et al.* from 1969 [Sla69] is in most cases cited as a reference. The same paper is often cited for a value of 50 000 cm^{-1}, i.e. about 6.2 eV (e.g. [Owe81]). However, in [Sla69] the absorption edge region is defined as $\geq$ 54 300 cm^{-1} ($\approx$ 6.73 eV) for which $\alpha \geq 10^3$ cm^{-1}.

[5]Dorenbos differentiates between the energy difference between the top of the valence band and the bottom of the conduction band as the threshold energy needed to create a free electron in the conduction band by means of optical excitation E_{VC}, and the fundamental absorption onset of the crystal E_{fa} whose final state is most often an exciton state, with its peak at E_{ex} [Dor03c]. The relation of the two is stated to be $E_{VC} \approx 1.08 E_{ex}$ [Dor05].

tical transitions. The experimental technique itself also can have an influence on the results. For example, band gaps measured using methods such as electron yield spectroscopy or electron energy loss spectroscopy could be significantly reduced from their true values because of the Franz-Keldish effect [Fra58, Kel58], in which the presence of an electric field causes the electron wavefunctions to extend exponentially into the band gap due to the potential energy variation across the crystal. Furthermore, doping with lanthanoids has an influence on the host band gap. The crystal lattice can be considerably disturbed depending on the difference in radius of the replaced host and dopant ions as well as the doping concentration. This shifts the fundamental absorption edge to about 5.17 eV ($\approx$ 240 nm) in the case of Nd:YAG even at Nd concentrations below 1% [Kru71]. Some difficulties encountered when measuring the band gap energy are summarised in [Thi03]. The value for the band gap energy of YAG used in this work is 6.5 eV. For discussion also see section 3.4.2.

Theoretical calculations of the YAG band structure can also be found in the literature. Calculations of Xu and Ching using the local density approximation show that the oxygen $2p$ levels constitute the upper valence band with a total width of about 6.5 eV [Xu99, Chi99]. The top of the valence band in YAG seems to be very flat with maximum variations of less than a few hundred meV throughout the Brillouin zone. A flat valence band is characteristic of aluminium and yttrium oxides [Thi01]. In the same work, the band gap was calculated to be 4.71 eV and considered direct at Γ. The much smaller value for the band gap energy is apparently an underestimation typical for the local density approximation used. At the bottom of the conduction band yttrium has the largest component so that one can say the band gap in YAG is primarily determined by interaction between oxygen and yttrium rather than between oxygen and aluminium. The band structure calculated by Xu and Ching is shown in figure 3.4.

3.4.2. Yb^{3+} and Yb^{2+} Electronic Energy Levels Relative to the YAG Host Bands

There are several approaches to determine the localised lanthanoid dopant energy level positions with respect to the delocalised host bands. With X-ray photoemission spectroscopy (XPS) [Sat76] and ultraviolet photoemission spectroscopy (UPS) [Thi01] the energy difference between the $4f$ ground state level and the valence band levels can be determined. With direct as well as two-step photoconductivity measurements the energy difference to the bottom of the conduction band can be determined [Ped86, Jia02], and with excited state absorption (ESA) measurements [Ham89, Law93] information on the transition from an excited $5d$ level to conduction state levels can be obtained. However, the interpretation of the experimental data is not always straightforward. The photoconductivity threshold for instance, does not need to coincide with the direct transition to the bottom of the conduction band. In Yb^{2+}:CaF_2 for example, the photoconductivity threshold coincides with the dipole-allowed transition to the $4f^{13}(^2F_{5/2})5d(E_g)$ level [Moi89]. The oscillator strength for a direct transition from the localised $4f$ level to the delocalised conduction band states is most likely too small to generate a significant photocurrent. Furthermore, the localised state to band absorption has a strength and shape that is highly dependent on the characteristic volume of the initial-bound-state wave function [Rid99]. Thus, the shape of the absorption curve from a localised state to the conduc-

tion band does not necessarily resemble the valence band to conduction band transition with a simple energy shift. This has also some impact on the interpretation of ESA measurements. As the $5d$ wave functions are much more diffuse than the $4f$ wave functions, the $5d$ to conduction band transition will have its maximum at a significant lower energy relative to the band edge than the $4f$ to conduction band absorption [Ham89]. For these reasons, care needs to be taken when analysing data obtained by photoconductivity and ESA measurements, particularly when deducing the level positions relative to the host bands.

The $4f$ ground state positions of the heavy trivalent lanthanoid ions relative to the host valence band of YAG have been measured by Thiel and coworkers [Thi01]. In this context, Yb:YAG single crystals with doping concentrations of 10%, 25% and 50% as well as one YbAG single crystal, all grown at Scientific Materials Corporation, USA by the Czochralski method, were investigated using resonant photoemission spectroscopy. The advantage of this method lies in the direct determination of the energies of both the valence and electronic states relative to a common reference, whereas the interpretation of other techniques such as photoconductivity or excited state absorption may be complicated by uncertainties regarding the nature of the initial and final states involved. Thiel *et al.* determined the $4f$ ionisation threshold, i.e. the energy required to remove one $4f$ electron and leave the remaining tetravalent lanthanoid ion in its ground state, as well as the binding energy of the valence band maximum (VBM). These measurements revealed that the $4f$ electron ground state binding energy of the Yb^{3+}-ion in YAG is about 3 eV larger than those of the electrons at the VBM. Of the Yb-doped samples, only the 10%Yb:YAG sample displayed a slightly different binding energy, which was 0.2 eV smaller than the other samples. It can be said that almost no concentration dependency of the binding energies is observed. The VBM in YAG was not significantly changed by the addition of any of the lanthanoid ions and exhibited a constant binding energy of 8.7 eV within the measurement errors[6]. For this reason the position of the Yb^{3+} and Yb^{2+} electronic energy states are given relative to the VBM binding energy.

A comprehensive energy level diagram with respect to the host bands can be estimated when using the measured ground state position [Thi01] together with the work of Dorenbos on the relative positions of the $4f^{n-1}5d$ energy levels of the trivalent [Dor00] and divalent [Dor03c, Dor03b] lanthanoids as well as on the systematics in the charge transfer energies of the trivalent lanthanoids in the different compounds [Dor03b, Dor05]. In figure 3.5 the electronic energy levels of Yb^{3+} and Yb^{2+} are schematically plotted together with the YAG host bands. The energy level positions of the Yb^{3+} $^2F_{7/2}$ ground state and its lowest $4f^{12}5d$ state from [Thi03], the latter determined by using a semi-empirical formula [Dor00], are drawn as solid black lines on the left. The level positions of the same states predicted by the semi-empirical model of Dorenbos using the level position of the Ce^{3+} ground state from [Thi03] as reference are drawn in the middle. The $^2F_{5/2}$ excited state is drawn at 1.3 eV above the ground state for completion. The level positions of the Yb^{2+}-ion's ground state $^1S_0$ and its lowest $4f^{13}5d$ state are plotted on the right of figure 3.5. These have been obtained by applying Dorenbos's model [Dor03b, Dor05] based on the assumption that the energy needed for the CT transition from a ligand oxygen to a trivalent lanthanoid ion coincides with the energy difference between the VBM to the corresponding divalent ion's ground state and using the charge transfer (CT) transition

[6]The accuracy of the experiment is not explicitly stated in [Thi01, Thi03] but the error is said to be negligible. In [Jia02], the accuracy of the level location determined by UPS is stated as within 1 eV.

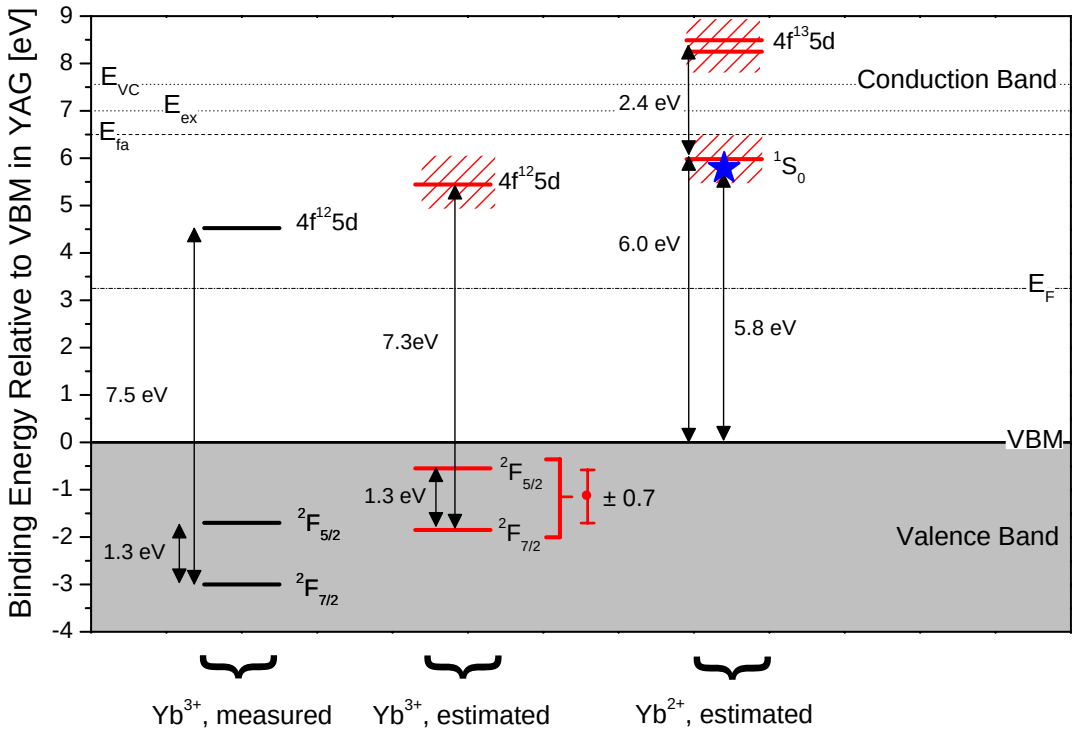

Figure 3.5.: On the left side: The $4f^{13}$ ($^2F_{7/2}$) ground state of Yb^{3+} together with its lowest $4f^{12}5d$ state according to [Thi03]. The $^2F_{5/2}$ excited state is drawn at 1.3 eV above the ground state. The position of the $4f^{12}5d$ excited state was determined using the empirical formula in [Dor00]. In the middle: The same energy states according to [Dor03b], obtained by using the Ce^{3+} ground state level [Thi03] as reference. On the right: The energy states of Yb^{2+} determined by using the empirical formula from [Dor05] and the CT value of Eu^{3+} as reference. The star corresponds to the observed CT absorption maximum of Yb^{3+} [Pie00, Gue01]. The shadings in the middle and the right indicate the errors connected to the estimated levels. E_F is the Fermi energy level located in the middle of the gap. The dashed line E_{fa} represents the most widely cited band gap value of 6.5 eV, which corresponds to the fundamental absorption onset. The peak value for exciton creation $E_{ex} = 7$ eV, and the onset of free carrier creation $E_{VC} = 7.56$ eV according to [Dor05] are represented by dotted lines.

energy of Eu^{3+} as reference. For the $4f^{13}5d$ configuration both, the lowest energy low-spin state as well as the lowest energy high-spin state are plotted, corresponding to spin forbidden and spin allowed transitions from the ground state, respectively. Additionally, the observed maximum in absorption for the excitation of the charge transfer state (CTS) in Yb:YAG [Pie00, Gue01] is indicated by the filled star. The shadings correspond to the errors connected to the estimated level positions. E_F is the Fermi energy level of YAG. The dashed line E_{fa} represents the most often cited value for the band gap energy of 6.5 eV. The value for E_{ex} of 7.0 eV taken from [Dor05] is the peak value for exciton creation in YAG. Using the empirical relation $E_{VC} = 1.08E_{ex}$ [Dor05], the value for free carrier creation was estimated at 7.56 eV. The values for the level positions in the plot are summarised in table 3.1[7].

The Yb^{3+} ground state level location estimated using the Dorenbos model deviates from

[7] A table with the corresponding energy values for all trivalent lanthanoids in YAG can be found in [Jia02]. However, despite using the same citation sources, there are some minor deviations to the values used in this work.

Energy Difference [eV]	Yb^{3+} (n=13)		Yb^{2+} (n=14)
	based on measurement	estimated	estimated
VBM - $4f^n$	-3.0 [a]	-1.9 ± 0.7 [c]	6.0 ± 0.5 [d]
VBM - $4f^{n-1}5d$	4.5	5.4 ± 0.7 [c]	8.5 ± 0.5 (8.3 ± 0.5)
$4f^n$ - $4f^{n-1}5d$	7.5 [b]	7.3 ± 1.4	2.5 (2.3) [e]
$4f^{n-1}5d$ - CB	2	1.2	-2 (-1.8)

Table 3.1.: The electronic energy level positions of Yb^{3+} and Yb^{2+} in YAG as used in figure 3.5. VBM: valence band maximum and CB: conduction band minimum. [a][Thi03], [b][Dor00], [c]reference value from [Thi03] and parameters from [Dor03c], [d]reference value from [Dor05] and parameters from [Dor03c] and [Dor05], [e][Dor05]. The band gap is assumed to be 6.5 eV. The brackets indicate the levels corresponding to spin forbidden transitions. All energies are given in eV.

the level position measured by Thiel, even though the level position of the Ce^{3+}-ion's ground state determined by Thiel was used as reference value. Unfortunately, the Yb^{3+} ground state is not accessible by simple photoconductivity or ESA measurements as the results would be severely obscured by the fundamental absorption. For the same reason, even direct excitation from the ground state into the lowest $4f^{12}5d$ state cannot be observed in simple absorption measurements. The uncertainty in the band gap value is another difficulty for the positioning of the electronic energy levels. Considering errors in the range of 1 eV for both estimation [Dor03c] and measurements [Jia02], the deviations in the level locations appear less significant. Nevertheless, the level position of the Ce^{3+} ground state in the forbidden gap estimated in [Thi03] is in good agreement with the photoconductivity measurements on Ce:YAG of Pedrini *et al.* [Ped86] and ESA measurements of Hamilton *et al.* [Ham89] if the band gap energy is considered to be 6.5 eV. For this reason and because Thiel's value for the Yb^{3+} ground state position is obtained by actual measurement, the values from [Thi03] as well as the band gap value of 6.5 eV for YAG are chosen as basis for the discussions in this thesis.

For Yb^{2+} in YAG, no photoemission spectroscopy results are available. According to the model of Dorenbos, the $^1S_0$ ground state is situated close to the conduction band edge so that even the lowest $4f^{13}5d$ state lies within the conduction band.

In the literature, the lanthanoid dopant's ground state is often considered to be located in the middle of the forbidden gap [Woj96, Hen01, Péd05]. This is probably due to misunderstandings and misinterpretations of diagrams showing at the same time localised and delocalised states such as in figure 3.5. The existence of energy levels, which give rise to optical transitions, within the completely occupied valence band obviously leads to confusion. Indeed, the level location of the Yb^{3+} ground state within the YAG valence band indicates a degeneracy in energy. However, it needs to be pointed out that the Yb^{3+} $4f$ orbitals are non-bonding orbitals displaying a core like character, even though the $4f$ shell is not completely filled. The $4f$ orbitals only overlap poorly with the environment, i.e. there is no significant overlap between the $4f$ wave functions with the ligand oxygen $2p$ and $2s$ wave functions. Hence, the $4f$ wave functions are

not involved in the chemical bond, therefore are not considered to be part of the Bloch wave functions constituting the valence band. Thus, the $4f$ wave functions are of localised nature [Mir96, Dol96][8]. Also, because of screening by the more spatially extended $5s$ and $5p$ core orbitals, the deep $4f$ levels retain their atomic character. Furthermore, the valence band and conduction band states as drawn in figure 3.5 are energy levels in a so-called one-electron jump diagram [Par59], constructed from the energies required to transfer a single electron between different multi-electron states. These energies do not represent the total energies of the initial electronic states but rather the energies associated with each possible way of removing a single electron from the multi-electron initial state of the system. The $4f$ localised energy levels on the other hand, usually described according to the *LS* coupling scheme by the notation $^{2S+1}L_J$, are electronic energy levels of the total many-electron system, i.e. an assemblage of all $4f$ electrons and should not be mistaken for independent one-electron states. Diagrams such as figure 3.5 which attempt to combine these two different schemes therefore need to be treated and interpreted with great care to prevent confusion. This representation considers exclusively the binding energy of electronic states so that the energies in the figure represent the relative energies required to remove a single electron from each state. Lattice relaxation effects in the excited states cannot be visualised by this kind of simple one-electron jump diagram. As these diagrams are usually constructed using the vertical binding energies for the ground state lattice configuration, they correspond to $Q = 0$ slices of the configurational coordinate diagrams [Thi03]. For this reason these diagrams are also often referred to as frozen lattice representation.

Some interesting deductions can be drawn from figure 3.5. YAG is a dielectric crystal and so, as in all insulators, its Fermi level is located midway between the top of the valence band and the bottom of the conduction band. The ground state level positions of Yb^{3+} and Yb^{2+} below and above the Fermi level, respectively also confirm that Yb^{3+} is the preferred oxidation state for Yb in YAG. For this oxidation state no localised core level is introduced into the forbidden gap, which can directly capture radiation- or otherwise induced holes. Neither ionisation threshold nor interconfigurational transitions will be observed below the band gap energy of 6.5 eV for Yb^{3+} in YAG. Thus, the Yb^{3+}-ion is excluded to act as a hole-trap in YAG. In contrast, as briefly mentioned in the introduction of section 3.3, Yb^{3+} is electron attractive, which is supported by the occurrence of ligand to metal charge transfer (LMCT) transitions below the lattice absorption edge of YAG. However, in higher order, e.g. highly excited to a $4f^{12}5d$ level, Yb^{3+} may be hole-attractive [Rob78]. Yb^{2+} on the other hand is hole-attractive and should easily oxidise by releasing an electron to the conduction band or trapping a radiation-induced hole from the valence band. From figure 3.5, Yb^{2+} ionisation thresholds and interconfigurational transitions below the lattice absorption edge are expected. Furthermore, the level position of the lowest $4f^{13}5d$ states within the conduction band of YAG gives rise to autoionisation upon excitation. The same deduction was drawn by Henke as no emission related to $4f^{13}5d$-$4f^{14}$ transitions could be found for Si,Yb:YAG, in which Yb^{2+}-ions are assumed to be stabilised by Si^{4+}-ions [Hen01]. Pumping into absorption bands attributed to Yb^{2+} in YAG also led to conductivity [Fag07], which further supports this assumption. However, there are discrepancies regarding

[8]Chemical bonds between lanthanoids and ligands in compounds are mainly of ionic character. However, covalency and contributions of the $4f$ orbitals to chemical bonding have been discussed in the literature. It has also been suggested that covalency and the admixture of $2p$ states play an important role in creating mixed parity states [Hub80]. For further information the reader is referred to [Kot92, Dol96, Str99, Cho02, Mak04].

the $4f^{14}$-$4f^{13}5d$ transition energies estimated by Dorenbos [Dor05] and the assignment of the Yb^{2+}-ion absorption bands in YAG [Hen01, Fag07], which will be discussed in detail in section 4.2.

Further information concerning the $4f^n$ ground state as well as the first $4f^{n-1}5d$ level positions of the other trivalent and divalent lanthanoid ions relative to the YAG host bands can be found in appendix A.

3.5. Ceramic and Single Crystalline Yb:YAG

Since the demonstration of the first solid-state laser by Maiman in 1960 [Mai60] several different laser materials have been developed. The active medium of a laser is said to be the ultimate material for optics as even tiny amounts of scattering centres, impurities or other defects can lead to severe losses and thus need to be eliminated. Glasses and single crystals are up to now the most established materials on this field and fabrication techniques have over the years undergone a number of optimisations. Single crystalline YAG grown by the Czochralski technique shows favourable qualities as listed in table 3.4 (see page 78) and is therefore the most widely used of the solid-state laser host materials. However, the currently known crystal growth techniques for laser quality single crystals have disadvantages, e.g.: Limitation in crystal size, the need to use expensive equipment with very high melting points such as Iridium crucibles, long fabrication times as the growing process needs its time, formation of facets as well as of a core which further reduces the useable crystal area, nonuniform and gradient doping concentrations for some dopants due to distribution coefficients deviating from 1, the impossibility to realise high doping concentrations for dopants with low distribution coefficients, etc. For these reasons high quality single crystalline laser materials cannot easily be mass produced and are expensive. Furthermore, the limitation in crystal size hinders the advancement of some research fields, e.g. laser fusion technology, which demands large gain media. All those disadvantages can be overcome by the implementation of transparent YAG ceramics of optical qualities rivalling those of single crystals.

Ceramics (from the Greek: Keramos) in the form of pottery objects made from clay are one of the earliest man made materials. Today, the term ceramics refers to all materials made from inorganic, non-metallic substances by heat treatment. It has to be noted that by this definition also glass and single crystals are ceramic materials. However, in the context of laser physics differentiation is made between amorphous glasses, single crystals and polycrystalline ceramics as different classes of solid-state laser materials. In this work the term ceramic solely refers to polycrystalline ceramic materials. A major difference between these classes lies in the temperature used for fabrication. Glasses and single crystals need manufacturing temperatures well above the melting point whereas ceramics are sintered and not molten. Therefore, ceramics are polycrystals built up of numerous single crystalline grains and thus incorporate grain boundaries, which may well be the most significant difference to the other two classes. Scattering at these grain boundaries is one of the main reasons for most ceramic materials to be non-transparent. As a consequence ceramic laser materials are, in the first instance, restricted to

optically isotropic cubic matrices[9] and much effort has been put into the optimisation of optical quality to reach laser standards. If the optical qualities are alike, the advantages of ceramic YAG over single crystalline YAG are obvious. Ceramic lasers are an attractive low cost alternative to single crystal materials since they offer greater flexibility in design and so open up new prospects for solid-state lasers. Whilst research using ceramic devices is still in its relative infancy, early indications suggest that they can offer small losses and high output powers that are competitive with today's commercial single crystal solid-state lasers. Furthermore, in contrast to conventional lasers, the flexibility in design of the physical and optical properties allows ceramics to be tailored to meet the particular specifications of each application and achieve an optimal trade off between performance and cost. For example, doping concentration does not primarily depend on the distribution coefficient and can be engineered as required, composite materials can be realised without the need for bonding and size is not a limiting factor. As grains and grain boundaries are the major differences between the ceramic and the corresponding single crystalline materials, the effects on physical properties are of interest and have been the focus of much research over the past years. For instance, it has been found that ceramic materials display improved mechanical toughness and hardness compared to their counterpart single crystals [Kam05b, Mez06]. Laser damage experiments in the nanosecond pulse regime showed that no significant differences between the materials occur, indicating that the grain boundaries do not lead to reduction of the optical damage limit [Bis03]. There have also been investigations which have found ceramics to have lower scattering losses compared to a reference single crystal [Qua05]. These results suggest that grains and grain boundaries are not necessarily a disadvantage for ceramic laser materials. Another important feature is the fabrication temperature, which is considerably lower. It is expected that lattice defects such as oxygen vacancies and antisites are much less pronounced or even non-existent in ceramic YAG.

In recent years considerable efforts have been made by Quarles and coworkers in comparing single crystalline YAG with ceramic YAG of multiple vendors, where over 1 000 pieces were tested [Qua07, Qua08]. Their results suggest that the two material classes are more or less identical in terms of thermo-optical coefficients, spectroscopic properties and laser performance upon diode-pumping. In terms of lamp pumped laser performance ceramic samples were inferior due to solarisation effects but comparable or even superior regarding wave-front distortion, stress fracture and scattering loss.

It is the purpose of this research to investigate the problems that occur in highly doped single crystalline Yb:YAG thin-disk lasers. As ceramics are a new generation of solid-state laser there is great interest to extend these investigations to Yb^{3+}-doped ceramics with different Yb concentrations, to determine whether ceramics suffer the same problems as single crystals or display any other different behaviour.

[9] Different approaches are currently intensively investigated to obtain transparent polycrystalline anisotropic matrices. Techniques involving the crystallographic alignment of the grains seem to be the most promising [Wis08].

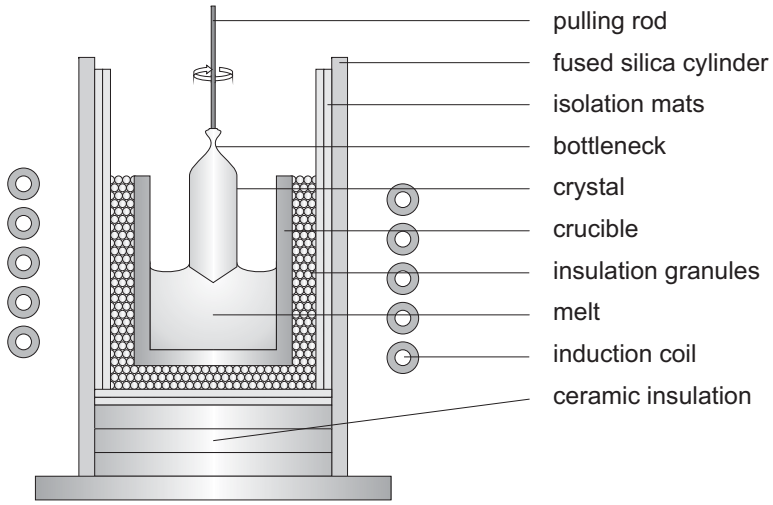

Figure 3.6.: Schematic of a standard setup for crystal growth based on the Czochralski technique [Krä08]

3.5.1. Crystal Growth and Fabrication Techniques

Single Crystalline Yb:YAG - The Czochralski Technique

The first Czochralski grown YAG crystal was presented by Linares in 1964 [Lin64]. The Czochralski process, developed 1916 and published in 1918 by Jan Czochralski [Czo18] is the most established technique for the commercial production of high quality laser crystals. Here, the raw materials usually in the form of high purity powders are mixed and filled into a crucible, which is placed inside a gastight chamber. An insulating setup around the crucible provides the temperature profile necessary to achieve ideal growth conditions. In the required atmosphere the crucible is then inductively heated until the starting materials become molten. The heating is reduced until the melt is marginally above its recrystallisation point. If a pulling rod, to which a seed crystal can be assembled, is dipped into the melt, crystallisation begins due to the heat transfer through the rod. This continues until an equilibrium between heat delivered from the crucible wall and heat transferred through the pulling rod is reached. The interface, i.e. the isothermal plane of the growing crystal and the melt is now stable. The rod, in most cases rotating, is then slowly pulled upward and the crystal grows layer by layer perpendicular to the pulling rod. The diameter of the growing crystal is controlled by adjusting the temperature of the crucible and thereby regulating the shape and dimension of the solid-liquid interface. To ensure single crystalline growth without the use of a seed crystal, the temperature is increased again after seeding so that a bottleneck like shape is obtained. By this procedure the number of different seed crystals is decreased and a single crystalline interface can be achieved. Crystals grown by this method usually have no stress and display very high optical quality as the growing crystal has no contact with the crucible.

The crucible material is usually chosen depending on the melting temperature of the starting materials. In the case of YAG with a melting point of 1940°C, iridium crucibles are typically used but rhenium crucibles can also be used. Previous research has revealed Fe- and

Figure 3.7.: Left: Prototype 15% Yb:YAG crystal #SK and right: Crystal #SNF, grown under optimised conditions using a seed crystal for defined orientation. Both crystals display a blueish turquoise colour due to the presence of colour centres formed by oxygen vacancies and Yb^{2+}, as is typical for as-grown crystals when grown under reducing conditions.

Ni-impurities of up to 600 ppm in Yb:YAG crystals grown from deep-drawn Iridium crucibles [Fag07]. It has been found that the crystals grown from 6N powder-metallurgically produced rhenium crucibles do not show any measurable amount of impurities incorporated during the growth process and therefore are of the highest purity. The growth of oxide crystals suggests the use of oxygen in the growth atmosphere. Yet, due to its sensitivity to oxygen the use of rhenium crucibles requires a reducing growth atmosphere whereas iridium crucibles can withstand oxidising atmospheres with up to 10% O_2. On the other hand, shortage of oxygen in the atmosphere leads to oxygen release from the melt resulting in strong colour centre formation in the crystal due to oxygen deficiency. Moreover, due to the release of oxygen from the melt the very reactive compound AlO can be formed, and as a result the grown crystal suffers from corrosion. Therefore, the growth atmosphere needs to be chosen and adjusted with due care. A schematic of a standard Czochralski growth setup is given in figure 3.6. Detailed descriptions of the Czochralski technique as employed at the Institute of Laser-Physics, University of Hamburg (ILP) and systematic investigations determining the influences of the crucible and insulating materials on the spectroscopic properties and the crystal quality can be found in the diploma works of V. Müller [Mül01] and N. Martynyuk [Mar02].

In this work two Yb:YAG single crystals with a doping concentration[10] of 15% in the initial compounds were grown at the ILP using a Crystalox growth apparatus (Crystalox Ltd., UK). An induction coil of 110 mm of diameter with seven turns has been employed allowing the use of crucibles with up to 45 mm diameter. The original apparatus has been modified enabling computer controlled growing of the crystal by weighing the whole setup during growth. A high frequency generator (HÜTTINGER Elektronik GmbH + Co. KG, Germany) with a maximum output voltage of 7 kV at a frequency of 400 kHz and 30kW maximum output power served as the power source. The crystals were grown from 5N raw materials (All-Chemie Ltd., USA) using a 6N powder-metallurgically produced rhenium crucible (Heraeus, Germany). The growth atmosphere was reducing, constituting of 1% CO_2, 4% CO and N_2[11]. The pulling rate

[10] All concentrations are given with respect to the Y-sites

[11] Atmosphere calculated by D. Klimm of the Institute for Crystal Growth, Berlin

was 2 mm/h and the rotation was 18 rpm. Zirconia granules and felt mats were used as insulating materials for the first crystal (figure 3.7, left) which was grown using a rhenium wire as the pulling rod. Due to its peculiar boot-like shape this prototype crystal is referred to as the "Schuhkristall" (#SK). As oxygen dispersion from the zirconia insulating materials was observed, yttria granules and felt mats were used for the second, so-called "Schuhnachfolger" (#SNF) crystal (figure 3.7, right). In this case a seeding crystal was implemented to allow for a defined growth orientation. Both crystals display a blueish turquoise colour which is typical for Yb:YAG crystals grown under a reducing atmosphere. This is due to the formation of colour centres during growth, most likely consisting of oxygen vacancies charge compensated by Yb^{2+}-ions. This colouration disappears completely when annealing the crystals in air at about 1 000°C for several hours.

Ceramic Yb:YAG - The Vacuum Sintering and Nanocrystalline Method

The first ceramic laser was based on a hot-pressed Dy^{2+}:CaF_2 demonstrated by Hatch and coworkers in 1964 [Hat64]. In the early 1970s Greskovich and Chernoch succeeded in laser demonstration of a flash lamp pumped Nd:Y_2O_3 ceramics material [Gre73, Gre74]. However, due to scattering centres present in the material the laser performance of the ceramics could not compete with those of Nd-doped glasses, the standard of that time. Despite the intensive research carried out on ceramic materials during the 1960s and 1970s, fabrication techniques could not be optimised in a way to meet the standards for laser materials and it was commonly believed that ceramics would never attain the optical qualities of single crystals and glasses. Indeed, the number of publications on transparent ceramics rapidly decreased during the 1980s and there are about 20 years of almost no reports on ceramics as potential laser materials since 1974. The first translucent ceramic YAG was reported by Gazz and Dutta in 1973 [Gaz73]. In 1984 de With and van Dijk presented translucent YAG ceramics prepared by vacuum sintering technique using YAG powders synthesised by a sulfate co-pyrolysis method [Wit84], the optical quality still being much too poor for laser application. It was not until the late 1980s to early 1990s that ceramic YAG gained again attention as a potential laser material. Sekita and coworkers developed the urea precipitation method using SiO_2 as sintering aid and obtained translucent to almost transparent YAG ceramics. They also investigated the spectroscopic properties of rare earth (Pr, Nd, Eu as well as Er) doped YAG ceramics, however due to residual background absorption lasing could not be realised with those materials [Sek89, Sek91]. The first ceramic Nd:YAG laser was demonstrated by Ikesue and coworkers[12]. Published in 1995 [Ike95b], after more than 20 years since the last publication in 1973 this actually was the third report of a ceramic based laser. Ikesue *et al.* fabricated their 1.1%Nd:YAG ceramic material by the solid-state reaction method using high purity (4N) Al_2O_3, Y_2O_3 and Nd_2O_3 powders, the particles measuring less than 2 µm in diameter, as starting materials. As a sintering aid tetraethyl orthosilicate was used. The mixture of the powders was milled for 12 h and the resulting slurry was then dried using a hot magnetic stirrer. After that the dried powders were isostatically pressed at 140 MPa into disks of 20 mm in diameter. These powder compacts were then sintered at about 1 750°C for over 10 h under 1.3×10^3 Pa pressure. In this way Nd:YAG

[12]The first demonstration of laser oscillation in Nd:YAG ceramics is claimed to date back to 1992 when Ikesue registered his patent [Ike92].

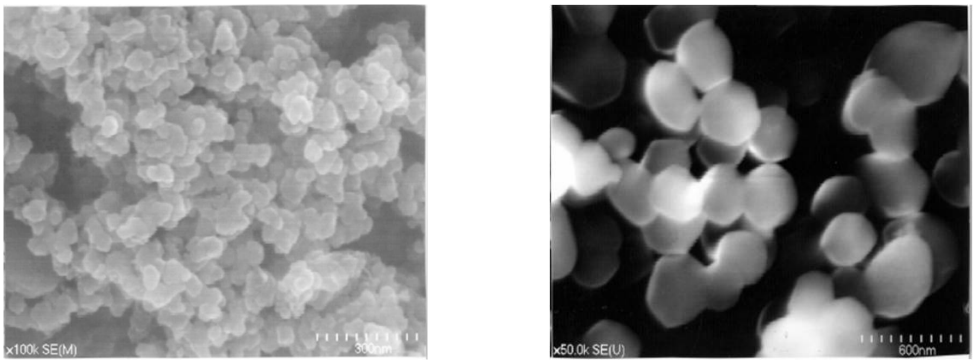

Figure 3.8.: Left: SEM picture of the YAG precursor after drying at 200°C and right: YAG powder with uniform particle size of about 200 nm after calcining at 1200°C [Yag07a].

ceramics with an average grain size of 50 µm and high transparency were obtained [Ike95a]. A 1.1%Nd:YAG ceramic sample polished to 2 mm thickness displayed a slope efficiency of 28% with respect to the incident pump power with a maximum of output power of 70 mW at 1 064 nm upon 550 mW of diode-pumping at 808 nm.

The ceramic Yb:YAG samples investigated within the framework of this research were provided by Konoshima Chemical Co. Ltd., Japan and fabricated by implementing vacuum sintering and nanocrystalline technology [Yan98a, Yan98b, Yan99, Yag04]. The method is therefore also referred to as the VSN method. In a first step the raw materials are prepared by wet chemical reaction and calcining. This treatment is necessary to obtain high purity, sinterable raw materials with very fine, uniform particles which do not agglomerate. Yttrium chloride (YCl_3) and aluminium chloride ($AlCl_3$) of 4N purity are both dissolved and 0.5 mol/l aqueous solutions of YCl_3 as well as of $AlCl_3$ are prepared. 15 l of YCl_3 and 25 l of $AlCl_3$ aqueous solution are then mixed together. This is added dropwise at 1.5 l/min to 40 l of an aqueous solution of ammonium bicarbonate (NH_4HCO_3) and ammonium sulfate ($(NH_4)_2)SO_4$), which is laced with ammonium (NH_4) until a pH of 8.20 is obtained. The temperature of all aqueous solutions should be 30°C. After that colloidal silica which acts as a sintering aid is added and the mixture is cured at 30°C for 48 h under constant agitation. The YAG precursor is produced from the sediment by repeating six times the steps of washing with ultra purity water and suction filtration followed by two days of drying at 200°C. High purity YAG powder with uniform particle sizes of approximately 200 nm is then obtained by calcining the precursor at 1200°C in air for 5 to 10 h. SEM (Scanning Electron Microscopy) pictures of the YAG precursor and the uniform YAG powder are given in figure 3.8. As a second step a high density green body needs to be prepared as existing voids are not easily removed by sintering and would remain as scattering centres. For this reason the approved slipcasting method is applied. The YAG powder is ball-milled with alcohol and an organic solvent for 20 h and thus a slurry is obtained. This slurry is then defoamed and agitated in vacuum for 30 min before being cast into a gypsum mould of desired shape. After three days of drying the gypsum is removed and the slurry is annealed at about 600°C for 5 h to obtain the YAG green body. The third and last process is the vacuum sintering. The green body is sintered in vacuum (1.3×10^{-3} mbar) at 1 700 to 1 750°C. In the process the temperature is raised with 450°C/h up to 1 400°C and then with 250°C/h until about 1 700°C. The temperature is held constant for 10 to 20 h and then reduced at 100°C/h until room

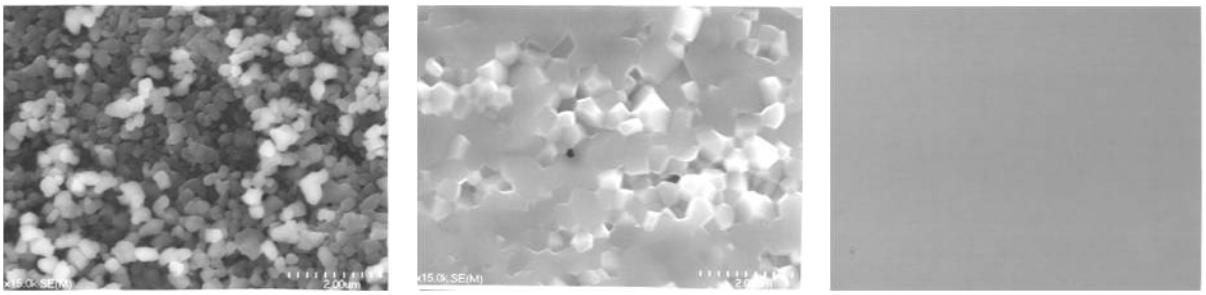

Figure 3.9.: SEM pictures illustrating the fabrication stages of laser ceramics. Left: The YAG green body made by the slip casting forming method, middle: Halfway through the sintering process at about 1700°C and right: YAG laser ceramics after vacuum sintering, no pores or other defects can be seen [Yag07a].

temperature is reached. After annealing pore free, transparent YAG ceramics are obtained. The SEM pictures in figure 3.9 visualise the structural change of the YAG green body to a pore free YAG laser ceramic during the sintering process.

The VSN method is currently one of the highest rated fabrication techniques for high quality ceramics used in laser devices. High purity, uniform grain sizes in the order of 2 to 3 µm (in the case of YAG)[13], very thin grain boundaries and the absence of pores, which act as the main scattering centres in conventional ceramics, are the characteristic features. The laser properties of variously doped ceramics made with this technique have been investigated and showed that this new generation of ceramic active media can easily compete with single crystals [Lu02, Tak03, Tok06, Tok07]. YAG samples with dimensions as of $400\times50\times8$ mm or $120\times120\times20$ mm, which currently cannot be realised with single crystals, have been demonstrated so far. A detailed description of the VSN method is found in [Yag07a].

3.5.2. Microscopy and Microprobe Analyses

Yb:YAG single crystals

The actual Yb-doping concentration of #SK has been determined by microprobe analysis to be $16.5\% \pm 0.5\%$ with respect to the available Y-sites, resulting in a distribution coefficient of 1.1. Previous measurements on nominal 7% and 2% Yb:YAG led to distribution coefficients of 1.17 and 1.2, respectively [Mix95]. Microprobe analysis has also been applied to a stoichiometric YbAG single crystal to investigate the antisite defect. The measurement showed that the sample contained about 1% more Yb-ions than available dodecahedral sites and correspondingly fewer Al-ions. On the other hand, from the data of #SK no significant difference between the sum of the measured Y- and Yb-concentrations, and the number of available dodecahedral sites in the garnet structure could be found. Those two observations suggest that antisites can exist in Yb:YAG single crystals grown from the melt, however the conditions for their occurrence are not straightforward.

[13] Commonly, transparency in ceramics is to some extent obtained by reducing the number of grain boundaries by choosing large grain sizes, usually in the range of 50 µm [Ike95a].

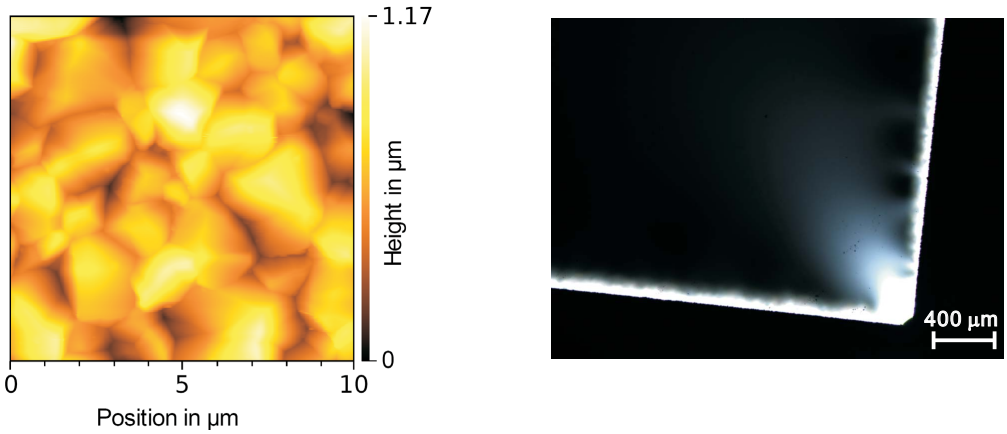

Figure 3.10.: Left: AFM image of the 1%Yb:YAG ceramic clearly revealing the individual grains. The grains have sizes between 1 µm to 3 µm. Right: Microscope image taken by placing the 15%Yb:YAG ceramic sample between two crossed polarisers. No stress induced birefringence can be observed. The observed features are attributed to stray light due to scattering at the edges.

Yb:YAG ceramics

SEM measurements on a polished undoped YAG ceramic sample that was thermally etched at 1 400°C for 2 h showed that the ceramic is built up of uniform single crystalline grains with an average size of 2 µm and that no pores or other defects are present. Furthermore, TEM (Transmission Electron Microscopy) measurements on a ceramic YAG plate of 50 µm thickness revealed that the grain boundary is thinner than 1.2 nm [Yag07a]. Indeed, the grain boundary of these ceramics was estimated by the heat pulse method [Iva85] to have thicknesses of between 1.7 to 4.6 Å [Bar04]. Thus, the grain boundary is orders of magnitudes smaller than the Yb:YAG laser wavelengths of about 1 µm and can be neglected as a possible scattering source. A wide transparency range, as wide as for single crystals can be expected.

The ceramic samples investigated within the framework of this research are the following: Undoped YAG, 0.3%, 1%, 9.8%, 12%, 15% and 20% Yb:YAG. All samples are transparent to the eye. AFM (Atomic Force Microscopy) measurements were performed using a Veeco ZP-100-02 in contact mode, in order to confirm the average grain size of 2 µm measured for undoped YAG by Yagi *et al.* and to see if deviations in grain size exists for Yb^{3+}-doped YAG ceramics. The samples were first polished and then etched for 15 min in H_3PO_4 at 200°C. After this treatment, all ceramics revealed their grained structure upon AFM measurement, an example of which is shown in the left of figure 3.10 for the 1%Yb:YAG ceramic sample. The noticeable differences in the visible grain sizes can be easily explained as being due to different cross sections. Taking this into account and assuming random distribution, the biggest cross sections can be interpreted as the grain diameters. All ceramic samples displayed grain sizes of about 1 µm to 3 µm in diameter and no obvious defects, e.g. pores could be observed. Microscope images with the polished ceramics placed between two crossed polarisers showed that the polycrystals do not suffer from internal strain or stresses, which would cause birefringence. An example of this is shown in the right of figure 3.10 for the 15%Yb:YAG ceramic sample, which had a thickness of about 3 mm. The sample is not completely dark, as would be expected for perfectly isotropic materials, and in particular, the sample's borders can be clearly recognised.

This is most likely due to scattering of light at the edges and is not an indication for stress induced birefringence. The rather shallow depth of field of the microscope is seen as the reason for the flaked feature of the corner.

The Yb-doping concentrations of the nominally 0.3%, 1%, 9.8%, 12% and 20%Yb:YAG were determined by microprobe measurements to be 0.3%, 1.0%, 10.9%, 13% and 21.5% with standard deviations of about 1%. The silicon concentration, which is found in the samples due to the use of colloidal silica as a sintering aid, is measured with respect to all Al-sites[14] to be about 0.1% for the 0.3% and 1%Yb:YAG and about 0.2% for the higher doped samples. The data of the microprobe analyses showed that a slight antisite defect exists also in the ceramic samples. In all cases the sum of the measured Y- and Yb-concentration is about 2% larger than the number of dodecahedral sites in YAG. Spatially resolved measurements could not be performed with the equipment available. A possibility is that the excess of rare earth ions is due to the nature of the grain boundaries. Otherwise this discrepancy cannot be understood with existing models as fewer antisites are expected in ceramics compared to single crystals.

3.5.3. Thermal Conductivity

Good thermo-mechanical and thermo-optic properties are desirable for active laser media, especially for high power applications and therefore often are the deciding properties when choosing a candidate host material. The term thermo-mechanical refers to mechanical properties of a material which change while the material is subjected to heat, e.g. the dimension of a sample due to thermal expansion (coefficient of thermal expansion dL/dT). On the other hand, thermo-optic properties are optical properties which are dependent on temperature, e.g. the refractive index (thermo-optic coefficient dn/dT). Other important thermal properties of a material include the thermal diffusivity α, the specific heat at constant volume c_V and the thermal conductivity λ which are connected to each other by following relationship [Vog97]:

$$\lambda = \alpha \cdot \rho \cdot c_V, \tag{3.1}$$

where ρ is the density of the material. The thermal conductivity is a key parameter for high power solid state lasers as lost heat generation is inevitable and this heat needs to be removed from the active media in order to ensure high beam quality. In literature many different values for λ at room temperature can be found for undoped and rare earth doped YAG. Values for undoped YAG vary from about $8.8\,\mathrm{Wm^{-1}K^{-1}}$ [Pad97] to $13.0\,\mathrm{Wm^{-1}K^{-1}}$ [Kle67]. Most of the published data on thermal conductivity are obtained by measuring the thermal diffusivity by the laser flash method [Par61, Cam02] and multiplying by the measured density and specific heat[15] at constant pressure c_p, which can be determined, e.g. by differential scanning calorimetry [AS01].

A comprehensive summary of the data found in literature is listed in table 3.2. It should be noted that even if the measurements on nominally identical samples were performed by the same

[14] Silicon is usually incorporated as Si^{4+} on the tetrahedral sites into the garnet structure [Gel67]. However, controversies do exist as discussed in [Wol09b].

[15] For solids the difference between the specific heats at constant pressure c_p and at constant volume c_V are marginal, so that most often the easier to determine c_p is used.

Yb^{3+} -concentration [%]	ρ [gcm^{-3}]	c_p [$Jg^{-1}K^{-1}$]	α [$10^{-6}\,m^2s^{-1}$]	λ [$Wm^{-1}K^{-1}$]	T [K]	method	reference
0.0	4.55	0.63	4.6	13	300	steady heat flow method	[Kle67]*
0.0				10.3	300		[Sla71]
0.0	4.544	0.5866	3.66	9.76	293	laser flash	[Kru86]
0.0				*8.8*	*296*	*laser flash*	[Pad97]
0.0				10.41	300	laser flash	[Con02]
0.0				10.7		phototherm. technique	[Gau03a]
0.0	4.53	0.603	4.73	12.9		laser flash	[Kuw04]
0.0	4.56	0.599	4.1	11.2	300	laser flash	[Agg05]
0.0	4.56	0.6		10.1	298	q1D flash method	[Sat06]
0.0	4.45	0.625	4.13	11.49	298	laser flash	[Hof06]
0.0	4.55	(0.609)	4.25	(11.78)	296	modified laser flash	[Mar09]
0.0	4.5	0.62	4.45	12.22		thermal wave analysis	[Bod09]*
2.0				9.2		phototherm. technique	[Gau03b]
2.0	4.60	0.57	3.2	8.6	300	laser flash	[Agg05]*
2.5		0.545	2.45	6.07	300	pulsed laser technique	[Qiu02]
3.0				6.8	303	laser flash	[Pet02]
3.0				8		laser flash	[Gau03b]
3.0	4.5	0.62	3.61	9.91		thermal wave analysis	[Bod09]*
4.0	4.62	0.58	3.0	8.2	300	laser flash	[Agg05]*
4.2				6.6	300	laser flash	[Con02]
5.0				7.9			[Pat01]
5.0				7.1	298	q1D flash method	[Sat09]
5.0				*6.8*	*298*	*q1D flash method*	[Sat09]
6.0				7.5		phototherm. technique	[Gau03b]
6.5				7.2		phototherm. technique	[Gau03b]
8.0				7		phototherm. technique	[Gau03b]
9.8				6.5	300	laser flash	[Con02]
9.8				6.4	298	q1D flash method	[Sat09]
10.0				*6.2*	*298*	*q1D flash method*	[Sat09]
11.5				6.3	300	laser flash	[Con02]
15.0	4.85	0.57	2.4	6.7	300	laser flash	[Agg05]*
15.0				7.8			[Pat01]
15.0				6		phototherm. technique	[Gau03b]
17.8				5.6	300	laser flash	[Con02]
20.0		0.54	1.93	4.74	300	pulsed laser technique	[Qiu02]
23.0		0.55		5.7	298	q1D flash method	[Sat09]
24.9				5.5	300	laser flash	[Con02]
25.0				5.5			[Pat01]
25.0	4.5	0.62	2.68	7.38		thermal wave analysis	[Bod09]*
25.0	5.35	(0.55)	2.01	(5.91)	296	modified laser flash	[Mar09]
40.0				5.5		phototherm. technique	[Gau03b]
50.0				5.4			[Pat01]
50.0		0.51		5.2	298	q1D flash method	[Sat09]
81.7	6.23	(0.459)	2.06	(5.89)	296	modified laser flash	[Mar09]
100.0				6.9	300		[Sla71]
100.0				7.2			[Pat01]
100.0		0.44		7.1	298	q1D flash method	[Sat09]
100.0	6.61	(0.43)	2.53	(7.19)	296	modified laser flash	[Mar09]

Table 3.2.: Summary of thermal transport properties of YAG, Yb:YAG and YbAG found in literature. The values for specific heat, density as well as the method of measurement are listed if available. Italic values refer to ceramic samples. Values in brackets were obtained assuming linear relationship for c_p with doping level (for YAG the average literature value is used). *The respective values do not match.

technique, very different values are obtained for the thermal diffusivity. Quality variations of the used samples might well be a major reason for the differing results. However, as YAG is a very well known and used standard material, quality differences should not be an issue especially for the recently published results. Thus, it can be deduced that the deviations still observed display the limits of accuracy for the determination of thermal diffusivity. For thermal conductivity the error of the specific heat adds up. Specific heat measurements performed on Yb:YAG and Yb:LuAG samples at the Institute for Crystal Growth in Berlin in the framework of the diploma work of K. Beil were said to have an error of 10% and underline the problems in measuring this parameter with high accuracy [Bei08]. Another difficulty arises as both thermal diffusivity and specific heat are dependent on temperature themselves. In this work, the thermal diffusivities of the samples used were measured by the temperature wave analysis at room temperature to compare the results for ceramic and single crystalline Yb:YAG with each other and with the values found in literature. In addition determining the dependence of the thermal conductivity on Yb^{3+}-doping concentration was another objective.

The temperature wave analysis is a method for measuring thermal diffusivity in the through-thickness direction of a thin flat sample based on the measurement of the phase shift of a temperature wave between the front and the rear surfaces of the sample. It is assumed that the heat flux is proportional to the temperature gradient and that the thermal diffusivity of the material is independent of position and time. One dimensional heat flow is assumed and heat flow normal to the thickness direction is neglected. Under these assumption one can obtain a direct relation between phase shift $\Delta\theta$ and thermal diffusivity α as follows:

$$\Delta\theta = -\sqrt{\frac{\omega}{2\alpha}} \cdot d - \frac{\pi}{4}, \tag{3.2}$$

where ω is the frequency of the applied heat wave and d is the sample thickness. The thermal diffusivity of a sample of known thickness is then obtained by measuring the phase shift for different heat wave frequencies and plotting $\Delta\theta$ against $\sqrt{\omega}$ from the resulting slope. A detailed description of the heat wave analysis method is found in [Mor98, Mor08].

The apparatus used for thermal diffusivity measurements was the ai-Phase Mobile 1 (ai-Phase Co., Ltd., Japan). The sample is placed between two contacts, one acting as the heater element and the other as a sensor. The ideal thickness for measurement depends itself on the thermal conductivity of the sample and cannot be generalised. Approved sample dimensions for the laser crystals usually investigated at the ILP are thicknesses of about 400 µm and diameters of 3 to 5 mm. However, for Yb:YAG no differences within the measurement error could be found for samples with same specifications but differing thicknesses in a range between about 140 µm and 800 µm. The measurements presented in this work were performed on samples with thicknesses around 140 µm. All samples were spectroscopy grade polished to ensure sufficient flatness and contact but almost no sensitivity to the quality of the surfaces could be found. The measurement of the thermal diffusivity was repeated five times for each sample to minimise errors through mismeasurement and estimate the accuracy of the device. At the same time the thickness of the sample was also measured by the ai-Phase Mobile 1 and was in good agreement with the thickness determined with a Dial Gage Stand DGS-M (Mitutoyo Mfg. Co., Ltd., Japan). The density and specific heat of YAG were taken from [Agg05] to be $4.56\,\mathrm{gcm^{-3}}$ and $0.599\,\mathrm{Jg^{-1}K^{-1}}$, respectively while the density of YbAG was calculated from knowledge

of the atomic masses and the lattice constant to be $6.62\,\mathrm{gcm}^{-3}$, and the value for the specific heat ($0.43\,\mathrm{Jg}^{-1}\mathrm{K}^{-1}$) was taken from [Bei08]. For both parameters a linear dependency on Yb-concentration was assumed to obtain the corresponding values for each investigated sample [Akh77].

material class	Yb^{3+} -concentration [%]	ρ [gcm^{-3}]	c_p [$\mathrm{Jg}^{-1}\mathrm{K}^{-1}$]	α [$10^{-6}\,\mathrm{m}^2\mathrm{s}^{-1}$]	λ [$\mathrm{Wm}^{-1}\mathrm{K}^{-1}$]	d [µm]
single crystal	16.5	4.90	0.564	1.77 ± 0.02	4.89 ± 0.06	144.5 ± 0.1
	80.0	6.22	0.462	2.13 ± 0.08	6.12 ± 0.22	140.2 ± 1.0
	100.0	6.62	0.430	2.44 ± 0.08	6.95 ± 0.23	144.9 ± 1.3
ceramic	0.3	4.57	0.589	3.17 ± 0.10	8.53 ± 0.27	143.2 ± 2.4
	1.0	4.58	0.588	2.88 ± 0.06	7.76 ± 0.15	146.9 ± 0.5
	9.8	4.77	0.574	2.04 ± 0.06	5.59 ± 0.16	145.5 ± 0.5
	12.0	4.81	0.571	1.91 ± 0.04	5.25 ± 0.11	137.8 ± 1.0
	20.0	4.97	0.558	1.85 ± 0.07	5.11 ± 0.19	145.5 ± 0.5

Table 3.3.: Thermal diffusivities measured at room temperature by the heat wave analysis method using an aiPhase mobile 1. Top: single crystals, bottom: ceramic samples. The values for specific heat and density of YAG and YbAG are taken from literature [Agg05, Bei08], to obtain corresponding values for the different concentration Yb:YAG sample, a linear dependency was assumed for both these parameters. The thickness d of the used sample is also given.

The results for the thermal conductivities calculated using equation 3.1 are listed in table 3.3 and are plotted together with values from literature (see table 3.2) and from [Bei08] in figure 3.11. The error bars of the values from this work account solely for the standard deviation of the measured thermal diffusivities' mean value. For the values from literature the mean was taken if more than one value was available and plotted together with its standard deviation. To visualise the dependency of the thermal conductivity on Yb^{3+}-doping concentration a fit function using the theory by Klemens [Kle60] was applied on the data from literature (solid curve). The dotted curves show the $\pm 5\%$ deviation from the fitted characteristics[16]. Details concerning the theory applied and the fit parameters used can be found in appendix B.

As can be seen in figure 3.11 the thermal conductivity of Yb:YAG follows a clear trend with increasing doping concentration. Thermal conductivity rapidly drops upon Yb-doping until a minimum at, according to the underlying theory, around 50% doping concentration is reached. The thermal conductivity then increases again and reaches a value comparable to about 6%Yb:YAG for the stoichiometric YbAG. However, the fit function needs to be treated very carefully and should not be misunderstood as depicting absolute values since the underlying literature values display very high dispersions. A lot of the literature values do not lie within $\pm 5\%$ deviation of the fit function. Furthermore, few publications deal with thermal conductivities of Yb:YAG with concentrations higher than 50% and therefore the fit has to rely on a very limited number of values in the high concentration regime. It has to be noted that all

[16] $\pm 5\%$ was chosen as the error margin since the error for the commonly used laser flash method is stated as $\pm 5\%$ [Sat06].

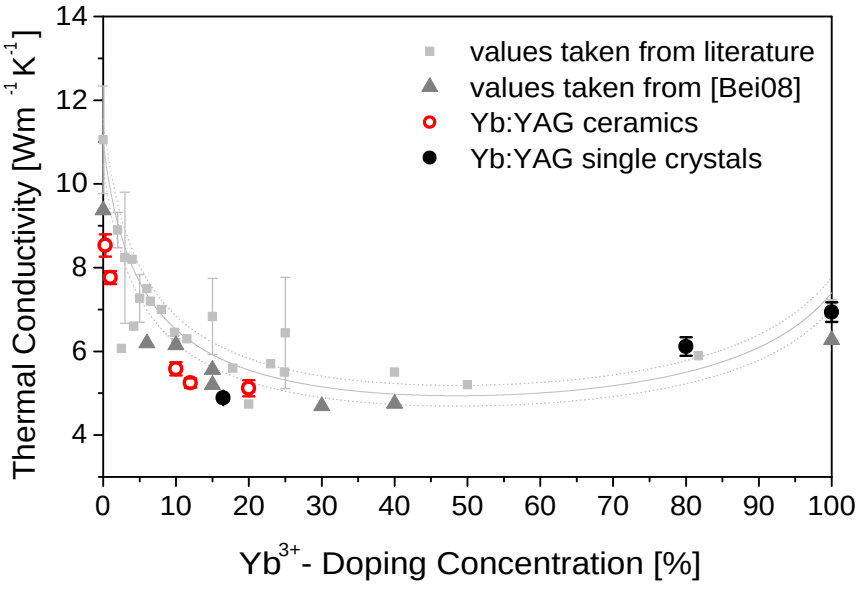

Figure 3.11.: Thermal conductivities of single crystalline (filled circles) and ceramic (hollow circles) Yb:YAG of different concentrations obtained by measurement of thermal diffusivity via the heat wave analysis method, assuming a linear relationship of density as well as for specific heat on doping concentration and using values for YAG and YbAG from literature [Agg05, Sat09]. For comparison, thermal conductivity values from literature (squares, see also table 3.2) and [Bei08] (triangles) are also plotted.

thermal conductivities determined at the ILP including the values by [Bei08], except the values for 80%Yb:YAG and YbAG of this work, lie about 10% below the fitted curve obtained using the literature values. This might lead to the conclusion that either all samples investigated at the ILP were of poor quality (e.g. facets, stresses or grains acting as scattering centres) or that a systematic error occurs. On the contrary, one has to take into account that all quantities in equation 3.1 used to calculate the thermal conductivity are afflicted with errors, which are not integrated into this examination. Considering also the dispersion of the literature values the error for measured thermal conductivity seems to be about $\pm$ 10%, to which the values obtained at the ILP would fit very well. From this point of view a statement on the reliability of the used measurement setup concerning the determination of absolute values cannot be given. Nevertheless, the measurements clearly show that thermal conductivity of Yb:YAG with doping concentrations between about 10% and 20%, which are interesting for thin-disk laser operation, is with 5 to 6 $\mathrm{Wm^{-1}K^{-1}}$ about 50% lower than undoped YAG. This decrease could be a disadvantage for Yb:YAG as a high power laser material when further power scaling to much higher power levels is an objective. Investigations by Beil suggest that Yb^{3+}-doped $Lu_3Al_5O_{12}$ might well be an attractive alternative to Yb:YAG for high power laser applications as the drop in thermal conductivity with Yb-doping concentration is much less pronounced due to the similar masses of Yb and Lu. At 10% Yb-doping LuAG displays with about 7.3 $\mathrm{Wm^{-1}K^{-1}}$ a 20% higher thermal conductivity compared to 10%Yb:YAG [Bei08, Bei09]. From the measurements it can also be deduced that regarding thermal conductivity no significant differences can be found

between single crystalline and ceramic Yb:YAG within the measurement errors. This result is not surprising as at room temperature thermal conductivity is not affected by the existence of grain boundaries since the internal thermal resistance is dominated by phonon-phonon interaction. The differences in thermal conductivity between single crystals and ceramics should only become evident at low temperatures where the phonon-phonon interaction is strongly reduced and contributions from extrinsic defects and grain boundaries become prominent. Indeed, temperature dependent investigations on thermal conductivity revealed that polycrystalline YAG displays lower thermal conductivities by about one order of magnitude at temperatures below 50K compared to its single crystalline counterpart [Yag07b].

Formula	$Y_3Al_5O_{12}$	[Yod51]
Acronym	YAG	[Kis66]
Lattice Symmetry	cubic	[War59]
Space Group (notation: Hermann-Mauguin, Schönflies)	$Ia\bar{3}d$, O_h^{10}	[Yod51]
Lattice Constant [Å]	12.000	[Dob04]
Point Symmetry of Cationic Sites (notation: Schönflies, Wycoff)	D_2, 24(c) (dodecahedral) C_{3i}, 16(a) (octahedral) S_4, 24(d) (tetrahedral)	[Men25] [Men25] [Men25]
Density of D_2-Sites (Y-Sites) [10^{22} cm^{-3}]	1.38	[Pet01]
D_2-Nearest Neighbour Distance (YAG) [Å]	3.676	[Mar04]
D_2-Nearest Neighbour Distance (YbAG) [Å]	3.654	[Mar04]
Number of Nearest Neighbours	4	[Lup98]
Coordination Number of D_2-Sites	8	[Yod51]
Ionic Radius of Y^{3+} (8-fold coordination) [Å]	1.019	[Kam90]
Ionic Radius of Yb^{3+} (8-fold coordination) [Å]	0.985	[Kam90]
Atomic Mass of Y [u]	88.91	[Cop96]
Atomic Mass of Yb [u]	173.04	[Cop96]
Doping Limit for Yb^{3+} [%]	100	[Fag07]
Melting Point [°C]	1940	[Cas80]
Standard Fabrication Techniques Crystal Growth Ceramic Fabrication (Konoshima Chemical Co. Ltd.)	 Czochralski VSN	 [Lin64] [Yag04]
Mohs Hardness	$8^1/_2$	[Kaz03]
Transparency Range ($\alpha \geq 1\,\text{cm}^{-1}$) [µm]	0.21 - 5.3	[Bas02]
Band Gap [eV]	6.97 - 6.5	[Pie00], [Thi01]
Maximum Phonon Energy [cm^{-1}]	700 - 860	[Kam90], [Sla69]
Refractive Index n	1.816	[Zel98]
Density ρ [gcm^{-3}]	4.45 - 4.56	[Hof06], [Agg05]
Specific Heat c_p [Jg^{-1}K^{-1}]	0.59 - 0.63	[Kru86], [Kle67]
Thermal Diffusivity α [10^{-6} m^{2}s^{-1}]	3.66 - 4.73	[Kru86], [Kuw04]
Thermal Conductivity λ [Wm^{-1}K^{-1}]	8.8 - 13	[Pad97], [Kle67]
Thermo-Optic Coefficient $\frac{dn}{dT}$ [10^{-6} K^{-1}]	7.8 - 10.5	[Bas02], [Wyn99]
Thermal Expansion Coefficient $\frac{1}{l}\frac{dl}{dT}$ [10^{-6} K^{-1}]	6.14 - 7.8	[Agg05], [Kle67]

Table 3.4.: *Selected crystallographic data of YAG. All values are given for undoped YAG at room temperature and for a wavelength of 1µm. For some parameters a variety of values can be found in the literature. In these cases the lowest and the highest values are given.*

3.6. State of the Art

Yb:YAG is one of the most relevant quasi-three-level laser materials to date. Much research has been carried out to reveal the parameters important for laser operation and much progress has been achieved over the last decades using this material in the different laser configurations. But, lasers and amplifiers are not the only fields of application for Yb:YAG. Recently, the charge transfer transition was extensively investigated as being attractive for the development of fast scintillators capable of distinguishing very short events. The following section summarises the current state of research regarding Yb:YAG as a scintillator material as well as the recent laser results.

3.6.1. Yb:YAG as Scintillator Material

Scintillator materials are widely employed to detect X-ray and gamma ray photons, accelerated charged particles as well as neutrons. For such applications wide bandgap semiconductor or insulator materials of high degree of structural perfection are most suitable. In general, fast and efficient transformation of incoming high energy photons or particles in a number of electron-hole pairs collected in the conduction and valence bands and their radiative recombination at luminescent centres in the material have to be accomplished. In 1997 the use of ^{176}Yb as a target for low-energy solar neutrino detection was proposed by Raghavan [Rag97]. Following his work intense research has been carried out to find suitable Yb containing scintillator materials. In this context UV fast scintillation in Yb:YAG has been found, opening up a new class of scintillating crystals with very peculiar luminescent properties [Ant01b]. Shortly after this discovery the observed luminescence was identified as charge transfer luminescence (CTL) [Gue01].

CTL is the reverse of the better known charge transfer absorption. In crystals doped with Yb^{3+}-ions the CTL manifests itself as two broad bands due to allowed transitions from the charge transfer state (CTS), which is formed by the transfer of an electron from the ligands to the metal Yb^{3+}-ion, to the $^2F_{7/2}$ ground and the only excited $^2F_{5/2}$ state of the Yb^{3+} $4f$ configuration (see section 2.2.3 for more details). This phenomenon was first observed by Nakazawa in the late seventies for Yb^{3+} in phosphate and oxysulfide matrices [Nak78, Nak79]. Most of the rare earth elements do not display such kind of luminescence because of the non-radiative relaxation from the CTS to the excited states of the $4f$ or $5d$ configuration. The CTS of Yb containing insulators is situated at a higher energy than the excited $4f$ state but lower than the $5d$ states, which makes CTL possible. Due to the short decay time from a few to tens of nanoseconds and the reasonable light yield, the CTL of Yb-doped crystals is attractive for the development of fast scintillators capable of discriminating very short events. Compared to the well studied f-f luminescence in the IR spectral range CTL is not well understood. In 2000, van Pieterson and coworkers presented a systematic study on CTL in several Yb^{3+}-doped materials [Pie00]. The reflection spectrum of a 2%Yb:YAG single crystal displayed an extra absorption band centred at 209 nm ($\approx$ 5.9 eV) absent in the undoped YAG crystal, which was ascribed to the transition from the $^2F_{7/2}$ ground state of Yb^{3+} to the CTS. However, this formulation might be a little confusing if the type of the describing concept is not given

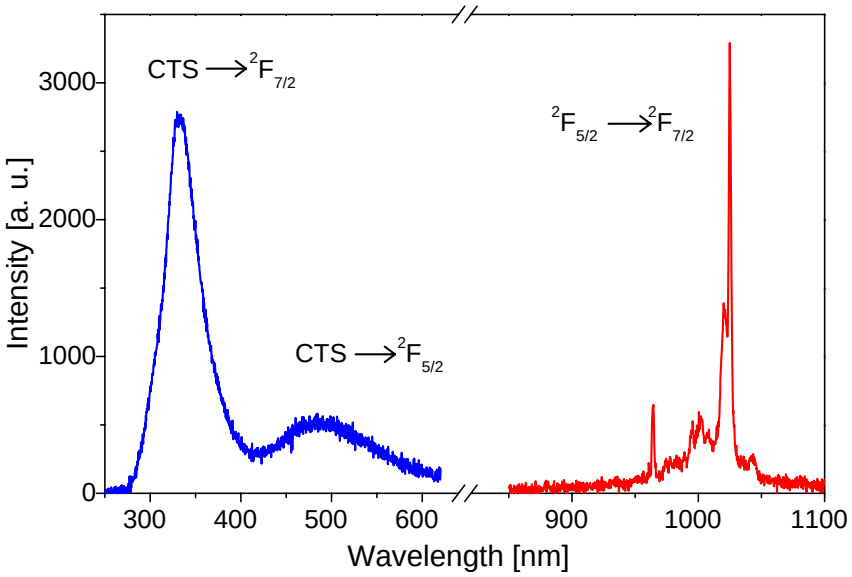

Figure 3.12.: Luminescence spectra of 15% Yb:YAG excited into the CTS at 140K [Kam05a].

and may only be valid for the description of CT using configurational coordinates (see also section 2.2.3). When exciting the Yb:YAG sample with radiation of 170 nm wavelength ($\approx$ 7.3 eV) at 10K, two strong emission bands around 330 nm and around 500 nm as well as Yb^{3+}-emission in the IR were observed (see figure 3.12). Since the separation between the two bands is close to 10 000 cm^{-1} ($\approx$ 1.24 eV), which is the separation between the two energy states of the Yb^{3+}-ion's $4f$ configuration, these bands are assigned to CTL occurring when the CTS relaxes into the $^2F_{5/2}$ excited or $^2F_{7/2}$ ground state of the Yb^{3+}-ion. The Stokes shift of the CTL is some 17 500 cm^{-1} ($\approx$ 2.17 eV)[17]. The lifetime of the CTS when excited at 210 nm was measured at 10K to be 30 ± 5 ns, which was much shorter than the corresponding CTS lifetimes in other Yb^{3+}-doped hosts but in the same order of magnitude as the lifetimes expected for such fully allowed transitions. Van Pieterson and coworkers suggested that in the Yb:YAG sample investigated the CTL was already partially quenched at 10K [Pie00]. This quenching behaviour of Yb containing compounds has been since intensively investigated [Gue01, Gue02, Kam05a].

The Yb^{3+} concentration dependency of the CTL has been investigated by Guerassimova and coworkers using variously doped Yb:YAG and YbAG crystals [Gue01, Gue02]. The total light yield was maximum for Yb^{3+} concentrations around 15%, the fluorescence intensity of YbAG being much weaker. The fluorescence lifetime of the CTS was found to be strongly concentration dependent, showing a single exponential behaviour for the 2%Yb:YAG sample under 210 nm excitation whereas the higher doped samples displayed non-exponential decay curves, most likely due to interactions between the Yb^{3+}-ions. This concentration quenching effect becomes dominant for concentrations of 20% and higher and can be neglected for lower doping levels (see figure 3.13). From these experiments the fluorescence lifetime for the CTS of the 2%Yb:YAG single crystal was determined to be about 85 ns at 12K [Gue01], which is much longer than the value of 30 ± 5 ns obtained by Pieterson *et al.* [Pie00] under comparable

[17] Nikl and coworkers found the Stokes shift at 80K to be about 1.96 eV [Nik04].

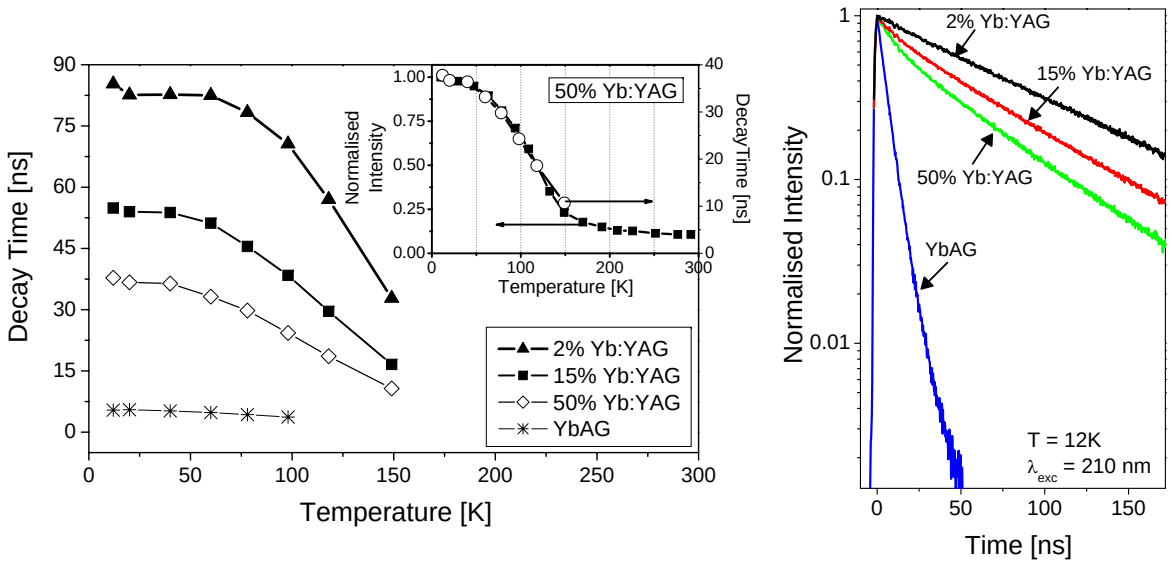

Figure 3.13.: Left: Temperature dependencies of CTL decay time as well as of CTL integrated intensity (insertion) and right: Decay profiles of Yb:YAG CTL at 12K, both under 210 nm excitation [Gue02].

conditions. At this stage, it is not possible to explain this discrepancy especially as no decay curve for the Yb:YAG sample is given in [Pie00].

It has also been found that Si-codoping has an influence on the scintillation behaviour of 50%Yb:YAG under X-ray excitation [Gue02]. The codoping of silicon resulted in the suppression of the thermoluminescence peak at around 100K and a significant reduction of decay time in this temperature regime. It is assumed that the introduction of silicon leads to a redistribution in structure and the population of electron levels in the forbidden gap which may reduce the trapping effect[18].

Kamenskikh *et al.* performed temperature dependent measurements of the CTL and f-f luminescence under excitation with 6.0 eV photons as shown on the left of figure 3.14 [Kam05a]. It was found that quenching of the CTL above 90K is due to thermally activated energy transfer to the $4f$ levels of trivalent ytterbium and not due to photoionisation of the CTS with the escape of a hole to the valence band. Under the same CTS excitation, it was also observed that the yield of the f-f luminescence increased again when the temperature was decreased below 70K. In the same work, there was found to be a significant difference between the room temperature and the low temperature excitation spectra. While at low temperatures the excitation spectrum for f-f luminescence reproduces that of the CT luminescence indicating that the emitting $^2F_{5/2}$ levels are populated via the CTS, this is no longer the case at room temperature (see figure 3.14, right).

[18]There are significant differences in the temperature dependencies of CT emission integrated intensity and CT emission decay time for direct excitation into the CTS (5.9 eV) and X-ray excitation. Excitation with energies higher than the band gap creates electrons and holes which can not only excite the CTS but also become trapped, the latter causing strong quenching of the CTL below 150K. The slower emission of X-ray excited CTS may be due to thermally stimulated release of trapped carriers with subsequent retrapping and emission at luminescent centres [Gue02].

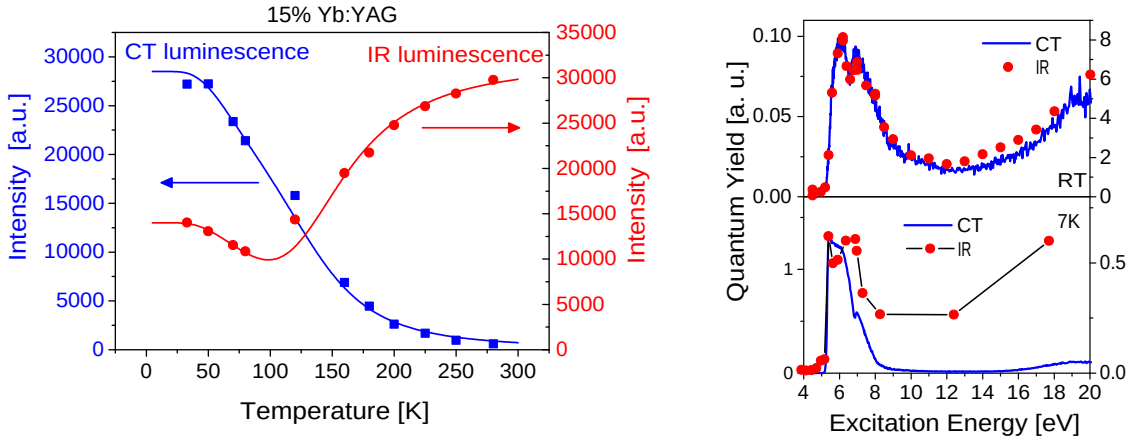

Figure 3.14.: Left: CT (solid lines) and $4f$ (circles) luminescence excitation spectra at RT (top) and 7K (bottom) and right: Temperature dependence of CT and $4f$ IR luminescence of 15%Yb:YAG excited at 6.0 eV. The solid lines represent results from simulation [Kam05a].

As a possible mechanism explaining these observations it is suggested that at low temperatures self-trapped holes could be trapped by Yb^{3+}-ions with subsequent capture of electrons followed by IR emission. It is also pointed out that this process could result in an increase of the yield of IR luminescence at low temperatures. Such a mechanism would be highly dependent on Yb^{3+}-concentration being at the same time also sensitive to inadvertent impurities competing with the Yb-ions.

However, the trapping effect as well as the temperature and concentration dependent quenching of the CTL in trivalent ytterbium containing materials are still not fully understood and is currently the subject of intensive research.

3.6.2. Laser Results

In the 1990s, in less than a decade diode-pumped Yb:YAG lasers increased from an average output power of just 23 mW [Lac91] to more than 1 kW [Bea00, Ste00]. Very different concepts and laser designs were realised and investigated as mentioned at the beginning of this chapter. In 2005, Bruesselbach and Sumida reported a continuous-wave (cw) average output power of 2.65 kW from a single Yb:YAG laser rod [Bru05]. An output power of 1.05 kW was demonstrated with the edge-pumped slab laser design in 2006 [Liu06]. Up to now, the most promising approach towards the development of highly efficient, high power solid-state lasers is the thin-disk laser concept. More than 5.3 kW of average output power has been achieved with a maximum optical efficiency of more than 60% from a single disk [Kil08]. In the same work, by combining three disk laser heads in series, output powers as large as 14 kW could be demonstrated. Theoretical work on the scaling laws of thin-disk lasers showed that the power limit for cw operation should be far beyond 40 kW from a single Yb:YAG disk [Gie07]. Today, various types of thin-disk lasers are commercially available. Even though Yb:YAG thin-disk

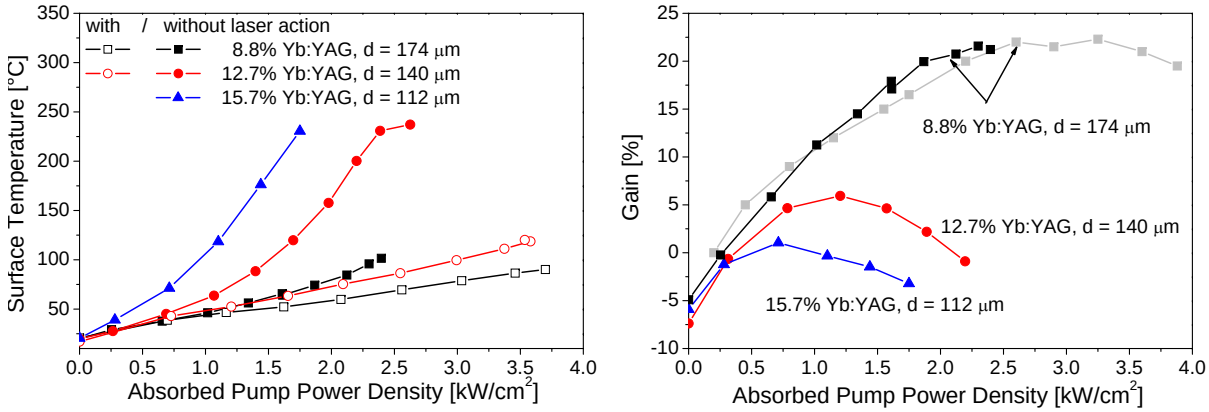

Figure 3.15.: Surface temperature (left) and measured gain (right) against the absorbed pump power density for differently concentrated Yb:YAG [Lar05]. The surface temperature is higher under non-lasing condition compared to under lasing condition for the same sample. The gain decreases significantly with concentration, the 15.7%Yb:YAG sample barely reaches laser threshold.

lasers have already found industrial application, laboratory based research is still ongoing to further increase efficiency and reaching even higher powers.

In 2005, Larionov and coworkers reported non-linear decay processes with high heat generation, which were observed in Yb:YAG thin-disk lasers under certain conditions [Lar05]. It was found that the rate of the decay depends on the density of the excited Yb^{3+}-ions and doping concentration as well as on temperature. Due to the rapid decay of the Yb^{3+} excited states the gain decreases, which significantly reduces laser efficiency especially for thin-disk lasers in pulsed operation that need high excitation densities. For doping concentrations higher than 15% not even cw operation could be realised. Surface temperature measurements revealed significant non-linear heating with absorbed pump power under non-lasing conditions whereas a linear increase in temperature was found in the case of laser action (see figure 3.15, left). The difference in temperature between lasing and non-lasing condition was greater the higher the doping concentration of the investigated Yb:YAG crystal. However, differences in heating were also observed for different crystals of nominally the same concentration, which indicates that trace impurities or other slight defects can contribute to the heating and deteriorate laser performance when high inversion densities are needed as is the case for the thin-disk laser. Gain measurements show a decrease in the number of excited Yb^{3+}-ions with pump power beginning at a certain absorbed pump power density (see figure 3.15, right). From these measurements the rate of non-linear decay processes was calculated and plotted against the density of excited Yb^{3+}-ions as can be seen in figure 3.16. The plot shows that the observed non-linear decays are strongly dependent on the density of Yb^{3+}-excitations and display a somewhat weaker dependency on temperature of the cooling water. Higher temperature seems to amplify the loss process once a certain rate of non-linear decay is reached. The losses also display a threshold behaviour, indicating that some threshold condition has to be reached for the losses to occur. According to the measurements, these losses are not only dependent on density of excited states but also on the doping concentration. The higher the Yb^{3+} doping concentration of the crystal, the lower the density of excitations needed for the set-in of the non-linear losses. In addition,

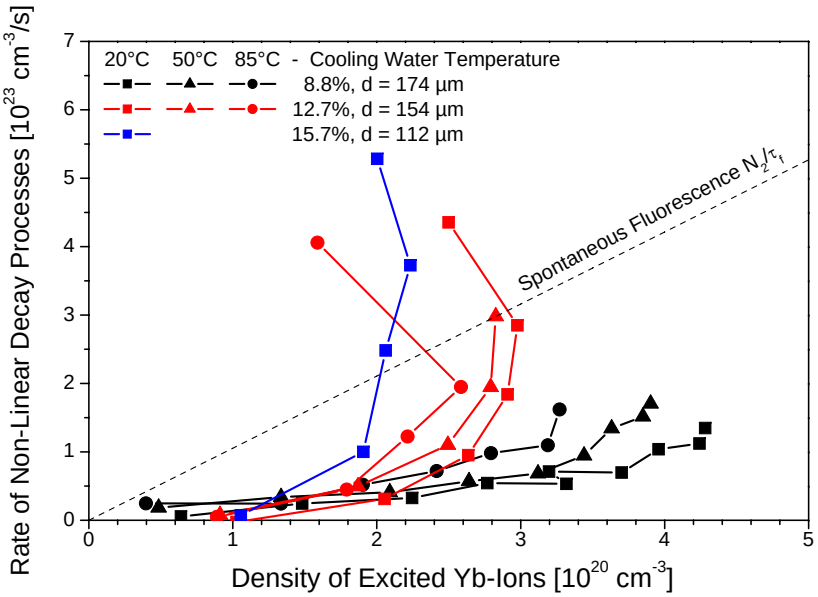

Figure 3.16.: Rate of non-linear loss processes plotted against the number of excited Yb^{3+}-ions for different Yb concentrations and cooling temperature from [Lar05]

another slow loss process seems to exist below the threshold of the non-linear rapid decay. Figure 3.16 might appear confusing, in particular regarding the plots belonging to the 12.7% and 15.7%Yb:YAG samples, as more than one decay rate is associated with one and the same value for the density of excited states. It needs to be pointed out that these data points having the same density of excited states actually differ in the amount of absorbed pump power. The graph should be interpreted as follows. With increasing absorbed pump power the density of excited Yb^{3+} states increases until some threshold condition is reached and a formerly not existing loss channel is unlocked. With further increase of absorbed pump power the rate of the losses rapidly increase while the rate of increase of the number of excited Yb^{3+} states diminishes. Eventually, the density of excited states saturates or even decreases.

From the current state of knowledge the dependency of the gain on absorbed pump power and especially the sudden decrease of the Yb^{3+} excited state population cannot be understood. Larionov *et al.* suggest that energy transfer to impurities or the excitation of a CTS or any other state needing the energy of several excited Yb^{3+}-ions might be a possible reason for the observed losses. Based on these results it has to be deduced that efficient laser operation is not possible for Yb:YAG thin-disk lasers with high concentrations and that excitation density is a crucial limit for further power scaling if the observed decay processes are of fundamental origin. Unrevealing the nature of these losses and gather understandings of the mechanisms involved are the main purposes motivating this research. The potential causes for this effect will be investigated in the following chapters.

4. Spectroscopic Investigations

Spectroscopic analyses such as measurement of emission and absorption spectra as well as fluorescence lifetime form the main investigations which reveal the existence of colour centres, unwanted rare earth contaminations and other impurities. It is the purpose of this chapter to compare single crystalline and ceramic Yb:YAG laser materials with each other regarding their optical quality. To obtain information on the losses observed in thin-disk laser experiments, spectroscopic investigations under similar conditions as for the laser experiments are of particular interest. The intrinsic fluorescence lifetime is a key factor for the quality of the samples. Therefore, the excitation energy dependence of the fluorescence lifetime is also studied extensively.

This chapter is organised as follows: first, the basic principles for the measurement of the fluorescence lifetime in quasi-three-level systems are discussed and the pinhole method is introduced as a measurement technique which considerably reduces the effect of reabsorption. The results of the fluorescence lifetime investigations are summarised and discussed at the end of this first section. Next, the absorption measurements are presented, particularly focussing on the transmission spectra in the short wavelength spectral range to identify possible defects and impurity centres. The subsequent section deals with the fluorescence measurements, followed by the charge transfer experiments performed on ceramic and single crystalline Yb:YAG The final section of this chapter summarises the results obtained. The laser relevant spectroscopic parameters used in the calculations in chapter 5 are summarised in table 4.2 at the end of section 4.4.

4.1. Fluorescence Lifetime

The excited state lifetime of the upper laser level is one of the most important spectroscopic parameters for a solid state laser gain medium. To achieve laser operation, the upper level lifetime has to be sufficiently long so that enough energy can be stored in the system to achieve population inversion. Furthermore, the accurate measurement of the radiative lifetime is of particular interest for the determination of the emission cross-sections with the Füchtbauer-Ladenburg method [Füc20, Lad21, Kru74]. Due to spontaneous emission, the population of an excited state is expected to decay exponentially with time (see section 2.2.1, equation 2.26). In this case, the measured fluorescence lifetime τ_{flu} would be equal to the radiative lifetime τ_{rad} of the excited state. However, the upper laser level lifetime can be quenched due to nonradiative decay (see section 2.2.1, Nonradiative Decay and Multiphonon Relaxation) or interionic energy transfer processes (see section 2.2.2). This results in the reduction of the quantum efficiency

and thus to a decrease in laser efficiency. Therefore, the fluorescence lifetime is a key parameter for the determination of sample purity and also of the suitability as a laser material.

In this work, the intrinsic fluorescence lifetimes of Yb:YAG single crystals with Yb-doping concentrations of 0.1%, 0.4%, 1.0%, 16.5%, 20.0%, 80.0% and that of an YbAG single crystal as well as Yb:YAG ceramic samples of Yb-doping concentrations of 0.3%, 1.0%, 10.9%, 13.0%, 15.0% and 21.5% were determined using the pinhole method. The ceramic samples were prepared from the same materials as those used in the laser and photoconductivity measurements in chapters 5 and 6. The single crystal of 0.4% Yb-concentration was provided by Forschungsinstitut für mineralische und metallische Werkstoffe -Edelsteine/Edelmetalle-GmbH (FEE), Germany. All others single crystalline samples except for the 16.5%Yb:YAG prepared from boule #SNF (see section 3.5.1) were grown at the Institute of Laser-Physics in the framework of the diploma works of V. Müller [Mül01] and N. Martynyuk [Mar02].

4.1.1. Radiation Trapping and the Pinhole Method

For laser transitions with unity branching ratio to the ground state manifold, as is the case in Yb:YAG, the measured fluorescence lifetime is often distorted by reabsorption processes (see section 2.2.2, Reabsorption). These processes lead to so-called radiation trapping, i.e. spontaneously emitted photons are reabsorbed by ions in the ground state, which then also spontaneously decay, emitting photons which are again reabsorbed and the whole process is repeated. Total internal reflection further enhances the average path length and thus the reabsorption probability. The effect of measurement over the volume of the sample is an increase of the fluorescence lifetime relative to the lifetime of a single isolated ion. Thus in highly concentrated Yb:YAG, the determination of the radiative lifetime is often complicated by two processes with opposite effects: migration to impurities (see section 2.2.2, Energy Migration), which quench the lifetime of the excited state and radiation trapping which artificially increases the measured fluorescence lifetime. In this work, the term intrinsic lifetime is used for this undistorted single ion fluorescence lifetime.

Motivated by the wide spread for the $^2F_{5/2}$ upper level lifetimes reported for Yb:YAG in the literature, ranging from 1.08 ms [DeL93] to 1.30 ms [Bog76], Sumida and Fan investigated on the effects of total internal reflection and proposed a measurement technique, which to a large extent eliminated radiation trapping [Sum94]. In their setup, optically thin plates of differently concentrated Yb:YAG were sandwiched between two pieces of undoped YAG. In this way, total internal reflection at the Yb:YAG-YAG interface was almost eliminated and a large fraction of spontaneously emitted light could escape the sample without reabsorption. Furthermore, an aperture was placed at the sample to limit the transverse area seen by the detector. Two different apertures of 0.5 mm and 2.5 mm diameter were used. It was found that up to 10% Yb-doping concentration the results were identical for both apertures within the measurement errors. For higher concentrations the radiation trapping effect was less reduced for the 2.5 mm aperture. Sumida and Fan determined the intrinsic lifetime of the the $^2F_{5/2}$ manifold in Yb:YAG to be $951\,\mu s \pm 15\,\mu s$. In 1997, Hehlen presented Monte Carlo simulations of radiative energy transfer in solids and measurements in a spherically refractive index matched geometry, which yielded an intrinsic lifetime of $948.9\,\mu s \pm 0.6\,\mu s$ for the upper level in Yb:YAG [Heh97]. It was

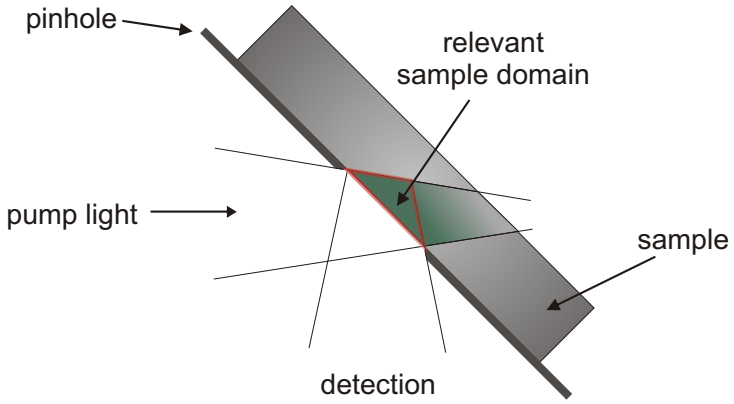

Figure 4.1.: Schematic of the relevant sample domain considered in the theoretical description of the pinhole method [Krä08].

concluded that experiments without refractive index matching lead to significant overestimation of the intrinsic lifetimes.

An alternative method for the determination of the intrinsic fluorescence lifetime of systems with overlapping emission and absorption spectra, which does not need any refractive index matching, was developed at the Institute of Laser-Physics, University of Hamburg, and first presented in 2004 [Krä04]. In this method, the sample is placed behind at least five different apertures with diameters varying from 0.5 mm to 2.5 mm, so that the fluorescence lifetime is measured as a function of this pinhole diameter. Plotting the measured lifetime against the pinhole diameters gives a linear relationship between the two. The intrinsic lifetime is then obtained by extrapolating to zero aperture of the pinhole. A theoretical description corroborating this relationship was introduced by Kühn *et al.* in 2007 [Küh07]. It was confirmed that a linear relationship exists between measured fluorescence lifetime and average path length of a spontaneously emitted photon with the radiative lifetime being the intersection with the ordinate axis. It was also found that the average path length is in the range of the pinhole radius. Since the relevant sample domain depicted in figure 4.1, has the same shape for each aperture while the diameter of this domain is proportional to the pinhole radius, a direct linear relationship between average path length and pinhole diameter was suggested.

4.1.2. The Experimental Setup

A schematic of the used experimental setup is depicted in figure 4.2. The Yb:YAG samples were excited by a frequency-tripled (THG) Nd:YAG laser pumped optical parametric oscillator (OPO) with 10 Hz, 10 ns pulses tuned to 968 nm (LQ 129, LG 103, LP 601, SOLAR Laser Systems, Republic of Belarus). For this wavelength the maximum pulse energy was 8.2 mJ. The samples were placed in an angle slightly different from 45° with regard to the incident pump light to avoid direct reflection of the excitation pulses into the detection system. The pump light emitted by the OPO was focussed onto the sample so that the pump spot diameter was equal to the diameter of the pinhole with largest aperture. The fluorescence signal spontaneously emitted by the excited Yb^{3+}-ions was collected by a lens and then focussed by another lens

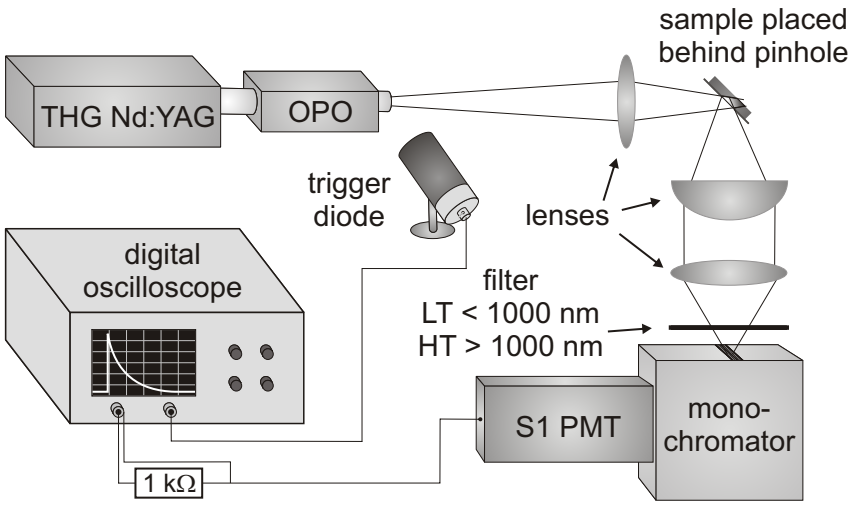

Figure 4.2.: Schematic of the experimental setup used in the fluorescence lifetime measurements [Krä08]. See text for detailed description.

onto the slit of a 0.5 m SPEX monochromator (SPEX Industries, USA) centred at 1 030 nm. An edge filter was placed in front of the entrance slit, which was highly reflective for light below 1 000 nm but ensured high transmission for light of longer wavelength. The signal was detected by a photomultiplier tube (PMT) with S1 characteristic (9684B, Thorn-Emi-Electron Tubes Ltd., USA) and recorded with a digital oscilloscope (LeCroy 9360, LeCroy Corporation, USA). As thermalisation within a manifold is reached on very short time scales (see section 2.2.1, Effective Cross-Sections) and as for Yb:YAG spontaneously emitted light in the 1 µm spectral range is expected to originate solely from the $^2F_{5/2}$ Yb^{3+} upper manifold, accurate wavelength selection was not required. Therefore, for the benefit of signal intensity in the measurements the entrance slit of the monochromator was set to its maximum width at 3 mm. To further enhance the signal intensity, the input resistance of the oscilloscope was set to 1 MΩ and a 1 kΩ resistance was connected in parallel. The RC time constant in this case was still much smaller than the expected fluorescence lifetime of Yb:YAG and thus did not affect the measurement results. The signal was averaged over several hundred to thousand pulses to obtain a good signal-to-noise ratio. To provide stable tracing, the excitation pulse detected by a Si-diode was used as an external trigger starting the event of recording. The raw data of the decay curves obtained were all baseline corrected before analyses. As the decay curves obtained for the pinhole with the smallest aperture displayed the lowest signal-to-noise ratio, the time interval used for evaluation was chosen according to the data obtained from the smallest pinhole in each set of measurements. The fluorescence lifetime was obtained by applying an exponential fit to the chosen time interval. A detailed description of the measurement procedure can be found in [Krä08].

4.1.3. Results and Discussion

No difference between single crystals and ceramics could be observed within the measurement error, which indicates that the materials have no significant differences in quality. All sam-

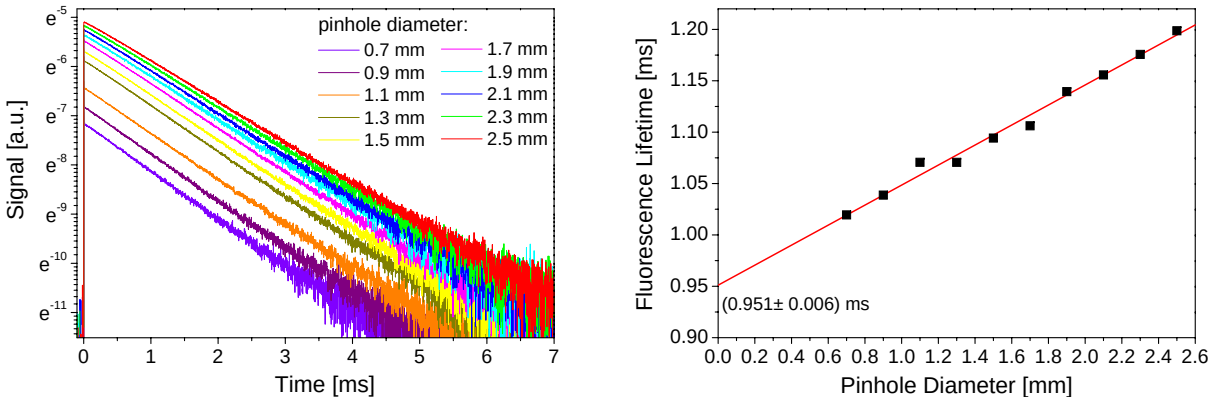

Figure 4.3.: Left: the decay curves of the spontaneous fluorescence of the 16.5%Yb:YAG single crystal (#boule SNF) with a thickness of $d = 250\,\mu m$ measured with different pinhole diameters. Right: The obtained fluorescence lifetimes of the 16.5%Yb:YAG single crystal as a function of pinhole diameter.

ples displayed single exponential decay characteristics which suggests that cooperative energy transfer processes to impurities are absent or at least not of significance. No radiation trapping effect was found for the 0.1%, 0.4% and 1.0%Yb:YAG single crystalline samples with thicknesses of 915 µm, 134 µm and 144 µm, respectively. Due to the low Yb-doping concentrations, both energy migration to impurities as well as radiation trapping are expected to be nonexistent in these samples. Therefore, the lifetimes obtained for these low concentrated samples are identified with the radiative lifetime of the single Yb^{3+}-ion in YAG. For these samples the intrinsic lifetime is obtained by averaging the lifetimes measured for different pinholes. The values found were 953 µs ± 6 µs , 942 µs ± 15 µs and 947 µs ± 10 µs for the 0.1%, 0.4% and the 1.0%Yb:YAG single crystal, respectively. These values are in very good agreement with the values for the radiative lifetime found by Sumida and Fan [Sum94] and Hehlen [Heh97].

The decay curves recorded for the 16.5%Yb:YAG single crystal (boule #SNF) are plotted as an example for the higher concentrated samples on the left side of figure 4.3. The ordinate axis is given in logarithmic scale and thus exponential functions are displayed as linear curves so that any deviations from single exponential decay behaviour can be easily recognised. The 16.5%Yb:YAG single crystalline sample had a thickness of 250 µm. Ten different pinholes with diameters between 0.7 mm and 2.5 mm were used. As expected the signal is higher and the obtained lifetime is longer the larger the pinhole diameter. On the right side of figure 4.3 the fluorescence lifetimes obtained are plotted against the respective pinhole diameters. Extrapolation to zero pinhole diameter yielded an intrinsic fluorescence lifetime of 951 µs ± 6 µs. Accordingly, the intrinsic lifetime of the 20.0%Yb:YAG single crystal (410 µm thickness) was determined to be 951 µs ± 23 µs and that of the 80.0%Yb:YAG crystal (144 µm thickness) 962 µs ± 9 µs. For the intrinsic lifetime of the YbAG single crystal of 100 µm thickness a value of 850 µs ± 9 µs was found.

The decay curves recorded for the ceramic Yb:YAG samples are plotted in figure 4.4. The thickness of the samples is stated at the bottom of the graphs. The slight deviation from single exponential decay behaviour at the beginning of the decay curves for the 15.0% and the 21.5%Yb:YAG ceramic samples is due to saturation effects of the detector and treated as an

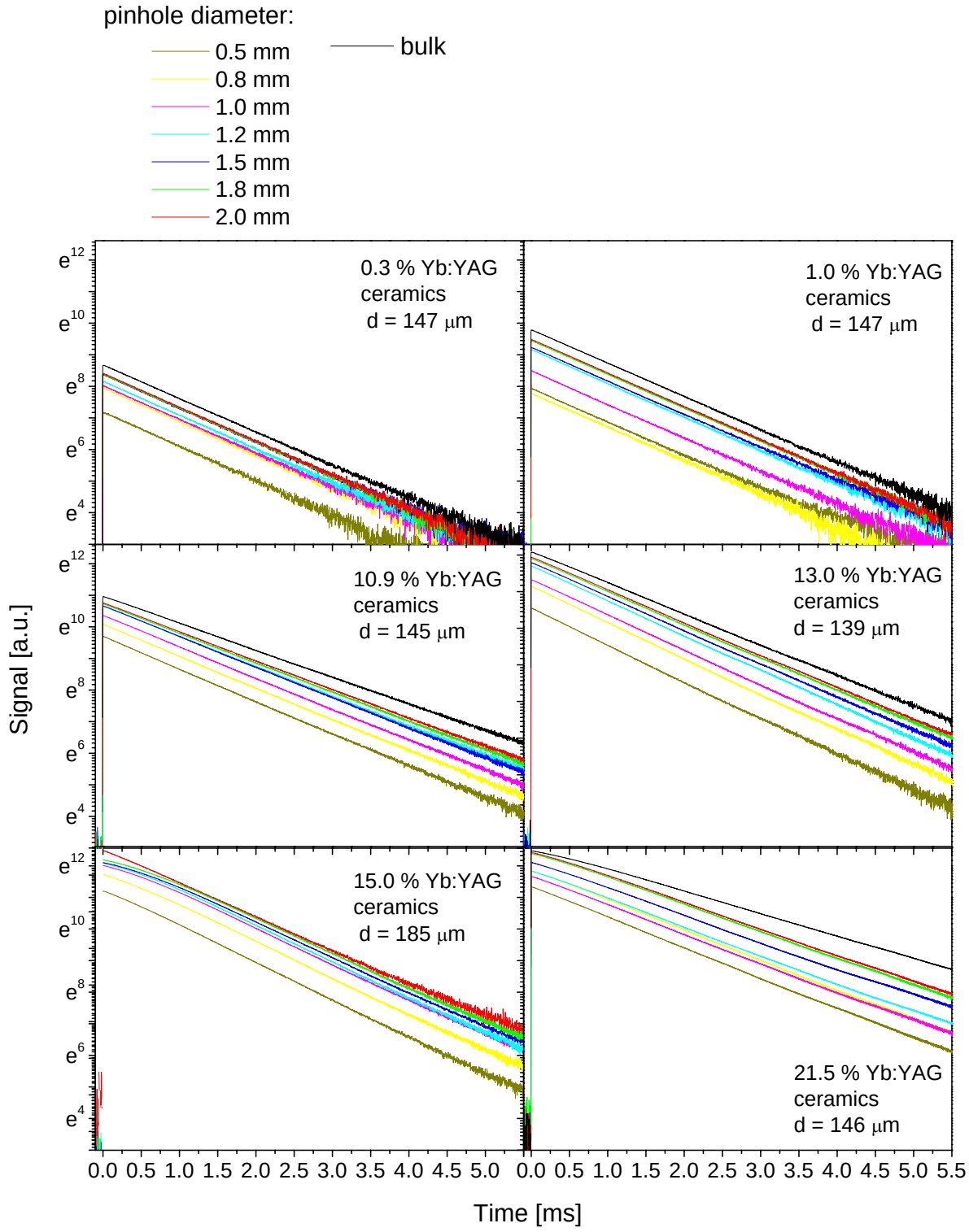

Figure 4.4.: Fluorescence decay curves of the ceramic Yb:YAG samples obtained for different pinhole diameters and without pinhole (denoted as bulk). The Yb-doping concentration and the sample thickness are given in the graphs. The legend for the used pinhole diameters is found at the top.

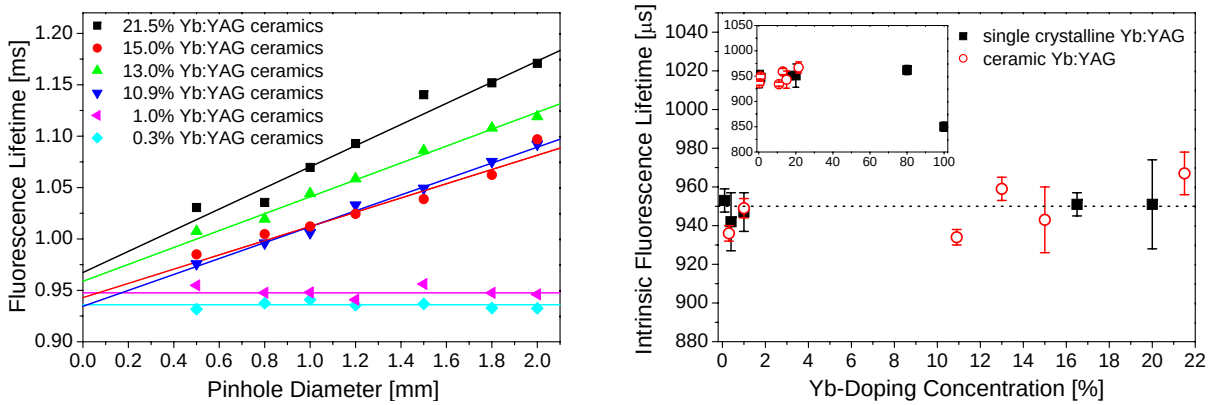

Figure 4.5.: Left: The obtained fluorescence lifetimes plotted against pinhole diameter for all ceramic Yb:YAG samples. Right: Intrinsic fluorescence lifetimes of ceramic (open circles) and single crystalline (filled squares) Yb:YAG plotted against Yb-doping concentrations up to 22%. The whole concentration range up to YbAG is shown in the inset. The dotted line is plotted just for orientation and marks 950 µs. The doping concentration is given with respect to the Y-sites in YAG.

artefact. As expected, the effect of reabsorption is stronger the higher the Yb-concentration of the sample. Same as for the single crystals of low Yb-doping concentration no effects of radiation trapping were observed for the 0.3% and the 1.0%Yb:YAG ceramic samples. The obtained lifetimes are plotted against the pinhole diameter for all ceramic samples together in figure 4.5, left. The strong effect of radiation trapping is clearly seen in the steep slopes of the higher doped samples. For the 21.5%Yb:YAG ceramics the fluorescence lifetime ranges between 1.17 ms obtained from the measurement with a pinhole diameter of 2.0 mm and 1.03 ms obtained with a pinhole diameter of 0.5 mm. The bulk fluorescence lifetime defined as the fluorescence lifetime obtained without any pinhole was even measured to be as high as 1.4 ms. The slopes of these characteristics seem to continuously decrease with Yb-doping concentration with exception for the 15.0%Yb:YAG ceramic sample. This might be due to the larger thickness of this sample compared to the others, which could lead to reduced total internal reflection. However, for the determination of the intrinsic lifetime by extrapolation to zero pinhole diameter the thickness of the sample was found to be irrelevant in a range between 100 µm and 2.3 mm and also for bulk materials [Hir07, Pet09]. Intrinsic fluorescence lifetimes of 967 µs ± 11 µs, 943 µs ± 17 µs, 959 µs ± 6 µs, 934 µs ± 4 µs, 949 µs ± 5 µs and 936 µs ± 4 µs were found for the Yb:YAG ceramic samples of 21.5%, 15.0%, 13.0%, 10.9%, 1.0% and 0.3% of Yb-doping concentrations, respectively.

The intrinsic lifetimes obtained for the Yb:YAG single crystalline and ceramic samples are plotted together in figure 4.5, right against Yb-doping concentration. Up to 22% of doping concentration no radiation trapping effect is observed. The intrinsic lifetime of the 80%Yb:YAG single crystalline sample also displays no significant increase of the lifetime compared to the lower doped samples, which corroborates the validity of the pinhole method. As can be seen, the ceramic and single crystalline samples display very similar intrinsic lifetimes in the investigated concentration regime. Furthermore, the lifetimes are in excellent agreement with the values found in literature for the Yb:YAG radiative lifetime [Sum94, Heh97] as well as those obtained in [Pat01] for the Yb:YAG powders of Yb-doping concentrations lower than 15%. It

is tempting to attribute the much lower intrinsic lifetime of the YbAG single crystal to quenching due migration to impurities. In the literature, different values for the radiative lifetime of the Yb^{3+}-ion in YbAG can be found. Both Patel *et al.* [Pat01] and Fagundes-Peters *et al.* [Fag07] proposed a decrease of radiative lifetime with increasing Yb-doping concentration due to small changes in the crystal field symmetry introduced by the incorporation of Yb^{3+}-ions into the YAG lattice. The radiative lifetime for YbAG was determined to be 869 µs in [Pat01] and 964 µs in [Fag07]. In this context, the notation of doping has to be reconsidered. Certainly, for Yb-concentrations of more than 10% of the available Y-sites the term doping has to be considered an underrating as the Yb^{3+}-ions also influence lattice parameters as bond length and crystal field. YbAG having different crystallographic properties, as e.g. a different lattice constant, has to be clearly considered a different crystal from YAG (see also section 3.3.2). However, the longer lifetime of the 80%Yb:YAG single crystal, which is very similar to the intrinsic lifetimes obtained for the lower doped samples does not fit into such a picture. From these results it has to be concluded that either the influence of the changes in the crystal field due to incorporation of Yb^{3+}-ions on the radiative lifetime is negligible and the lifetime of the YbAG sample is quenched or the intrinsic lifetime obtained for the 80%Yb:YAG single crystal is still increased because the radiation trapping effect could not be completely eliminated by the pinhole method or a mixture of both effects. Similar observations for an initial increase in intrinsic fluorescence lifetime obtained by the pinhole method with Yb-concentration were observed for Yb:YVO_4 and Yb:$LaSc_3(BO_3)_4$ [Krä08] and for Yb:$NaGd(WO_4)_2$ as well as Yb-doped sesquioxides [Pet09]. Furthermore, it also has to be mentioned that the radiative lifetime for low concentrated Yb:YAG crystals presented in [Fag07] is with 1 040 µs about 10% higher than those obtained in this work, while in [Hir07] using comparable samples the radiative lifetime is stated to be about 930 µs. Due to the excellent agreement with most of the literature values and the good reproducibility of the intrinsic fluorescence lifetime values obtained in this work, it is strongly suggested that at least for Yb:YAG single crystals and ceramics up to a concentration of 22%, the radiative lifetime is identical to the intrinsic fluorescence lifetime of about 950 µs. Thus, a unity quantum efficiency is expected for the laser samples used in the thin-disk laser experiments in chapter 5. However, the results also lead to the conclusion that intrinsic fluorescence lifetimes can only be given with an accuracy of about 10% of the obtained value regardless of the determination method applied. A summary of the intrinsic fluorescence lifetimes in Yb:YAG obtained in this work and found in the literature is given in table 4.1 at the end of this section.

The fluorescence lifetime of as-grown 80%Yb:YAG was presented in [Fag04]. The decay curves were non-exponential and the fluorescence lifetime was strongly quenched. Excitation energy dependent lifetime measurements showed that a cooperative energy transfer exists in these samples. The extrapolated maximum fluorescence lifetime was found to be about 40 µs. This value is not corrected for radiation trapping effects. It is strongly suggested that the lifetime is quenched due to cooperative energy transfer from two excited Yb^{3+}-ions to one Yb^{2+}-ion, which is stabilised by and oxygen vacancy[1]. Excitation energy dependency of the fluorescence lifetime was investigated for the annealed single crystalline and ceramic samples in this work. As expected from the single exponential behaviour of the decay curves, no such dependence

[1]For a rate equation formalism describing such transfer processes see [Fag07]. In this paper a similar process with Fe^{3+}-ions as quenching centres is described.

was found suggesting that cooperative energy transfer processes are absent in these samples.

Sample	this work		[Sum94]		[Pat01]		[Fag07]	
	d [µm]	τ_{int} [µs]	d [µm]	τ_{int} [µs]	d [µm]	τ_{int} [µs]	d [µm]	τ_{int} [µs]
0.1%Yb:YAG	915	953 ± 6						
0.3%Yb:YAG	*147*	*936 ± 4*						
0.4%Yb:YAG	134	942 ± 15						
1.0%Yb:YAG	*147*	*949 ± 5*						
1.0%Yb:YAG	144	947 ± 10	unspecified	~ 950				
2.0%Yb:YAG							unspecified	$1\,042 \pm 10$
5.0%Yb:YAG					powder	969		
5.5%Yb:YAG			200	~ 940				
10.0%Yb:YAG					powder	943		
10.8%Yb:YAG			unspecified	~ 960				
0.9%Yb:YAG	*145*	*934 ± 4*						
13.0%Yb:YAG	*139*	*959 ± 6*						
15.0%Yb:YAG	*185*	*943 ± 17*			powder	952		
16.5%Yb:YAG	250	951 ± 6	unspecified	~ 910				
18.0%Yb:YAG					powder	815		
20.0%Yb:YAG	410	951 ± 23					unspecified	$1\,034 \pm 15$
21.5%Yb:YAG	*146*	*967 ± 11*						
25.0%Yb:YAG					powder	856		
25.1%Yb:YAG			unspecified	~ 780				
40.0%Yb:YAG							unspecified	$1\,013 \pm 15$
50.0%Yb:YAG					powder	655		
60.0%Yb:YAG							unspecified	949 ± 15
80.0%Yb:YAG	144	962 ± 9					unspecified	870 ± 8
80.0%Yb:YAG*							unspecified	40
YbAG	100	850 ± 9			powder	664	unspecified	961 ± 15

Table 4.1.: Summary of intrinsic fluorescence lifetimes τ_{int} obtained in this work and values found in the literature [Sum94, Pat01, Fag07]. *d* is the sample thickness. *Italics* refer to ceramic samples. The * denotes as-grown sample. See text for details.

4.2. Absorption and Transmission Spectra

Transmission spectra are usually recorded to obtain the absorption cross-sections of optically active ions and centres in a host material. The small signal absorption coefficient α_0 can be determined according to the Beer-Lambert law from the transmission spectrum if the sample thickness is known (see section 2.2.1, equation 2.24). To obtain the absorption cross-sections also the concentration of the absorbing centres has to be known accurately, which often complicates the determination. In the literature, different values for the absorption cross-sections can be found for Yb:YAG single crystals at the typical pump absorption band centring at 941 nm. Values range between 6.7×10^{-21} cm^2, obtained for a 6.5%Yb:YAG crystal [Lac91]

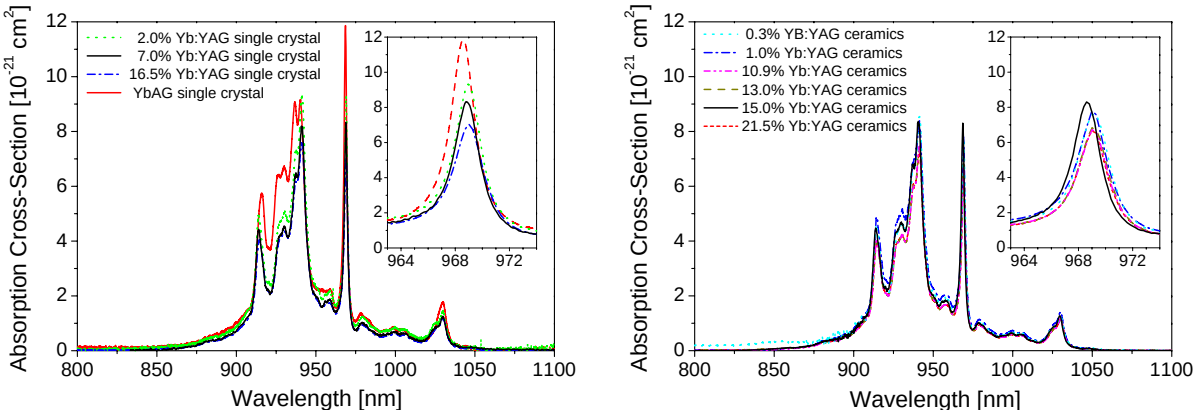

Figure 4.6.: Left: the absorption cross-sections calculated from transmission spectra recorded for Yb:YAG single crystalline samples of different Yb-doping concentrations together with that of YbAG. The data for the 2%Yb:YAG and the YbAG cross-sections are taken from [Fag07], the data of the 7%Yb:YAG crystal is taken from [Mix95]. Right: absorption cross-sections calculated from the transmission spectra of the ceramic Yb:YAG samples. The inset in both graphs shows the zero-line at around 968 nm in larger scale.

and 9.3×10^{-21} cm^2, obtained for a 2%Yb:YAG crystal [Fag07]. The transition cross-sections should in theory be independent of doping concentration. However, as for the fluorescence lifetimes discussed above, it is expected that also the cross-sections deviate for low and high doping concentrations due to a distortion of the crystal field. Yet, between 2% and 6.5% Yb:YAG such a distortion effect is considered negligible and it is assumed that the differences found in the literature are mainly due to uncertainties in the doping concentration.

In figure 4.6, left the absorption cross-sections obtained for single crystalline Yb:YAG of four different Yb-doping concentrations are plotted. The data for the 2%Yb:YAG and the YbAG single crystal are taken from [Fag07] and the data of the 7%Yb:YAG are taken from [Mix95]. The cross-sections for the 16.5%Yb:YAG single crystal (boule #SNF) were obtained in this work. The transmission spectra for the samples investigated in this work were recorded with a Cary 5000 UV-VIS NIR spectrophotometer (Varian Inc., USA). On the right side of figure 4.6 the absorption cross-sections obtained for the ceramic samples are shown. The absorption bands of the Yb^{3+}-ion are rather broad compared to those of other trivalent lanthanoid ions due to stronger electron-phonon coupling (see section 2.2.1, The Influence of Phonons). The absorption bands with their maximum around 940 nm and 968 nm exhibit the highest absorption cross-sections. The 940 nm band is due to its broad band width particularly suitable for diode laser pumping. The absorption line at 968 nm was identified by many researchers to be the so-called zero-line, which corresponds to the transition between the two lowest Stark levels of the $^2F_{7/2}$ and $^2F_{5/2}$ manifolds [Buc67, Bog76]. Comparison of the absorption spectra of the single crystalline and ceramic samples show that both materials are identical in their absorption characteristics. The differences between ceramics and single crystals are in the same order of magnitude as the deviations for the different concentrated Yb:YAG samples of the same type of material. Only the absorption spectrum of YbAG displays significant differences to the Yb:YAG spectra.

Transmission spectra are also very useful in the characterisation of impurities, defects and

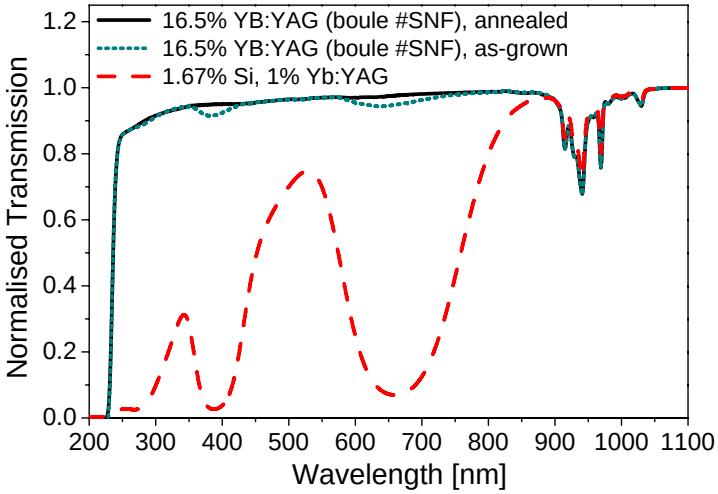

Figure 4.7.: Transmission spectra of as-grown (dotted line) and annealed (solid line) 16.5%Yb:YAG (boule #SNF) together with that of 1%Si,1.67%Yb:YAG

colour centres, which usually manifest themselves as broad absorption bands in the short wavelength range close to the fundamental absorption. As briefly described in section 3.2, some of these centres have been identified for YAG but for many defect centres the identification and the association to energy levels with respect to the YAG host bands as well as their influence on laser property remains uncertain. In the following section, the absorption bands found in the short wavelength spectral range for the single crystalline and ceramic Yb:YAG samples used in this work are examined in detail. An assignment of the impurities and defect states is attempted.

Figure 4.7 shows the transmission spectra of as-grown and annealed 16.5%Yb:YAG (boule #SNF) together with that of 1%Si,1.67%Yb:YAG (nominal concentration). The Yb:YAG crystal was grown under reducing atmosphere (see section 3.5.1) and thus oxygen vacancies are expected in the as-grown sample. The transmission edge at around 230 nm should not be mistaken with the fundamental absorption which in Yb:YAG is found around 190 nm (see section 3.4.1). The absorption band leading to the transmission edge in the 16.5%Yb:YAG crystal is associated to the strong charge transfer absorption centred at around 210 nm (see section 4.4), which leads in the high concentred Yb:YAG samples to such a transmission edge at longer wavelength. For this reason, the determination of the optical band gap energy from transmission spectra is particularly complicated in YbAG. The broad absorption bands found in the as-grown crystal centring around 650 nm, 380 nm and 270 nm are attributed to the presence of divalent Yb-ions [Hen01, Kre03]. The same bands are found in Si-codoped Yb:YAG crystals, which led to the assumption that silicon is incorporated in its tetravalent state into YAG and thus stabilises ytterbium in its divalent state[2]. All bands disappear at the same temperature of 800°C when annealing the crystal in air, suggesting that they belong to the same centre. Excitation into these bands did not yield any luminescence, which leads to the assumption that the excited states of this centre lie in the conduction band. This was confirmed by photoconductivity measurements (see section 6.2.1). The straight identification of these absorption bands with the interconfigurational transitions from the $^1S_0$ ground state to the $4f^{13}5d$ states of the

[2]This assumption is not fully correct. For discussions see [Wol09b] and section 6.3.1.

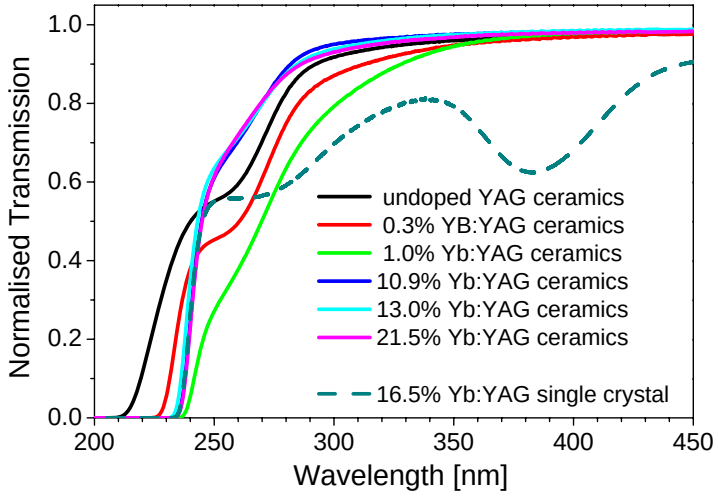

Figure 4.8.: Transmission spectra of the ceramic Yb:YAG samples and that of 16.5% single crystalline Yb:YAG (boule #SK)

Yb^{2+}-ion is not indisputable. While the absorption bands at 380 nm and 650 nm are attributed to the interconfigurational transitions of the Yb^{2+}-ion, in [Kre03] the band centred at 650 nm is associated to inter-valence charge transfer transitions between Yb^{2+}- and Yb^{3+}-ions[3]. However, conclusive evidence for this assignment has not been given up to now. In addition, the back transfer transition should be observed in this case as the final state of such a charge transfer is not necessarily stabilised by oxygen vacancy. It also has to be mentioned that the value of 2.3 eV and 2.5 eV estimated for the lowest interconfigurational transitions of the Yb^{2+}-ion in YAG in section 3.4.2 (see figure 3.5 and table 3.1) are in agreement with the 650 nm absorption band if a reasonable error of ± 0.5 eV is assumed in the estimation.

The transmission spectra of the ceramic Yb:YAG samples are depicted in figure 4.8. For comparison the transmission spectrum of the as-grown 16.5%Yb:YAG single crystal (boule #SK) is also plotted. All ceramic samples and in particular the samples of lower Yb-concentration and pure YAG display a broad absorption band centred at 255 nm. This band is not found in the single crystalline Yb:YAG samples grown from rhenium crucibles and is commonly attributed to a charge transfer transition from oxygen ligands to iron [Sco74, Che88, Rot89b]. Probably, the iron originates from the tools and moulds used in the fabrication process of the ceramics. However, the sharp absorption lines at 407 nm and 415 nm which are attributed to Fe^{3+}-ions are not observed, suggesting that iron impurities are present in the ceramics but their concentration is very low. The transmission edges for the Yb:YAG ceramics with Yb-concentrations of 1.0%, 10.9%, 13.0% and 21.5% are found at comparable wavelengths as the 16.5%Yb:YAG single crystal (see above). The 0.3%Yb:YAG ceramic sample has its edge at slightly shorter wavelength and as expected the undoped YAG sample has its edge at significantly shorter wavelength. However, also for the undoped YAG sample the absorption edge was found to be at lower energies than the expected band gap. This is probably due to absorption bands of defect centres, e.g. the iron charge transfer transition obscuring the fundamental absorption edge.

[3] An inter-valence charge transfer between Yb^{2+}- and Yb^{3+}-ions could be understood as a electron hopping mechanism as also discussed in section 6.3.2. The association with the absorption band centred at 650 nm would lead to an activation energy of about 1.9 eV.

Another possible absorption centre could involve silicon as SiO_2 is used as sintering aid in the fabrication process (see section 3.5.1). In Si:YAG an absorption band centring at 230 nm was found, which was attributed to singlet to singlet transitions in Si^{2+} [Fag04] (see also appendix F). F- and F^+-centres (oxygen vacancies with two and one electron(s), respectively) also have absorption bands centring between 230 nm and 240 nm [Spr91]. In the ceramics and the annealed Yb:YAG crystals oxygen vacancies are not expected. Nevertheless, even in the as-grown samples these centres could not be clearly identified from the transmission spectra. In the case of F^+-centres, this is due to the second absorption band centring around 370 nm, which is also associated to F^+-centres [Spr91], cannot be found as it is totally obscured by the Yb^{2+} interconfigurational transition which is centred at 380 nm. Similarly, the charge transfer transition between oxygen ligands and Yb-ion centred at around 210 nm obscures the second absorption band attributed to F-centres at 200 nm. However, the presence of large numbers of F^+-centres in as-grown Yb:YAG has been clearly confirmed by electron spin resonance microscopy (ESR) [Fag07].

It is concluded that both, the single crystalline and the ceramic Yb:YAG samples investigated in this work are of high optical quality. Iron was detected as an impurity in the ceramics, however its concentration is assumed to be negligible as also suggested by the fluorescence lifetime measurement results, which did not reveal any quenching to impurity centres. The Yb^{2+}-ions as well as F- and F^+-centres, which are present in the as-grown single crystalline samples, disappear upon annealing in air.

4.3. Emission Spectra

Figure 4.9 shows the emission cross-sections of Yb:YAG obtained from differently concentrated samples [Mix95, Fag07][4]. The emission cross-section at the principal lasing wavelength of 1030 nm varies between about $1.9\times10^{-20}\,cm^2$ obtained from the emission spectrum of the 7.0%Yb:YAG sample to $3.1\times10^{-20}\,cm^2$ for the YbAG sample. As mentioned also when discussing the absorption cross-sections, transition cross-sections should not be dependent on doping concentration. Most likely the deviations are due to different assignments of the Stark levels of the Yb^{3+}-ion in YAG (see also section 3.3.2) and also different radiative lifetimes (see above). In the literature, values between $1.6\times10^{-20}\,cm^2$ and $2.3\times10^{-20}\,cm^2$ can be found for the 1030 nm emission of Yb:YAG [Sum94]. Due to the difficulties in the Stark level assignment in Yb:YAG, the error for the emission cross-sections calculated by the reciprocity method was estimated to be about 20% [Mix99]. Still, despite considering that for the calculation of the emission cross-sections of the 2%Yb:YAG crystal a radiative lifetime of 1 040 µs was used, while a value of 950 µs was used for the 7%Yb:YAG crystal, the difference in the cross-sections for the two single crystals in figure 4.9 are puzzling. Because most of the cross-sections values found in the literature are close to that obtained with the 7%Yb:YAG single crystal, for the calculations in chapter 5 a value of $1.89\times10^{-20}\,cm^2$ is used. In accordance to the difference in the fluorescence lifetime, the significantly different value obtained for the YbAG crystal emission cross-section can be attributed to differences in the crystal field strength.

[4]For a detailed discussion on the determination of emission cross-sections by the combination of the reciprocity method [McC64] and the Füchtbauer-Ladenburg equation [Kru74] see [Krä08]

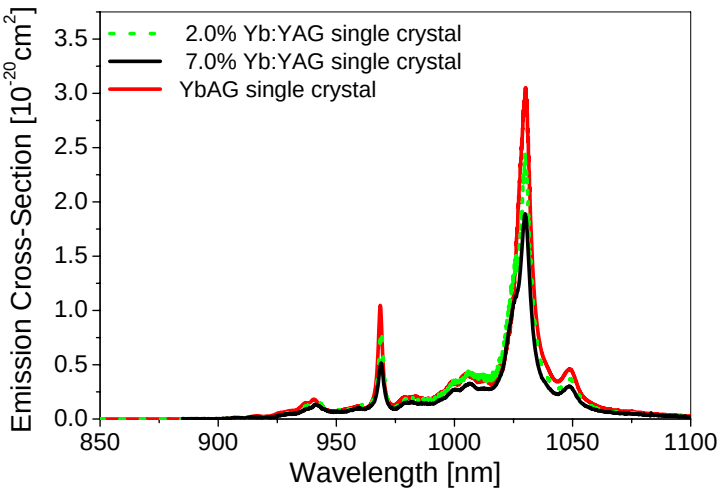

Figure 4.9.: Emission cross-sections of Yb:YAG obtained from emission spectra of Yb:YAG single crystals of different Yb-doping concentrations [Mix95, Fag07].

Emission measurements under Yb^{3+}-excitation were also performed for the visible spectral range to identify possible luminescent impurities to which Yb^{3+}-excitation energy is transferred. The obtained spectra are shown in figure 4.10. The existence of Er^{3+}- as well as Tm^{3+}-ions was proven in all the Yb:YAG samples investigated. These are impurities introduced through the raw materials. From the measurements on Yb:YAG and YbAG single crystals (figure 4.10, left) it could be deduced that the Tm^{3+}-impurities are found in the Y_2O_3 powder and the Er^{3+}-ions are introduced through the Yb_2O_3 raw material (see also [Fag07]). The broad emission band centring around 515 nm was tentatively attributed to cooperative emission of Yb^{3+}-pairs (see section 2.2.2, Cooperative Processes and appendix C).

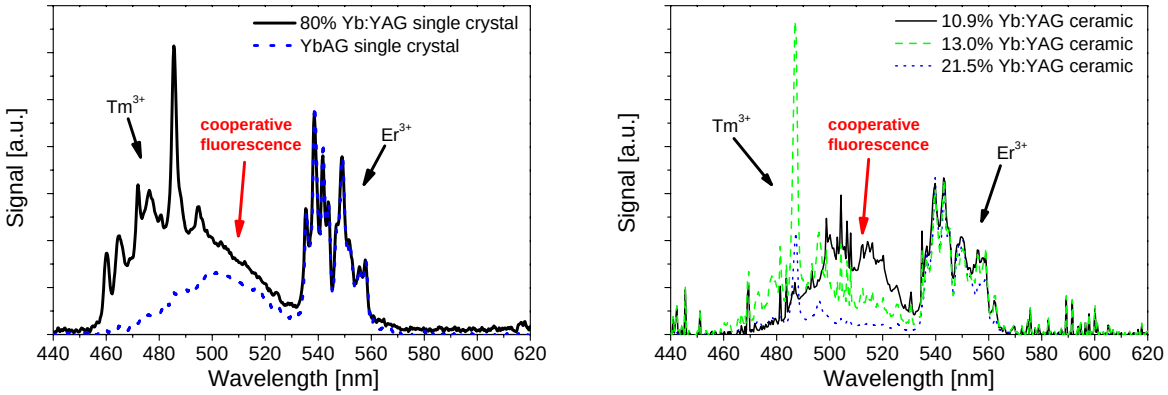

Figure 4.10.: Left: the luminescence spectra in the visible spectral range obtained for 80%Yb:YAG and YbAG single crystals. Right: the same for the Yb:YAG ceramic samples. The emission lines between 530 nm and 570 nm were identified to belong to Er^{3+}-ions and those found between 450 nm and 500 nm were attributed to Tm^{3+}-ions. The broad emission band centred at around 515 nm could be due to cooperative emission of two Yb^{3+}-ions.

4.4. Charge Transfer

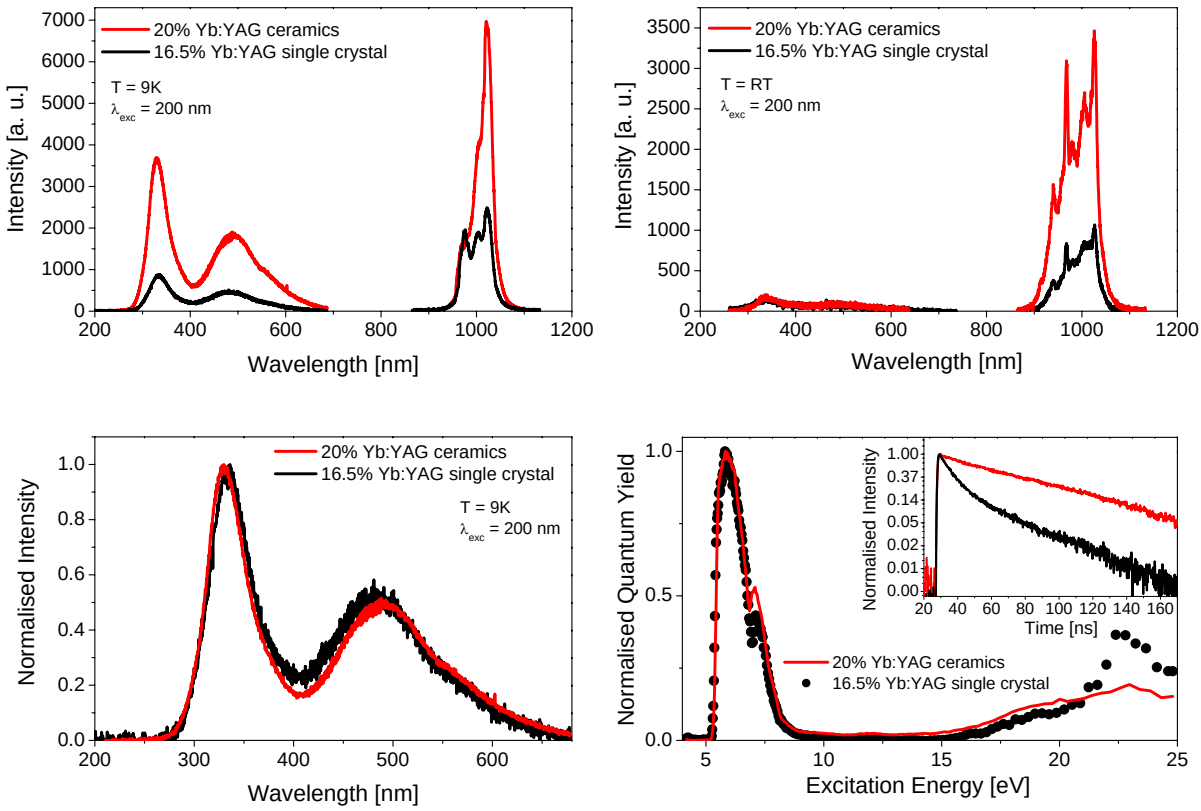

Figure 4.11.: CT and $4f$ luminescence of single crystalline 16.5% Yb:YAG and ceramic 20% Yb:YAG excited at 200 nm at 9K (above left) and room temperature (above right). For better comparison the normalised CT luminescence spectra are shown at the bottom left. The CT luminescence excitation spectra at 9K of both samples are shown together with the CT luminescence decay curves (inset) on the bottom right.

Charge transfer (CT) measurements were conducted at the SUPERLUMI test bench of the Doris positron storage ring, HASYLAB, DESY in Hamburg [Zim07]. Ceramics of different Yb-concentrations and single crystalline Yb:YAG grown from Re-crucibles with doping concentrations of 16.5% (boule #SNF) and 20% have been investigated regarding their CT properties and compared with each other. In addition, the fluorescence lifetime of the CT state of a 20%Yb:YAG crystal codoped with 0.2%Ce[5] was measured. The Ce-codoped sample was chosen because Ce is known as a fast recombination centre, often used for so-called radiation hardening in space applications [Dic01]. An influence of the Ce-codoping on the also observed photocurrent and a connection to the CT properties was assumed (see chapter 6 for details). The samples were placed inside an ultra high vacuum chamber ($\approx 10^{-10}$ mbar) and could be cooled down to 4K. The excitation was performed by synchrotron radiation with pulse durations of 130 ps with intervals of 200 ns and wavelengths between 30 to 334 nm (3.7 eV to about 40 eV). Since three different spectrometers are available, the test bench offers a wide detection range from 1 240 nm to 62 nm (1 eV to 20 eV).

[5]The concentration of Ce is given as found in the melt.

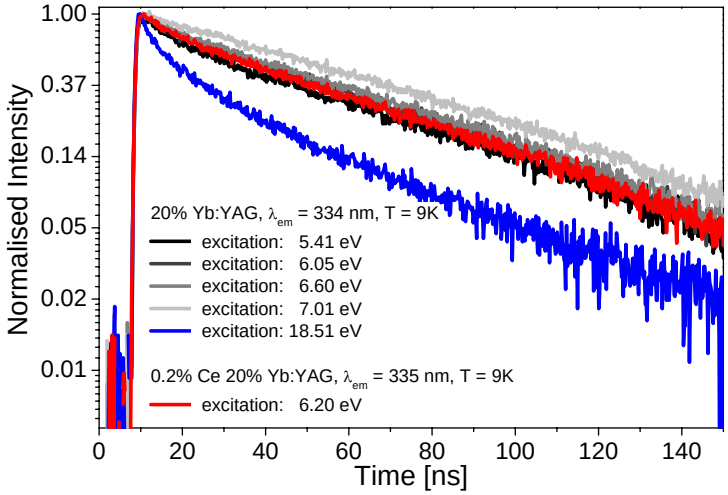

Figure 4.12.: Fluorescence lifetime of the CT state of a 20%Yb:YAG single crystal for different excitation energies and a 20%Yb:YAG single crystal codoped with 0.2% Ce, both measured at 9K.

Though an absolute comparison could not be made due to different sample dimensions, it was observed that ceramics demonstrate better scintillation properties than the single crystals. Figure 4.11 shows the luminescence spectra of single crystalline 16.5%Yb:YAG and ceramic 20%Yb:YAG excited with synchrotron radiation of 200 nm wavelength at 9K (top left) and room temperature (top right). The CT luminescence light yield of both materials is strongly reduced at room temperature, which is in agreement with previous results on Yb:YAG CT measurements (see section 3.6.1). For better comparison the CT luminescence spectra of the 16.5%Yb:YAG single crystal and the 20%Yb:YAG ceramic sample are normalised and plotted together in figure 4.11 bottom left. The shape of the two broad emission bands as well as the position are the same for both samples. Nevertheless, it seems that the 20%Yb:YAG ceramic sample displays higher light yields and less quenching. This can clearly be seen in the inset of figure 4.11 bottom right, where the CT luminescence decay curves of the single crystal and the ceramic for 310 nm excitation are plotted together in logarithmic scale. The decay profile of the 16.5%Yb:YAG single crystal shows a strongly non-single exponential decay characteristic with an initial rapid part whereas the 20%Yb:YAG ceramic hardly shows any deviation from single exponential decay behaviour. The fluorescence lifetime of the ceramic sample was about 53 ns, whereas the lower doped single crystal quenched to about 33 ns. From this result it seems that Yb:YAG ceramics show negligible concentration quenching of the CT luminescence compared to the single crystalline counterparts. The reason for this difference in characteristic is not known at present and is subject of current research. A first attempt to investigate on the impurity distribution in those two samples did not reveal any substantial difference, which could account for the observed behaviour.

The CT luminescence properties of the 20%Yb:YAG single crystal codoped with 0.2% Ce did not show any peculiarities compared to the corresponding sample without codoping. The fluorescence lifetime of the CT state was measured at 9K as shown in figure 4.12. The lifetime of the CT state in 20%Yb:YAG was measured for different excitation energies, however no clear trend could be found for a possible excitation energy dependence in the range of 5.41 eV

to 7.01 eV. The lifetimes indeed seem to increase from about 52 ns to 58 ns, but these differences are of the same magnitude as the measurement errors. The decay profile of the CT states under interband excitation with 18.51 eV is noticeably different to those under direct excitation into the CT states. The profile is clearly non-single exponential and the lifetime is 41 ns, about 25% shorter than for the direct excitation. This indicates that an additional source of quenching occurs when exciting with X-rays [Gue02]. The fluorescence lifetime of the CT states in the Ce-codoped sample was also measured at 9K for excitation with 6.20 eV photons directly into the CT states. The decay characteristics as well as the fluorescence lifetime of about 53 ns cannot be distinguished from that of the 20%Yb:YAG without codoping. The codoping of 0.2% Ce seems to have no influence on the CTL properties of Yb:YAG. Currently, the scintillating properties of Yb:YAG ceramics [Kam09] as well as Yb:YAG single crystals with various codopants (e.g. Si and Ca) are under extensive investigation.

τ_{flu} [µs]	σ_{abs} at 941 nm [10^{-21} cm^2]	σ_{em} at 1030 nm [10^{-21} cm^2]	$E_{CT,abs}$ [eV]	FWHM$_{CT,abs}$ [eV]	E_{CTL} [eV]	FWHM$_{CTL}$ [eV]
950	8.2	18.9	5.8	∼1.3	3.8, 2.5	∼0.6, ∼1.8

Table 4.2.: Summary of the spectroscopic data of Yb:YAG. The laser relevant parameters were used in the calculations used in chapter 5.

4.5. Concluding Remarks

In conclusion no significant spectroscopical differences between ceramics and single crystals were found and it can be said that both materials are of the same quality.

The presence of Yb^{2+}-ions stabilised by oxygen vacancies lead to significant quenching in the as-grown Yb:YAG single crystals grown under reducing atmosphere. However, these quenching centres disappear upon annealing in air at 1 000°C for several hours. Despite traces of iron were found in the Yb:YAG ceramic samples, no influence on the fluorescence lifetimes could be observed, so that the contribution of iron as a quenching centre is considered negligible. In both, ceramic and annealed single crystalline Yb:YAG samples no excitation energy dependence of the fluorescence lifetimes was found. Together with the single exponential behaviour of the decay curves this finding suggests that no cooperative energy transfer processes exist in the samples investigated. The intrinsic fluorescence lifetimes of all samples were determined by the pinhole method. Regardless of the single crystalline and ceramic nature of the Yb:YAG samples, an intrinsic lifetime of about 950 nm was obtained for Yb-concentrations up to 22%. This value is considered equal to the radiative lifetime and thus a quantum efficiency of 1 is suggested. Other impurities found were Er^{3+}- and Tm^{3+}-ions introduced through the 6N Yb_2O_3 and Y_2O_3 raw materials. These impurities are only found in emission measurements under Yb^{3+}-excitation. No absorption bands associated to these ions could be found in the transmission spectra, confirming the very low concentrations. The contribution of these ions as

quenching centres is also considered negligible. In the visible spectral range, also a broad emission band centring at about 515 nm was found which was attributed to cooperative emission of Yb^{3+}-pairs.

The investigations on the CT properties of the Yb:YAG single crystalline and ceramic samples indicated that the ceramic samples display higher light yields and concentration quenching behaviour compared to their single crystalline counterparts.

It also has to be mentioned that excited state absorption measurements were performed. In these experiments the Yb^{3+}-ion was excited at 940 nm and the transmission spectrum in a wavelength range from 400 nm to 1 100 nm was recorded. The measurement technique was similar to that described in [Sou03]. However, no absorption bands other than those attributed to Yb^{3+} intraconfigurational $4f$ transitions could be observed. In spectroscopic measurements under high intensity pumping melting of the samples accompanied with very intensive broad band emission (black body radiation) was observed. This suggests that despite no peculiarities were found in the fluorescence lifetime measurements, processes are existent in Yb:YAG, which lead to significant heat generation at high intensity pumping, eventually resulting in the melting of the samples. The melting point of YAG is stated to be 1 940°C [Cas80]. This temperature cannot be reached by the quantum defect as the only source for heat generation. For details on the experiments see [Bis07a] and [Hir07].

5. Thin-Disk Laser Experiments

Owing to the simple energy level structure of the trivalent Yb-ion with only two $4f$-manifolds (see section 3.3.2), quenching processes such as cross-relaxation and upconversion should not be observed in Yb^{3+}-doped materials. Therefore, these materials are favourably used in thin-disk lasers where high doping levels are needed so that sufficient absorption is achieved, and high inversion densities are required to reach laser threshold. However, Yb:YAG thin-disk lasers suffer from decay processes, which are known to be dependent on doping concentration, inversion level and temperature, resulting in significant heat generation. Thus, at present, efficient thin-disk laser operation is limited to Yb:YAG crystals with doping concentrations of 10% ($1.38{\cdot}10^{21}\,\mathrm{cm}^{-3}$) and lower [Lar05] (see also section 3.6.2).

In this chapter, the results from thin-disk laser experiments are presented and discussed. Both, single crystalline and ceramic Yb:YAG of different doping concentrations are used as active media. First, a brief description of the pump source used is given. Next, the laser results for the different Yb:YAG samples are presented, focussing on laser efficiency and the estimation of internal losses. In the following section, with particular emphasis on inversion dependent phenomena, peculiarities observed in the laser performance are pointed out and discussed. The final section summarises the thin-disk laser results and attempts an over all evaluation for highly Yb-doped YAG single crystals and ceramics as gain media.

5.1. The Pump Source

The pump source used was a fiber coupled InGaAs laser diode with a NA of 0.22 and a fiber diameter of 600 µm (JOLD-75-CPXF-2P, JENOPTIK Laserdiode GmbH, Germany). The nominal maximum output power of this laser diode is 75 W with a centre wavelength of 938 nm and a full width half maximum of 5 nm at 25°C heat sink temperature. Two thermoelectric coolers (TEC) on the diode bars allow a variation of the centre wavelength between 930 nm and 945 nm with a typical dependence of 0.3 nm/°C. However, the available temperature controllers had a maximum power of 70 W, and so could not provide the specified maximum cooling power of 346 W to stabilise the wavelength of the laser diode at high output powers. For this reason, 45 W was chosen as the maximum pump power for the thin-disk laser experiments. The laser diode operating temperature suggested by the manufacturer ranges between 15°C and 30°C. In this temperature range, the optimum pump wavelength of 941 nm for Yb:YAG could not be reached for lower output powers and therefore a much higher operating temperature of 40°C was chosen in the experiments after consulting the manufacturer. At this temperature, the centre wavelength changed from 937.6 nm to 941.5 nm between operation currents of 7 A and 38.5 A. It was also observed that the emission profiles of the two diode bars did not necessarily always

perfectly overlap. This is probably due to the fact that the TECs and the respective temperature sensors are placed at different location on each of the diode bars, and that the sensors could not be placed sufficiently close to the emitters. However, this change in pumping wavelength is not of relevance for Yb:YAG in a thin-disk laser setup since the absorption lines are sufficiently broad in this spectral region and multiple pump passes through the active medium allow for high enough absorption. The input-output characteristic as well as some emission profiles for operating currents between 7 A and 38.5 A at 40°C operating temperature of this pump source can be found in appendix D. The emission profile at an intermediate operating current of 20 A, which corresponds to an output power of 20 W is shown together with its Gaussian fit on the left side of figure 5.1.

5.2. Sample Preparation

Yb:YAG single crystalline laser samples of different doping concentrations and from different sources were examined in the thin-disk laser experiments. The crystals grown in the framework of this research at the ILP (#SK and #SNF) had an Yb-doping concentration of 16.5%[1]. This concentration is somewhat higher than the doping concentration of 15.7% for which Larionov *et al.* could not achieve cw laser operation in their Yb:YAG thin-disk laser [Lar05] (see also section 3.6.2). In the same experiments it was found that efficient Yb:YAG thin-disk laser operation, especially for pulsed operation is limited to crystals with doping concentrations of 10% and lower. In this work, the Yb-doping concentration of 16.5% for the single crystalline gain material was chosen to extensively investigate the limiting effects of doping concentration and to see if high purity, highly doped Yb:YAG crystals grown from powder-metallurgical rhenium crucibles suffer from the same problems as commercial samples. The other Yb:YAG single crystal examined was a 10%Yb:YAG commercial sample from Scientific Materials Corporation, USA (#L754), which served as the reference material as 10% Yb-doping concentration is a standard for high power Yb:YAG thin-disk lasers. The ceramic Yb:YAG samples investigated were provided by Konoshima Chemical Co. Ltd., Japan and had Yb-doping concentrations of 10.9%, 13%, 15%[2] and 21.5%. The ceramic laser materials were investigated to determine whether ceramics suffer the same problems as single crystals or display different behaviour. For the fabrication techniques of the laser materials see section 3.5.1. Fluorescence lifetime measurements confirm high purity for all of the laser samples and a quantum efficiency of 1 is strongly suggested (see also section 4.1).

The thin-disk laser samples were polished[3] to thicknesses between 100 µm and 180 µm according to their Yb-doping concentrations to ensure more than 90% of pump light absorption in the thin-disk laser setup. For this, the dependence of absorption efficiency η_{abs} on the thickness z was examined for each concentration used in Yb:YAG. The absorption efficiency was

[1] All concentrations are given with respect to the Y-sites.

[2] The doping concentration of the 15%Yb:YAG ceramics is the nominal concentration stated by the producer, whereas the concentrations of all other ceramics were determined by microprobe measurements (see section 3.5.2).

[3] Polishing was performed by Forschungsinstitut für mineralische und metallische Werkstoffe - Edelsteine/Edelmetalle- GmbH (FEE), Germany

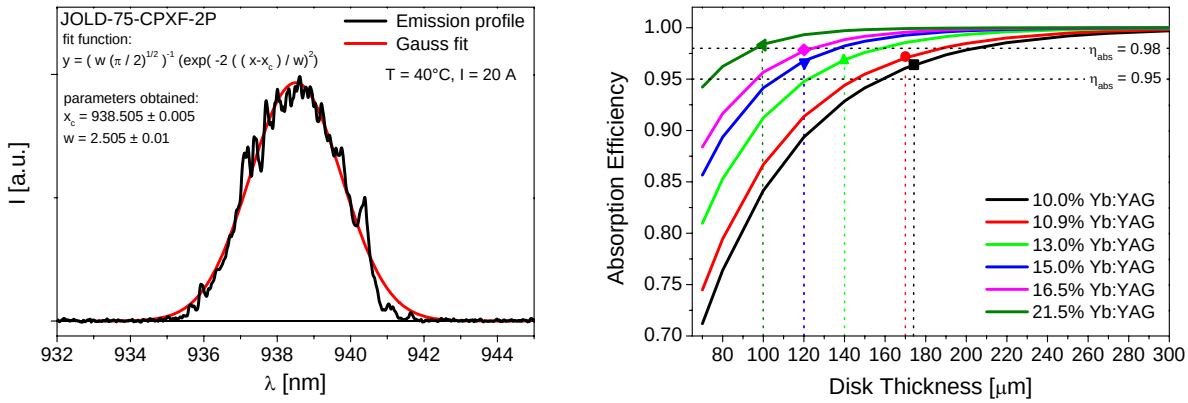

Figure 5.1.: Left: Emission profile of the laser diode used (JOLD-75-CPXF-2P) at an operating current of $I = 20A$ ($P_{out} = 20$ W). The operating temperature was stabilised at 40°C. Right: Yb:YAG absorption efficiency according to equation 2.89 for the emission profile depicted at the left for all Yb-doping concentrations investigated ($M_p = 24$, $L_{int} = 0.1\%$, $T_{OC} = 3\%$)

calculated with equation 2.89, with $M_p = 24$ for the number of pump passes, using expression 2.87 for the bleaching factor f_B, the respective total Yb-doping concentration N_t and the threshold upper level population $N_{2,th}$ calculated from expression 2.93 for typical internal losses $L_{int} = 0.1\%$ and typical optimum outcoupling rate $T_{OC} = 3\%$ for Yb:YAG. Furthermore, as the pump light is not a delta function but has a finite width, an effective pump absorption cross-section σ_{abs}^{pump} has to be determined, which is the convolution product of the line shape of the Yb:YAG absorption cross-section and the laser diode emission profile. The emission profile of the laser diode used at an operation current of 20 A yielding an output power of about 20 W is depicted together with the respective Gaussian fit in figure 5.1, left. Figure 5.1, right shows the dependence of the Yb:YAG absorption efficiency η_{abs} on the sample thickness for all Yb-concentrations investigated at the intermediate pump power of 20 W. The vertical lines represent the thicknesses actually chosen for the thin-disk laser samples. These thicknesses ensured an absorption efficiency of at least 90% for all outcoupling rates and pump powers used in the experiments. However, it has to be noted that the equations used for calculation are based on the zero-dimensional model (see also section 2.3.2), which does not account for temperature broadening of the Yb:YAG absorption spectrum.

The high reflection coating for the pump and laser wavelengths on the back as well as the anti reflection coating on the front of the laser samples were applied at JENOPTIK Laser, Optik, Systeme GmbH, Germany by the advanced plasma sputtering (APS) technique. For the high reflection coating a design was applied, which has a total thickness of 5.7 µm and consists of 15 sequences of alternating layers of Ta_2O_3 (high reflection at 1 030 nm) and SiO_2 (low reflection at 1 030 nm), a copper metallisation of 150 nm thickness, an Al_2O_3 (90 nm) and nickel (300 nm) diffusion barrier and a gold layer of 300 nm thickness, which provides the wettability needed for the soldering of the laser sample onto a heat sink. The heat resistance of this coating is estimated to be about 6 Kmm^2/W [Lar08]. For further details on the applied coatings refer to [Lar08, Krä08].

In addition to the laser samples addressed above, four samples of thicknesses between 80 µm and 400 µm were prepared from the boules #SK and #SNF to assess the differences in laser

performance at different inversion densities for the same outcoupling transmission rate. As-grown samples were also included to investigate the influence of Yb^{2+}-ions that may be present. However, due to their low fluorescence lifetimes which suggest quantum efficiencies much lower than 1 (see section 4.1), laser operation is expected to be impossible.

All laser samples except for the reference 10%Yb:YAG single crystal were soldered onto copper heat sinks at the ILP. An In50Sn50 alloy was used for the solder. For a detailed description of the applied soldering technique refer to [Krä08]. The reference crystal was soldered onto a copper tungsten heat sink at the Technologiegesellschaft für Strahlwerkzeuge GmbH (TGSW), Germany.

5.3. Thin-Disk Laser Results

The experimental setup used was based on a commercial thin-disk laser module allowing for 24 pump passes through the active medium (TGSW Stuttgart, Germany). The laser samples were soldered onto a water-cooled copper heat sink. A water temperature of 17°C was chosen for the experiments unless stated otherwise. The laser experiments were performed using a plano-concave resonator, which was built by the highly reflective coating on the backside of the gain medium and an outcoupling mirror with a radius of curvature of $R_{OC} = 100\,\text{mm}$, (see also figure 2.9). Outcoupling mirrors with transmission rates between 0.4% and 26% on the lasing wavelength were used[4]. The resonator length was adjusted for maximum output in each experiment but was mostly between $L_R = 7\,\text{mm}$ and 8 mm. In such an almost hemispherical resonator, the TEM_{00} fundamental mode has a beam waist diameter of about 200 µm. The incoupling unit achieved a 1:2 image of the fiber end surface on the active medium resulting in a pump spot diameter of 1.2 mm. This configuration led to multimode operation with reduced beam quality but ensured stable laser operation at high efficiencies and thus highly reproducible results. Unless stated otherwise, a LM-45 HTD sensor together with a powermeter of the FieldMaster-GS Series (Coherent, Inc., USA) was used for the laser power measurements. Since in such a setup the pump power actually absorbed is not directly accessible, the efficiencies stated in the following are given with respect to the incident pump power.

5.3.1. Single Crystalline Yb:YAG

On the left side of figure 5.2 the input-output characteristics of the 10%Yb:YAG reference single crystal for all outcoupling transmission rates investigated are presented. The highest efficiencies were obtained for outcoupling transmission rates between $T_{OC} = 2.2\%$ and $T_{OC} = 3.3\,\%$. For the outcoupling mirror with $T_{OC} = 2.2\%$, the highest output power of 28.2 W at a pump power of 44.6 W was achieved resulting in a maximum optical-to-optical efficiency of $\eta_{opt} = 63\%$. The highest slope efficiency of $\eta_s = 72.8\%$ was obtained with an outcoupling transmission

[4]The transmission rate of the outcoupling mirrors with the lower outcoupling rates (up to $T_{OC} = 3.3\%$) were constant in a spectral range between 1000 nm and 1080 nm. The typical lasing wavelengths of Yb:YAG is 1030 nm.

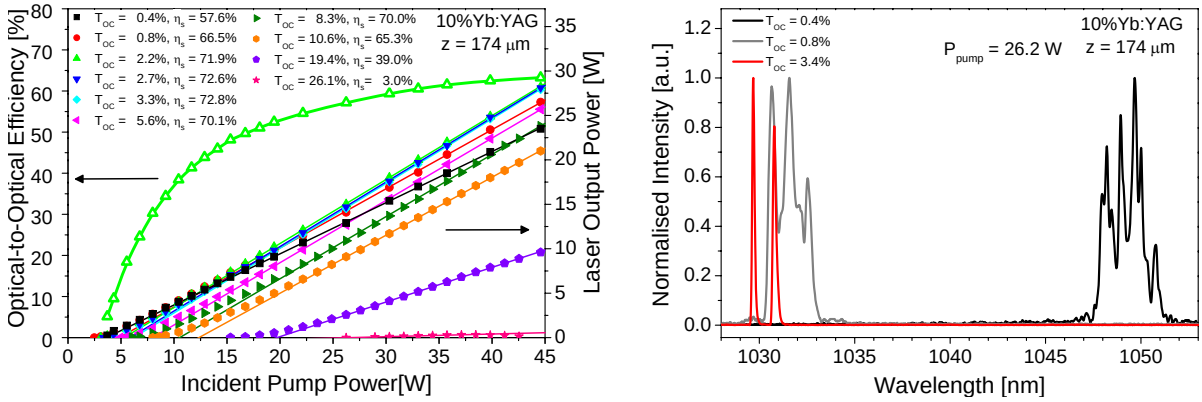

Figure 5.2.: Left: Laser output power plotted against the incident pump power for all outcoupling transmission rates investigated for the 10%Yb:YAG reference single crystal (thickness $z = 174\,\mu m$). For the outcoupling transmission rate of $T_{OC} = 2.2\%$ the optical-to-optical efficiency is also plotted (open triangles). Right: Laser emission spectrum for three different outcoupling transmission rates at a pump power of 26.2 W. For all other transmission rates the emission spectra were identical to that of $T_{OC} = 3.3\%$.

rate of $T_{OC} = 3.3\%$. The high and almost constant slope efficiencies for outcoupling transmissions between $T_{OC} = 2.2\%$ and $T_{OC} = 3.3\,\%$ suggest very low internal losses that are much lower than these outcoupling transmission rates. Usually, internal losses are determined by the Findlay-Clay method, originally developed for four-level-laser systems [Fin66]. This method can also be applied to three-level and quasi-three-level systems, however accurate knowledge of the threshold pump powers for each outcoupling mirror used is needed, a parameter which is not always simple to determine. In the case of ground state lasers, the emission and absorption spectra are particularly sensitive to heating as is the gain spectrum. This might result in very different conditions for the laser operating near threshold and operating in the high power regime. For the 10%Yb:YAG reference single crystal, by applying the Findlay-Clay method and using the measured threshold pump powers, single pass internal losses of $L_{int} = 2\%$ were obtained which clearly contradict the high laser efficiencies at the outcoupling rate of $T_{OC} = 2.2\%$. Another well established method for the determination of internal losses is a technique developed by Caird *et al.* [Cai88]. This method however, is based on the assumption that the slope efficiency should linearly increase with the outcoupling mirror's transmission rate, which is only valid for true four-level laser systems. Still, even though the Caird method cannot be applied for quasi-three-level lasers, an upper limit for the internal losses L_{int} can be roughly estimated from the examination of the slope efficiency obtained for the mirror with the lowest outcoupling transmission rate using expression 2.100. Here, it is assumed that the total resonator losses T_{tot} are equal to the outcoupling transmission rate T_{OC} and that the absorption efficiency $\eta_{abs} = 1$, an assumption which can be made for an upper estimate of the internal losses. It has to be noted that any imperfections such as scattering losses at the outcoupling mirror and the high reflection coating on the backside of the sample are not separately considered and will be included in the internal losses. This gives $L_{int} = 0.1\%$ as an upper estimate, which is a typical value for internal losses in efficient thin-disk lasers [Lar08]. Similar estimates and considerations were made in [Krä08] for Yb-doped borates and vanadates, arriving at the same conclusion that the Findlay-Clay method does not accurately model observed characteristics. However, the slope efficiency obtained with a mirror of adequate transmission rate can give useful estimates of

internal losses. In the investigated power regime, no so called roll-over[5] was observed except for the mirror with an outcoupling transmission rate of $T_{OC} = 26.1\%$, for which laser operation was limited to pump powers below 42 W. These observations at high inversion densities will be discussed in detail in section 5.4.1. On the right side of figure 5.2 the normalised laser emission spectra for three different outcoupling mirrors are shown. The spectra were recorded with an Equinox 55 FTIR/FTNIR spectrometer (Bruker Optik GmbH, Germany). The laser emission spectra of all other outcoupling mirrors closely resembled that of the mirror with $T_{OC} = 3.3\%$. As expected, the laser operates at longer wavelengths for $T_{OC} = 0.4\%$, due to a reabsorption reduced net gain for the short wavelength region at low excitation levels (see also section 2.3.1). The laser emission wavelength changes according to the inversion dependent gain profile, resulting in laser emission at the wavelength of highest emission cross-section around 1030 nm for all other outcoupling rates. Regardless of the mirror used, it is evident that more than one longitudinal laser mode was oscillating. Furthermore, an almost equidistant modulation[6] imposed on the laser emission spectrum is found, which is possibly due to an etalon effect with the crystal itself despite its anti reflection coating acting as a filter. However, the actual crystal thickness of $z = 174\,\mu m$ could not be obtained from the free spectral bandwidth of about $\Delta E = 10.4\,cm^{-1}$ found in these spectra. Possible sources of errors are temperature dependent changes in the refractive index of Yb:YAG, thermal expansion of the material as well as non-perfect parallelism of the disk. All investigated Yb:YAG thin-disk lasers exhibited comparable emission spectra regardless of their Yb-doping concentration, thicknesses, and regardless of being of single crystalline or ceramic in nature.

Even though thin-disk laser operation could not be realised with Yb:YAG single crystals of 15.7% Yb-concentration in [Lar05] (see also section 3.6.2), thin-disk laser operation could be achieved with 16.5%Yb:YAG laser samples prepared from boules #SK and #SNF grown at the ILP. This confirms that Yb-doping concentration itself is not the limiting factor for laser operation in this concentration regime, but other parameters, e.g. purity are decisive. From the boules #SK and #SNF samples of four different thicknesses were prepared. The input-output characteristics for the 16.5%Yb:YAG single crystal of thickness $z = 120\,\mu m$, prepared from the boule #SNF are shown on the left side of figure 5.3. In contrast to the 10%Yb:YAG reference crystal, laser operation could not be achieved using the outcoupling mirror with $T_{OC} = 26.1\%$. The highest output power was again realised for $T_{OC} = 2.2\%$, yielding a maximum output power of 24.2 W at a pump power of 44.6 W and an optical-to-optical efficiency of $\eta_{opt} = 54.3\%$. The highest slope efficiency of $\eta_s = 63.4\%$ was also obtained with the same mirror. The single pass internal losses were estimated from the slope efficiency obtained with the lowest outcoupling rate to be $L_{int} = 0.1\%$. This value is the same as that found for the reference crystal and confirms a very high quality comparable to commercial samples for the 16.5%Yb:YAG single crystal #SNF. However, the laser efficiency of the 16.5%Yb:YAG is much lower compared to that of the 10%Yb:YAG reference crystal for all outcoupling mirrors investigated. For the mirrors with $T_{OC} = 8.3\%$ and $T_{OC} = 10.6\%$ a strong roll-over is observed starting at pump powers of about 34.0 W and 19.4 W respectively, which eventually lead to the termination of the laser at higher pump powers. These deviations in laser performance between the two laser

[5] As a roll-over, one understands a significant power reduction at high pump powers usually ascribed to heating effects, for which reason it is also often referred to as thermal roll-over.

[6] The modulation is only equidistant for the respective frequencies.

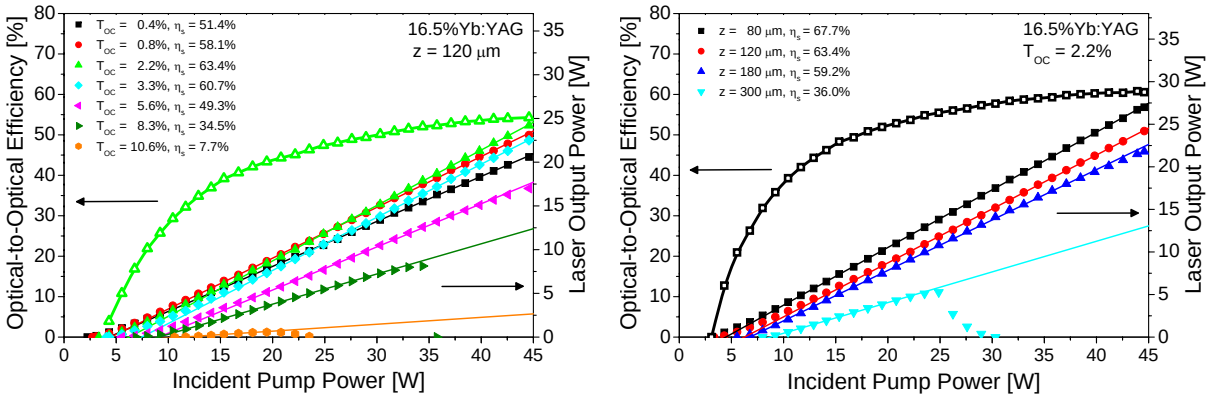

Figure 5.3.: Left: Laser output power plotted against the incident pump power for all outcoupling transmission rates investigated for the 16.5%Yb:YAG single crystal (boule #SNF, thickness $z = 120\,\mu m$). For the outcoupling transmission rate of $T_{OC} = 2.2\%$ the optical-to-optical efficiency is also plotted (open triangles). Right: 16.5%Yb:YAG input-output characteristics for three different thicknesses at an outcoupling transmission rate of $T_{OC} = 2.2\%$. For the sample of thickness 80 µm also the optical-to-optical efficiency is plotted (open squares). See text for discussion.

crystals despite their comparable internal losses, strongly substantiate the presence of laser loss channels connected to the Yb^{3+}-doping concentration and the actual inversion density during laser operation (see also section 3.6.2). On the right side of figure 5.3, the input-output characteristics of four 16.5%Yb:YAG crystals (boules #SK and #SNF) of different thicknesses are plotted for $T_{OC} = 2.2\%$. For all four samples the highest efficiencies were realised with this outcoupling transmission rate. The highest output power ($P_{out} = 27.0\,W$ at $P_{in} = 44.6\,W$) as well as the highest efficiencies ($\eta_S = 67.7\%$, $\eta_{opt} = 60.6\%$) were obtained with the thinnest sample of thickness $z = 80\,\mu m$. The optical-to-optical efficiency for this laser sample is also plotted in the same figure. The upper limit for the single pass internal losses were estimated as described above to be about $L_{int} = 0.1\%$ for the laser samples of thickness $z = 80\,\mu m$ and $z = 120\,\mu m$ (both #SNF), $L_{int} = 0.2\%$ for $z = 180\,\mu m$ (#SNF) and $L_{int} = 0.3\%$ for $z = 300\,\mu m$ (#SK). Assuming active medium independent resonator losses of 0.1% due to scattering at the outcoupling mirror as well as the coatings on the front and back side of the laser sample, a rough upper limit for the crystal internal losses of between $2\%cm^{-1}$ and $4\%cm^{-1}$ can be found for the crystals prepared from the boule #SNF. The sample with $z = 300\,\mu m$ shows a considerable decrease in output power at about $P_{in} = 25\,W$, resulting in the termination of the laser. The poor laser performance of this sample is most likely not due to the increased thickness but may be ascribed to the lower quality of the boule #SK (see section 3.5.1). The maximum obtainable efficiency and output power seem to decrease with increasing thickness, which suggests that the lower absorption efficiency is not necessarily a disadvantage but the higher cooling efficiency for the thinner samples is decisive. However, thin-disk laser experiments on Yb-doped borates with much lower thermal conductivity than YAG showed an increasing laser efficiency with thickness for otherwise identically specified samples [Krä08], which suggests that higher cooling efficiencies due to decreased thicknesses should not be of too much significance, especially in the power regime investigated. Furthermore, laser samples prepared from the same crystal boule should require higher threshold incident pump powers at the same outcoupling mirror the thinner they are, because of their reduced gain, which was not observed in these experiments.

On the contrary, the lowest threshold was observed for the thinnest sample. For this reason it is concluded that these experimental results do not allow deductions regarding a connection between laser efficiency and laser sample thickness but rather represent the laser quality of the individual sample.

As-grown 16.5%Yb:YAG thin-disk laser samples of thicknesses $z = 120\,\mu m$ and $z = 150\,\mu m$ were also prepared to see the influence of oxygen vacancy stabilised Yb^{2+}-ions on the laser. As expected from the very low fluorescence lifetimes, laser operation could not be achieved for both samples.

5.3.2. Ceramic Yb:YAG

Thin-disk laser operation could be achieved with all ceramic samples available regardless of their Yb-concentration. The input-output characteristics for the 10.9%Yb:YAG ceramic sample are plotted on the left of figure 5.4. The sample had a thickness of $z = 170\,\mu m$. A maximum output power of 22.8 W was obtained with an outcoupling transmission rate of $T_{OC} = 2.2\%$ for a pump power of 44.6 W, resulting in an optical-to-optical efficiency of $\eta_{opt} = 51.1\%$. Thickness and doping concentration of this ceramics are very similar to that of the reference laser sample so that a solid basis is given for comparison. As for the reference crystal, the highest output power was obtained for $T_{OC} = 2.2\%$ and the highest slope efficiency was found for $T_{OC} = 3.3\%$. However, for all transmission rates except for $T_{OC} = 26.1\%$ a much lower laser efficiency was found, suggesting much higher resonator internal losses for this laser sample. An upper limit for the single pass resonator internal losses of $L_{int} = 0.3\%$ was estimated for the 10.9%Yb:YAG ceramic thin-disk laser. At outcoupling transmission rates as high as $T_{OC} = 26.1\%$ internal losses of this scale should not have any significance. However, the higher slope efficiency for the ceramic sample using this mirror cannot be explained with the current understanding of loss mechanisms.

On the right side of figure 5.4 the input-output characteristics for the 13%Yb:YAG ceramics thin-disk laser are plotted. For this sample (thickness $z = 140\,\mu m$), a maximum output power of 22.0 W at 44.6 W of pump power was obtained with an outcoupling transmission rate of $T_{OC} = 3.3\%$ resulting in an optical-to-optical efficiency of $\eta_{opt} = 49.3\%$. For $T_{OC} = 26.1\%$ no laser operation could be realised. The upper limit for the single pass resonator losses was estimated to be about $L_{int} = 0.3\%$. It is particularly noticeable that the output power for $T_{OC} = 0.4\%$ starts decreasing at a pump power of about 30 W. A tendency pointing towards a similar behaviour was also observed for the 10.9%Yb:YAG ceramic sample. A change of the lasing mode could not be confirmed from the laser emission spectra taken at low and high pump powers. The reason for this behaviour cannot be explained with the current understanding of loss mechanisms, but it is strongly assumed that the relatively high resonator losses play a significant role.

From the 15%Yb:YAG ceramics, two laser samples of different thicknesses were prepared. Figure 5.5 shows the input-output characteristics of the 15%Yb:YAG ceramic thin-disk laser for a thickness of $z = 120\,\mu m$ (left) and $z = 100\,\mu m$ (right). With the sample thicknesses investigated, laser operation could not be achieved for $T_{OC} = 26.1\%$ for the 15%Yb:YAG ceramic in the thin-disk laser setup. For both thicknesses the highest output powers and laser efficiencies were obtained with $T_{OC} = 2.2\%$. A maximum of 25.9 W output power was obtained for the laser

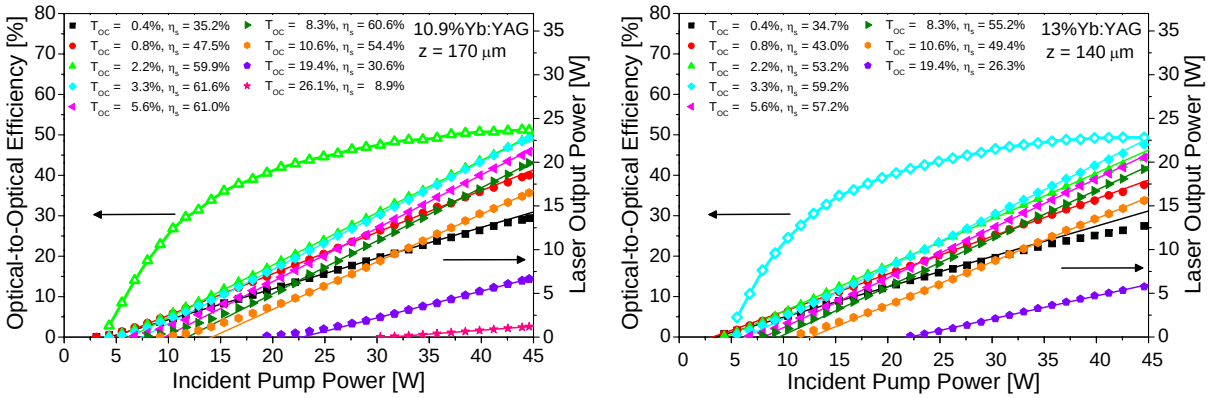

Figure 5.4.: Left: Laser output power plotted against the incident pump power for all outcoupling transmission rates investigated for the 10.9%Yb:YAG ceramic sample (thickness $z = 170\,\mu m$). For the outcoupling transmission rate of $T_{OC} = 2.2\%$ the optical-to-optical efficiency is also plotted (open triangles). Right: The same for the 13%Yb:YAG ceramic sample (thickness $z = 140\,\mu m$). For this sample the highest efficiencies were obtained for $T_{OC} = 3.3\%$ (open diamonds).

sample with $z = 120\,\mu m$ and 23.5 W for the sample with $z = 100\,\mu m$ thickness at a pump power of 44.6 W, resulting in optical-to-optical efficiencies of $\eta_{opt} = 58.1\%$ and $\eta_{opt} = 52.7\%$, respectively. Overall, a slightly lower laser efficiency was obtained for the laser sample of $z = 100\,\mu m$ thickness compared to that with $z = 120\,\mu m$. Also, with the thinner sample laser operation could not be achieved for $T = 19.4\%$. Both these observations are as expected and can, in first instance, be explained by the lower absorption efficiency of the thinner sample (see also section 5.4.1). The Yb-doping concentration and the thickness of $z = 120\,\mu m$ are comparable to those of the 16.5%Yb:YAG single crystal laser sample (see figure 5.3, left). However, compared to this single crystal, a much higher efficiency was achieved with the 15%Yb:YAG ceramic sample for every outcoupling mirror investigated. Most notably, for the ceramic sample laser operation could be realised with $T_{OC} = 19.4\%$, whereas this was not possible for the single crystal. For $T_{OC} = 8.3\%$ and $T_{OC} = 10.6\%$, prominent roll-overs resulting in the termination of the laser were observed for the 16.5% single crystal, which were not found for the 15%Yb:YAG ceramic thin-disk laser. For $T_{OC} = 19.4\%$, a slight tendency towards a roll-over can be detected. It is also noted that in contrast to the 16.5%Yb:YAG single crystal, higher efficiencies as well as lower threshold pump powers were found for the thicker 15%Yb:YAG ceramic sample (see above). The upper limit for the single pass resonator losses was estimated to be about $L_{int} = 0.09\%$ for the 15%Yb:YAG ceramic sample with $z = 120\,\mu m$ and $L_{int} = 0.1\%$ for the sample with thickness $z = 100\,\mu m$. However, the prominent differences in laser performance for the ceramic and the single crystal cannot be explained solely by the difference in the internal losses, especially as internal losses in the sub-percent range should not have any significant effect on the laser performance when using outcoupling transmission rates as high as 10%.

The input-output characteristics for the 21.5%Yb:YAG ceramic sample is shown on the left side of figure 5.6. The thickness of the sample was $z = 100\,\mu m$. With this sample laser operation could be achieved for outcoupling transmission rates up to $T_{OC} = 10.6\%$. The highest efficiency was found for $T_{OC} = 3.3\%$ and a maximum output power of 20.8 W was obtained at a pump power of 44.6 W resulting in an optical-to-optical efficiency of $\eta_{opt} = 46.7\%$. The upper

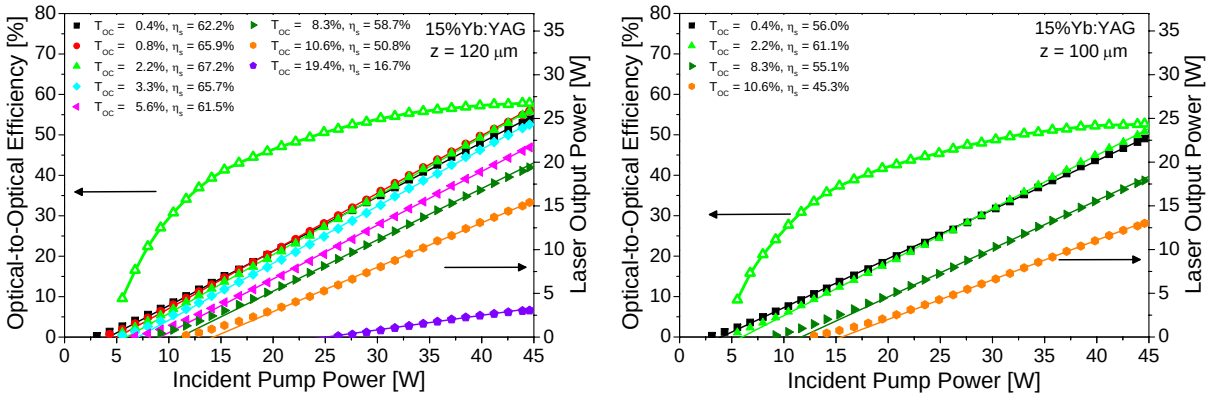

Figure 5.5.: Left: Laser output power plotted against the incident pump power for all outcoupling transmission rates investigated for a 15%Yb:YAG ceramic sample of $z = 120\,\mu m$ thickness. Right: The same for a 15%Yb:YAG ceramic sample of $z = 100\,\mu m$ thickness. For both thicknesses the optical-to-optical efficiency for $T_{OC} = 2.2\%$ is also plotted (open triangles).

limit for the single pass resonator internal losses was estimated to be about $L_{int} = 0.3\%$. For $T_{OC} = 10.6\%$ a strong roll-over is found, beginning at about 36 W of pump power and leading eventually to the termination of the laser at higher pump powers. Also, a decrease in laser efficiency is found for $T_{OC} = 0.4\%$ and $T_{OC} = 0.8\%$ at higher pump powers. In contrast to the 13%Yb:YAG ceramic sample, a change in laser mode for low and high pump powers could be observed for this sample. The laser emission spectra plotted on the right side of figure 5.6 for $T_{OC} = 0.4\%$ at pump powers of 5.5 W close to the laser threshold and 44.6 W show that at low pump powers the laser oscillates at different wavelengths and only in the longer wavelength region at high pump powers. This suggests that initially, for the lower outcoupling transmission rates the gain is comparable at around 1030 nm and 1050 nm but is shifted towards longer wavelength at higher pump powers because of thermal effects. Heating of the laser sample also occurs during laser operation and leads to a change of the absorption and emission properties of the material. Broadening of the spectral lines leads to higher overlap and an increase of reab-

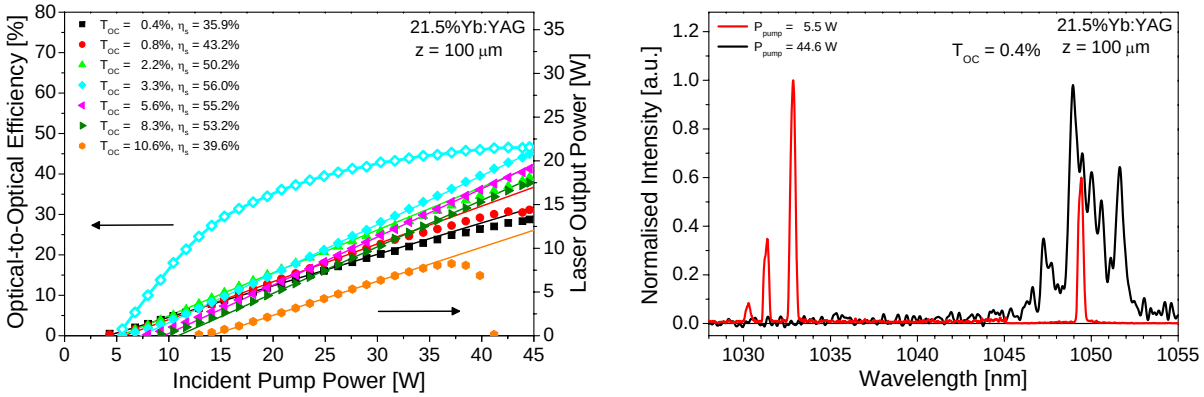

Figure 5.6.: Left: Laser output power plotted against the incident pump power for all outcoupling transmission rates investigated for the 21.5%Yb:YAG ceramic sample ($z = 100\,\mu m$). The optical-to-optical efficiency for $T_{OC} = 3.3\%$ is also plotted (open diamonds). Right: Laser emission spectra for pump powers of 5.5 W and 44.6 W at an outcoupling transmission rate of $T_{OC} = 0.4\%$.

sorption at shorter wavelengths and thus decreases the gain. As a consequence, the oscillating laser modes switch at higher pump powers.

Of the ceramic samples investigated, the highest efficiencies comparable to those of the reference single crystal were found for the 15%Yb:YAG sample. The results from the other samples suggest a decrease in desirable thin-disk laser performance with increasing Yb-doping concentration. However, the results of the 15%Yb:YAG ceramics does not fit into this picture. Furthermore, it has to be noted that relatively high resonator internal losses of up to $L_{int} = 0.3\%$ have been estimated for the ceramics with 10.9%, 13% and 21.5% of Yb-doping concentration whereas very low losses of under $L_{int} = 0.1\%$ were found for the 15%Yb:YAG sample. The 15%Yb:YAG ceramic sample was fabricated much later than all the other ceramic samples, which suggests that possibly an optimised fabrication technique was applied reducing the sources of laser losses, e.g. scattering centres.

5.4. Peculiar Observations

Several deductions can be drawn from the thin-disk laser results for the different Yb:YAG samples described in the previous section but some questions are left unanswered. Some of the observations made cannot be explained by the zero-dimensional model introduced in section 2.3.2. In the following these peculiar observations will be discussed focussing on the inversion density dependence of the laser performance.

5.4.1. Inversion Dependency of the Laser Performance

Regardless of the Yb-doping concentration, thickness and the single crystalline or ceramic nature of the materials investigated, laser efficiency peaked for outcoupling mirrors $T_{OC} = 2.2\%$ to $T_{OC} = 3.3\%$ and then decreased with increasing transmission rates. For some laser samples even strong roll-overs were observed at high outcoupling rates, leading to the termination of the laser at high pump powers. These observations confirm that the conditions in the laser material are not fixed to the conditions at laser threshold but, due to the introduction of heat, do change during laser operation with increasing pump powers. As the available pump power was the same for all thin-disk laser experiments, it has to be concluded that the amount of pump energy turned into heat increases with the outcoupling transmission rate, i.e. with the inversion density.

As a first step to investigate the dependency of the laser performance on the density of excited Yb^{3+}-ions, the conditions at laser threshold were more closely examined. Despite appearing quite simple to determine and to analyse, the laser threshold of a system needs rather careful interpretation. Especially in systems with very low laser thresholds, the threshold can be too close to the lasing threshold of the pump laser. Also, the step size with which the pump power is controlled might be too crude for a thorough determination. Furthermore, in a multimode laser system, some of the modes are likely to start oscillating before others since homogeneity of all relevant parameters, such as the pump power density, are just theoretical assumptions which are usually not realised. To that, the temperature dependent changes in the absorption and emission spectra of the material cannot be neglected. The conditions in the low power regime close to

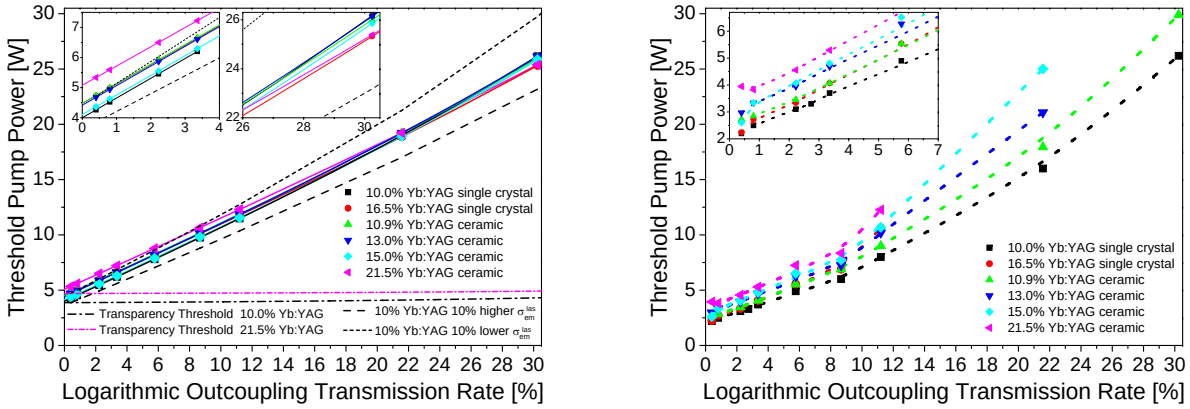

Figure 5.7.: Threshold pump powers calculated using equation 2.96 (left) and measured (right) for the laser samples investigated, both plotted against the logarithmic outcoupling transmission rates $\gamma_{OC} = -ln(1 - T_{OC})$. The dashed and the short dashed curves in the left figure show the calculated threshold pump powers for the 10.0%Yb:YAG single crystalline laser sample with 10% higher and 10% lower emission cross-sections, respectively. The dash dotted and short dash dotted curves represent the transparency threshold pump powers for the 21.5%Yb:YAG and the 10.0%Yb:YAG laser sample, respectively. The dotted curves in the right figure represent an assumed trend and are shown solely for clarity reasons.

the threshold are thus usually quite different from the high power regime, in which the laser is in most cases meant to operate. There are different ways to determine or define the threshold of a laser system (for discussions see e.g. [Fre04, Krä08]). The measured laser threshold is the lowest pump power, for which laser operation can be observed. This threshold value of a system can differ depending on whether the pump power is chosen for which the laser just went off or just started to operate, whether the resonator was adjusted to highest output powers or to lowest threshold and as stated above, the accuracy of the measurement is limited by the step size of the pump power controller. A kind of average threshold can be determined by applying a linear fit on the input-output characteristics and use the intersection with the abscissa. In this way, a laser threshold is obtained which corresponds to the slope efficiency achieved. This average threshold is in a lot of cases preferable due to its lower sensitivity to measurement errors. However, in cases where due to the introduction of heat, significant pump power dependent changes in the laser conditions have to be assumed, the average laser threshold (as well as the respective slope efficiency) may not give any straight forward information regarding the physics behind it. Therefore, in the following the measured thresholds will be discussed as the conditions for which laser operation could be just achieved at a minimum impact of the heat.

Figure 5.7 shows the theoretical pump powers calculated (left) and the measured threshold pump powers (right) for all laser samples investigated. The data are plotted against the logarithmic outcoupling transmission rates $\gamma_{OC} = -ln(1 - T_{OC})$ because the approximation made in equation 2.92 does not apply for transmission rates higher than $T_{OC} = 5\%$. The dotted curves in the right figure represent the assumed characteristics for each sample and are plotted solely for clarity purpose. The threshold pump powers on the left side of figure 5.7 were calculated for the laser wavelength of 1030 nm from equation 2.96 using the thicknesses and concentrations of the samples investigated, the values for the internal losses obtained above and the spectroscopic cross-sections as well as the fluorescence lifetime of $\tau = 950\,\mu s$ discussed in chapter 4. As

can be seen in this plot, in the investigated range of outcoupling rates theoretically the threshold pump powers should follow a more or less linear characteristics with γ_{OC}. This is due to the absorption efficiency η_{abs} decreasing only slightly in this output coupler transmission rate regime (see also equation 2.96). At lower transmission rates, the samples with lower internal losses L_{int} have the lower threshold pump powers whereas at high outcoupling rates, the higher concentrated samples have the lower thresholds. This is due to the much higher impact of internal losses at low γ_{OC}, which results into lower resonator efficiencies. At higher outcoupling transmission rates, the internal losses can usually be neglected. The higher transmission rates however, demand higher inversion densities to overcome the resonator losses, which in turn lead to a significant decrease in absorption efficiency (see equations 2.87 and 2.89). This bleaching of the ground state absorption is, for the chosen sample thicknesses, much more significant for the lower concentrated laser samples. However, as can be seen on the left of figure 5.7, the differences in threshold pump powers are expected to be small for the different Yb^{3+}-concentrated laser samples as their thicknesses were chosen to achieve similar absorption efficiencies in the performed experiments.

The measurement results plotted in figure 5.7, right show that almost regardless of the internal losses, the threshold pump power is higher for the higher Yb-concentrated samples. This difference in threshold pump power is more pronounced the higher the outcoupling rate. Also, it has to be noted that up to $T_{OC} \simeq 8\%$ the measured threshold pump powers seem to follow a more or less linear relationship with the outcoupling rate, from which a more significant departure is observed the higher the doping concentration. Comparison between the theoretical plot and the measurement result shows that the actual threshold conditions deviate a lot from the conditions predicted by the zero-dimensional model. Up to an outcoupling rate of about $T_{OC} = 10\%$, the measured threshold pump powers were significantly lower than the calculated ones and also lower than the calculated transparency threshold for the used Yb^{3+}-doping concentrations. Taking into account that the laser was actually oscillating at 1050 nm for $T_{OC} = 0.4\%$ and assuming much lower internal losses, does not help in understanding these differences. It may be possible that the errors in the used cross-sections, especially in the Yb:YAG emission cross-sections, are responsible for this deviations. For the 10%Yb:YAG single crystalline laser sample, two additional curves are plotted in figure 5.7, left, which account for 10% lower (dashed) and 10% higher (short dashed) emission cross-sections at 1030 nm. As can be seen, the effect of too low emission cross-sections should be more pronounced at high T_{OC} and would result in too low threshold pump powers for the higher outcoupling rates. A much more likely reason for these deviations is the inhomogeneous distribution of the pump power, which is more distinctive at low power levels. The zero-dimensional model used for the calculations is based on homogeneity of all relevant parameters, an assumption, which apparently is not valid at low pump powers.

The qualitative differences between calculated and measured threshold pump powers are even more striking for the higher outcoupling transmission rates, where homogeneity of the pump power density is a much more valid assumption. The calculations clearly show that at these outcoupling rates, the drop in absorption efficiency should be the crucial factor for the deviations in the threshold pump powers for the different concentrated samples. However, the measurements demonstrate that another factor has to be decisive, which demands higher threshold pump powers for higher Yb-doping concentrations. In the zero-dimensional model, no thermal effects

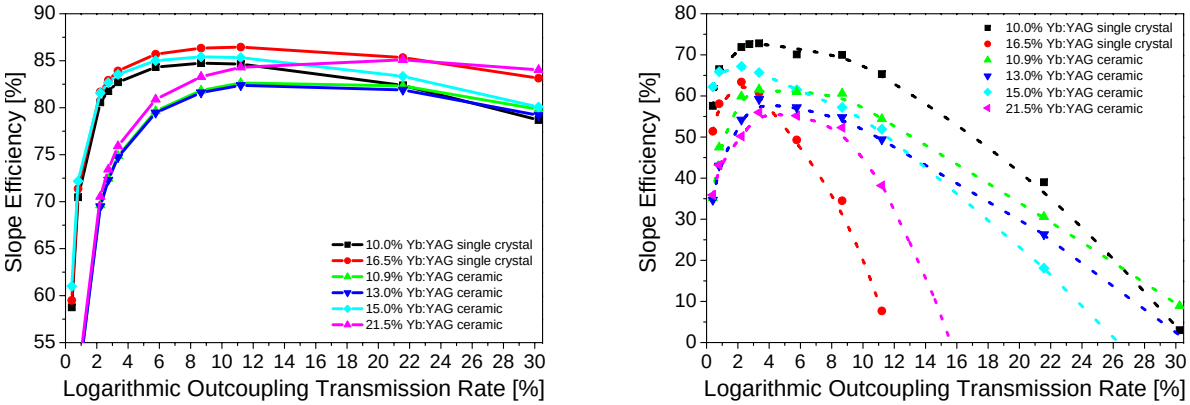

Figure 5.8.: Slope efficiencies calculated using equation 2.100, $\eta_{S,cal}$, (left) and obtained from measurements, $\eta_{S,mes}$, (right) for the laser samples investigated, both plotted against the logarithmic outcoupling transmission rate $\gamma_{OC} = -ln(1-T_{OC})$. The dotted curves in the right figure represent an assumed trend and are shown solely for clarity reasons. Note that the scales of the ordinates are different in the two figures.

are considered, which could partly explain the deviations. According to equation 2.93, a linear relationship should exist between the density of excited states $N_{2,th}$ and the (logarithmic) outcoupling rate, which suggests also a linear increase of the temperature if the only source of heating is the quantum defect. On the other hand, heating results in a higher population of the lower laser level and thus to a higher transparency threshold, which is per se larger for the higher doped samples. For this reason, at threshold at the same outcoupling rate, the higher doped thinner laser samples have a higher temperature compared to the lower doped thicker samples, because the density of excited states and also the total number of excited ions is always higher for these samples (see equation 2.93) leading to higher temperature generation due to the quantum defect. However, the threshold pump powers measured are in a power regime, where significant heating is not expected and the changes of the cross-sections with temperature are still approximately linear [Lar08][7]. In addition, the better cooling as well as the reduced stresses and resulting thermal lens effect for the thinner samples have not been included in the above considerations. Therefore, it has to be concluded that the higher transparency thresholds for the higher concentrated samples cannot be the only reason for the observed massive differences in threshold pump powers between the different concentrated laser samples. The observations indicate that at high outcoupling transmission rates an additional loss mechanism is unlocked, which is more effective for the higher doped, thinner Yb:YAG samples. These considerations show that it is not possible to deduce the actual density of excited Yb^{3+}-states from the measured threshold pump powers (using e.g. equation 2.97 assuming constant absorption efficiency) as long as the additional loss mechanism is not identified.

Figure 5.8 shows $\eta_{S,cal}$, the slope efficiencies calculated from equation 2.100 (left) and $\eta_{S,mes}$, the slope efficiencies obtained from the thin-disk laser measurements (right) plotted against γ_{OC} for all the samples investigated. For clarity reasons the ordinate axes of the two figures were chosen differently. The slope efficiencies calculated for the lower outcoupling transmission rates are affected by quite high errors, because of the high impact of the internal losses L_{int},

[7]The temperature dependence of the absorption and emission cross-sections is not linear but is commonly approximated to as being linear for temperatures up to 200°C, which are typical for thin-disk lasers [Lar08].

which were estimated in the previous section as an upper limit using $\eta_{abs} = 1$. This influence can be neglected for higher outcoupling transmission rates as can be seen by the increase of slope efficiency with transmission rate at the beginning of the curves in both figures. The calculated slope efficiencies are only limited by the Stokes efficiency, which is $\eta_{St} = 0.91$ for Yb:YAG pumped at 940 nm and lasing at 1030 nm, and by the absorption efficiency η_{abs}, which decreases with the density of excited states (see equation 2.89). This bleaching of the ground state absorption is the reason for the decrease of the calculated slope efficiency at higher outcoupling rates. The overlap efficiency is assumed to be 1 in the thin-disk laser setup at multimode operation. For up to $T_{OC} \approx 10\%$ clearly the samples with the lower internal losses should have the higher slope efficiency and of the ones with similar losses always the higher concentrated samples have the higher slope efficiencies. At even higher outcoupling rates bleaching becomes the dominant factor and at $T_{OC} \approx 30\%$ the sequence of slope efficiencies seems only to be dependent on the Yb^{3+}-concentration of each sample. It has to be noted that the highest slope efficiency does not necessarily correspond to the highest optical-to-optical efficiency in the available pump power regime. In contrast, the slope efficiencies obtained from the laser measurements shown in figure 5.8, right clearly show that the zero-dimensional model used and the assumptions made for the calculations are not valid. The maximum of the slope efficiencies calculated is for all of the samples higher than $\eta_s = 82\%$ whereas the slope efficiencies obtained did not even nearly reach $\eta_s = 80\%$. In accordance to the calculations, at the lower outcoupling rates the samples with the lower internal losses have the higher slope efficiencies. The maximum slope efficiency is found at $T_{OC} \approx 2\%$ to $T_{OC} \approx 4\%$ for all samples, after which a decrease with outcoupling rate follows, which in contradiction to the calculations is stronger the higher the Yb^{3+}-doping concentration of the sample. The characteristics of the 16.5%Yb:YAG laser sample has to be considered as an exception as the decrease is even steeper than that of the 21.5%Yb:YAG sample and way different compared to the 15%Yb:YAG sample, which has comparable doping concentration and thickness. As stated in the previous section, the measurement results to a wide extent cannot be regarded as general but have to be seen as individual results. However, some basic, general trends can be deduced. At high outcoupling transmission rates not the bleaching of the ground state absorption seems to be the limiting factor but the Yb^{3+}-doping concentration. Even though the number of samples was not sufficient to carry out significant systematic studies, as a trend it can be said that ceramic samples seem to suffer less than their single crystalline counterparts from this effect.

Ideally, the samples and the respective laser results are compared under identical physical conditions, which in this case would be comparing these at the same density of excited Yb^{3+}-states $N_{2,th}$. This however, cannot be accomplished as long as the mechanisms leading to the observed behaviour are not understood. Instead of using the physically correct but non-accessible density of excited states, in the following the logarithmic outcoupling transmission rate γ_{OC} will be kept as the abscissa. This is chosen for two reasons: Firstly, the outcoupling rate is a known quantity, that is not affected by any theoretical assumptions and thus plotting against γ_{OC} gives a correct and by no assumption modified representation of the measurement results. Secondly, from the simplest model for the threshold condition (equation 2.92) $N_{2,th}$ is linearly dependent on γ_{OC} (see also appendix E). It is the purpose of these investigations to reveal the deviations from this simplest model and to find indications for possible processes underlying the observations.

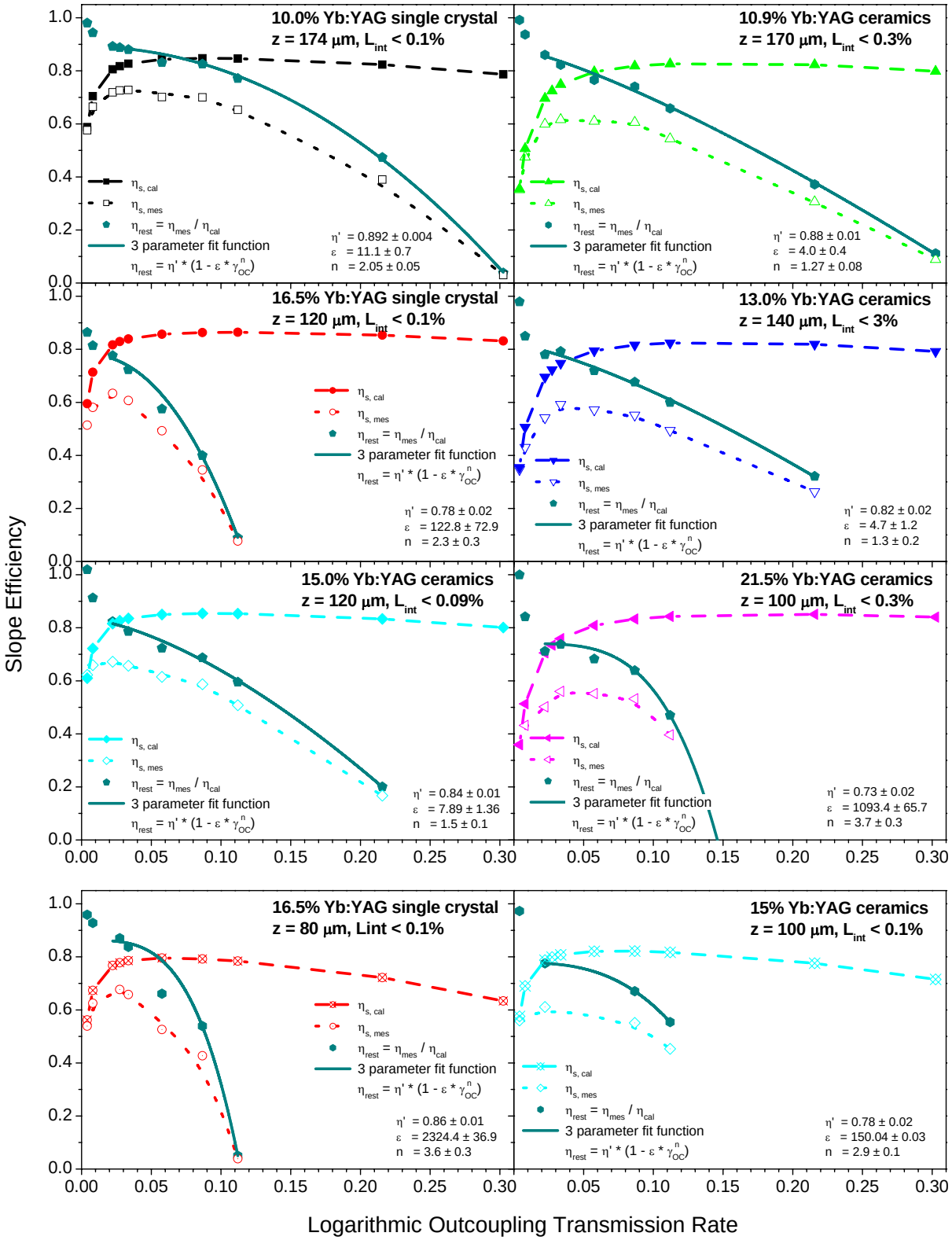

Figure 5.9.: Residual efficiency accounting for the γ_{OC}-dependent reduction in efficiency observed, obtained as a ratio between measured and calculated slope efficiency. A three parameter fit function was applied for analyses of the dependencies and to find a measure for the strength of efficiency reduction.

To obtain some measure for the strength of the observed deviation between measurement and zero-dimensional model, the measured slope efficiencies were divided by the calculated ones. In this way a kind of residual efficiency $\eta_{rest}(\gamma_{OC})$ is obtained, which is a function of γ_{OC} and accounts for the observed outcoupling transmission rate dependent losses additionally reducing the total efficiency:

$$\eta_{S,mes} = \eta_{S,cal}\,\eta_{rest}(\gamma_{OC}). \tag{5.1}$$

Figure 5.9 shows the corresponding plots for the samples investigated. The filled pentagons represent the residual efficiency η_{rest}, to which a three parameter fit of the form

$$\eta_{rest} = \eta'(1-\varepsilon{\gamma_{OC}}^{n}) \tag{5.2}$$

was applied. Here, η' is the product of all efficiencies considered to be 1 in the zero dimensional model and which are independent of the outcoupling transmission rate, e.g. the overlap efficiency. Any constant errors in the Stokes efficiency, resonator efficiency or absorption efficiency, which are linked by multiplication are also taken account for in η'. The efficiency $\left(1-\varepsilon{\gamma_{OC}}^{n}\right)$ accounts for the output coupler transmission dependent losses observed in the measurements. The interpretation of ε is not simple. This parameter can be considered as a coupling parameter, giving the strength of the found efficiency reduction with increasing outcoupling transmission rate. For $\varepsilon = 0$ no outcoupling transmission dependent decrease of efficiency would be found. Further discussion will be found later in this section. The parameter n gives the nonlinearity of the found dependency between efficiency reduction and outcoupling transmission rate. ε and n are linked to each other in a way that $\varepsilon = 0$ if $n = 0$. All found fit parameters also absorb any existing thermal effects as these are not considered in the model and are therefore additionally afflicted with errors. Deviations of the absorption efficiency due to heating, which is not caused by the quantum defect, will most likely be accounted for by a contribution nonlinear in γ_{OC}. The fit was performed for $T_{OC} > 0.8\%$ to avoid the influence of the error-prone internal losses and excluding the results for $T_{OC} = 5.6\%$ as the slope efficiencies obtained using this mirror clearly deviated from the found characteristics in all measurements.

In figure 5.10, the fit parameters η', n and ε obtained as a measure for the strength of the observed outcoupling rate dependent efficiency reduction are plotted against the doping concentrations and the thicknesses of the Yb:YAG thin-disk laser samples investigated. The XY-plane in these plots shows the dependency existing between sample thickness and Yb^{3+}-doping concentration. To ensure an absorption efficiency of at least 90% for all outcoupling rates investigated in the laser experiments, the thicknesses of the different concentrated samples were appropriately chosen based on the zero-dimensional model (see section 5.2). Using equation 2.87, 2.89 and 2.93, where T_{OC} has been replaced by $\gamma_{OC} = -\ln(1-T_{OC})$, an expression for the absorption efficiency η_{abs} is found:

$$\eta_{abs} = 1-\exp\left[(\sigma_{abs}^{pump}+\sigma_{em}^{pump})\left(\frac{\sigma_{abs}^{las}}{\sigma_{em}^{las}+\sigma_{abs}^{las}}N_t + \frac{M_r L_{int}+\gamma_{OC}}{M_r z(\sigma_{em}^{las}+\sigma_{abs}^{las})}\right)M_p z - M_p z\sigma_{abs}^{pump}N_t\right]. \tag{5.3}$$

Solving this equation for N_t, gives

$$N_t = \frac{\ln(1-\eta_{abs}) - \frac{M_p}{M_r}(M_r L_{int}+\gamma_{OC})}{\left[(\sigma_{abs}^{pump}+\sigma_{em}^{pump})\frac{\sigma_{abs}^{las}}{\sigma_{em}^{las}+\sigma_{abs}^{las}} - \sigma_{abs}^{pump}\right]M_p}\,\frac{1}{z}, \tag{5.4}$$

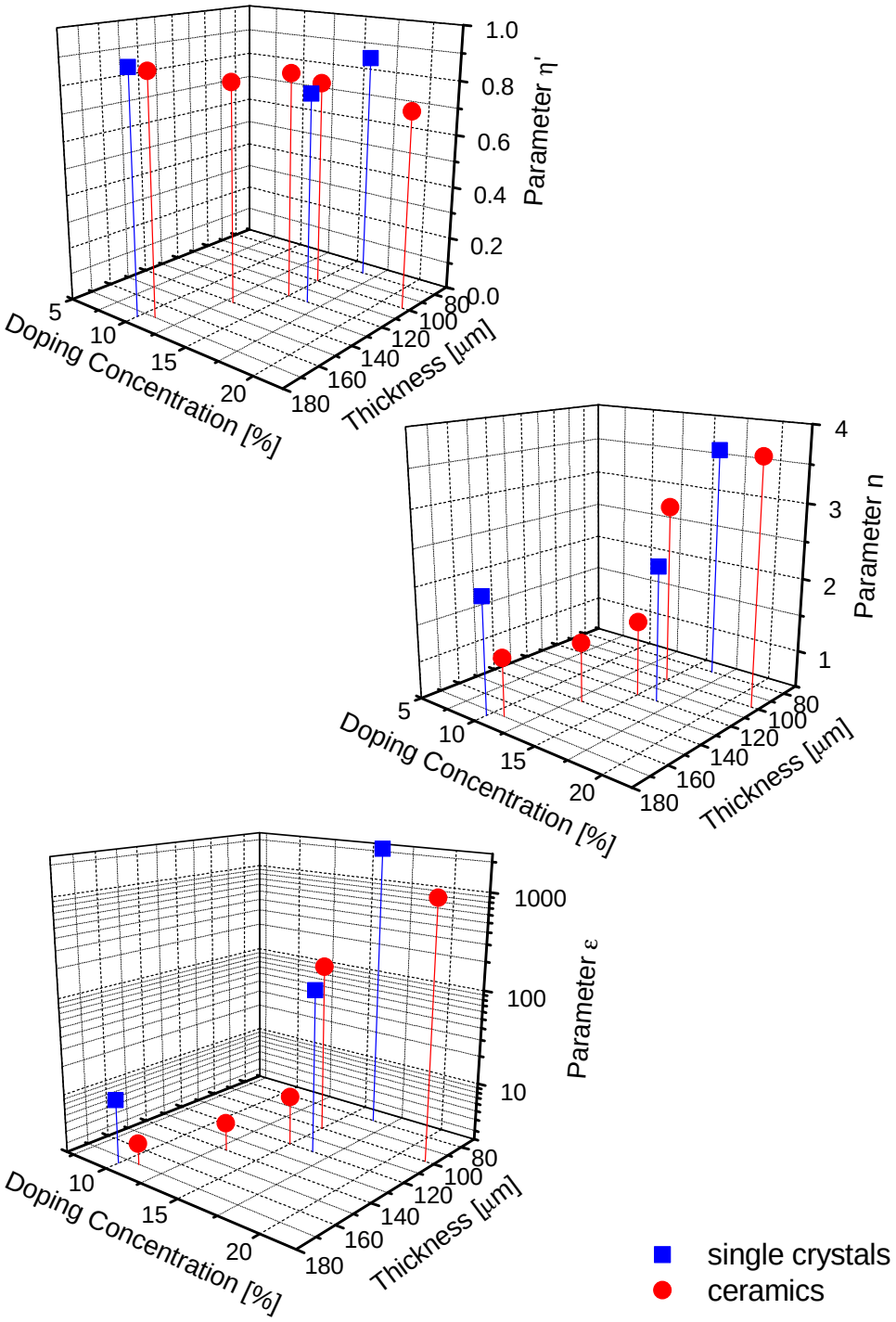

Figure 5.10.: The fit parameters η' (top), n (middle) and ε (bottom) obtained from the three parameter fit performed in figure 5.9, plotted against the Yb-doping concentration and the thickness of the Yb:YAG laser samples investigated.

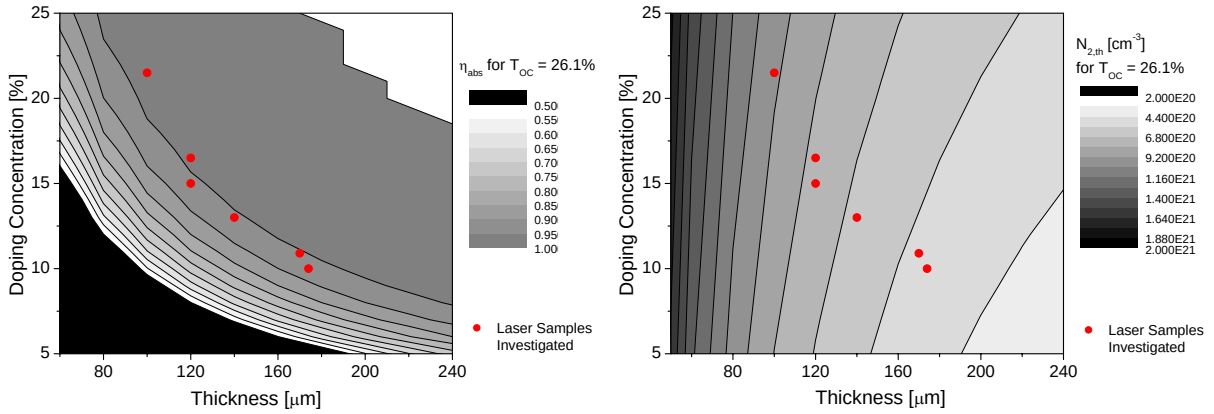

Figure 5.11.: Grey scale contour diagram of the absorption efficiency (left) and density of excited Yb^{3+}-states calculated for an outcoupling rate of $T_{OC} = 26.1\%$ plotted against Yb-doping concentration and sample thickness. The red dots represent the Yb:YAG samples investigated in the thin-disk laser experiments. As can be seen in the left figure, samples of equal absorption efficiency are located on hyperbolae in the XY-plane.

i.e. a hyperbolic relationship is given between doping concentration N_t and thickness z if a constant absorption efficiency is set as required condition ($N_t z \approx$const.). Exemplary, the absorption efficiency calculations done for $T_{OC} = 26.1\%$ are plotted as a grey scale contour diagram on the left of figure 5.11. As can be seen, the samples investigated (filled dots) are located more or less on the same hyperbola. The position on this hyperbola determines $N_{2,th}$, i.e. the actual density of excited Yb^{3+}-ions needed to reach the laser threshold, which is shown on the right of figure 5.11 (see also equation 2.93). This should not be confused with the inversion level $\frac{N_{2,th}}{N_t}$, for which also holds that samples of same inversion levels are located on hyperbolae in the $N_t z$-plane[8].

Substituting equation 5.4 into equation 2.93 and requiring $N_t z =$const., the ratio of the density of excited states for two different samples with N_{t1}, z_1 and N_{t2}, z_2 is given by

$$\frac{N_{2,th1}}{N_{2,th2}} = \frac{z_2}{z_1} = \frac{N_{t1}}{N_{t2}} \tag{5.5}$$

and it follows

$$\left(\frac{N_{2,th1}}{N_{2,th2}}\right)^2 = \frac{z_2 N_{t1}}{z_1 N_{t2}} = \frac{N_{t1}}{z_1}\frac{z_2}{N_{t2}}. \tag{5.6}$$

Thus, for samples located on the same hyperbola of equal absorption efficiency, the density of excited states $N_{2,th}$ has a linear dependency on the square root of the ratio between doping concentration and thickness:

$$N_{2,th} \propto \sqrt{\frac{N_t}{z}}. \tag{5.7}$$

In this case, the proportionality constant is dependent on the respective losses which need to be overcome for the laser to oscillate, i.e. the proportionality constant is predominantly determined by the outcoupling transmission rate. $\sqrt{\frac{N_t}{z}}$ is thus understood as a characteristic sensitivity

[8] Indeed, the investigated laser samples all have almost the same inversion levels for the same output coupler.

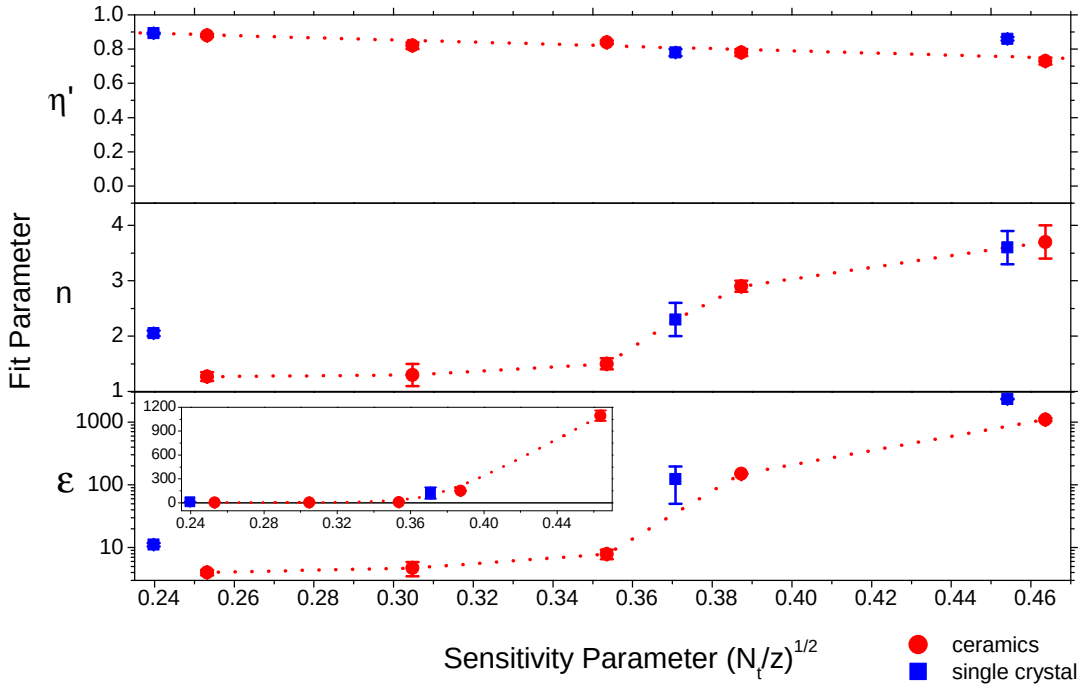

Figure 5.12.: The fit parameters η' (top), n (middle) and ε (bottom) obtained from the three parameter fit performed in figure 5.9 plotted against the sensitivity parameter $\sqrt{\frac{N_t}{z}}$, where N_t is the Yb-doping concentration and z is the thickness of the respective sample. The inset in the bottom graph shows the fit parameter ε in linear scale. See text for discussion.

parameter of a laser sample for how strongly the density of excited ions will change when the lasing conditions, particularly the resonator losses are altered. In other words, a sample with higher $\sqrt{\frac{N_t}{z}}$ will always have a higher density of excited states in the same resonator setup compared to samples with lower $\sqrt{\frac{N_t}{z}}$.

For reason of clarity, the fit parameters shown in figure 5.10 are plotted in figure 5.12 against the sensitivity parameter $\sqrt{\frac{N_t}{z}}$ introduced above. As can be seen, the parameter η' obtained from the fit is comparable for all laser samples investigated. Its value slightly but steadily decreases from $\eta' = 0.89$ for the lowest doped and thickest Yb:YAG sample to $\eta' = 0.73$ for the highest doped, thinnest sample. The single crystalline or ceramic nature of the samples does not seem to have any influence on this parameter. As briefly stated above, η' accounts for any efficiencies, which are constant with the output coupler transmission rate and are not considered in the zero-dimensional model. This parameter being different from 1 is the reason for the deviations between zero-dimensional model and measured slope efficiency observed for the lower output coupler transmission rates (i.e. $T_{OC} \approx 1\%$-3%). The fit parameter n has a value between $n = 1.27$ and $n = 1.5$ for the ceramic samples $N_t = 10.9\%$, $z = 170\,\mu\text{m}$, $N_t = 13.0\%$, $z = 140\,\mu\text{m}$ and $N_t = 15.0\%$, $z = 120\,\mu\text{m}$, i.e. the ceramic samples for which $\sqrt{\frac{N_t}{z}} < 0.36\,\text{cm}^{-2}$.

Between $\sqrt{\frac{N_t}{z}} \approx 0.36\,\mathrm{cm}^{-2}$ and $0.39\,\mathrm{cm}^{-2}$, the value of the fit parameter n rapidly increases to close to $n = 3$, after which the increase is more gently reaching $n = 3.7$ for the ceramic sample with $N_t = 21.5\%$ and $z = 100\,\mu\mathrm{m}$. The parameter ε shows a very similar dependency on the sensitivity parameter $\sqrt{\frac{N_t}{z}}$ as the parameter n. While $\varepsilon < 10$ for $\sqrt{\frac{N_t}{z}} < 0.36\,\mathrm{cm}^{-2}$, its value changes orders of magnitude for higher sensitivity parameters. Except for the sample with $N_t = 10.0\%$ and $z = 174\,\mu\mathrm{m}$, which has the lowest value for $\sqrt{\frac{N_t}{z}}$, the n-parameter for the single crystalline samples are fitting very well onto the characteristics drawn by the ceramic samples. For the ε-parameter, the single crystalline samples seem to have always higher values compared to the ceramic ones. Comparing the characteristics of ε in logarithmic scale and that of n in figure 5.12, it is evident that these two parameters are not independent. The n-parameter describes the nonlinearity of the loss process leading to the decrease in efficiency for higher outcoupling transmission rates. Usually, according to basic rate equations the density of excited states $N_{2,th}$ is a linear function of the outcoupling rate (see equation 2.93). In this case, the fit parameter n would describe the number of excited Yb^{3+}-states involved in the loss process. It is particularly noticeable that the 10.9%, 13.0% and the 15.0%Yb:YAG ceramic laser samples with a sensitivity parameter up to $0.36\,\mathrm{cm}^{-2}$ have n-parameters close to 1, suggesting that a linear process is dominant for the reduction in efficiency. For the samples with higher sensitivity parameter values, the underlying process would then be interpreted as nonlinear and of the order of 2 to almost 4, meaning that at least 2 and up to 4 excited Yb^{3+}-ions would participate in the loss process. However, this interpretation has to be treated with great caution. It is unlikely that lower doped thicker samples experience different physical processes compared to higher doped thinner samples under the same conditions. Therefore, it has to be concluded that plotting against the output coupling rate in figure 5.9 does not give the characteristics of the decrease in efficiency under the same physical conditions for all samples. As the underlying rate equation model is not known, $N_{2,th}$ being linearly dependent on γ_{OC} is merely an assumption, which is most likely not true. Moreover, the observed deviations between model and experiment and especially the n-parameter being different from 1 for some samples, underline the inadequacy of the assumptions made in section 2.3.2. This conclusion is also supported by the comparison between theoretical and measured threshold pump powers. See also appendix E for more details.

Nevertheless, some phenomenological deductions for laser application can be drawn from the analyses attempted in this section. The ceramic samples are less prone to the losses nonlinear in γ_{OC} compared to their single crystalline counterparts. Samples with $\sqrt{\frac{N_t}{z}} < 0.36\,\mathrm{cm}^{-2}$ yield higher efficiencies in thin-disk laser resonators compared to samples with $\sqrt{\frac{N_t}{z}} > 0.36\,\mathrm{cm}^{-2}$ when using higher outcoupling transmission rates.

It has to be noted that all these considerations and the comparison between samples are based on the requirement that Yb^{3+}-doping concentration and thickness of the laser samples are chosen to achieve similar absorption efficiencies for all samples.

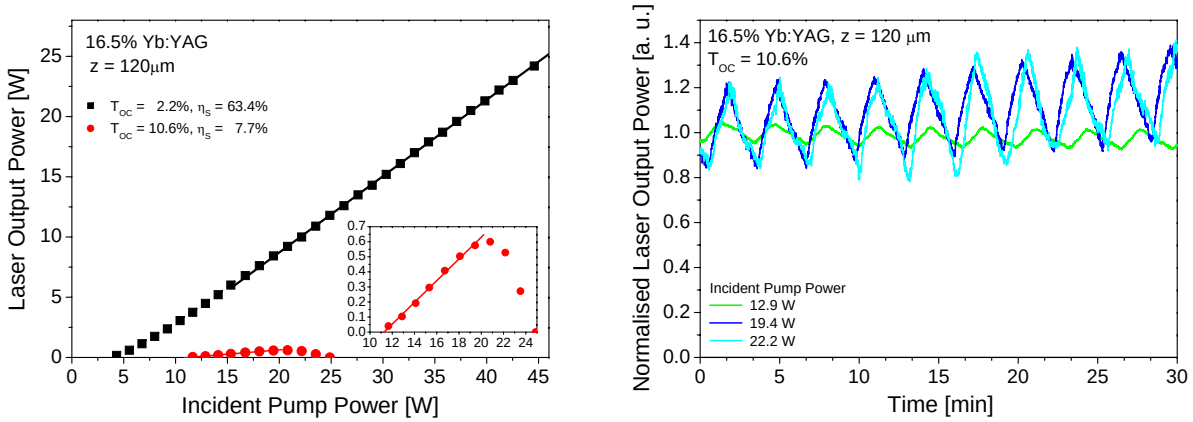

Figure 5.13.: Input-output characteristics for the 16.5%Yb:YAG single crystal ($z = 120\,\mu m$) for $T_{OC} = 2.2\%$ and $T_{OC} = 10.6\%$ (left) and normalised laser output power using outcoupling mirror $T_{OC} = 10.6\%$, measured over 30 minutes for three different incident pump powers (right).

5.4.2. Time Monitoring of the Laser Output Power

In Yb^{3+}-doped silica fiber lasers degradation of laser efficiency denoted as photodarkening is a well known phenomenon, that is also supposed to be connected to the density of excited Yb^{3+}-ions. The degradation of the Yb-fibers develops over time and seems to be permanent, so that special treatment is necessary to bring the fibers back to their initial performance. The processes involved in photodarkening are not yet fully understood and subject of ongoing research [Jet09, Eng09]. To investigate possible similarities between the photodarkening in Yb-fibers and the decrease in efficiency found in the Yb:YAG thin-disk laser experiments, time monitoring of the laser output power was performed.

The same thin-disk laser setup as described above was used for these experiments. The output power was measured using a 10A-V1.1-SH sensor and a NOVA II power meter (Ophir Optronics Ltd., Israel), which was connected to a computer to monitor the laser power over time. As can be seen exemplary for the 16.5%Yb:YAG #SNF single crystal of 120 µm thickness in figure 5.13, right, no degradation of laser performance over time could be found for the Yb:YAG single crystals. The oscillations superimposed onto the laser signal are due to small temperature differences of the cooling water, which was set to 17°C. The cycle period of the cooler compressor is equal to the 4 minute cycle observed in the measurements. In this figure, the laser output power detected over 30 minutes using the output coupler $T_{OC} = 10.6\%$ is shown for three different incident pump powers. The outcoupling mirror was chosen as this mirror had the highest outcoupling transmission rate for which thin-disk laser operation was possible with the 16.5%Yb:YAG single crystal. The efficiency of the laser using this output coupler was significantly reduced compared to the other outcoupling transmission rates investigated and displayed a strong roll-over, which led to termination of the laser operation (see figure 5.13, left). Therefore, the effects of possible degradation processes were expected to be strongest for this mirror. The incident pump powers of $P_{in} = 12.9\,W$, $19.4\,W$ and $22.2\,W$ were chosen to monitor the behaviour of the laser at some level above threshold, at maximum possible output power and just before termination, respectively. The output power does not decrease over time

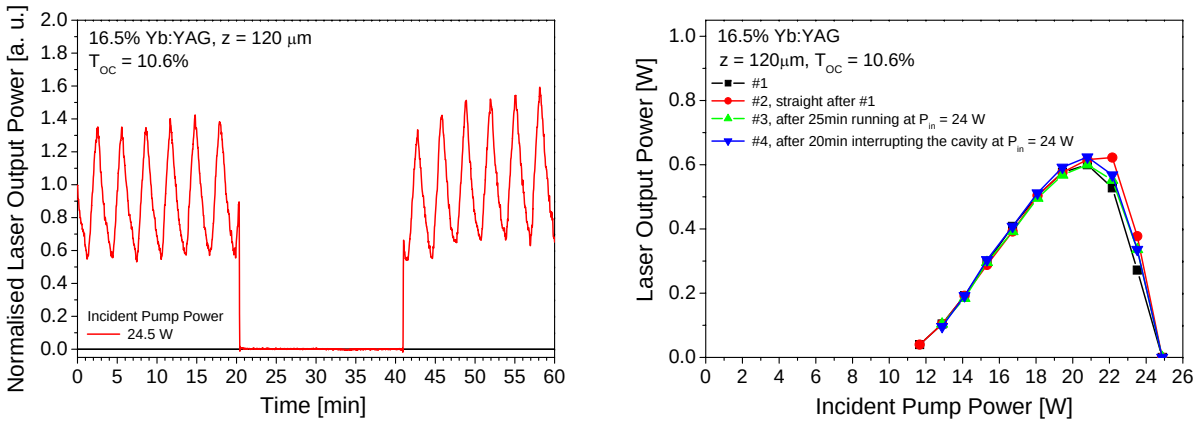

Figure 5.14.: Normalised laser output power using outcoupling mirror $T_{OC} = 10.6\%$, measured over 60 minutes for an incident pump power of 24.5 W intercepting the cavity for more about 20 minutes (left) and input-output characteristics taken at different times confirming the reproducibility of the laser performance (right).

at any point of the input-output characteristics. Instead, it seems that the output power would slightly but steadily increase over time at higher pump powers. Such a behaviour cannot be understood and is as for now attributed to systematic errors of the measurement device. The percentage of the oscillations increases with the pump power. At higher pump powers more heat is introduced into the laser material. Thus these observations could be interpreted as at higher pump powers small changes of the cooling water temperature have a higher impact onto the laser. However, as the laser disk and the pump laser diode were connected to the same cooling circuit, the waste heat of the laser diode led to further warming of the cooling water at higher pump powers. Stronger variability of the cooling water temperature is thus expected at higher pump powers.

To acquire more information on the impact that high inversion densities have on laser performance, the laser cavity was interrupted for more than 20 minutes at a pump power of 24.5 W. At this pump power the laser is just about to terminate. On the left of figure 5.14, the behaviour of the laser output power is shown over a time duration of 60 minutes. After running for 20 minutes the cavity was interrupted for 20 minutes, so that the laser crystal was still irradiated by the pump light but the laser could not oscillate. Under this condition the density of excited states increased compared to under lasing condition as the energy pumped into the active material is stored in the upper laser level and, ideally is only reduced by spontaneous emission (see also section 2.2). However, no change in laser performance could be found after removing the blockade from the cavity, confirming that in the investigated power and inversion regime no permanent degradation over time exists in Yb:YAG thin-disk lasers. The input-output characteristics shown in figure 5.14, right also prove this conclusion. The laser output power was measured a total of four times: #1 from lower pump powers to higher pump powers, #2 straight after #1 from higher pump powers to lower pump powers, #3 after running for 25 minutes at 24.5 W of pump power and #4 after having been irradiated with 24.5 W of pump power for 20 minutes under non-lasing conditions. The curves reproduce each other very well. At the current state of knowledge, the slight deviations are not considered significant.

It has to be mentioned that a totally different behaviour was found for Yb^{3+}-doped Lu_2O_3

thin-disk lasers [Fre09, Pet09]. Showing a similar decrease in laser efficiency for high outcoupling transmission rates as Yb:YAG, Yb:Lu_2O_3 thin-disk lasers were found to suffer from permanent degradation once experiencing high inversion levels. For a 5%Yb:Lu_2O_3 single crystal of 200 µm thickness and using an outcoupling mirror with $T_{OC} = 0.8\%$, at 25 W of pump power no degradation resulting in termination of the laser was observed. However, strong degradation resulting in termination of the laser was observed at 24.5 W of pump power in the case of an outcoupling transmission rate of $T_{OC} = 8.1\%$. According to present results, it is not possible to reach laser threshold with the same outcoupling mirror again once degradation led to termination of the laser. However, changing back the mirror to $T_{OC} = 0.8\%$, the laser crystal seems to have suffered no degradation and reproduces the previously recorded laser characteristics. From these observations it is suggested that some permanent loss centres are created at high densities of Yb^{3+}-excitations in the case of Yb:Lu_2O_3, which are only active as quenching centres at high inversion levels.

5.5. Concluding Remarks

In this work, thin-disk laser experiments in multimode operation were performed with differently concentrated Yb:YAG single crystalline and ceramic samples. The highest efficiencies were obtained between output coupler transmissions of $T_{OC} = 2.2\%$ and $T_{OC} = 3.3\%$.

It was found that all samples suffer from a significant drop in efficiency with increasing outcoupling transmission rate. The input-output characteristics of the different samples show that regardless of the internal losses no roll-over is present at pump powers as high as 45 W for outcoupling transmission rates up to $T_{OC} = 3.3\%$ if the laser oscillates at 1030 nm. However, the laser performance dramatically drops when raising the transmission rate. Roll-over leading to termination of the laser was observed below the pump power of 45 W in all the samples if a sufficiently high outcoupling transmission rate was chosen. The decrease in efficiency is stronger with outcoupling rate the higher the doping concentration and the thinner the laser sample. The measured threshold pump powers fit very well to these observations: using the same output coupler, the threshold pump power is higher the higher the Yb^{3+}-concentration and the thinner the sample. As the introduced pump power and thus the heat generated through the quantum defect should be the same in all the experiments, it has to be concluded that an additional process leading to heat generation has to exist. The observations suggest that the loss mechanism in question is dependent on the density of excited Yb^{3+}-states. Tentatively, it is suggested that this loss mechanism is nonlinear in the density of excited states, i.e. two to four neighbouring excited Yb^{3+}-ions are needed for the losses to occur. However, a fourth order process is very low in probability, especially in Yb:YAG crystals and ceramics, for which clustering is not of significance (see also appendix C).

The 16.5%Yb:YAG single crystalline laser sample prepared from the #SNF boule, which was grown out of a powder-metallurgically produced rhenium crucible to ensure high purity, fell short of the expectations. The measurement of the fluorescence lifetime indicated that the crystal is not contaminated by impurities reducing the quantum efficiency. Also, the upper limit of the internal laser losses estimated from the thin-disk laser experiments were comparable to that of the reference laser sample. However, the laser efficiency of this sample was lower

compared to that of the reference crystal for all output couplers investigated. Moreover, among all the laser samples, despite its supposedly high purity, the 16.5%Yb:YAG single crystalline sample displayed the strongest decrease in efficiency with increasing outcoupling transmission rate. As quality is thus not considered as the main reason for this behaviour, the thin-disk laser results and their analyses lead to the assumption that the ceramic samples are less prone to the nonlinear loss process compared to the single crystalline samples. However, much more samples with different specifications are needed to conclusively confirm this statement.

It was not possible to achieve laser operation with the as-grown Yb:YAG single crystalline samples. The presence of Yb^{2+}-ions stabilised by oxygen vacancies leads to significant reduction of the quantum efficiency (see chapter 4), which is currently considered the only reason for not being able to reach laser threshold with these samples.

In contrast to Yb:Lu_2O_3 thin-disk lasers, no permanent degradation of laser performance over time could be observed for Yb:YAG thin-disk lasers. While the creation of permanent loss centres at high densities of excitation, similar to the photodarkening phenomenon in Yb^{3+}-doped fiber lasers, is suggested for Yb:Lu_2O_3, the cause for the decrease of laser efficiency in Yb:YAG has to be considered due to a separate mechanism.

6. Photoconductivity

Photoconductivity is an optical and electrical phenomenon also often referred to as photoelectronic effect [Bub92], which is characterised by an increase of electric conductivity of a certain material due to the absorption of electromagnetic radiation. The effect was first discovered by Smith in 1873 in selenium, which due to a combination of photoconductivity and the photovoltaic effect decreased its resistance upon irradiation [Smi73]. Since then, the phenomenon of photoconductivity has been intensively studied and used advantageously in several fields of science and technology, especially in photodetection measurements [Jos90]. To date, photoconductivity measurements are largely employed in semiconductor physics to study the band-band transitions or the location of so-called impurity levels and bands within the forbidden gap [Bub58, Kya08]. Usually, the current carrying bands are associated with the conduction band (electron-type conduction) and the valence band (hole-type conduction). The basic principles typically involved in photoconductivity are schematically represented in figure 6.1: when a sample is irradiated with photons of energy greater than that of the band gap of the material, mobile electrons or holes or both are created in the conduction and valence band, respectively, increasing the conductivity in the sample. This is accomplished by either intrinsic absorption, which corresponds to the raising of an electron from the valence band to the conduction band (figure 6.1 a.) or extrinsic absorption, which corresponds to the raising of an electron from an impurity level to the conduction band (ionisation process or donor transition, figure 6.1 b.) or the raising of an electron from the valence band to an impurity level (charge transfer process or acceptor transition, figure 6.1 c.). Free electrons and holes can also be captured by an impurity level, which often leads to a recombination process of electrons and holes (figure 6.1 d. and e.). The free carrier can also be just trapped by an impurity level and then released again after some time (figure 6.1 f.). It should be noted that in the intrinsic absorption case, two types of charge carriers, i.e. electrons and holes, are created, while in the extrinsic absorption case only one type of charge carriers, i.e. either electrons or holes, is created. All these processes belong to electron exchange processes, which are not restricted by any selection rules and characterised by high transition cross-sections (see sections 2.2.3 and 2.2.4). Typically one-electron jump diagrams are used to describe transitions and phenomena associated with conductivity, since this model scheme allows the visualisation of the mobility of charges [Par59].

This chapter deals with the photoconductivity measurements performed on Yb:YAG single crystalline and ceramic samples of various Yb-doping concentrations under 940 nm excitation. First, some general ideas and the relevance of photoconductivity in the determination of the energy level structure of ions with respect to the energy bands of the host are given. Next, the experimental setup used in this work is introduced. The measurement results are presented and evaluated in the final section, with particular focus on the influence of Yb-doping concentration and valence stability. The impact of the observed photoconductivity on applications such as thin-disk lasers is also discussed.

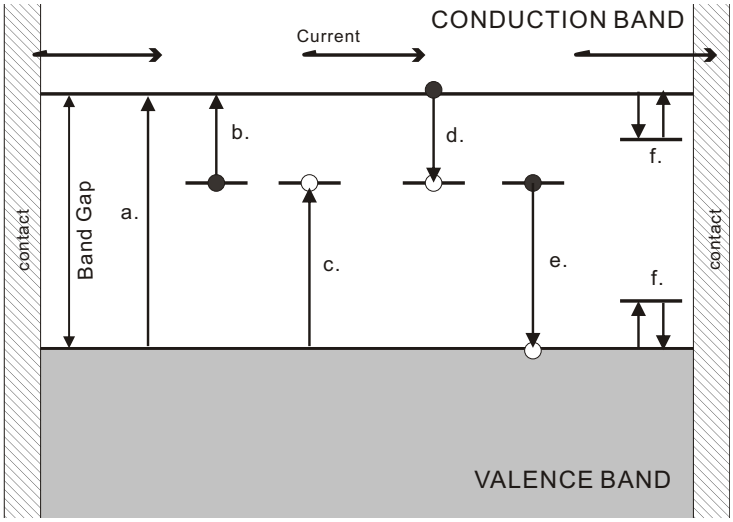

Figure 6.1.: Schematic representation showing the major optical transitions associated with the effect of photoconductivity in homogeneous semiconductors [Bub92]: a. intrinsic absorption, b. and c. extrinsic absorption, d. and e. capture and recombination, f. trapping and detrapping. Filled circles represent electrons, open circles holes. In each case, the initial state of the transition is shown.

6.1. Electron Transfer Processes and Photoconductivity in Lanthanoid-Doped Insulators

Photoconductivity measurements have been widely implemented to determine the position of dopant ion energy levels with respect to the host bands in doped insulators, e.g. [McC85, Ped86, Yen99, Hap00]. Particularly, the properties of high lying excited states of optically active ions such as the trivalent lanthanoids and transition metal ions and their interactions with the host lattice are of interest. In the case of the trivalent lanthanoids, which are $4f^n$-type systems, the high energy region begins with the $4f^{n-1}5d$ states. The wave functions of these states are spatially more extended than those of the core-like $4f$ states and consequently are more sensitive to the crystal field and other near neighbour interactions (see section 2.1.1, The $4f^{n-1}5d$ Configuration). Additionally, if the $5d$ wave functions overlap with the wave functions of the ligands constituting the energy bands of the host, the nature of the binding of the dopant ion might change and charge exchange processes occur (see sections 2.2.3 and 3.4.2). To determine the position of the lanthanoid ground state with respect to the conduction band, the measurement of photoconductivity can be a powerful tool, which however needs to be complemented by standard absorption, excited state absorption (ESA) as well as excitation spectra. In cases where the ground state of the optical ion is located in the host band gap, as is mostly the case with e.g. the Ce^{3+}-ion, one-step photoconductivity measurements can be performed to study its photoionisation threshold [Ped86]. If the ground state of the dopant ion lies below the valence band maximum, as is the case for the Yb^{3+}-ion in YAG [Thi01] (see also section 3.4.2), one-step photoconductivity measurements are not successful. For these ions the ionisation thresholds are higher in energy than the absorption band edge of the host. In such cases, two-step photoconductivity measurements can be useful, where the lanthanoid ion is first excited to a metastable, localised lanthanoid excited state that lies above the top of

the valence band. A second light source then excites the ion to higher lying localised levels and a photocurrent is measured if the conduction band is reached [Jia02]. The interpretation of the photoconductivity measurement results is not always simple. Direct transition from the lanthanoid $4f$ ground state to the bottom of the conduction band does usually not lead to a significant photocurrent. Often the photoconductivity threshold lies higher in energy, see e.g. [Ped79], which illustrates that the photoconductivity threshold does not need to coincide with the direct transition to the bottom of the conduction band. For an optical transition to occur, the overlap of the initial and final state wave functions is of crucial importance (see section 2.2.4). The core-like lanthanoid $4f$ wave functions and the delocalised Bloch wave functions of the host conduction band states are very different in nature and in general have no significant overlap. Therefore, optical transitions between these states are rarely observed [Sch98]. The $5d$ wave functions however, due to their more extended nature, do overlap with the wave functions of the host energy bands. Therefore, even if a direct transition from a $4f^n$ state to the bottom of the conduction band would be lower in energy, the optical transition occurs between the $4f^n$ ground state to the $4f^{n-1}5d$ excited state first, before a transition to the host band states can take place.

6.2. Investigations on Photoconductivity in the Yb:YAG System

For the Yb^{3+}-ion with the lowest $4f^{12}5d$ level lying more than 7 eV above the ground state in YAG [Dor00], which has a band gap of about 6.5 eV (see also section 3.4.1), both one-step as well as two-step photoconductivity measurements will not be successful in the determination of the location of the energy levels with respect to the host bands. However, investigations on the photoelectronic properties of Yb:YAG are still of interest. In connection with photodarkening in Yb^{3+}-doped silica fibers, the formation of colour centres by the involvement of six to seven excited Yb^{3+}-ions, which corresponds to the band gap energy of the fiber material, has been suggested [Shu07, Kop08]. This would imply strong interaction between the localised $4f$ states and the host lattice states at high densities of Yb^{3+}-excitation, resulting in the creation of free carriers. Even though a high order process as this is low in probability, such an energy transfer process would still be a severe loss process for the ytterbium laser. The decrease in laser efficiency at high densities of excitations found in Yb^{3+}-doped oxide thin-disk lasers, which was extensively investigated for the laser material Yb:YAG in this work (see chapter 5), could be related to a similar phenomenon. Indeed, the relatively strong electron-phonon coupling (see sections 2.2.1, The Influence of Phonons, and 3.3.2) and particularly the presence of the charge transfer transition (see sections 2.2.3 and 3.6.1) strongly indicate the existence of significant interaction between the $4f$ and the ligand wave functions in Yb^{3+}-doped systems.

6.2.1. Initial Experiments

The first photoconductivity measurement in an Yb-doped YAG system was performed using a as-grown Si-codoped 1%Yb:YAG single crystal [Fag07]. The concentration of the Si content is

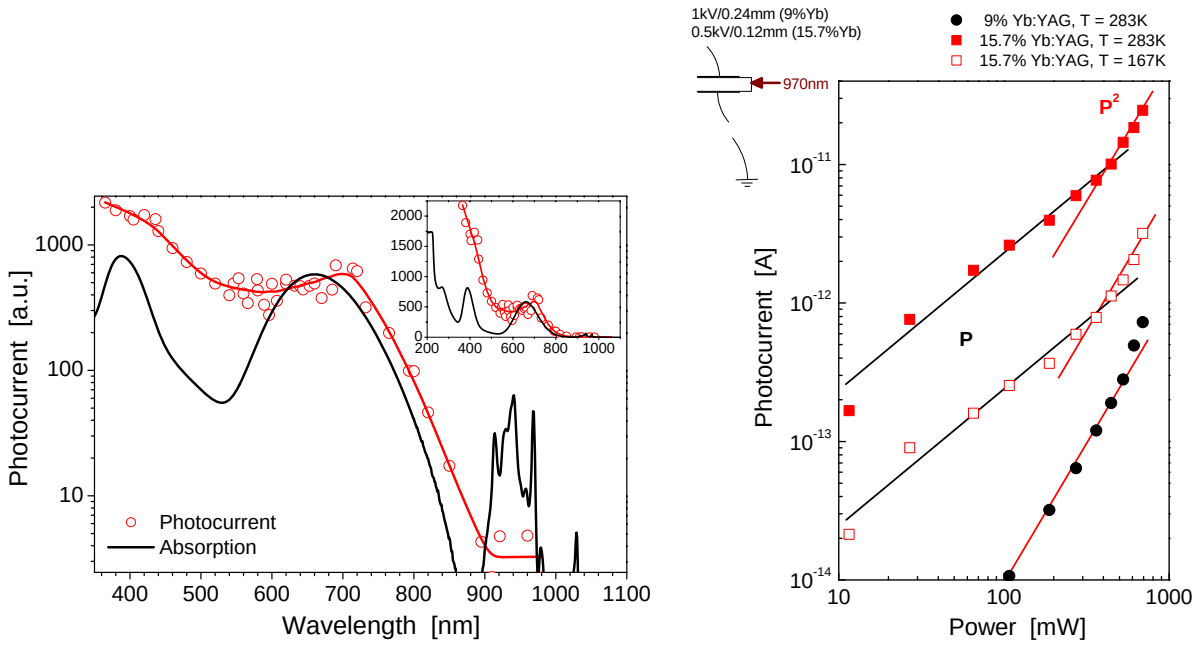

Figure 6.2.: Left: Spectral characteristics of the measured photocurrent in an as-grown 0.3%Si, 1%Yb:YAG single crystal together with the corresponding absorption spectrum plotted in logarithmic scale [Fag07]. The inset shows the same data in linear scale. Right: photocurrent measured for 9% (circles) and 15.7%Yb:YAG (squares) single crystals plotted against the incident pump power in double logarithmic scale [Bas05]. The photocurrent for the 15.7%Yb:YAG sample was measured for two temperatures, $T = 283$K as for the 9%Yb:YAG sample and additionally at $T = 167$K. The x in P^x gives the power dependency found from the fit.

stated as 0.3%[1]. It was the purpose to firstly confirm the suggestion of Henke that the lowest Yb^{2+} $4f^{13}5d$ state lies inside the conduction band in YAG [Hen01], and secondly to determine the energetic positions of the Yb^{2+} ground state with respect to the conduction band of YAG. The measurements were performed using a mercury-vapour lamp, a xenon lamp and a tungsten lamp with different colour filters as excitation sources. The results are plotted together with the corresponding absorption spectrum on the left of figure 6.2. As can be seen, the measured photocurrent clearly follows the long wavelength wing of the broad band absorption peak centred at about 660 nm associated with the Yb^{2+}-ion (see also section 4.2). After reaching a peak at about 700 nm, the photocurrent seems to slightly decrease but then starts increasing again at about 500 nm. These findings strongly suggest that excitation into the lowest $4f^{13}5d$ state of the Yb^{2+}-ion leads to autoionisation due to superposition of the $4f^{13}5d$ and the conduction band states. The onset of the photocurrent at about 900 nm could be treated as an indication for the Yb^{2+} ground state position to be at about 1.4 eV below the bottom of the conduction band. However, this deduction needs to be treated with great care. The position of the bottom of the conduction band itself is not distinctly defined (see sections 3.4.1 and 3.4.2). Furthermore, as stated above the probability of a transition to occur does not only depend on the selection rule but also depends on the overlap of the wave functions of the initial and final states. Even though ionisation from the $4f$ ground state is not based on dipole-dipole interaction and thus is not restricted by any selection rule, as long as the overlap of the wave functions in question is not

[1] Probably given with respect to the available tetrahedral Al-sites.

significant, the respective optical transition will not be accompanied with a high cross-section if observable at all [Sch98] (see also section 3.4.2).

On the right side of figure 6.2 the results of photoconductivity measurements on 9%Yb:YAG and 15.7%Yb:YAG single crystalline laser samples are presented [Bas05]. These samples, originally prepared for thin-disk laser experiments, had thicknesses of 240 µm and 120 µm, respectively and are comparable to those used in the experiments of Larionov *et al.* [Lar05]. The samples were excited at 970 nm by a xenon lamp using colour filters. The measured photocurrent is plotted against the incident pump power in double logarithmic scale. In both samples photocurrents could be detected upon Yb^{3+}-excitation. Both samples exhibited photoconductivity of so-called superlinear (also supralinear) character, i.e. a stronger than linear increase of photocurrent with the intensity of the exciting radiation [Bub92]. The lower doped, thicker Yb:YAG sample had a higher photoconductivity threshold and a pump power dependency of power two. The higher doped, thinner Yb:YAG sample had a lower photoconductivity threshold and at first exhibited a linear increase with pump power up to about 400 mW. For pump powers above 400 mW, also a power two dependency between photocurrent and pump power was observed. The change from a linear to a quadratic relationship between photocurrent and pump power for the 15.7%Yb:YAG crystal suggests that two different types of charge generation processes occur in this sample upon excitation of the Yb^{3+}-ion: at low pump powers a one-step process seems to be responsible for the creation of free carriers, whereas at higher pump powers a higher order process involving two photons seems to be dominant. The 9%Yb:YAG sample displays only the quadratic relationship, which indicates that either the linear process is missing in this sample or simply the sensitivity of the used electrometer was not high enough to detect the photocurrent generated by the linear process. For the 15.7%Yb:YAG sample the photoconductivity measurements were performed for two different temperatures. It was found that the photocurrent drops one order of magnitude when decreasing the temperature from 283K to 167K, while the characteristic itself did not change. This decrease in photocurrent with temperature is suggested to be due to a decreasing mobility of the carriers at lower temperatures.

6.2.2. Photoconductivity Experiments

From the energy level scheme of the Yb^{3+}-ion in YAG, with its ionisation energy larger than the band gap energy (see figure 3.5, section 3.4.2), and the rather simple charge carrier creation mechanisms based on intrinsic or extrinsic absorption processes described above, the photoconductivity observed upon Yb^{3+} excitation cannot be explained. To identify the charge generation routes, further investigations on the photoconducting behaviour of Yb:YAG have been performed in the framework of the diploma works of C. Hirt [Hir07] and U. Wolters [Wol09b], with particular focus on the influence of Yb-doping concentration and the role of divalent Yb-ions, respectively. Additionally, photoconductivity measurements were performed on Yb:YAG ceramic samples. As-grown and annealed Yb:YAG single crystalline samples were compared regarding their photoconductivity properties.

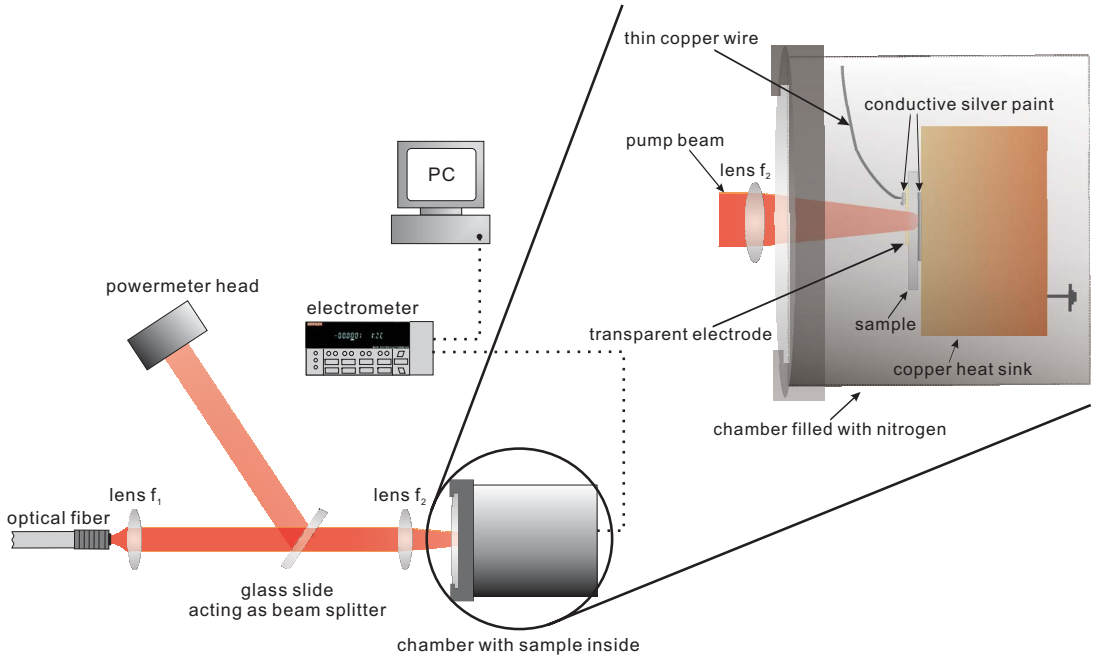

Figure 6.3.: Schematic of the experimental setup used in the photoconductivity investigations. Left: a fiber coupled diode laser emitting at 940 nm is used as pump source. The beam is collimated and focussed onto the sample with a set of lenses which are chosen depending on the desired pump spot size. In the collimated beam a glass slide is positioned as a beam splitter to allow for in-situ monitoring of the pump power. The photocurrent is measured with a picoammeter. For readout the signal is transferred to a computer. Right: the polished sample is attached to the copper heat sink with conducting silver paint, which acts as one of the electrodes. The other electrode is a 2wt.%Al:ZnO layer sputtered onto the front of the sample, which has a high transmittance over a wide spectral range. A thin copper wire is used to apply a voltage of 500 V. The sample is placed inside a chamber filled with dry nitrogen to protect the setup from humidity.

Experimental Setup

If not otherwise stated, the samples were spectroscopy grade polished to about 150 µm thickness and placed between two electrodes on top of a copper heat sink as schematically shown in figure 6.3. The pump source was a fiber-coupled laser diode with an NA of 0.22 and a fiber diameter of 400 µm, which initially was capable of generating a maximum output power of 100 W at 940 nm (JOLD-100-CPXF-2X2P, JENOPTIK Laserdiode GmbH, Germany). The centre wavelength of the laser diode was controlled by a thermoelectric cooler and stabilised between 937 nm and 940 nm in the experiments. Different sets of lenses were used to collimate and focus the pump beam in order to generate different pump spot diameters within the sample. A glass slide was placed at an angle into the collimated pump beam to act as a beam splitter. In this way about 9% of the pump light were reflected so that in-situ monitoring of the pump power was possible. For the laser power measurements a LM-10 HTD sensor together with a powermeter of the FieldMaster-GS Series (Coherent, Inc., USA) was used. To protect the setup from humidity it was placed in a chamber filled with dry nitrogen at a pressure of 200 mbar. A window allowed light to enter the chamber, the transmission rate being about 55% at 940 nm. As the pump light is aligned perpendicular to the sample and the electrodes, one of the electrodes is required to be transparent at the pumping wavelength. Therefore, a 2% Al:ZnO layer of 1 µm thickness and

1 mm×2 mm area was sputtered onto one side of all samples[2]. The Al:ZnO layer has an almost constant transmission rate over a wide wavelength range, only varying between 76% and 78% from 900 nm to 2 700 nm. The other electrode was a thin layer of conductive silver paint located between the sample and the heat sink. A thin copper wire was used to apply a voltage of 500 V. The generated photocurrent was measured with a picoammeter (6485/E, Keithley Instruments, Inc., USA) and data acquisition was controlled by a personal computer using a LabVIEW-based programme. A NTC10K thermistor was attached to the copper heat sink to allow for qualitative monitoring of the heat introduced during the measurements.

The impact of different experimental parameters was investigated to prevent systematic errors and thus ensure comparable and reproducible results [Hir07, Wol09b]. The current-voltage characteristics of the different Yb:YAG samples all exhibited ohmic character below 1 kV of applied voltage. For higher voltages, sparkovers were observed. It has also been found that the quality of the electrodes is not always homogeneous and the photocurrents measured thus varied for different positions on the same sample. The found power law dependencies however, did not significantly change for the different positions. Misalignment of the focus also showed no significant changes in the photocurrent to pump power characteristic so that the alignment of the setup is considered of minor importance regarding the quality of the photoconductivity measurements. The influence of heating was roughly estimated by measuring the photocurrent for a sample, one time allowing it to cool before increasing the pump power and thus keeping the temperature of the heat sink constant and another time without allowing to cool so that the heat sink temperature increased about 6K during measurements. The exponent obtained from the power law dependence was marginally smaller in the case of cooling. However, the differences observed were not of significance in the investigated pump power regime. Yb:YAG samples of different thicknesses prepared from the boule #SNF revealed slightly different exponents in their power law dependencies, however these differences were also of minor importance. Overall it has been concluded that the differences observed due to misalignment, heating and different thicknesses do not significantly influence the results in a qualitative manner. However, the exponents found in the power law dependencies between photocurrents and pump power have to be considered as being afflicted with an error of at least ± 0.2. As for now, quantitative comparison between the photocurrents measured for different samples is not possible.

The Influence of Doping Concentration

To evaluate the dependency of the photoconducting behaviour on doping concentration, Yb:YAG single crystals of concentrations between 10% and 80% as well as YbAG were investigated [Hir07]. All samples were spectroscopy grade polished to a thickness of 150 µm except for the 80%Yb:YAG sample, which had a thickness of 100 µm. For these measurements two lenses with focal lengths of $f_1 = f_2 = 25$ mm were used to achieve a 1:1 image of the fiber end surface onto the crystal resulting in a pump spot diameter of 400 µm.

The measurements confirmed the existence of free carriers in these materials when the Yb^{3+}-ion is excited. The results obtained are plotted in figure 6.4. On the left side the measured pho-

[2]The sputtering of the Al:ZnO layer was performed at the Institute of Micro System Technology, Hamburg University of Technology (TUHH)

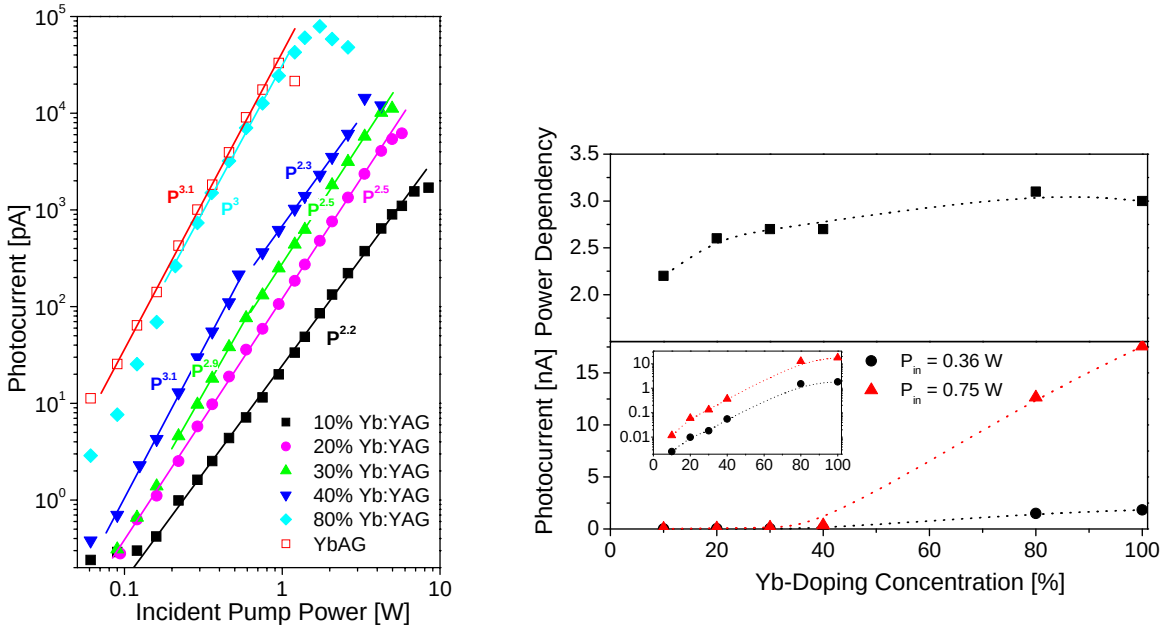

Figure 6.4.: Left: photocurrents measured for Yb:YAG single crystalline samples with Yb-concentrations between 10% and 80% as well as YbAG plotted against incident pump power in double logarithmic scale [Hir07]. The pump wavelength was about 940 nm. All samples had a thickness of 150 µm except for the 80%Yb:YAG sample, which has a thickness of 100 µm. Right: obtained power dependency (top) and photocurrents for two different incident pump powers, $P_{in} = 0.37$ W and $P_{in} = 0.75$ W (bottom) plotted against the Yb-doping concentration. The dotted curves represent assumed trends and are given solely for clarity purpose. See also [Wol09b].

tocurrents are plotted against the incident pump powers in double logarithmic scale. In these experiments, as can be seen on the bottom right of figure 6.4, at same incident pump powers the photocurrent measured is always higher for the sample with the higher Yb-doping concentration. However, as stated above quantitative comparison of the photocurrents measured for different samples have to be treated with great care. In all of the investigated Yb:YAG samples the photocurrent increases superlinearly with pump power. A power two to three dependence between the measured photocurrent and pump power at 940 nm is demonstrated. The exponent of the found power law dependence increases from 2.two to three.1 with Yb-doping concentration as shown on the top of figure 6.4, right. For the 30% and the 40%Yb:YAG samples abrupt changes in the power law dependencies have been found. For both samples in this figure the average of the two found exponents is plotted. In these experiments, all samples displayed some roll-over behaviour, i.e. a decrease in photocurrent with increasing pump power at high excitation levels. It is assumed that this roll-over is occurring due to thermal effects. The sub 100 mW regime was not accessible with the setup used, which could be the reason for the linear relationship between pump power and photocurrent observed in [Bas05] not being observed in these measurements. No photocurrent could be detected for undoped single crystalline YAG samples under 940 nm pumping [Hir07, Wol09b] (see figure 6.5, left).

In addition to these initial measurements [Hir07], photoconductivity measurements were performed on Yb:YAG single crystalline samples of 2% and 6% Yb-doping concentration with thicknesses of 220 µm and 240 µm, respectively. In these measurements the focal lengths of the collimating lens was $f_1 = 45$ mm and that of the focussing lens was $f_2 = 25$ mm. With this imag-

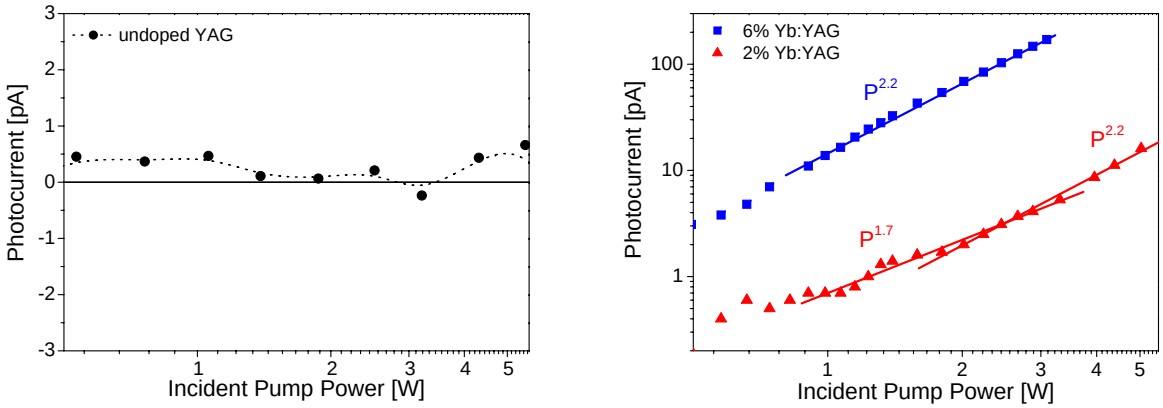

Figure 6.5.: Left: no photocurrent could be measured for undoped YAG at 940 nm pumping [Wol09b]. Right: photocurrents measured at 940 nm pumping for 2% and 6%Yb:YAG single crystalline samples with thicknesses of 220 µm and 240 µm, respectively, plotted against incident pump powers in double logarithmic scale. Note that the axis of ordinate is linear on the left and logarithmic on the right.

ing setup a pump spot diameter of about 150 µm was measured at the sample position[3]. For both samples photocurrents could be detected upon 940 nm pumping. The photocurrent measured for the 2% and the 6%Yb:YAG samples are plotted against the incident pump power in double logarithmic scale on the right side of figure 6.5. The photocurrent measured for 6%Yb:YAG sample was about one order of magnitude higher compared to that for the 2%Yb:YAG sample at the same incident pump power and displayed a power law dependence with exponent 2.2 on the incident pump power. The 2%Yb:YAG sample displayed a change in power law dependence on incident pump power from exponent 1.7 to 2.2. However, currents below 1 pA are very close to the sensitivity limit of the measurement device so that the power law dependency on pump power with the exponent of 1.7 can be neglected. The value of 2.2 for the exponent is the same as found for the 10%Yb:YAG single crystalline sample.

Photoconductivity in the Presence of Divalent Yb-Ions and Oxygen Vacancies

Photoconductivity measurements under irradiation with 940 nm pump light on a as-grown 20% Yb:YAG single crystal of 150 µm thickness, using $f_1 = 45$ mm and $f_2 = 25$ mm imaging, revealed one order of magnitude higher photocurrents compared to its annealed counterpart (see figure 6.6, left). However, in these measurements both samples displayed the same power law dependence between photocurrent and pump power with an exponent of 2.1. This exponent is more than 10% smaller than the value found for 20%Yb:YAG in [Hir07]. However, as stated above the error estimated for the exponent is in the same order of magnitude and thus the deviations between these values are considered not significant. The difference in the magnitude of the photocurrents measured for the two samples suggests strongly the involvement of either divalent Yb-ions or oxygen vacancies or both in the enhancement of the photoconductivity. Therefore, under the assumption that silicon is incorporated into YAG as Si^{4+} on the

[3]The beam profile of the pump spot was measured using a CCD camera of the FK-7512-IQ series (Pieper GmbH, Germany)

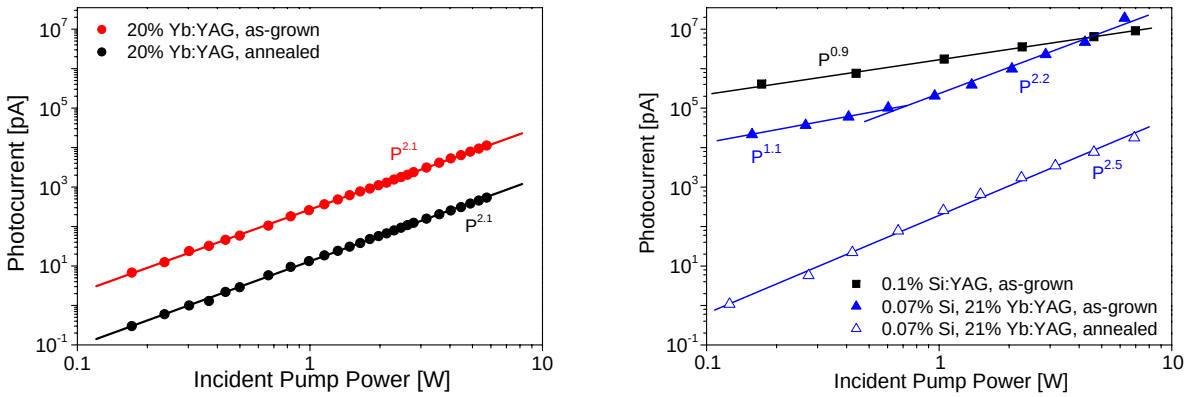

Figure 6.6.: Left: photocurrents measured in annealed and as-grown 20%Yb:YAG single crystals of 150 µm thickness plotted against incident pump powers in double logarithmic scale. Right: photocurrents measured in as-grown, single crystalline 0.1%Si:YAG of 1.7 mm thickness as well as as-grown and annealed 0.07%Si,21%Yb:YAG single crystalline samples of 150 µm thickness plotted against the incident pump power in double logarithmic scale [Wol09b].

tetrahedral sites [Gel67] and stabilises divalent Yb-ions, 21%Yb:YAG samples with different Si-codoping were grown and investigated together with a 0.1%Si:YAG sample[4] regarding their photoconducting properties [Wol09b]. As an example, on the right of figure 6.6 the photocurrents measured under 940 nm pumping for the as-grown 0.1%Si:YAG single crystal of 1.7 mm thickness are plotted against the incident pump power in double logarithmic scale together with those for as-grown and annealed 0.07%Si, 21%Yb:YAG single crystalline samples[5], both of which had a thickness of 150 µm. The 0.1%Si:YAG sample displayed an almost linear increase with pump power with an exponent of 0.9. The photocurrents for the Si-codoped Yb:YAG samples dropped several orders of magnitude after annealing. Furthermore, the characteristics of the pump power dependence changed upon annealing. For the as-grown sample at lower incident pump powers an almost linear relationship was found between photocurrent measured and pump power. For higher incident pump powers a close to quadratic power law dependence on pump power was found. In contrast, no linear relationship in the low power regime could be observed for the annealed samples. Over the whole measurement range, a close to quadratic relationship, or as in the case depicted in figure 6.6, right for the 0.07%Si, 21%Yb:YAG sample, a power law dependence with exponent 2.5 was found. No photocurrent could be detected under 940 nm irradiation in the 0.1%Si:YAG sample after annealing. It should be noted that no Al:ZnO coating was applied to the 0.1%Si:YAG sample.

Photoconductivity in other Yb-Doped Materials

In the same setup, Yb:YAG ceramic samples were investigated regarding their photoconducting properties and compared to their single crystalline counterparts. The results for the 15.0% and the 21.6%Yb:YAG ceramic samples are shown in figure 6.7, left and right, respectively together

[4]Nominal Si-concentration, probably given with respect to the available tetrahedral Al-sites.

[5]Si-concentration given with respect to the available tetrahedral Al-sites and Yb-concentration given with respect to the available Y-sites. Both determined by microprobe measurements [Wol09b].

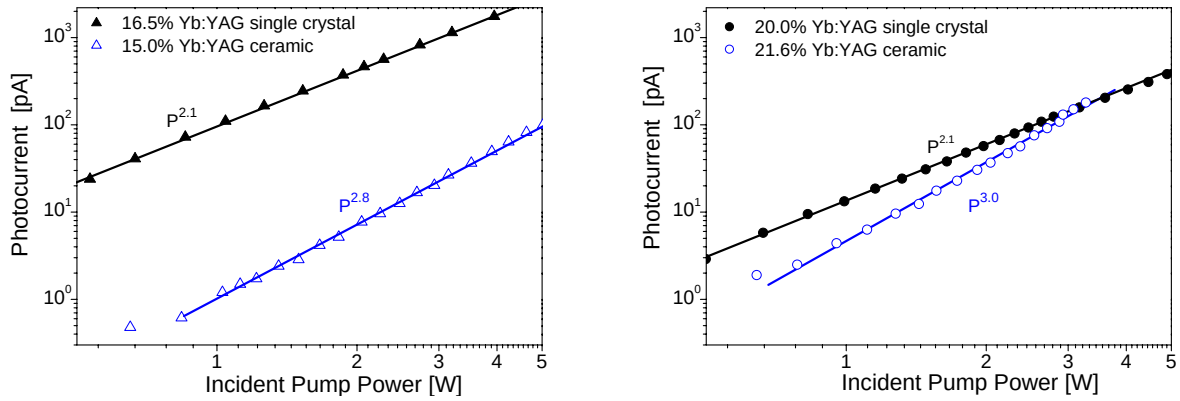

Figure 6.7.: Left: photocurrents measured for a 15.0%Yb:YAG ceramic sample of 150 µm thickness and for comparison that for a 16.5%Yb:YAG single crystal of 170 µm thickness (boule #SNF) plotted against incident pump power in double logarithmic scale [Wol09b]. Right: photocurrents measured in a 21.6%Yb:YAG ceramic sample together with those for a 20.0%Yb:YAG single crystalline sample plotted against incident pump power in double logarithmic scale. Both samples had a thickness of 150 µm.

with those obtained for single crystalline 16.5%Yb:YAG and 20.0%Yb:YAG, respectively. The ceramic samples and the 20.0%Yb:YAG single crystal had all a thickness of 150 µm and the 16.5%Yb:YAG single crystal had a thickness of 170 µm. As stated above, quantitative comparison between the measurement results need to be treated with great care. However, the results obtained indicate that at low pump powers the ceramic samples exhibit lower photocurrents than single crystalline samples with comparable Yb-doping concentrations. Regardless of the Yb-doping concentration, the ceramics displayed an almost cubic power law dependence on pump power whereas a nearly quadratic dependence was found for the single crystalline counterparts.

Photoconductivity measurements with $f_1 = f_2 = 25$ mm imaging of the pump light were also performed on various Yb:YAG single crystalline samples codoped with cerium, chromium and erbium [Hir07] as well as one YbAG single crystal codoped with iron [Wol09a]. Cerium and chromium can both be incorporated into the YAG lattice as trivalent as well as tetravalent ions. Cr^{4+} usually occupies the tetrahedral lattice site in YAG. Charge compensation is needed and usually accomplished by divalent codoping of calcium or magnesium. Cr^{3+} is also incorporated on the octahedral site [Küc95]. These two ions were chosen as they are both known as fast recombination centres for free carriers, used for radiation hardening in space applications [Dic01]. Erbium was chosen as a codopant since this lanthanoid is an often found impurity in the Yb_2O_3 raw material used for the growth of Yb:YAG crystals. Iron is also an often found impurity which is usually introduced during crystal growth from the crucible into the melt [Fag07]. Iron usually is incorporated in its trivalent oxidation state onto both the aluminium sites in YAG. The Al^{3+}-ions can successively be substituted by the Fe^{3+}-ions so that YAG and YIG ($Y_3Fe_5O_{12}$) form a solid solution. Even though energy transfer processes from excited Yb^{3+}-ions to Er^{3+}-ions are well known in Er,Yb:YAG systems, codoping of erbium did not show any significant effect on the photoconducting properties of Yb:YAG. As can be seen on the left of figure 6.8, the measured photocurrents were in the same order of magnitude as for the pure Yb:YAG counterpart. A cubic dependency on pump power was found for this sample. The Ce-codoped Yb:YAG

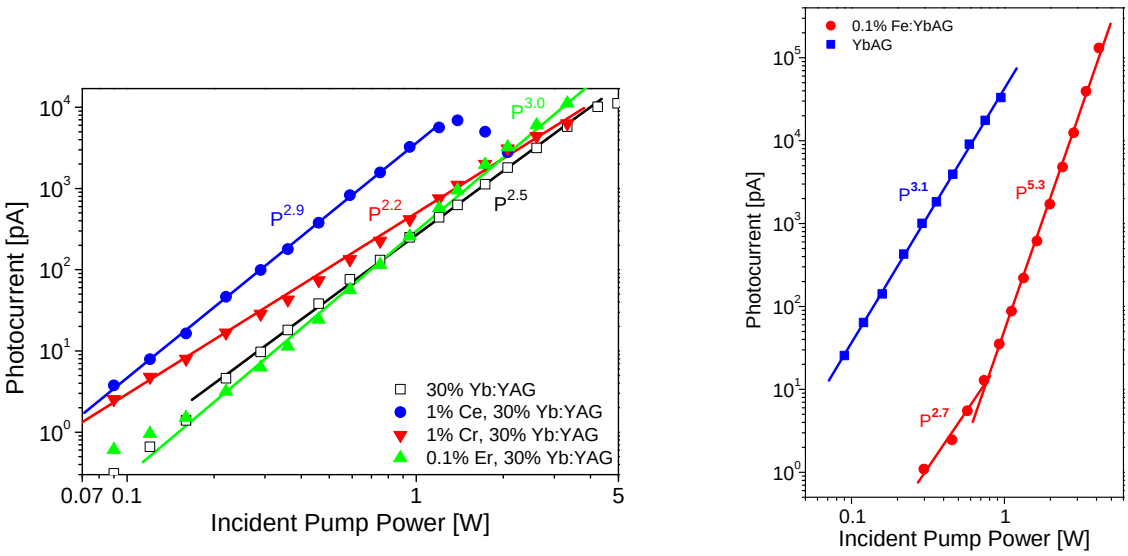

Figure 6.8.: Left: photocurrents measured for pure and codoped 30%Yb:YAG plotted against incident pump power in double logarithmic scale. The investigated codopants were cerium, chromium and erbium. All samples had a thickness of 150 µm. Data taken from [Hir07]. Right: photocurrents measured for 0.1%Fe:YbAG under irradiation with 940 nm pump light together with those measured for YbAG plotted against incident pump powers in double logarithmic scale [Wol09a].

samples displayed almost one order of magnitude higher photocurrents compared to Yb:YAG samples of the same Yb-doping concentration. The exponent of the power law dependence between photocurrents measured and pump power was found to be between 2.5 and 3 for the Ce-codoped samples, which is comparable to those found for the pure Yb:YAG samples of corresponding Yb-concentrations. In contrast, codoping with chromium led to a slight change of the photocurrent characteristics in 30%Yb:YAG. At lower pump powers, an almost one order of magnitude higher photocurrent was measured for the Cr-codoped sample compared to the pure Yb:YAG counterpart. The exponent obtained from the power law dependence suggests a close to quadratic relationship between photocurrent and pump power, which is smaller than the exponent found for pure 30%Yb:YAG. The YbAG single crystalline sample codoped with iron exhibited significantly different behaviour compared to the pure YbAG sample in the photoconductivity measurements as shown on the left of figure 6.8. $f_1 = 45\,\text{mm}$ and $f_2 = 25\,\text{mm}$ imaging was used in these measurements. At lower pump powers the relationship between the photocurrent measured for the 0.1%Fe:YbAG sample and the pump power was close to cubic, which is in accordance to the relationship found for the pure YbAG single crystalline sample over the whole pump power regime investigated. At higher pump powers however, the characteristic for the Fe-codoped sample changes to a power law dependence with an exponent of more than 5.

The results obtained from the photoconductivity measurements for the different samples are summarised in table 6.1.

Sample	d [µm]	Pump Spot ∅ [µm]	$I_{photo,max}$ [nA]	P_{pump} [W]	Exponent	Comment
YAG	150	150	-	5.5	-	
2%Yb:YAG	220	150	0.02	5.1	2.2	
6%Yb:YAG	240	150	0.2	6.2	2.2	
10%Yb:YAG	150	400	1.7	8.5	2.2	
15%Yb:YAG	*150*	*150*	*0.1*	*5.0*	*2.8*	*ceramic*
16.5%Yb:YAG	170	150	1.8	3.9	2.1	boule #SNF
20%Yb:YAG	150	400	6.2	5.7	2.5	
20%Yb:YAG	150	150	0.5	5.8	2.1	
20%Yb:YAG	150	150	11.3	5.8	2.1	as-grown
21.6%Yb:YAG	*150*	*150*	*0.2*	*3.3*	*3.0*	*ceramic*
30%Yb:YAG	150	400	11.2	5.0	2.7	
40%Yb:YAG	150	400	61.0	2.6	2.7	
80%Yb:YAG	100	400	79.0	1.7	3.0	
YbAG	150	400	33.1	1.0	3.1	
0.07%Si, 21%Yb:YAG	150	150	17.8	6.9	2.5	
0.07%Si, 21%Yb:YAG	150	150	1.9×10^4	6.3	1.1 / 2.2	as-grown, n.c.
0.1%Si:YAG	1700	150	-	-	-	n.c.
0.1%Si:YAG	1700	150	9.1×10^3	7.0	0.9	as-grown
1%Ce, 30%Yb:YAG	150	400	6.9	1.4	2.9	
1%Cr, 30%Yb:YAG	150	400	6.3	3.3	2.2	
0.1%Er, 30%Yb:YAG	150	400	11.2	3.3	3.0	
0.1%Fe:YbAG		150	131.0	4.2	2.7 / 5.3	n.c.
10%Yb:Lu_2O_3	150	400	82.0	0.7	1.4 / 2.0	see appendix G
5%Yb:$LiYF_4$	900	150	1.3	6.7	2.3	see appendix G
30%Yb:$LiYF_4$	320	150	6.3	3.8	1.0 / $>$ 10.0	see appendix G

Table 6.1.: Summary of experimental results obtained from the photoconductivity measurements under 940 nm irradiation for the different samples. Sample thickness d, pump spot diameter ∅, the maximum obtained photocurrent $I_{photo,max}$ and the corresponding pump power P_{pump} and the exponent obtained from the power dependency of the photoconductivity characteristics are given. n.c. stands for nominal concentration. All samples were annealed under oxidising conditions if not otherwise stated. Dashes indicate that no photocurrent could be observed for the respective sample under the experimental conditions applied. The ceramic samples are indicated by italic letters. See text for discussion.

6.3. Discussion and Model Descriptions

The experimental results leave no doubt that free carriers are created and currents up to several hundreds of nanoamperes are generated in Yb-doped materials under 940 nm excitation. Irradiation of undoped YAG with 940 nm pump light did not lead to conductivity and thus confirmed for Yb:YAG the involvement of Yb-ions in the current generating process. The exponents found from the power law dependence between photocurrent measured and pump power in the case of the Yb-doped oxides (except for the Fe- and Si-codoped systems) ranged typically between 2 and 3. The value of this exponent is usually associated with the order of the process, i.e. the exponent gives the number of pump photons needed for the creation of one free carrier [Bas92, Jou04][6]. If the absorption efficiency stays constant over the measurement range, plotting against incident pump power and absorbed pump power would both lead to characteristics with the same exponent. The value of the exponent is then, because the pump quantum efficiency in Yb:YAG is 1, directly associated with the number of excited Yb^{3+}-states involved in the process. This assumption however, is not unrestrictively valid for Yb:YAG. Due to bleaching, the absorption efficiency decreases at high intensities (see also section 2.2.1, Saturation of the Ground State Absorption). The pump saturation intensity of Yb:YAG is about 24 kW/cm^2 [Bru97]. For the photoconductivity measurements where the 1:1 imaging was applied, the maximum pump intensity was about 8 kW/cm^2, so that in first approximation the effect of bleaching can be neglected. For the experiments with a pump spot diameter of about 150 µm, the situation is much different as in this case pump intensities as high as 45 kW/cm^2 might have been reached. In this case, the observed slopes in the photocurrent incident pump power characteristics would lead to an underestimate for the true exponent value and the order of the process. However, as the measurements on the same sample using the two imaging setups led to comparable results and the dependency between photocurrent measured and pump power did not change in the measurement range, the effect of pump absorption saturation is in the following discussion neglected. For further discussion of the problem also refer to [Wol09b]. The photoconductivity measurement results are thus understood in a way that two to three excited Yb^{3+}-ions are needed in the creation process of one free carrier. The investigations on different experimental parameters led to a systematic error estimate of the exponent of at least 0.2. An exponent of 2.5 obtained from the measurements can thus stand for either a quadratic or a cubic relationship, which leads to the conclusion that at present a clear distinction between quadratic and cubic relationship is not possible (see also [Wol09b]). Therefore, despite the measurements on differently concentrated Yb:YAG samples suggested a slight increase of the order of the process with Yb-doping concentration, it is assumed that the physical process leading to the generation of current is the same in the Yb:YAG samples regardless of their concentration. The comparison between as-grown and annealed 20%Yb:YAG revealed the same characteristics for both samples, but an one order of magnitude higher photocurrent for the as-grown sample. This suggests that the same process is responsible for the generation of photocurrent in the samples, but the presence of divalent Yb-ions or oxygen vacancies or both in the as-grown sample enhances photoconductivity.

[6] It should be noted that in semiconductor physics often superlinearity of photocurrent versus pump power is attributed to the recombination properties and different classes of ground states in the material investigated, see e.g. [Ros55].

However, from the energy level structure introduced in section 3.4.2 for Yb:YAG, photoconductivity upon Yb^{3+}-excitation is not expected in this material. In the following sections the experimental results are discussed, with particular regard to possible current generating mechanisms.

6.3.1. The Role of Codopants

Codoping with silicon led to significantly higher photocurrents compared to the pure Yb:YAG samples and at lower powers a linear dependency between photocurrent and pump power was observed. The pump power dependence of the photocurrent at higher powers was the same as for the pure, annealed Yb:YAG samples. The as-grown 0.1%Si:YAG sample displayed a linear photocurrent pump power characteristic over the whole range of measurement, however after annealing no photocurrent could be detected under 940 nm irradiation. In the case of the Si-codoped Yb:YAG samples, the photocurrent measured did not only decrease several orders of magnitude after annealing, but also lost its linear relationship in the lower pump power regime. Therefore, it is deduced that in as-grown Si-codoped Yb:YAG at lower pump powers the photocurrent is generated by an Yb-independent one-photon process with the involvement of silicon and oxygen vacancies. At higher pump powers however, the same process as for the pure Yb:YAG samples becomes dominant. It has been shown that silicon does not only occupy the tetrahedral site in YAG in its tetravalent state but is also incorporated into YAG in its divalent state onto the centrosymmetric octahedral site, especially when the crystal is grown under reducing atmosphere. In the first case, the Si^{4+}-ion stabilises a divalent rare earth ion. In the latter case, the Si^{2+}-ion is charge compensated by an oxygen vacancy with one electron, i.e. an F^{+}-centre. Such a complex centre was identified in as-grown Si:YAG by low temperature electron nuclear double resonance (ENDOR) measurements, which confirmed the presence of loosely bound electrons in the vicinity of the silicon nuclei [Fag07]. It is suggested that this complex centre has an electron donor state located close to the minimum of the conduction band, so that 940 nm light is sufficient to create free electrons in the conduction band. It is thus also possible that the Si^{2+}-ion alone is the electron donor state responsible for the current generation under 940 nm irradiation [Wol09b]. A similar process was proposed in [Fag04] (see appendix F). Some publications locate the F^{+}-centre within 1 eV below the conduction band minimum, e.g. [Rot85, Che94][7], so that this centre might also act as an electron donor. However, as no linear power law dependence was found in the photocurrent pump power characteristics of as-grown Yb:YAG samples, in which the presence of F^{+}-centres was clearly identified (see section 4.2), the contribution of F^{+}-centres as electron donor states under 940 nm irradiation is neglected. The disappearance of photoconductivity after annealing in air observed in the 0.1%Si:YAG sample suggests that the Si^{2+}-ions are oxidised to another valency and thus cannot longer act as electron donors. It was expected that codoping with cerium and chromium would lead to a decrease in photocurrent as both ions are known as fast recombination centres for electrons in the conduction band. However, such an effect could not be observed. In the contrary, for lower pump powers the photocurrents in the codoped Yb:YAG samples were even about one order of

[7] The notation of oxygen vacancies and colour centres is not consistent in the different publications (Kröger-Vink notation, historical labels, etc. See also [Bri90].). It is assumed that in [Che94] some errors might have slipped in.

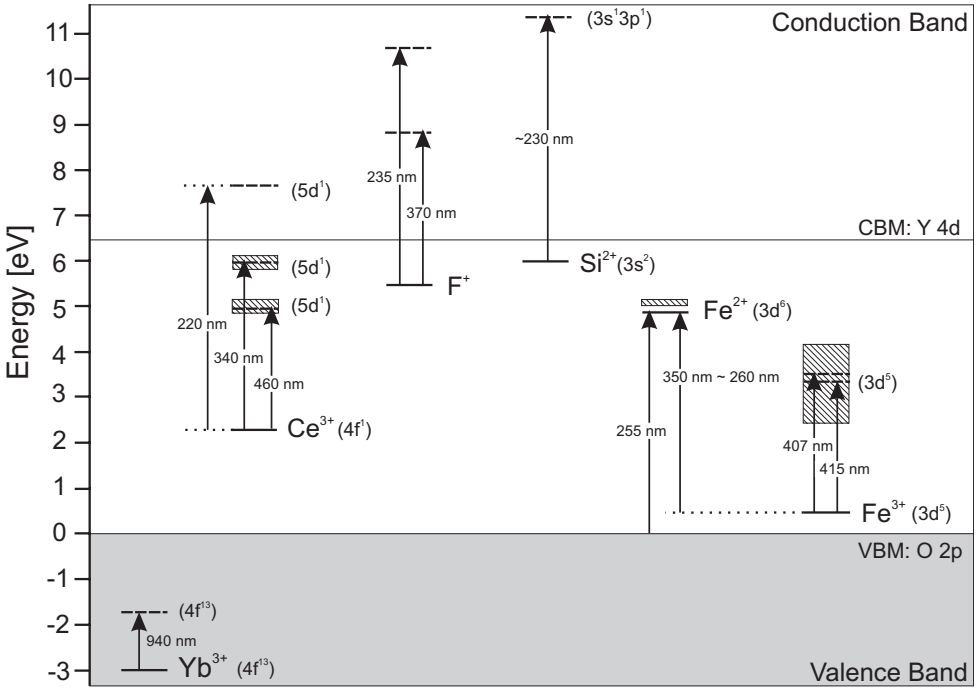

Figure 6.9.: Schematic representation of the energy level locations of the codopants investigated in the photoconductivity measurements, the F^+-centre and the Yb^{3+}-ion relative to the YAG host bands. CBM stands for the conduction band minimum and VBM for the valence band maximum. The solid lines give the binding energies of the ground states relative to the maximum of the valence band and the dashed lines indicate energy levels of different electronic configurations of the different centres. The associated electron configuration is given in brackets. Hatched boxes indicate broad energy bands typical for *d*-states. The Yb^{3+} and Ce^{3+} binding energies are according to section 3.4.2, the Ce^{3+} interconfigurational transitions as well as the position of the F^+-centre are according to [Rot85], the absorption bands of the F^+-centre are taken from [Spr91], the Si^{2+} binding energy is estimated from the photoconductivity measurements [Wol09b, Fag04], the assignment of the singlet to singlet absorption band for the Si^{2+}-ion is based on [Zha97], the charge transfer band $O^{2-} + Fe^{3+} \rightarrow O^- + Fe^{2+}$ at 255 nm is taken from [Sco74]. The position of the Fe^{3+} ground state is according to [Sco77] as are the assignments of the iron to iron charge transfer bands $Fe^{3+} + Fe^{3+} \rightarrow Fe^{2+} + Fe^{4+}$. The intraionic transitions of Fe^{3+} are taken from [Rot89b]. For the level position of Fe^{3+} no difference was made between octahedral and tetrahedral lattice sites in this schematic representation. A detailed description can be found in [Sco74, Sco77].

magnitude higher than for pure Yb:YAG. This behaviour cannot be explained at the current state of knowledge. Nevertheless, the observations could be an indication for the current not being generated by free electrons in the conduction band but somewhere else. The photoconductivity characteristics of the 0.1%Fe-doped YbAG sample suggests that at lower pump powers the same mechanism is responsible for the generation of photocurrent as for the Yb:YAG samples whereas a different process leading to an exponent of more than 5 is dominant for higher pump powers. According to [Sco74], the lowest excited state of the Fe^{3+}-ion in YAG $^4T_{1g}$ is located about 1.4 eV above the ground state $^6A_{1g}$ and belongs to the octahedral site. Despite the absorption being rather weak on this transition due to parity selection rules together with the inversion symmetry of the octahedral site, it is possible that the Fe^{3+}-ions are directly excited by the 940 nm pump light used in the photoconductivity measurements. The Fe^{3+}-ion can also be excited by cooperative energy transfer from two excited Yb^{3+}-ions [Fag07], which could lead to the power 2.3 observed for the lower pump power regime. Yet, excitation of trivalent

iron cannot explain the conductivity observed. On the other hand, the $^5T_{2g}$ ground state of divalent iron is known to be located about 1 eV below the conduction band minimum [Che94]. Even though the 0.1%Fe:YAG crystal investigated was transparent and no oxygen vacancies or impurities stabilising the Fe^{2+}-ion are expected, it is possible that divalent Fe-ions were present in the sample. However, no linear relationship between photocurrent and pump power could be observed. Although iron is known to induce an impurity band[8] within the band gap of YAG, in which electrons can be transported through a small polaron process[9] with an activation energy of 0.7 eV [Rot98], the concentration of nominally 0.1% iron of the sample is much too small for such a band to be formed. At the current state of knowledge, the highly nonlinear dependence on pump power with an exponent of 5 for the 0.1%Fe:YbAG at higher pump powers cannot be explained.

In figure 6.9 the binding energies associated with the different optical centres are given with respect to the maximum of the valence band in YAG. The corresponding references are given in the caption. The binding energies and energy levels for the Cr^{3+}- and Cr^{4+}-ions are not included. For the location of these energy levels in YAG see e.g. [Bik90, Chi99].

6.3.2. Charge Transport Models

Although the measurement results obtained from photoconductivity experiments using differently codoped Yb:YAG samples provided some useful information, the generation of photocurrents in Yb:YAG observed under 940 nm irradiation could not be explained. A lot of questions are left unanswered. Key questions concern the nature of the carriers, where the free carriers come from and where the current is carried. In the following, to find possible underlying physical mechanisms for the observations, these questions are discussed in detail.

General Considerations

The nature of the charge carriers is probably the most straight forward to identify. There are three possibilities: the current can be transported by either electrons, holes or ions in a solid. Typically, the mobility of electrons in solids is due to their smaller effective masses much higher than those of holes or ions so that electrons in most cases are the majority charge carriers in occurring currents [Yac03]. Even though the contributions of other charge carriers cannot be excluded at the current state of knowledge, these can be in first approximations be neglected. Also, the quite high values of up to several nanoamperes for the photocurrents found point towards electronic conductivity.

Before discussing the possible initial and final states of the current generating process in Yb:YAG, some basic considerations regarding charge transport models should be addressed. There are two possibilities for charge transport in a doped non-metallic solid [Mot61]: as briefly

[8] The $3d$ orbital of Fe^{3+} is partially filled with 5 electrons. At high concentrations, these $3d$ orbitals start to overlap and the electrons begin to delocalise over the Fe-ions. The width of this impurity band is dependent on the Fe-concentration [Rot98] (see also section 6.3.2).

[9] A polaron can be understood as a slow electron plus associated ionic polarisation [Bub54]. A small polaron process can be described as a hopping process.

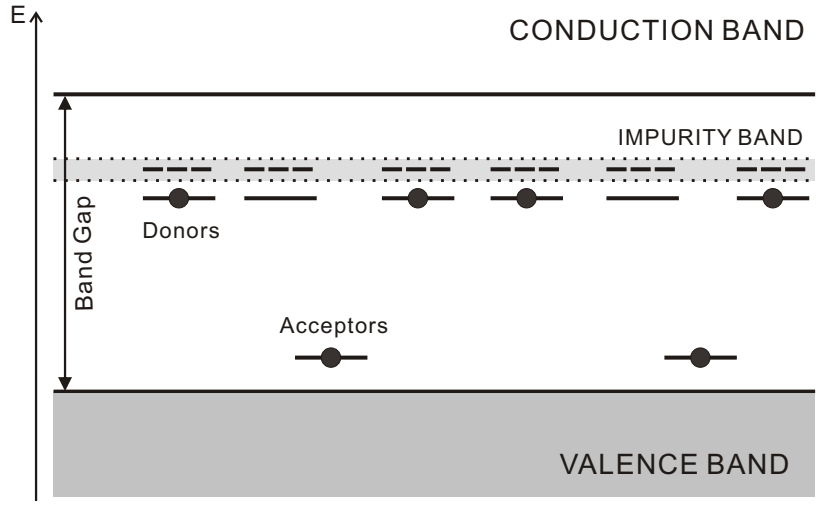

Figure 6.10.: Schematic illustrating the formation of an impurity band in an n-type semiconductor following [Erg52] and [Mot61]. Solid lines represent centres and filled circles electrons in them. Dashed lines represent excited states of the localised centres. If the concentration of electron donor states is large and the centres start interacting with each other, it is possible that the more extended wave functions of the excited states begin to overlap with each other and form a so-called impurity band. If the donor ions are excited into these states, electrons can be transferred to neighbouring, due to the presence of acceptors empty, donor states. In this way, electrons can be transported by a kind of hopping mechanism through the lattice. See text for details.

described in the beginning of this chapter, in semiconductors occurring (electronic) currents are mainly carried by electrons in the conduction band. Nonetheless, it is also possible that an overlap exists between the wave functions of electrons on neighbouring donor states. Under certain circumstances a conduction process is possible in which the electron moves between donor centres without activation into the conduction band states. Such a conduction is referred to as impurity conduction and the overlapping donor states are referred to as an impurity band. The impurity band is usually formed by the interaction of the excited states of the dopant ions and is strongly dependent on the doping concentration [Erg50]. At low concentrations the wave functions are localised and their presence has no effect on the conduction mechanism. As the doping concentration is increased, neighbouring ions approach each other. Overlapping begins between the wave functions of the excited states[10] and as indicated in figure 6.10, the energy levels broaden into quasi-continuous band-like states. The bottom of this band is lower in energy the higher the concentration of the dopants and thus the stronger the delocalisation of the excited states [Erg52]. For an impurity current to occur, an activation energy is required, which promotes the bound electron from its ground state into this impurity band. In addition, for electrons to be transported through this impurity band, some of the electron donor states have to be empty, i.e. a certain amount of acceptor states is also needed [Mot61]. As the electrons jump from occupied to unoccupied donor states, the positive vacancies move through the host lattice. These charge transfer transitions from occupied to unoccupied donor states can also be understood in terms of a hopping process. At high concentrations, the donor ions might be located so close to each other that very strong interactions take place and metallisation occurs [Mot61]. In this case, neither the presence of acceptor centres nor an activation energy is

[10]The wave functions of excited states are usually more extended and the associated electrons have lower binding energies compared to the ground state (see e.g. section 2.2.1).

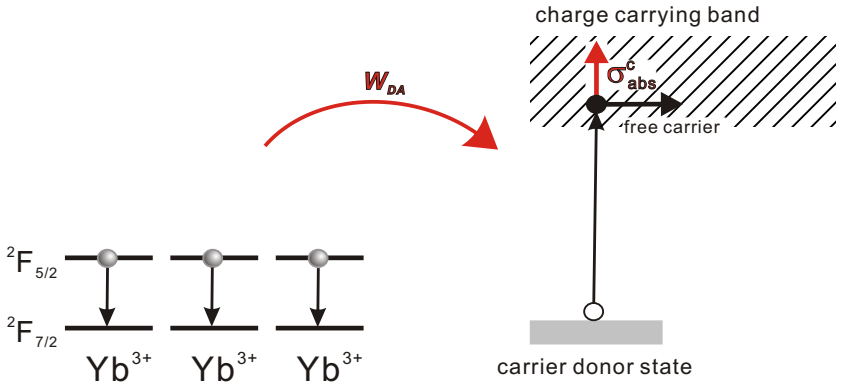

Figure 6.11.: Schematic representation for the energy transfer mechanism involving three excited Yb^{3+}-ions leading to the creation to free carriers. The results of photoconductivity measurements carried out under 940 nm irradiation in Yb:YAG suggest the involvement of two to three excited Yb^{3+}-ions in the current generating process. In this schematic model the Yb^{3+} excited states are indicated by grey spheres on the black lines labelled with $^2F_{5/2}$. The interaction occurs between the excited Yb^{3+}-triplet and the electron donor state, where the coupling parameter is denoted W_{DA}. The electron donor state and the current carrying band are depicted in the style of one-electron jump diagrams: filled circles represent electrons and open circles holes. The possibility of free carrier innerband absorption is indicated by the absorption cross-section σ^c_{abs}.

needed, i.e. already in the ground state the electrons behave like a degenerate electron gas and are delocalised over all donor states. In general, compared to currents in the conduction band, currents carried in an impurity band are orders of magnitudes smaller due to the much lower carrier mobility. It should be also noted that in such a classical impurity conduction mechanism the initial and the final states of the process both belong to the donor ion and no host energy states are involved.

Electron Transport in Yb:YAG

Assuming that the photocurrents observed are based on electron transport, the initial state of the process needs to be an electron donor state. The measurement results using Yb:YAG indicate the involvement of two to three Yb^{3+}-excitations in the current generating process. The current carrying band thus needs to be located at about 2.5 eV to 4 eV above the electron donor state as schematically depicted in figure 6.11.

In the case of the as-grown Yb:YAG samples, in which divalent Yb-ions are present, the interpretation is less complicated. From the excitation spectrum of photoconductivity in the as-grown Si-codoped 1%Yb:YAG sample [Fag07] (see also figure 6.2, left), it is known that direct excitation of the Yb^{2+} $4f^{13}5d$ state leads to measurable photocurrents. From fluorescence lifetime measurements it is also known that cooperative energy transfer processes from two excited Yb^{3+}-ions to one Yb^{2+}-ion exist in as-grown Yb:YAG crystals [Fag07]. With the energy level positions of the Yb^{2+}-states relative to the YAG host bands discussed in section 3.4.2 (see also figure 3.5), a quite complementary picture for the physical mechanism underlying the photoconductivity in as-grown Yb:YAG can be deduced. In these samples, the electron donor state is identified as the ground state of the Yb^{2+}-ion and the current carrying band is the conduction band as schematically shown in figure 6.12. The energy of two excited Yb^{3+}-ions

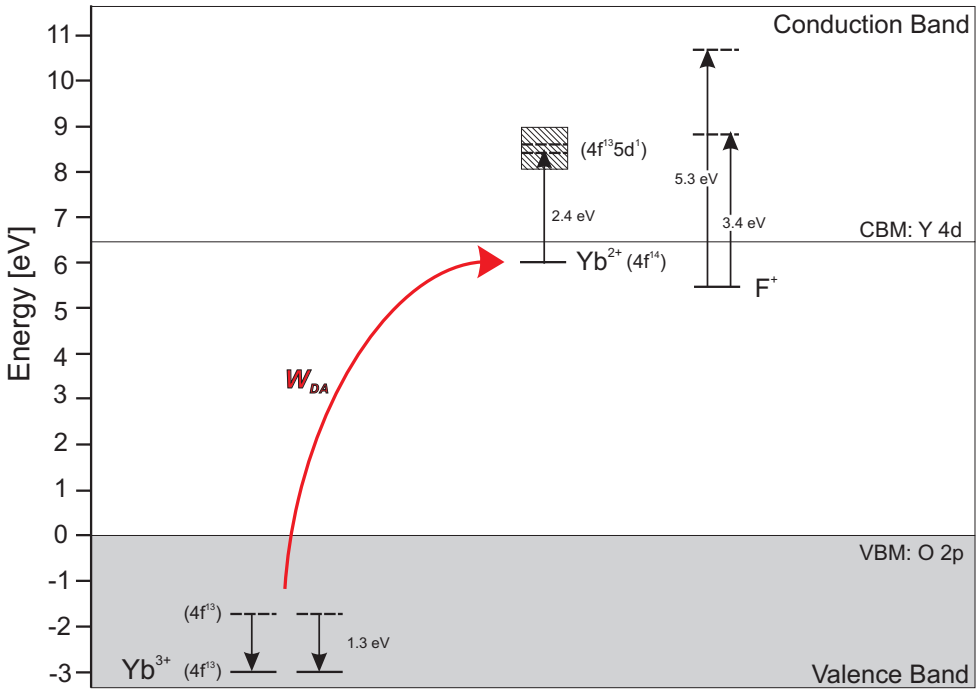

Figure 6.12.: Schematic representation of the energy transfer process leading to photoconductivity in as-grown Yb:YAG samples. The 940 nm pump light raises Yb^{3+}-ions to their excited state. Two excited Yb^{3+}-ions with a coupling parameter W_{DA} cooperatively transfer their energy to an Yb^{2+}-ion charge compensated by an F^{+}-centre. The ground state of the Yb^{2+}-ion acts as an electron donor state from which an electron is first promoted to a $4f^{13}5d$ configuration and subsequently autoionised to conduction band states. See also [Wol09b].

is transferred to the Yb^{2+}-ion, which is excited to the $4f^{13}5d$ state, from which an electron is subsequently transferred by autoionisation to conduction band states (see also [Wol09b]).

For annealed Yb:YAG samples, the presence of oxygen vacancies which could stabilise Yb-ions in their divalent oxidation states is considered unlikely. Despite the existence of defects and impurities which might stabilise Yb^{2+} cannot be excluded in the samples, from the spectroscopical results obtained in chapter 4, their concentrations are assumed to be negligible. Therefore, at first the contribution of Yb^{2+}-ions as electron donor states has to be dismissed for the photoconductivity process in annealed Yb:YAG samples. Since the band gap of YAG is about 6.5 eV [Thi01] (see also discussion in section 3.4.1), the energy equivalent to two to three Yb^{3+}-excitations is not enough for an intrinsic absorption mechanism, where electrons are excited from the top of the valence band into the conduction band. Thus, if the electron donor state is the top of the valence band, the conduction band is excluded to be the current carrying band. On the other hand, if the current carrying band is the conduction band, the electrons cannot originate from the top of the valence band. The second case requires electron donor states about 2.5 eV to 4 eV below the minimum of the conduction band if direct ionisation is possible or impurity states which have an excited state about 2.5 eV to 4 eV above their ground state inside the conduction band, from which autoionisation can occur. This can be compared to the situation in as-grown Yb:YAG, where the Yb^{2+}-ion acts as the electron donor. Furthermore, the presence of impurities in the investigated samples is considered low and thus this second case is not further discussed.

Impurity Band Conduction in Yb:YAG

In the following the first case is discussed in detail. An empty band in the forbidden gap of the host is needed, into which electrons can be raised from the valence band. In line with the concept of the classical impurity band briefly introduced above, one can think of empty states with overlapping wave functions. From now on, the terms donor and acceptor will be used according to the initial states of the current generating process. As a first step impurities are considered to be present in the YAG host crystal, which have an electron acceptor state at about 2.5 eV to 4 eV above the top of the valence band in the forbidden gap. These states are populated by a charge transfer (CT) process, where an electron is transferred from a ligand oxygen ion to the acceptor ion. A current can be transported if electrons raised into the acceptor states are subsequently transferred to neighbouring empty acceptor states. This however, can only be accomplished if the acceptor ions are located close to each other so that their wave functions display significant overlap. In addition, the activation energy for the inter-acceptor CT transition needs to be low enough so that thermal activation is possible already at room temperature. The first condition certainly cannot be achieved by impurities which usually are found in ppm order. The only candidate acceptor ion, which could accomplish this requirement in high purity Yb:YAG has to be the Yb-ion. Indeed, the Yb^{3+}-ion has an electron acceptor state in the band gap. This state is the Yb^{3+}/Yb^{2+} CT state described and discussed in sections 3.6.1 and 4.4. For the optical excitation of the Yb^{3+}/Yb^{2+} CT state in Yb:YAG, pump light of about 209 nm is needed [Pie00], which corresponds to an energy of 5.9 eV, much higher than the available 2.5 eV to 4 eV. However, optical transitions have to satisfy the Franck-Condon priciple [Fra26, Con26] (see also section 2.2.1), which can lead to substantially larger excitation energies compared to cases where the excitation is accomplished thermally or otherwise (see, e.g. [Bus97]). This could also explain why such a band is not found in the transmission spectrum of the samples. It is thus possible that the CT transition from the oxygen ligands to the Yb^{3+}-ion is found at lower energy than the optically observed 5.8 eV, since the energy transfer process between the excited Yb^{3+}-ions to the electron at the top of the valence band occurs nonradiatively. The large Stokes shift of about 2 eV found between CT absorption and emission in Yb:YAG [Pie00, Nik04] suggests a lattice relaxation energy of about 1 eV for the CT state[11]. Assuming an energy depression as described for impurity bands in [Erg50, Erg52] of the order of 1 eV, a scenario where the empty Yb^{3+}/Yb^{2+} CT states form an impurity band into which electrons could be excited through a nonradiative cooperative energy transfer process involving two to three excited Yb^{3+}-ions as depicted in figure 6.13 could be imagined. Since this impurity band is empty from the beginning no other ions are needed for compensation. With an activation energy of E_A the electron could be transferred from one CT state to another, leaving the hole behind until it finds another recombination centre. In this way, electrons might be carried through the crystal by a hopping process from Yb-ion to Yb-ion (see also [Hir07]). From the information available, nothing can be said about the width of such a CT band.

However, some striking arguments exist which challenge this picture. Firstly, impurity band conduction should be strongly dependent on concentration. If an energy level depression is assumed due to increasing delocalisation at high concentrations, the acceptor level should be

[11] It should be noted that Dorenbos suggests that the lattice relaxation energy is compensated for by Coulomb interaction with the hole left behind [Dor03c].

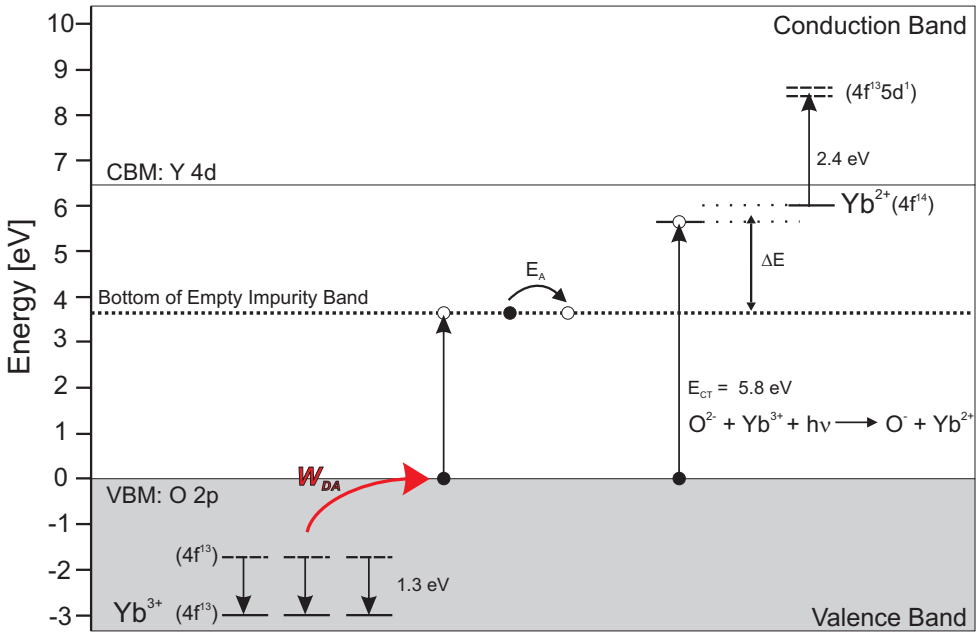

Figure 6.13.: Schematic representation of the energy transfer process leading to photoconductivity in Yb:YAG samples involving CT. Solid lines indicate binding energies of the respective ion in its ground state. Dashed lines correspond to different configurations of the ions. The associated electron configurations are given in brackets. Filled circles represent electrons and open circles holes, thus e.g. an open circle on a solid line represents an empty one-electron state. Two to three excited Yb^{3+}-ions cooperatively transfer their energy with a coupling parameter W_{DA} to an electron at the top of the valence band (VBM). The CT state is optically excited by photons of 5.8 eV energy. The position of the stabilised Yb^{2+}-ion relative to the host valence band equals the CT excitation energy within an error of 0.5 eV [Dor03c] (see also section 3.4.2 and figure 3.5). It is possible that the excitation level is significantly lower for nonradiative transitions as the Franck-Condon principle does not need to be satisfied [Bus97]. In addition, at high concentrations the level could be also depressed due to delocalisation of the acceptor states [Erg52]. The resulting impurity band is indicated by the dotted line and the total energy depression is indicated by ΔE. two to three Yb^{3+}-excitations might thus be enough to promote an electron from the top of the valence band to the acceptor state. An electron in the impurity band can be transferred with an activation energy E_A to neighbouring empty states via a hopping mechanism. See also [Hir07].

closer to the valence band maximum, the higher the Yb-concentration. Indeed, under same measurement conditions higher concentrated Yb:YAG samples always displayed significantly higher photocurrents, which could be attributed to higher mobility and lower activation energies of the electrons in the CT band due to stronger delocalisation. Nevertheless, the exponents found in the power law dependence of the photocurrent characteristics as discussed above are considered the same value for all samples, i.e. comparable values are found for the 2%Yb:YAG and the YbAG crystal. The measurements even suggest an increase of this exponent value with increasing Yb-concentration (see figure 6.4, top right). Secondly, the exponent is found to have a value of between 2 and 3. Photoconductivity on some of the samples strongly point towards two Yb^{3+}-excitation being enough for the generation of current. However, a level depression of a total of more than 3 eV for a possible Yb^{3+}/Yb^{2+} CT band seems to be too much of an overestimation. Thirdly, the Yb^{3+}/Yb^{2+} CT state is a complex centre, where the final state of the CT transition is formed by the Yb^{2+}-ion and a hole at the top of the valence band. The Coulomb interaction between the electron and the hole left behind surely has influence on the effective mass of the electron and thus to the mobility of the electron in the impurity band.

This condition is significantly different from the classical concept of impurity bands described before. Fourthly, the Yb^{2+} ground state has a $4f^{14}$ electronic configuration. The $4f$ orbitals are known to be core like, i.e. they are shielded from influences of ligands by the outer closed $5s$ and $5p$ orbitals (see sections 2.1 and 2.2.1). Furthermore, the already confined $4f$ wave functions are even lesser extended at the end of the series because of the lanthanide contraction (see section 2.2.1, The Influence of Phonons). In other words, even at very high concentrations direct overlap of the $4f$ wave functions of neighbouring Yb-ions are not likely to occur. This statement is supported also by the fact that direct transitions from the Yb^{2+} ground state to conduction band states are not observed and that the electron needs to be first excited to a $4f^{13}5d$ state for ionisation (see sections 3.4.2 and 6.2.1). If there is even no significant overlap between the $4f$ wave functions and the supposedly highly extended Bloch wave functions of the conduction band states, the probability of overlapping $4f$ wave functions has to be considered low.

Gedankenexperiment: YbAG

To gain deeper understanding, a gedankenexperiment is performed, where the problem is discussed for an ideal single crystalline YbAG. In YbAG all Y^{3+}-ions are replaced by Yb^{3+}-ions, thus the Yb^{3+}-ions are not considered as dopant ions anymore but as belonging to the host material. In this case, the top of the valence band constitutes also of the filled oxygen $2p$ states but at the minimum of the conduction band in this case the Yb-ions have the largest component. It is strongly suggested that these states constitute of the Yb^{2+} excited states which have $4f^{13}5d$ electronic configuration [Dor10]. Due to the more extended nature of the $5d$ wave functions, these states display increasing overlap with increasing concentrations and eventually give rise to delocalised Bloch states. Fundamental absorption thus can also be understood as a kind of CT transition between oxygen ligands and ytterbium, where both initial and final states are delocalised Bloch states. As both states are delocalised no lattice relaxation is found. Unfortunately, not much information can be found regarding band calculations or regarding investigations on the band gap of YbAG in the literature. The spectroscopic investigations in section 4.2 suggest similar band gap energies for YbAG as for Yb:YAG. Investigations on the scintillation properties of YbAG also showed very similar optical excitation energies and similar Stokes shifts between the Yb^{3+}/Yb^{2+} CT excitation band centred at about 5.8 eV and the typical emission bands at about 3.7 eV and 2.5 eV for YbAG as for Yb:YAG [Gue01, Gue02]. These findings suggest that on the one hand the position of the Yb^{2+} $4f^{13}5d$-states are depressed in YbAG probably due to delocalisation, so that these states are located about 2 eV lower than compared to in Yb:YAG (see section 3.4.2, figure 3.5 and table 3.1). However, on the other hand the optically accessible energy level position of the Yb^{3+}/Yb^{2+} CT state is not much changed. The fact that strong lattice relaxation is observed for this CT transition indicates that in contrast to the fundamental absorption, in this case localised states are involved. Thus, it is concluded that at high Yb-concentrations the energy levels belonging to the $4f^{13}5d$ configuration of the Yb^{2+}-ion do show significant overlap of the corresponding wave functions and eventually form delocalised Bloch states, but energy levels belonging to $4f$-states do not show significant overlap of wave functions even at maximum possible Yb-concentrations.

Conclusive Remarks

Based on these considerations, a conduction mechanism in an impurity band constituting of delocalised Yb^{3+}/Yb^{2+} CT states has to be understood as being highly improbable. However, given that the CT state is populated, a hopping mechanism between neighbouring Yb-ions cannot be excluded. It should also be noted that cooperative processes involving energy levels belonging to the $4f$ configuration of neighbouring Yb^{3+}-ions, as e.g. suggested also for the excitation mechanism underlying the generation of currents in the photoconductivity measurements, do exist in Yb:YAG. These cooperative processes are suggested to be based on superexchange type interactions, which require significant spatial overlap of the involved wave functions, i.e. neighbouring Yb^{3+}-ions are understood to interact with each other via their common oxygen ligand (see also section 2.2.2, Cooperative Processes). Therefore, despite a hopping process based on direct exchange interaction between neighbouring Yb-ions is due to lack in overlap of the respective $4f$ wave functions low in probability, as for the cooperative processes a hopping mechanism based on superexchange interaction could be imagined for the electron transport process in Yb:YAG.

Another possible charge transport mechanism which was dismissed at the beginning of this section due to presumably lower charge mobility is hole conduction. The hole left behind at the top of the valence band after the CT process might gain enough energy to be activated as a free carrier into the valence band. Thermal activation could be possible at room temperature. Despite the usually lower mobility of holes, this charge transport process has the advantage that the valence band is a proper band described by delocalised Bloch wave functions. At the current state of knowledge, no estimate can be given whether the electron hopping model or the hole conduction are associated with the higher effective masses and which of the possible charge carriers display higher resistance. Provided that the Yb^{3+}/Yb^{2+} CT process is involved at all, it has to be considered that contributions of both charge transport processes might exist. It should also be noted that investigations on YAG as ionic conductors also exist [Rot85, Rot90]. These findings are not considered for the discussions of the results in this work.

6.3.3. Photoconductivity in Yb:YAG Ceramics

The 15.0%Yb:YAG ceramic sample displayed orders of magnitude lower photocurrents compared to the 16.5%Yb:YAG single crystalline sample in the measurement range investigated. For lower pump powers, the 21.6%Yb:YAG ceramic sample also exhibited lower photocurrents compared to a 20.0%Yb:YAG single crystal. However, for both ceramic samples an exponent of about 3 was found for the power dependence of the photoconductivity characteristics, whereas a close to power 2 dependence was found for the single crystalline counterparts. From the current state of knowledge one can only speculate on the reasons for the difference in the behaviour observed. The lower currents for the ceramic samples could be explained by higher resistivity due to scattering of the charge carriers at the grain boundaries. It is assumed that the same physical processes occur in single crystalline and ceramic Yb:YAG samples under the same conditions. If Yb^{3+}/Yb^{2+} CT transitions are involved in the current generating process, a higher exponent for the ceramics indicate a clearly higher CT level position relative to the valence band maximum compared to the single crystals. Strain and stresses are known to have effects on energy

level positions. This also applies to delocalised band states: tensile stress results in a decrease of the energy band gap while a compressive strain causes an increase of the band gap [Sun09]. No strain or stress effect was found for the ceramic samples (see section 3.5.2) and respective effects in the single crystalline samples were assumed to be negligible, particularly in the samples polished down to below 150 µm thickness. Despite these findings, it cannot be excluded that these slight differences in the sample properties of the Yb:YAG single crystalline and ceramic samples cause CT energy level depressions of different magnitudes. However, it should be noted that the CT state in the Yb:YAG ceramic samples was optically excited at the same photon energies as the Yb:YAG single crystals (see also section 4.4).

6.4. Photoconductivity and Thin-Disk Laser Performance

The observed photoconducting behaviour in Yb:YAG under 940 nm irradiation needs to be discussed regarding its impact on laser performance. The creation of free carriers due to the excitation of Yb^{3+}-ions is for multiple reasons expected to be of great impact for Yb:YAG lasers. In particular, the effect is assumed to be high for thin-disk lasers, for which high densities of excitations are required (see section 2.3.2 and chapter 5) and thus the probability for the availability of excited Yb^{3+}-pairs or triplets is higher compared to rod lasers.

In the following, the main sources for possible laser losses associated with free carrier generation are listed and discussed. Firstly, the creation of one free carrier by an upconversion process involving two to three Yb^{3+}-excitations is a loss process, which depopulates the upper laser level. The effect might not be of great significance as the probability for the cooperative upconversion process itself is considered to be rather low. However, as nothing is known about the efficiency of the current generating mechanism, one should be careful not to jump to conclusions. Secondly, the free carrier might absorb the 1030 nm laser radiation or even directly the 940 nm pump laser light, which would lead to further losses. This possible loss mechanism is indicated with the absorption cross section σ^{c}_{abs} in the schematic representation shown in figure 6.11. A rate equation based discussion for this loss mechanism was performed by H. Kühn (see also [Fre10]). In this case, a broadened band-like state of at least 1.2 eV width is needed for the final state of the electron transition, otherwise innerband absorption is not to be expected. It might also be possible that the hole left behind in the CT process absorbs the laser and also the pump light, i.e. the hole could be excited deeper into the valence band. Yet, it also has to be pointed out that first excited state absorption measurements could not provide any evidence for such a band. However, the presumably very low density of states and the up to now unknown lifetime[12] in the current carrying energy level very much complicate these measurements, so that conclusive statements cannot be given for now. Thirdly, the relaxation process to the creation of free carriers is supposed to generate significant amounts of waste heat. Unfortunately, at the moment nothing is known about this back transfer process. It is strongly assumed that the excitation energy of two to three Yb^{3+}-ions is lost to the laser, i.e. the energy will not be transferred back resulting in two to three excited Yb^{3+}-ions at the end of the cycle. Most likely, the free carriers will find some recombination centres with which they will recombine.

[12] The Yb^{3+}/Yb^{2+} CT state typically has a lifetime of a few nanoseconds [Gue01].

The recombination process to some extent could also be of radiative nature, but particularly at room temperature a nonradiative process is much more likely (see also section 3.6.1). Assuming that due to the Franck-Condon principle optical transitions of the electron back to the electron donor state are not permitted, waste heat generation in the order of the excitation energy of 2.5 eV to 4 eV needs to be considered. The Yb:YAG laser as a quasi-three level laser is particularly sensitive to heating (see also section 2.3.1): as the thermal load increases, the lower laser level is more and more populated, leading to an increase in reabsorption and the need for higher pump powers to maintain population inversion. Heating thus leads to deterioration of laser performance and efficiency.

It is suggested that the reduction in laser efficiency at high outcoupling transmission rates observed in the thin-disk laser experiments of this work (see chapter 5) as well as the inversion density dependent losses found by Larionov et al. [Lar08] are connected to the photoconducting properties of Yb:YAG. The laser results led to the conclusion that the heat generated through the quantum defect alone could not account for the observed decrease in laser efficiency and thus an additional loss process has to exist (see section 5.4.1). From investigations on the inversion dependency of the laser performance it was tentatively suggested that a nonlinear relationship between laser losses and density of excited states exists. According to that, two to four neighbouring excited Yb^{3+}-ions are needed for the losses to occur. Although a process of the order of 4 is considered highly unlikely, the similarity to the deductions drawn from the photoconductivity measurements is striking. In addition, the analyses of the thin-disk laser results suggested a lower sensitivity to the nonlinear loss process for the ceramic laser samples compared to the single crystalline samples. This behaviour could also be connected to the lower photocurrents measured for the ceramic samples. However, conclusive evidences for a connection between the decrease in laser efficiency with increasing density of excited states and the photoconductivity observed in Yb:YAG are yet to be found and are currently subject of intensive research.

7. Resume

7.1. Summary

It was the subject of this research to investigate on the laser properties of highly Yb-doped $Y_3Al_5O_{12}$ (Yb:YAG) gain materials with particular regard to their applications in high power thin-disk lasers. In this context, Yb:YAG single crystalline and ceramic samples of different doping concentrations have been compared regarding their spectroscopic and thin-disk laser properties. The investigations focussed on laser losses observed at high densities of excited Yb^{3+}-ions. These loss processes were found to be nonlinearly dependent on the transmission rate of the laser outcoupling mirror, suggesting the participation of an ensemble of two to four excited Yb^{3+}-ions in a formerly unknown process generating significant heat. Because an involvement of the host energy band states was assumed, a comprehensive energy level scheme of the Yb^{3+}- and also the Yb^{2+}-ion with respect to the YAG conduction and valence bands was compiled and discussed. Photoconductivity measurements under Yb^{3+}-excitation revealed the creation of free carriers in Yb:YAG. The measurements also indicated a high order process with the participation of two to three excited Yb^{3+}-ions in the generation of current, pointing towards a cooperative upconversion mechanism. It was proposed that a hopping mechanism via the Yb^{3+}/Yb^{2+} CT state might be involved. A connection between the nonlinear laser losses observed in the thin-disk laser experiments and the photoconducting behaviour of Yb:YAG is strongly suggested.

In the first part of this work, the laser material Yb:YAG was introduced and the energy level positions of the localised trivalent as well as divalent Yb-ion with respect to the delocalised YAG Bloch states were discussed. The final state of the charge transfer between oxygen ligand and Yb^{3+}-ion was identified with a complex centre consisting of the Yb^{2+} ground state and a hole in the valence band. It was concluded that neither ionisation threshold nor interconfigurational transitions will be observed below the bandgap energy of 6.5 eV for the Yb^{3+}-ion in YAG. Thus, the trivalent Yb-ion is excluded to act as a hole trap. Moreover, the Yb^{3+}-ion is electron attractive, which is confirmed by the observation of ligand to metal charge transfer transitions. In contrast, ionisation threshold as well as interconfigurational transitions below the lattice absorption edge are anticipated for the divalent Yb-ion and thus, the Yb^{2+}-ion is expected to act as an electron donor state. Photoconductivity measurements confirmed this assumption. However, direct ionisation from the ground state of the Yb^{2+}-ion into conduction band states could not be observed. This result strongly suggests that the $4f$ wave function associated to the Yb^{2+} ground state has no significant overlap to the Bloch wave functions of the conduction band but with the wave functions associated to the Bloch states constituting the top of the valence band. The latter is confirmed by the observation of ligand to metal charge transfer transitions in this material. This can be explained as follows: the Bloch states at the top of the valence band constitute of

the $2p$ orbitals of the oxygen ligands and the bottom of the conduction band is constituted by states ascribed to the yttrium $4d$ states. Due to the Yb-ion being much closer to the oxygen ligands than to the Y-ion in the YAG lattice, the spatial overlap between the valence band Bloch wave functions and the $4f$ wave functions is much more significant compared to the overlap between the $4f$ wave functions and the conduction band Bloch wave functions.

The fabrication techniques for single crystalline and ceramic Yb:YAG were presented. Both materials were investigated regarding their crystallographic properties. Yb:YAG single crystals and ceramics were found to exhibit very similar properties regarding strain and stresses as well as thermal conductivity. The fluorescence lifetimes of Yb:YAG single crystals and ceramics of Yb-concentrations between 0.1% and 21.5% were measured using the pinhole-method. No difference between the two materials could be observed regarding this physical quantity, which indicates that the materials have no significant differences in quality. Within a measurement error of 10%, a fluorescence lifetime of 950 µs was found for all annealed samples regardless of their concentration. Excitation energy dependent measurements did not reveal additional information, suggesting that quenching processes depending on density of Yb^{3+}-excitation are absent in these materials. Absorption and fluorescence spectra were recorded for the different samples. The absorption cross-sections of the Yb:YAG single crystals and ceramics were found to be nearly identical and fitting the literature values very well. Transmission and fluorescence spectra in the short wavelength range were extensively investigated to identify possible quenching centres. It was revealed that iron is the major impurity found in the ceramic samples. Absorption bands associated with iron were absent in the high purity Yb:YAG single crystals grown from 6N powder-metallurgically produced rhenium crucibles. The absorption bands ascribed to the Yb^{2+}-ion and colour centres formed by oxygen vacancies disappeared upon annealing in air at temperatures higher than 800°C. The fluorescence spectra in the visible region confirmed that trivalent erbium and thulium ions are present in both materials. It was found that these erbium and thulium impurities were introduced by the raw material Yb_2O_3 and Y_2O_3, respectively. Excited state absorption measurements did not reveal any peculiarities apart from the expected excitation energy dependent bleaching of the ground state absorption. In conclusion, the influence of the detected defect and impurity traces on quantum efficiency were found to be negligible in the annealed samples.

Thin-disk laser experiments were performed using a commercial thin-disk laser module allowing for 24 pump passes through the active medium. The thickness of the laser samples was chosen according to their Yb-doping concentrations so that pump light absorption of at least 90% was ensured for all used outcoupling transmission rates. Laser operation was realised with all samples investigated except for the as-grown 16.5%Yb:YAG single crystal, which due to the high presence of Yb^{2+}-ions displayed a reduced quantum efficiency. The single pass internal losses of the ceramic samples from a prior fabrication series were found to be lower than 0.3%, while the more recently fabricated 15%Yb:YAG ceramic sample displayed internal losses of below 0.1%. The latter value for the single pass internal losses is comparable to those of the 16.5%Yb:YAG sample prepared from the boule #SNF grown in the framework of this research and the reference 10%Yb:YAG single crystal, which is a typical commercial thin-disk laser sample. Of all the samples, the reference crystal displayed the highest slope efficiency with almost 73%. It was found that all samples suffer from significant drops in laser efficiency with increasing outcoupling transmission rate, which could not be solely attributed to the expected

decrease in absorption efficiency. The input-output characteristics of the different samples for lasing at 1030 nm show that regardless of the internal losses no roll-overs are present at pump powers as high as 45 W for outcoupling transmission rates up to 3.3%. However, the laser efficiency dramatically drops if the transmission rate is increased further. Roll-overs leading to termination of the laser were observed in all samples already at pump powers below 45 W if a sufficiently high outcoupling transmission rate was chosen. It was also found that the decrease in laser efficiency with increasing transmission rate is stronger the higher the Yb-doping concentration and the thinner the Yb:YAG laser sample. Since the available pump power was the same in all the experiments and the thicknesses of the samples were chosen to ensure similar absorption, the amount of heat generated due to the quantum defect should be at least comparable for all samples in all experiments. Moreover, the expected bleaching effect at higher outcoupling transmission rates would result in lower pump absorption, i.e. a reduction of the pump power introduced into the sample is expected which should lead to lower intrinsic heating. Therefore, it was concluded that an additional process leading to heat generation has to exist. The investigations on the inversion density dependence of the thin-disk laser performance led to the conclusion that this loss process is nonlinearly dependent on the density of excited Yb^{3+}-ions and it was suggested that an ensemble of two to four neighbouring excited Yb^{3+}-ions is needed for the losses to occur. However, a fourth order process is regarded to be very low in probability, particularly in Yb:YAG crystals and ceramics for which clustering is stated to be not of significance. The laser properties of the 16.5%Yb:YAG single crystalline laser sample fell short of the expectations: despite the crystal was grown with optimised crystal growth parameters, which ensured high purity, and despite the upper limit of the internal laser losses was found to be comparable to that of the reference crystal, this sample displayed the strongest decrease in laser efficiency with increasing outcoupling transmission rate. Since this single crystal was found to be of comparable optical quality as the reference crystal and even displayed lower laser losses compared to most of the ceramics, optical quality is excluded as being decisive for the nonlinear laser losses. It was also suggested that the ceramic samples are less prone to the nonlinear loss process compared to the single crystalline samples. However, a lot more samples of different specifications need to be examined to conclusively confirm this statement. In contrast to Yb:Lu_2O_3 thin-disk lasers, time monitoring of the laser output power for Yb:YAG thin-disk lasers did not reveal any permanent degradation of the laser performance over time.

The photoconductivity results obtained in Yb:YAG samples of different Yb-doping concentrations and codopants were presented. It was deduced that regardless of their doping concentrations the same physical process leads to the generation of current in the Yb:YAG samples. Assuming that the order of the process given by the exponent found in the photocurrent pump power characteristics can be directly associated with the number of excited Yb^{3+}-ions involved, a cooperative upconversion mechanism with the participation of two to three neighbouring excited Yb^{3+}-ions is suggested for the current generating process. The possibility of the Yb^{3+}/Yb^{2+} charge transfer state acting as an impurity band was discussed. Although this charge transfer state needs an optical excitation energy of 5.8 eV, it cannot be excluded that still an electron transfer process from the valence band maximum to the Yb^{2+} ground state might be possible also at lower energies if the Franck-Condon principle does not need to be satisfied. This could also explain, why neither a candidate for an electron donor state nor a possible

current carrying band could be observed in the visible spectral range by optical measurement techniques. Nevertheless, to reach the charge transfer state with an energy equal to two to three Yb^{3+}-excitations, an energy level depression of at least 2 eV has to be accomplished. The probability of delocalised Yb^{3+}/Yb^{2+} charge transfer states acting as an impurity band constituting of overlapping $4f$ wave functions was considered low due to the confined nature of the $4f$ wave functions, which usually do not even show significant overlap with the more extended yttrium $4d$ wave functions. However, a hopping mechanism between neighbouring Yb-ions as a charge transport process might be possible. For as-grown samples, the Yb^{2+}-ion was identified as the major electron donor state and the current is strongly suggested to be carried in the conduction band. The photoconducting behaviour under 940 nm irradiation of Yb:YAG single crystalline and ceramic samples was compared. In comparison to their single crystalline counterparts, lower photocurrents are generated in ceramic samples at lower pump powers. This could be explained by the presence of grain boundaries, which might increase the resistivity of the ceramics. In addition, the current generating process was found to require three Yb^{3+}-excitations for the ceramics compared to two for the single crystals. This points towards a difference in the energy level position of the current carrying states with respect to the carrier donor states for the two materials.

A connection between the nonlinear losses observed in thin-disk lasers and the found photoconductivity of Yb:YAG under 940 nm irradiation was strongly suggested. The current generating process involving two to three Yb^{3+}-excitations is already on its own a loss process, which could reduce the quantum efficiency. However, excitation dependent fluorescence lifetime measurements could up to now not confirm this assumption, which is most likely due to the very low probability for such high order processes to occur. It was also suggested that the major impact of the photoconductivity phenomenon on the laser efficiency lies in the presumably high heat generation at the recombination of the free carriers. Due to the quasi-three-level nature of the Yb:YAG laser, heating leads to significant decrease of the laser efficiency. The possibility of free carriers absorbing the signal and even the pump laser light causing additional losses and further heating was also considered. Up to now, such a band could not be observed in excited state absorption measurements. However, the low density of states and the presumably very low lifetime of the current carrying states complicate these measurements so that a conclusive statement regarding such an innerband absorption could not be given.

7.2. Outlook

One of the major tasks of future work will be to find conclusive evidences for the connection between the photoconductivity properties under 940 nm irradiation and the inversion density dependent losses found in Yb:YAG thin-disk lasers.

As a first step, the phenomenon of photoconductivity in Yb:YAG needs to be intensively studied to unveil the mechanism behind it. One of the key points will be the identification of the current carrying states. One possible way of confirmation for the involvement of the Yb^{3+}/Yb^{2+} charge transfer states would be the observation of the characteristic charge transfer luminescence under 940 nm irradiation. Furthermore, photoconductivity for direct optical excitation into the charge transfer band is expected and needs to be proven. If a hopping mechanism

is in fact the underlying charge transport mechanism, an activation energy has to be overcome and thus the resulting photocurrent is expected to be highly sensitive to temperature. Therefore, temperature dependent photoconductivity measurements are planned for the near future. Nevertheless, charge transport via states or bands other than the Yb^{3+}/Yb^{2+} charge transfer states should also be taken into account. In this context, the nature of the major charge carriers has also to be reassessed. For clarification, photo-Hall measurements are in progress. The actual number of created carriers is also of interest to gain information on the efficiency of the current generating process. Another point which needs confirmation is the association of the number of involved Yb^{3+}-excitations with the exponent found in the photocurrent pump power characteristic. For this purpose, not only the process of current generation including the influence of saturation of the Yb^{3+} ground state absorption is needed, but also the recombination process of the charge carriers has to be understood. Thermal luminescence measurements are underway to find possible trap centres just below the current carrying states. The determination of a comprehensive rate equation model is desirable. Further laser experiments with highly Yb-doped YAG single crystals at high densities of excitations are necessary to conclusively confirm the compared to the ceramics higher sensitivity of single crystalline gain media on the nonlinear loss processes. To acquire further information on the occurring losses, monitoring of the heat generated during laser operation for the high outcoupling transmission rates would be of great interest. For completion, gain measurements should also be performed under these conditions. Additionally, the investigations should be extended to other laser concepts, e.g. to channel wave guide lasers, which are known for good laser performance despite their high resonator losses. Although the spectroscopic properties of Yb:YAG are assumed to be well understood, further investigations are needed. Spectroscopic investigations under high excitation densities are of particular interest. Complemental excited state absorption measurements for different excitation energies and time constants will have to be performed to find evidence for the current carrying states.

The main task of future work will be the investigation on possible solutions for the laser losses. The prevention of the occurrence of photoconductivity seems to be a major step. This could be accomplished by the incorporation of suitable recombination centres as in the case of radiation hardening in space applications. Another idea is to destabilise the oxidation state of the ions, which constitute the current carrying states. In the case of Yb^{3+}/Yb^{2+} charge transfer states, the incorporation of calcium might be effective. If grown under reducing atmosphere, calcium is incorporated in its divalent oxidation state into the YAG crystal. In this way, centres which usually assist to stabilise divalent ytterbium could be deactivated. Indeed, previous experiments showed that as-grown Ca-codoped YbAG crystals suffer less from quenching by energy transfer to Yb^{2+}-ions compared to as-grown pure YbAG crystals [Fag04].

For further understanding of these phenomena, it would be of great interest to extend these investigations and discussions to other Yb-doped laser media. The comparison of the influence of different host properties such as the ionic or covalent character of the bonds, the band gap energy, etc. on the laser performance, particularly at high densities of Yb^{3+}-excitations, could greatly improve the current state of understanding.

A. The Electronic Energy Levels of the Lanthanoids Relative to the Host Bands

The ground state binding energies of the trivalent lanthanoids relative to the host valence band of YAG were presented by Thiel and coworkers in 2001 [Thi01]. The measurements were done on YAG doped with the heavier lanthanoids (Gd^{3+} to Lu^{3+}) using resonant photoemission spectroscopy. Photoemission spectroscopy measures the kinetic energy distribution of electrons ejected from a sample which is exposed to monochromatic light. From this, together with the knowledge of the photon energy the binding energy distribution of the electronic states in the sample can be derived. The photoemission spectrum thus contains information about both the $4f$ electrons of the lanthanoid dopant ion and the electronic states of the host, allowing the energies of the states to be measured relative to a common reference. The $4d$-$4f$ photoemission resonance was used to separate and identify the $4f^N$ and valence band components of the spectra. Theoretical $4f$ photoemission spectra were fitted to the experimental results to accurately determine the electron binding energies. No concentration dependency of the $4f$ binding energies were observed. To describe the relative energies of the $4f^N$ ground states in these materials an empirical, two parameter model was used, which can be expressed as

$$E_{4f} = I_{4f} - E_L + \alpha_R(R - R_0) - E_{VBM}, \tag{A.1}$$

where I_{4f} is the free ion ionisation potential, E_L is the uniform binding energy shift relative to the free ion value experienced by the lanthanoid ions in a certain host, α_R is the binding energy shift per unit change in ionic radius, R and R_0 are the effective ionic radii of the trivalent lanthanoid ion and the ionic radius reference, respectively and E_{VBM} is the binding energy of the valence band maximum (VBM), which is the low binding energy edge of the valence band. For YAG the corresponding values are $R_0 = 1.019$ Å, the ionic radius of the trivalent yttrium ion in eightfold coordination and $E_{VBM} = 8.7$ eV. Fitting this model to the observed binding energies indicates an $E_L = 31.6$ eV shift and an $\alpha_R = 8.3$ eV/Å effect from the change in ionic radius for YAG[1]. Using these two parameters the model allows extrapolation to the binding energies of the lighter lanthanoids, for which the error is estimated to be between 0.5 eV and 1 eV.

Together with the work of Dorenbos on $4f^{n-1}5d$ level positions of the trivalent [Dor00] and divalent [Dor03b, Dor03c][2] lanthanoids as well as on systematics in the charge transfer energies of the trivalent lanthanoids in the different compounds [Dor03c, Dor05], a pretty much

[1] In [Thi03] the values for these two parameters for YAG differ from those in [Thi01] with $E_L = 31.5$ eV and $\alpha_R = 9.7$ eV/Å. No explanation has been given.

[2] The energy difference between the ground state of the lanthanoid ions to the lowest energy state of the $4f5d$

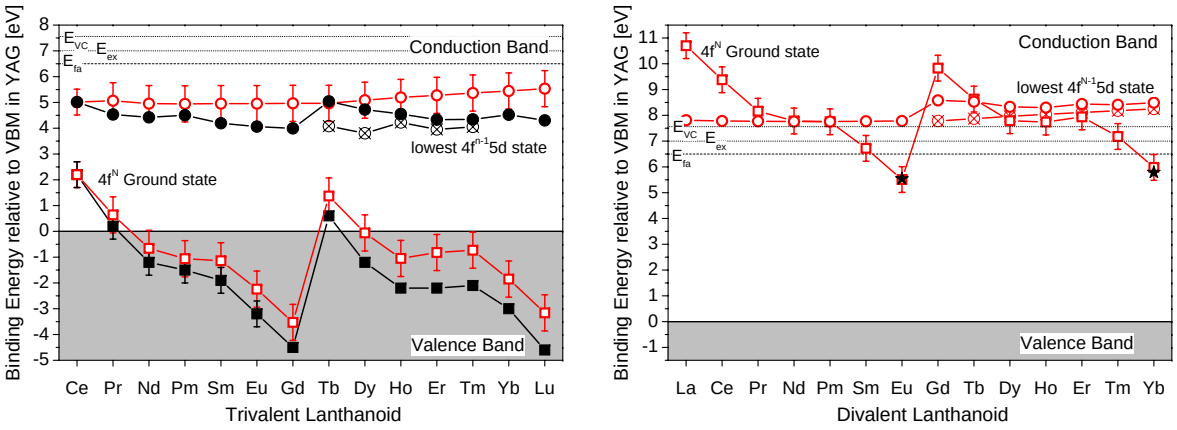

Figure A.1.: The $4f^n$ ground state (squares) and lowest $4f^{n-1}5d$ excited states (circles) relative to the VBM according to [Thi03] (filled symbols) and [Dor03c, Dor05] (open symbols) for the trivalent (left) and the divalent (right) lanthanoids. The $4f$ binding energies from [Thi03] for Gd^{3+} up to Lu^{3+} are measured values, the values for Ce^{3+} up to Eu^{3+} extrapolated ones. The $4f^{n-1}5d$ states from [Thi03] were determined by adding the $4f^n$ to $4f^{n-1}5d$ transition energies and the crystal field depression from [Dor00], where the solid circles represent the spin allowed and the crossed out circles the spin forbidden transitions. The Dorenbos values for the trivalent lanthanoids were obtained by using the Ce^{3+} levels of [Thi03] as reference and the parameters from [Dor03c]. The values for the divalent lanthanoids are determined from the CT value of Eu^{3+} and parameters taken from [Dor05]. The filled stars correspond to observed CT absorption maxima of Eu^{3+} [Dor03c] and Yb^{3+} [Pie00, Gue01]. The dashed line E_{fa} represents the most often cited band gap value of 6.5 eV, which corresponds to the fundamental absorption onset. The peak value for exciton creation $E_{ex} = 7$ eV and the onset for free carrier creation E_{VC} according to [Dor05] are represented by dotted lines.

comprehensive energy level scheme for all trivalent and divalent lanthanoids with respect to the host bands can be estimated. The binding energies of the trivalent lanthanoids in YAG are schematically plotted relative to the valence band maximum (VBM) on the left of figure A.1. Squares represent the $4f$ ground states and circles the lowest $4f^{n-1}5d$ states. Values from [Thi03] are shown in solid and crossed out symbols. The values predicted using the semi-empirical model of Dorenbos with the level position of Ce^{3+} from [Thi03] as reference are shown in open symbols. The $4f^{n-1}5d$ states from [Thi03] were determined from the $4f^n$ binding energies and the $4f^n$ to $4f^{n-1}5d$ transition energies of [Dor00]. The solid circles mark the lowest energy high spin-states (spin allowed transitions) and the crossed out circles the lowest energy low-spin states (spin forbidden transitions). The $4f^{n-1}5d$ levels by Dorenbos are the lowest ones, i.e. for the lighter lanthanoids the levels reached from the ground state by spin allowed transitions and for the heavier lanthanoids the levels reached by spin forbidden transitions are shown. Despite using the Ce^{3+} level position from [Thi03] to obtain those for all other trivalent lanthanoids with the Dorenbos model, the values deviate considerably from each other, especially for the heavier lanthanoids. Another difficulty in locating lanthanoid energy levels with respect to the host energy bands lies in the uncertainty regarding the band gap, as mentioned before. In figure A.1 the most often cited band gap value of 6.5 eV is represented

configuration shows always a systematic pattern through the lanthanoid series. The transition energy is large with half (Eu^{2+}, Gd^{3+}) or fully (Yb^{2+}, Lu^{3+}) filled $4f$ shells and small for $4f$ shells filled with one (La^{2+}, Ce^{3+}) or eight (Gd^{2+}, Tb^{3+}) electrons (also see figure 2.2 and section 2.1.1). This behaviour is in direct relation to the binding energy of the $4f$ electrons and is in accordance to Jørgensen's spin pairing theory [Jør62].

by the dashed line E_{fa}. The value for E_{ex} of 7.0 eV is taken from [Dor05] and marks the peak value for exciton creation in YAG. Using the empirical relation $E_{VC} = 1.08E_{ex}$ from [Dor05] the value for free carrier creation was estimated. E_{ex} and E_{VC} are both shown as dotted lines. The photoconductivity measurements by Pedrini *et al.* on Ce^{3+}:YAG [Ped86] locate the Ce^{3+} at about 3.8 eV below the conduction band. Thus, according to Dorenbos the ground state of Ce^{3+} should be about 3.76 eV above the VBM in disagreement to Thiel's estimation. Furthermore, the ESA measurements on Ce^{3+}:YAG of Hamilton *et al.* [Ham89] locate the Ce^{3+} ground state also at about 3.8 eV below the conduction band minimum. This value is in excellent agreement with Thiel's estimations if the band gap is considered to be 6.5 eV, which suggest that in Ce-doped YAG E_{VC} indeed coincides with E_{fa}. The good agreement further supports the validity of Thiel's extrapolation method. For these reasons and since the binding energy of the heavy lanthanoids are obtained from measurements, the values from [Thi03] as well as the band gap value of 6.5 eV for YAG are chosen as basis to all following discussions in the course of this thesis.

The situation is somewhat more complicated for the divalent lanthanoids in YAG as measured data are sparse. Figure A.1 right shows the energy levels of the $4f^n$ and lowest $4f^{n-1}5d$ states relative to the YAG host bands for the divalent lanthanoids. This energy level scheme has been obtained by applying Dorenbos's model [Dor03c, Dor05], which is based on the assumption that the energy needed for CT from the valence band to the trivalent lanthanoids coincides with the energy difference between the VBM and the $4f$ ground state of the corresponding divalent lanthanoid. The open squares represent the $4f^n$ and the circles the lowest $4f^{n-1}5d$ high spin-states (open) and low spin-states (crossed out) of the divalent lanthanoids. The filled stars correspond to observed CT absorption maxima of Eu^{3+} [Dor03c] and Yb^{3+} [Pie00, Gue01]. From this energy level diagram it has to be deduced that all $4f^{n-1}5d$ levels of the divalent lanthanoids for YAG lie within the conduction band.

B. The Dependence of Thermal Conductivity on Doping Concentration

In insulating materials, such as the dielectric crystal Yb:YAG investigated in this work, heat is transferred almost solely through phonons. In the theoretical description heat conduction occurs as a transport phenomenon in a phonon gas, where the energy is transported by diffusion maintaining the thermal gradient. The thermal conductivity λ can then be defined as the proportionality constant between the local heat flux $\overrightarrow{\Phi_q}$ and the temperature gradient ∇T by the equation

$$\overrightarrow{\Phi_q} = -\lambda \nabla T, \tag{B.1}$$

also known as Fourier's law. Using the Debye theory to describe the lattice heat capacity, the thermal conductivity can be expressed as

$$\lambda = \frac{1}{3} C_{Vol}\, v_{ph}\, \Lambda, \tag{B.2}$$

where C_{Vol} is the heat capacity per unit volume, v_{ph} the average phonon velocity (in the Debye approximation the phonon dispersion is neglected) and Λ the mean free path of the phonons between collisions [Kit99, Bro05]. It can be shown that C_{Vol} has a $\propto T^3$ temperature dependence for temperatures significantly lower than the Debye temperature Θ_D ($T < \Theta_D/10$). At $T = 0$K, C_{Vol} becomes zero and so does the thermal conductivity λ. The phonon propagation speed v_{ph} is nearly constant with temperature in the range between 0K and room temperature and decreases slowly as temperature is further increased. The mean free path Λ is constant for low temperatures being of the order of the sample dimensions and monotonically decreases with increasing temperature. As a result, at low temperatures the dependency on specific heat dominates and thermal conductivity is proportional to T^3, while at high temperatures the dependence is that of the mean free path and thermal conductivity follows $\propto T^{-1}$. A maximum of thermal conductivity is expected at around $T \approx \Theta_D/20$ [Bro05].

However, the phonon mean free path is affected by different phonon scattering mechanisms which might have different influence at different temperatures. For example, in amorphous or glassy materials the mean free path is determined by local structural disorder and is nearly independent of temperature [Bro05]. As a consequence, the thermal conductivity in these materials follows approximately the temperature dependence of the specific heat. For most polycrystalline materials the grain boundaries are an effective scattering wall that limits the phonon mean free path to the mean grain size at low temperatures [Kle94]. In polycrystalline YAG with very thin grain boundaries fabricated by the VSN method (see section 3.5.1 for details) it has been found that below 20K contribution from grain boundaries to the scattering rate is the dominant phonon scattering mechanism. However, the average phonon mean free path at low

temperature has been determined to be significantly larger than the mean grain size of about 3 µm and to decrease with temperature as T^{-2}, which results in a $\propto T$-dependency for thermal conductivity in this low temperature regime. This finding was ascribed to different acoustic properties for the grain itself and the grain boundary layer [Bis07b].

For a more detailed understanding one needs to take into account that the thermal conductivity at temperature T results from contributions of a spectrum of lattice excitations and (B.2) is expressed more generally as

$$\lambda = \frac{1}{3}\int_0^{\omega_D} C_{Vol}(\omega)\, v_{ph}^2\, \tau(\omega)\, d\omega, \tag{B.3}$$

where $\omega_D = \frac{k_B \Theta_D}{\hbar}$ is the Debye frequency, with k_B being the Boltzmann constant and $\hbar$ the reduced Planck constant, $C_{Vol}(\omega)$ the contribution to the heat capacity of the phonon with frequency ω and $\tau(\omega) = \Lambda(\omega)/v_{ph}$ is its effective relaxation time. Different scattering mechanisms contribute additively and independently to $1/\tau$, the phonon scattering probability per unit time. Known scattering processes contributing to the thermal resistance of an insulator are the so-called Umklapp process, which is an anharmonic three-phonon process where momentum is quasi-conserved in the form $\overrightarrow{k_1} + \overrightarrow{k_2} = \overrightarrow{k_3} + \overrightarrow{g}$ with $\overrightarrow{g}$ being a reciprocal lattice vector [Pei29] and scattering at point defects, which disrupt the periodicity of the crystalline lattice. Point defects can be any imperfections such as dislocations, vacancies, coexistence of several isotopes of an element, but may also be deliberately implemented such as doping of YAG with Yb^{3+}-ions. The latter will be discussed in the following paragraphs in accordance with the theoretical work of Klemens [Kle60] to describe the influence of Yb^{3+}-doping concentration on the thermal conductivity of Yb:YAG. The resulting expression is used in section 3.5.3 to apply a fit function to the available literature values.

The phonon scattering by point defects contributes to the scattering rate as

$$\frac{1}{\tau_{pd}} = A\,\omega^4, \tag{B.4}$$

with A being a constant depending on the nature of the defect and its concentration. In general, the point defects act as scattering centres mainly by virtue of their mass difference. Under this assumption the parameter A is given by

$$A = \frac{a^3\,\varepsilon}{4\pi\, v_{ph}^3}, \tag{B.5}$$

where a^3 is the atomic volume and ε the relative mass variance of the lattice substitution site:

$$\varepsilon = \sum_i c_i \left[(M_i - M)/M\right]^2 \tag{B.6}$$

with

$$M = \sum_i c_i M_i, \tag{B.7}$$

where c_i and M_i are the concentration and mass of atoms of type i. In the case of Yb:YAG this is

$$\varepsilon = \frac{C(m_{Yb} - M)^2}{M^2} + \frac{(1-C)(m_Y - M)^2}{M^2}, \tag{B.8}$$

and

$$M = C\,m_{Yb} + (1-C)\,m_Y, \tag{B.9}$$

with C being the Yb^{3+}-doping concentration (i.e. $C = 0$ for YAG and $C = 1$ for YbAG), m_{Yb} and m_Y the atomic masses of Yb and Y, respectively. Umklapp processes contribute to the scattering rate as

$$\frac{1}{\tau_U} = B\,\omega^2, \tag{B.10}$$

with B being a parameter proportional to the temperature T. Assuming no other processes contribute to the internal thermal resistance, the total relaxation time is given by

$$\frac{1}{\tau} = \frac{1}{\tau_{pd}} + \frac{1}{\tau_U} \quad \Leftrightarrow \quad \tau = \frac{\tau_{pd}\tau_U}{\tau_{pd}+\tau_U}. \tag{B.11}$$

Substituting this term for $\tau(\omega)$ into equation (B.3) and approximating the heat capacity for the high temperature limit, i.e. for temperatures well above the Debye temperature, to

$$C_{Vol}(\omega) = \frac{3k_B}{2\pi^2}\frac{\omega^2}{v_{ph}^3}, \tag{B.12}$$

the following expression for the thermal conductivity is obtained:

$$\lambda = \frac{k_B}{2\pi^2 v_{ph}} \int_0^{\omega_D} \omega^2 \frac{\tau_{pd}\tau_U}{\tau_{pd}+\tau_U} d\omega. \tag{B.13}$$

Defining a phonon frequency $\omega_0 = \sqrt{\frac{B}{A}}$, for which the intrinsic mean free path due to Umklapp processes is equal to that of point defects, the thermal conductivity can be written as

$$\lambda = \frac{k_B}{2\pi^2 v_{ph}} \frac{\omega_0}{B} \tan^{-1}\frac{\omega_D}{\omega_0}. \tag{B.14}$$

The intrinsic thermal conductivity λ_i without point defect scattering is given by

$$\lambda_i = \frac{k_B}{2\pi^2 v_{ph}} \frac{\omega_D}{B}, \tag{B.15}$$

so that λ of equation (B.14) can be expressed in terms of λ_i:

$$\lambda = \lambda_i \frac{\omega_0}{\omega_D} \tan^{-1}\frac{\omega_D}{\omega_0}. \tag{B.16}$$

Using

$$\omega_0 = \sqrt{\frac{B}{A}} \propto \sqrt{\frac{T}{\varepsilon}} \tag{B.17}$$

and summarising all constants in equation (B.16) in χ the following expression is obtained for λ:

$$\lambda = \lambda_i \frac{1}{\chi}\sqrt{\frac{T}{\varepsilon}} \tan^{-1}\chi\sqrt{\frac{\varepsilon}{T}}. \tag{B.18}$$

m_{Yb} [u]	m_Y [u]	T [K]	λ_{YAG} [$Wm^{-1}K^{-1}$]	λ_{YbAG} [$Wm^{-1}K^{-1}$]	χ [$\sqrt{K}$]
173.04	88.91	300	11	7.4	113.02

Table B.1.: Fit parameters used to obtain the characteristic change in thermal conductivity with Yb^{3+}-doping concentration in Yb:YAG (figure 3.11, section 3.5.3). The three parameters on the left were predetermined, the three on the right were free.

Now, the intrinsic thermal conductivity λ_i of Yb:YAG can also be described by the rule-of-mixtures [Pad97] as

$$\lambda_i = C\lambda_{YbAG} + (1-C)\lambda_{YAG}, \tag{B.19}$$

where λ_{YbAG} and λ_{YAG} are thermal conductivities with the end compositions $C = 1$ and $C = 0$, i.e. in the case of Yb:YAG YbAG and YAG, respectively at a given temperature. With this equation (B.18) becomes:

$$\lambda = [C\lambda_{YbAG} + (1-C)\lambda_{YAG}]\,\frac{1}{\chi}\sqrt{\frac{T}{\varepsilon}}\,\tan^{-1}\chi\sqrt{\frac{\varepsilon}{T}}. \tag{B.20}$$

This equation was used in section 3.5.3 as a fit function on the available literature values for the thermal conductivities of different concentrated Yb:YAG with χ, λ_{YAG} and λ_{YbAG} being the free fit parameters (see also figure 3.11). The parameters used and the resulting fit parameters are given in table B.1.

Strictly speaking, this analytical expression is only valid in the high temperature regime well above the Debye temperature Θ_D (in YAG about 750K [Agg05]) for which the assumptions were made. However, Madarasz and Klemens proved that this expression is also in reasonable agreement for the intermediate temperature range $\Theta_D > T > 0.5\Theta_D$ when point defect scattering is strong [Mad87]. In their work, the high temperature approximation has been shown to have, at room temperature, an error of about 10% for a Ge-Si system. Under the assumption that the error of this approximation is for Yb:YAG in a similar range, equation (B.20) can still be used as a reasonable fit function considering the magnitudes of the measurement errors themselves.

It should be noted that there are different publications dealing with the concentration dependency of the thermal conductivity especially in garnets. Gaumé and coworkers presented a slight modification to the theoretical description of Klemens taking into account the structural properties of the host [Gau03b]. Sato *et al.* developed a different model which proposes the minimum thermal conductivity to be at a composition of about 80%Yb:YAG at room temperature [Sat09].

C. Pair Formation and Cooperative Effects

The formation of pairs, or dimers, which in the case of Yb:YAG are two Yb^{3+}-ions on neighbouring dodecahedral sites, leads to additional effects on the spectroscopic properties. Pairs can manifest themselves in the optical spectra as satellite lines or shifted lines in the vicinity of the single ion lines similar to those observed for the antisite effect mentioned previously. As for the antisites these observations are mostly due to modifications in the local crystal field. The distortions are due to stresses induced into the lattice by the dopant and therefore are more prominent for large ions in matrices with a smaller host cation. Indeed, such lines due to pairs of dopants on dodecahedral sites in YAG have been reported for Pr^{3+} and Nd^{3+} [Lup95], whereas no shifted lines that can be connected with these kind of pairs have been observed for small ions such as Er^{3+} or Yb^{3+} [Lup98, Lup03]. Pairs can also manifest themselves in the optical spectra as splitting of lines through ion-ion interaction effects of the high order multipolar as well as of the superexchange type [Ant01a]. However, the main effects of these interactions for optically active rare earth ions are on the emission kinetics, i.e. in most cases interionic energy transfer processes. These processes, e.g. cross relaxation and up-conversion can lead to strong quenching of the upper laser level's fluorescence lifetime. For Yb^{3+} due to its electronic structure energy transfer by the mentioned processes should not be observed. Nevertheless, the strength of ion-ion interaction for Yb^{3+} can be probed by the investigation of cooperative processes that induce absorption as well as emission lines in spectral regions where no single ion energy level is present. The electronic structure of the Yb^{3+}-ion with only two $4f$ manifolds, $^2F_{7/2}$ and $^2F_{5/2}$, separated by about $10\,000\,cm^{-1}$, is very suitable for the observation of cooperative processes which appear as absorption and emission in the green spectral range at the sum of energies of the two single ions. The spectral lines corresponding to cooperative processes are in most cases weak owing to their second order character and are usually found only in highly concentrated samples. However, the spatial distribution of the dopant in the host is not necessarily homogeneous and therefore cooperative luminescence has also been discussed as a tool to probe clustering in crystals and glasses [Gol02].

Cooperative luminescence of Yb-pairs was first observed by Nakazawa and Shionoya in 1970 for $YbPO_4$, and cooperative processes have been studied in numerous Yb-doped compounds since [Sch75, Weg95, Gol97, Sch00, Mon01, Wan08]. Hehlen and coworkers extensively investigated on the phenomenon of intrinsic optical bistability (IOB)[1] of the Yb pair fluorescence

[1] IOB refers to the presence of two stable emission intensity values for one excitation density depending on the excitation history of the system without the use of an optical cavity. Different attempts have been made to explain this observations for the cooperative luminescence of Yb^{3+}-ions [Heh96, Gam00, Gui01]. A summary of some of the theories and a description of the phenomenon is found in [Pet01]. Up to now, the underlying mechanism has not been fully understood.

in 10%Yb:$Cs_3Y_2Br_9$ [Heh93, Heh94] as well as 1%Yb:$CsCdBr_3$ [Heh99], both being systems in which charge compensation favours formation of rare earth pairs. Motivated by these findings and in search for fast optical switches Noginov *et al.* studied cooperative transitions in several Yb^{3+}-doped oxides including Yb:YAG and YbAG [Nog02]. Rather weak cooperative absorption and emission was found for these materials and it was suggested that not only the minimum distance but also the strength of the covalent coupling between the ions is relevant for the efficiency of cooperative transitions. This interpretation is in accordance with the early results of Schugar and coworkers, who could not find any correlation between known Yb nearest neighbour distances and intensities of cooperative absorption in their experiments [Sch75]. These observations do not necessarily contradict the suggestion of Goldner *et al.* stated above to use cooperative luminescence intensity as a probe for clustering, but point towards a different interpretation of the mechanism underlying pair transitions. Investigations on 15%Yb:YAG waveguides by Malinowsky and coworkers confirmed the fluorescence lifetime of the dimer state to be about half that of the single ion excited state [Mal01], which is in agreement with the results of the rate equation model for the cooperative process [Gol97]. Another noteworthy characteristics of the cooperative absorption and emission spectra are the clearer and much better defined peaks compared to the single ion spectra in the infrared. At low temperature the intensity of vibronic sidebands is even reduced by a factor of up to 20 in the cooperative Yb transitions. An explanation for this photon selection effect is given by Hehlen and Güdel [Heh93] for the cooperative excitation mechanism, who suggest that a fast relaxation step occurs between the absorption of the first and the second photon, which leads to a different energy for the second photon to achieve the same excited state as the first due to slightly different vibrational energies in the ground and excited state. The implication is that cooperative transitions corresponding to summation of energies of two pure electronic states have much higher probability than those involving summation over vibrational mode energies. Taking advantage of this property the Stark energy levels of Yb^{3+} in sesquioxides could be redetermined with higher accuracy [Pet01].

Most theoretical descriptions follow the concept proposed by Dexter based on a hypothetical two ion scheme [Dex62]. It is the conventional assumption that the Coulomb interaction between two electrons on each ion acts as a perturbation to the electric dipole moment, giving rise to some probability for the initially forbidden cooperative transition. The results of Schugar *et al.* indicate that the mechanism of pair transition is not primarily based on multipole type interactions or direct overlap of the $4f$ wave functions [Sch75]. Their investigations on the relation between chemical bonds and the cooperative transition probability suggest a superexchange type interaction, which is an indirect exchange interaction via the bridging ligands. The results led further to the deduction that an increase in covalency[2] of the metal-ligand bond contributes to the pair intensity by increasing the pair integral between the two Yb^{3+}-ions. The influence of covalency and bridging ligands on cooperative optical effects has also been theoretically treated in Mironov and Kaminskii [Mir94]. In their work, the interaction between the coupled lanthanoid ions is regarded as a generalisation of the superexchange interaction mechanism, referred to as covalent coupling. The importance of the nature of chemical bonding is further supported by the observations of Wegh and Meijerink, in which cooperative luminescence could

[2]It should be noted that covalency also lowers the energy of the ligand to metal charge transfer band (see also section 2.2.3).

not be observed in Yb^{3+}-doped $LiYF_4$, a host displaying ionic bonding character, whereas it could be observed in Yb^{3+}-doped La_2O_3, which displays covalent bonding character [Weg95]. In 2005, Ishii presented first-principle calculations for the cooperative transitions of Yb^{3+} pairs in YAG based on a molecular-orbital theory, taking into account the relation between covalency and cooperative transition probability [Ish05]. This theoretical work accurately describes the experimental observations and seems to confirm the cooperative transitions to occur via the $4f$-$2p$ overlaps between the Yb and O atoms[3].

The probability of the occurrence of pairing can be calculated by different models of distribution and is strongly dependent on doping concentration as well as the crystallographic structure surrounding the dopant [Lup03]. Though the distribution of the ions in garnets is said to be random in [Lup03], the possibility of ions occupying nearest neighbour sites forming pairs or even higher ensembles or clusters cannot be completely excluded. Malinowski *et al.* even found indications of clustering in their 15%Yb:YAG waveguide, in which the average separation between the Yb^{3+}-ions should be about 7.8 Å when a uniform distribution of the ions is assumed. As this value is larger than the critical distance of the order of 5 Å reported for dipole-dipole interaction in glass the observed cooperative emission was suggested to be an indication for pairing [Mal01].

From the current level of understanding, the cooperative emission of an excited Yb^{3+} pair is not a significant loss channel for the upper laser level due to the much lower probability of this transition compared to that of the single ion. However, pairs as well as higher order clusters can also transfer their excitation energy to impurities or other loss centres via cooperative upconversion mechanisms as is discussed later in section 5.4.1.

[3]It should be pointed out that the $4f$ shell is in general treated as core like, i.e. the $4f$ orbitals do not participate in bonding as there is no significant overlap with the ligand valence orbitals. The contribution of $4f$ orbitals to chemical bonds together with their influence on covalency is discussed in the literature [Kot92, Dol96, Cho02, Mak04].

D. Characteristics of the Pump Source

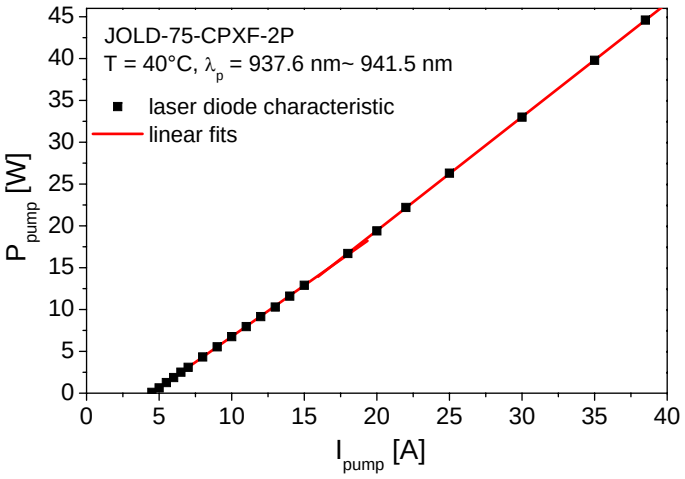

Figure D.1.: Input-output characteristic of the laser diode used as pump source (JOLD-75-CPXF-2P) at 40°C operating temperature

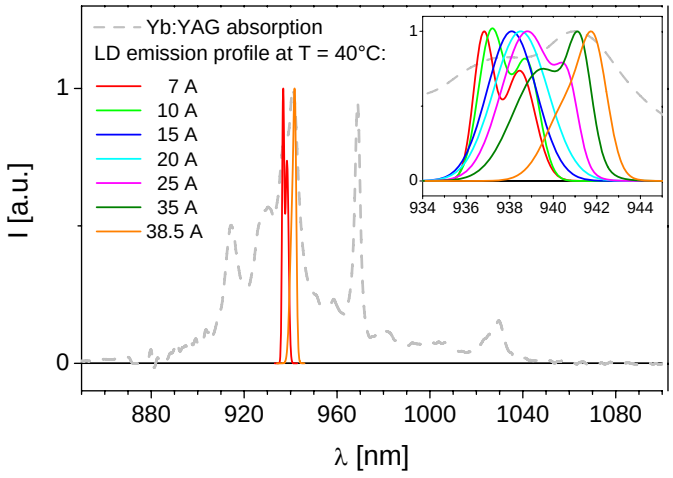

Figure D.2.: Emission profiles of the laser diode used (JOLD-75-CPXF-2P) with multiple Gaussian fits for different operating currents together with the absorption spectrum of Yb:YAG. The operating temperature was stabilised at 40°C. Even though the centre wavelength changes with the operating current, the absorption line of Yb:YAG is still matched.

E. Slope Efficiencies Obtained from Thin-Disk Laser Experiments

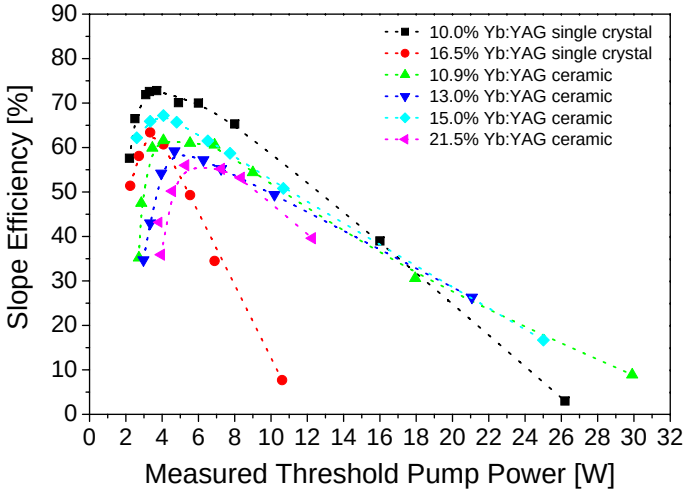

Figure E.1.: Slope efficiencies obtained from thin-disk laser experiments plotted against the measured threshold pump powers.

In figure E.1 the slope efficiencies of the samples investigated, obtained from thin-disk laser experiments are plotted against the measured threshold pump powers. On the left of figure E.2, the slope efficiencies are plotted against the measured threshold pump powers normalised with the sample thicknesses. As can be seen in both cases after reaching a maximum value, the slope efficiencies seem to decrease more or less linearly with increasing threshold pump power. According to the zero-dimensional model, the relationship between density of excited states and threshold pump power should be close to linear, since for the investigated outcoupling transmission rates the absorption efficiency is supposed to be nearly constant (see also equation 2.97)[1]. The thicknesses of the samples were chosen so that the absorption efficiency is the same for the different concentrated samples (see section 5.2). Under this assumption, the different samples should have the same number of excited ions at the same threshold pump power (see equation 2.97), which suggests the same amount of heat introduced through the quantum defect. If the physical condition during laser operation is only determined by heating through the quantum defect, figure E.1 would be the representation, which is suited best for comparison of the laser efficiency of the different samples. Indeed, the ceramic samples all seem to follow the same

[1] In [Fre09], this relationship was exploited to calculate the density of excited states by assuming an absorption efficiency of 1.

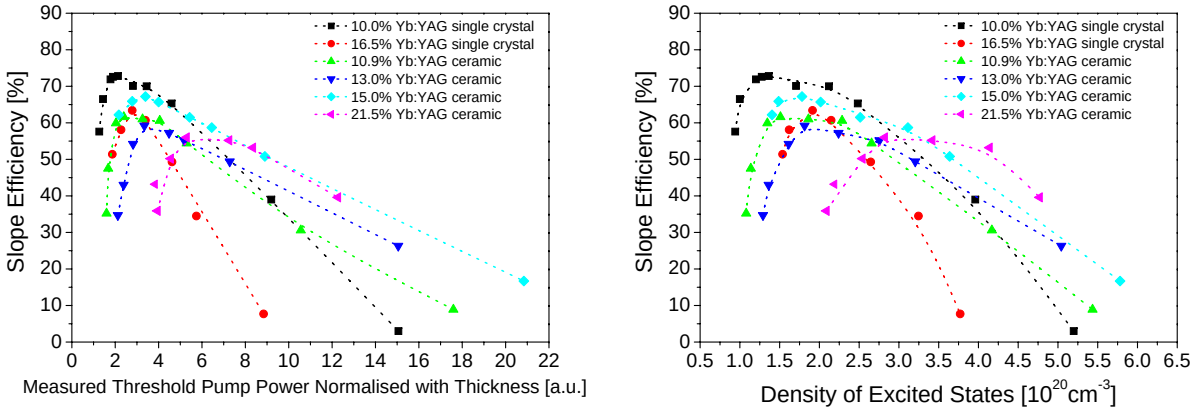

Figure E.2.: Slope efficiencies obtained from thin-disk laser measurements plotted against measured threshold pump powers normalised with sample thickness (left) and plotted against density of excited Yb^{3+}-states calculated from equation 2.93 (right).

characteristic. However, the behaviour of the single crystals do not at all fit into these considerations. It has to be noted that most likely the assumption of same absorption efficiency is not valid as thermal effects have been neglected altogether in the theoretical considerations in section 2.3.2. Also, thinner samples are expected to exhibit improved heat removal, which has not been included in the discussions. If upconversion mechanisms such as cooperative energy transfer to some acceptors are considered significant, the density of excited states is decisive and thus plotting against the density of excited states represents the physical conditions better. However, in figure E.2, left also the curves for the ceramics do not match each other anymore. This could indicate that the density of excited states is not the crucial factor. Figure E.2, right shows the same slope efficiencies plotted against the density of excited Yb^{3+}-ions calculated from equation 2.93. In the absence of excited state absorption and upconversion processes depleting the upper laser level, the density of excited states should be well represented by this expression and the characteristics should be the same as in figure E.2, right. This, apparently is not the case. In figure E.1, the relationship between slope efficiencies and density of excited states is highly non-linear. As mentioned above, these calculations and considerations are all based on the zero-dimensional model without implementation of any upconversion or excited state absorption processes, neglecting any thermal effects. Therefore, neither figure E.2, left nor E.2, right represent the exact relationship between laser efficiency and density of excited Yb^{3+}-ions. At this point, the true physical relationship between density of excited states, threshold pump power and slope efficiency cannot be given. However, figures E.2, right and E.1 show how different the characteristics of the slope efficiencies plotted against the density of excited ions can be, depending on how the density of excited states was determined, even though the same model description is used. Therefore, all deductions regarding the physics behind drawn from these results have to be treated with great care. The assumptions made always need to be pointed out to not confuse tentative models and firm experimental results.

For this reason, in section 5.4.1 the data obtained from measurement are all plotted against the logarithmic outcoupling transmission rate as this represents the experimental results without implying any theoretical assumptions.

F. Photoconductivity in Si:YAG

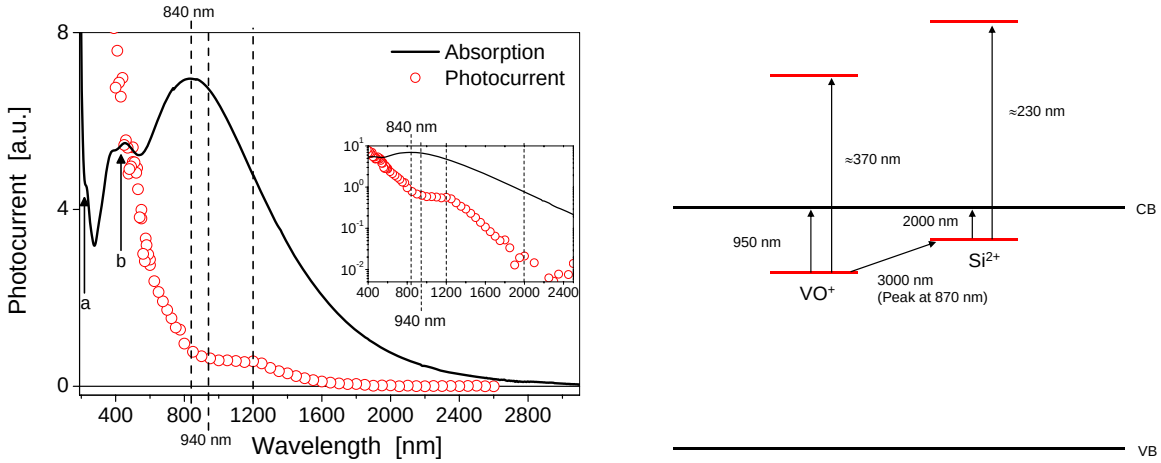

Figure F.1.: Left: excitation spectrum of photoconductivity in as-grown Si:YAG according to [Fag04]. The inset shows the same spectra in logarithmic scale. The vertical dashed lines denote 2 000 nm (see inset), 1 200 nm, 940 nm and 840 nm, which correspond to the first onset of photoconductivity, beginning of constant photocurrent, pump wavelength in the laser experiments and the second onset of photoconductivity, respectively. The arrows marked *a* and *b* indicate the proposed lines for the singlet to singlet absorption band of Si^{2+} [Zha97] and an absorption band associated with a F^{+}-centre [Kar85], respectively. Right: schematic for the tentative model proposed [Fag04]. See text for discussion.

The excitation spectrum of the photoconductivity in as-grown Si-doped YAG [Fag04] is plotted together with the corresponding absorption spectrum in figure F.1, left. The onset of photoconductivity was identified at about 2 000 nm. The photocurrent steadily increases up to 1 200 nm, staying constant until 840 nm, where it starts increasing again. This onset of the second increasing of the photocurrent at 840 nm coincides with the peak of the very broad band absorption band of Si:YAG. The arrows marked *a* and *b* indicate the proposed lines for the singlet to singlet absorption band of the Si^{2+}-ion [Zha97] and an absorption band usually ascribed to a F^{+}-centre [Kar85], respectively. Figure F.1, right shows a schematic describing the model proposed in [Fag04]. The broadband absorption with the peak at 870 nm is here associated with a charge transfer transition between the F^{+}-centre and the Si-ion. However, since such a broad absorption band is not observed in as-grown Si-codoped Yb:YAG samples (in contrast to as-grown Si-codoped Ho:YAG) and because the final state of the proposed charge transfer transition should be the ground state of Si^{+}, of which the energetic position is not known, this interpretation needs to be reassessed. Nevertheless, the experimental results leave no doubt that the complex centre built by the Si^{2+}-ions and the F^{+}-centres lead to the creation of carriers by a one-photon process when excited at 940 nm.

G. Photoconductivity in Yb:Lu_2O_3 and Yb:$LiYF_4$

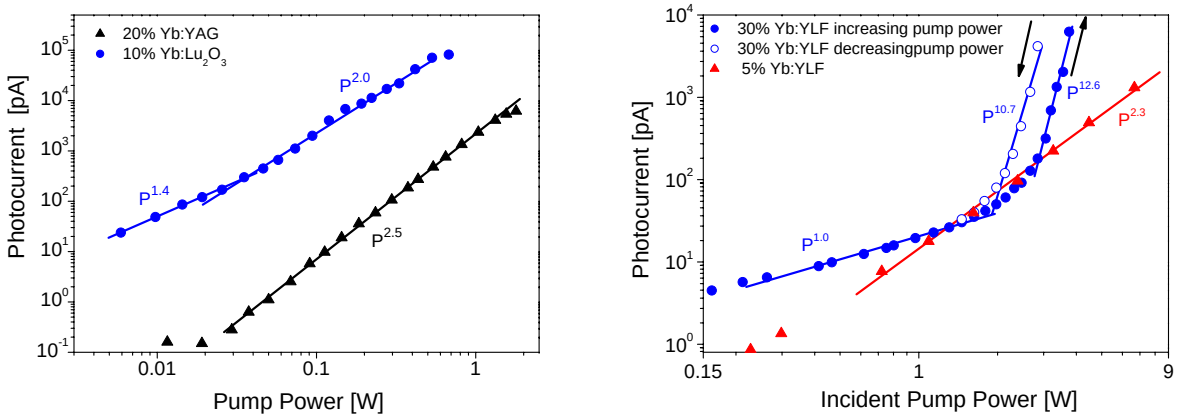

Figure G.1.: Left: photocurrents measured for 10%Yb:Lu_2O_3 and 20%Yb:YAG single crystals of 150 µm thickness under irradiation with 940 nm pump light plotted against pump power in double logarithmic scale [Hir08]. The samples have comparable Yb-ion densities. Right: photocurrents measured for a-cut 5%Yb:YLF [Wol09a] and 30%Yb:YLF single crystalline samples under irradiation of 940 nm pump light plotted against incident pump power in double logarithmic scale. The samples had thicknesses of about 900 µm and 320 µm, respectively.

Photoconductivity measurements were also performed on different host materials doped with ytterbium. The results obtained for a 10%Yb:Lu_2O_3 single crystalline sample of 150 µm thickness are plotted on the left of figure G.1 [Hir08]. In these measurements $f_1 = f_2 = 25$ mm imaging of the pump light was used. The Yb-ion density of the 10%Yb:Lu_2O_3 sample is about $2.85 \cdot 10^{21}$ cm^{-3} [Pet09], which roughly corresponds to the density of Yb-ions in 20%Yb:YAG. As can be seen, the photocurrent measured for the 10%Yb:Lu_2O_3 sample displayed a power law dependence on pump power of exponent 1.4 in the lower power regime and a close to quadratic dependence at higher pump powers. This characteristic is significantly different compared to that found for the 20%Yb:YAG sample, which exhibited a power law dependence with exponent 2.5. The results for the 20%Yb:YAG sample are also plotted in figure G.1, left for comparison. Additionally, photoconductivity measurements were performed on a-cut[1] 5% and 30% Yb:$LiYF_4$ (Yb:YLF) single crystalline samples of about 900 µm and 320 µm, respectively. The crystals were provided by the New Materials for Laser Application Laboratory of the University of Pisa. $f_1 = 45$ mm and $f_2 = 25$ mm imaging of the 940 nm pump light was used in these experiments. The photocurrents obtained are plotted on the right of figure G.1 against the incident pump power in double logarithmic scale. For the 5%Yb:YLF sample, an almost

[1] The optical c-axis is parallel to the polished end faces.

quadratic dependence between photocurrent and pump power is found, which is a characteristic similar as for the Yb:YAG samples. In contrast, the 30%Yb:YLF sample displayed a very different behaviour. In the lower pump power regime the relationship between photocurrent and pump power was clearly linear. At higher powers the photocurrent increased steeply with a power law dependence with an exponent higher than 10. A kind of hysteresis behaviour was found for the photocurrent when turning down the pump power.

For the 10%Yb:Lu_2O_3 single crystalline sample investigated, a similar hopping mechanism with the involvement of CT states for the conduction process is proposed (see also [Hir07]). Sesquioxides display more covalent bonding character compared to the garnets [Weg95]. The term more covalent refers to a higher overlap between the ligand and metal wave functions, which results in the binding electrons being shared among the ions participating in the bond. The more the bonding is covalent in character, the smaller is the band gap and the lower are CT excitation energies of a compound (see section 2.2.3). The band gap of Lu_2O_3 is stated to be 5.51 eV at room temperature [Kim00] and 5.8 eV at 8K [Gue05]. The maximum of the Yb^{3+}/Yb^{2+} CT excitation band is found at about 5.5 eV photon energy at 8K [Gue05]. Assuming as for Yb:YAG an energy level depression in the order of 2 eV for the CT state, two Yb^{3+}-excitations would be enough for the CT transition to occur. Higher covalency of the bonds supports higher mobilities for the electrons in a potential CT band, which could explain the higher photocurrents compared to in Yb:YAG. However, as for the case of Yb:YAG further information and intensive studies are needed to conclusively understand the phenomenon of photoconductivity in this material.

In contrast to the sesquioxides the fluorides are compounds known fr the strongly ionic bonding character, resulting in large band gaps [Weg95]. The host material $LiYF_4$ (YLF) is known for its particularly wide band gap of about 10.55 eV [Kru97]. The photoconductivity results obtained for the 5% and 30%Yb:YLF single crystalline samples displayed very different characteristics. While the photocurrent pump power characteristics of the 5%Yb:YLF sample exhibits high similarities to the characteristics found for the Yb-doped oxides, the 30%Yb:YLF sample displays a unique characteristic. The linear relationship for the lower pump power regime in the higher doped sample might be due to non-intentional impurities located at about 1.3 eV below the conduction band minimum acting as electron donor states. However, neither the abrupt change to a higher than power 10 dependency nor the hysteresis behaviour can be explained at the current state of knowledge. The exponent of 2.3 found for the 5%Yb:YLF seems to be reasonable at first sight. However, the CT excitation band in this material is found at about 7.8 eV at 10K [Pie00]. This is, even if a energy level depression of 3 eV is considered not possible to reach with two Yb^{3+}-excitations. Therefore, it has to be concluded that a hopping mechanism between Yb-ions involving a Yb^{3+}/Yb^{2+} CT transition has to be excluded as the current generating process for both of the Yb:YLF samples investigated. At the current state of knowledge, the physical mechanism underlying the photoconducting behaviour observed in the Yb:YLF samples under 940 nm excitation cannot be understood.

Bibliography

[Agg05] R. L. Aggarwal, D. J. Ripin, J. R. Ochoa and T. Y. Fan. *Measurement of Thermo-Optic Properties of $Y_3Al_5O_{12}$, $Lu_3Al_5O_{12}$, $YAlO_3$, $LiYF_4$, $LiLuF_4$, BaY_2F_8, $KGd(WO_4)_2$, and $KY(WO_4)_2$ Laser Crystals in the 80-300 K Temperature Range*. Journal of Applied Physics **98** (2005).

[Akh77] S. F. Akhmetov, G. L. Akhmetova, G. A. Gazizova, V. S. Kovalenko and T. F. Mirenkova. *Rare Earth Metal Aluminum Garnets*. Russian Journal of Inorganic Chemistry **22**, 1613 (1977).

[Ant01a] E. Antic-Fidancev, J. Hölsä, M. Lastusaari and A. Lupei. *Dopant-Host Relationships in Rare-Earth Oxides and Garnets Doped with Trivalent Rare-Earth Ions*. Physical Review B **64** (19), 195108 (2001).

[Ant01b] P. Antonini, G. Bressi, G. Carugno and D. Iannuzzi. *Scintillation Properties of YAG:Yb Crystals*. Nuclear Instruments and Methods in Physics Research A **460** (2-3), 469 (2001).

[AS01] Vol. 14.02 Anual Book of ASTM Standards. *Test Method E1269-01: Standard Test Method for Determining Specific Heat Capacity by Differential Scanning Calorimetry* (2001).

[Ash77] M. Kh. Ashurov, Yu. V. Voronko, V. V. Osiko, A. A. Sobol and M. I. Timoshechkin. *Spectroscopic Study of Stoichiometry Deviation in Crystals with Garnet Structure*. physica status solidi (a) **42** (101), 101 (1977).

[Auz66] F. Auzel. *Compteur Quantique par Transfert D'Energie Entre Deux Ions de Terres Rares dans un Tungstate Mixte et Dans un Verre*. Comptes Rendus Hebdomadaires des Seances de l'Academie des Sciences. Serie B **262** (15), 1016 (1966).

[Auz94] F. Auzel, D. Meichenin, F. Pellé and P. Goldner. *Cooperative Luminescence as a Defining Process for RE-Ions Clustering in Glasses and Crystals*. Optical Materials **4**, 35 (1994).

[Auz02] F. Auzel. *A Relationship for Crystal Field Strength along the Lanthanide Series; Application to the Prediction of the ($^2F_{7/2}$) Yb^{3+} Maximum Splitting*. Optical Materials **19**, 89 (2002).

[Bar04] Yu. N. Barabanenkov, S. N. Ivanov, A. V. Taranov, E. N. Khazanov, H. Yagi, T. Yanagitani, K. Takaichi, J. Lu, J. F. Bisson, A. Shirakawa, K. Ueda and A. A. Kaminskii. *Nonequilibrium Acoustic Phonons in $Y_3Al_5O_{12}$-Based Nanocrystalline Ceramics*. JETP Letters **79** (7), 342 (2004).

[Bas92] S. A. Basun, S. P. Feofilov, A. A. Kaplyanskii, B. K. Sevastyanov, M. Yu. Sharonov and L.S. Starostina. *Photoelectric Studies of Two-Step Photoionization of Ti^{3+} Ions in Oxide Crystals*. Journal of Luminescence **53**, 28 (1992).

[Bas02] T. T. Basiev, E. V. Zharikov and V. V. Osiko. *Crystals for Photonics*. Crystallography Reports **47** (1), 15 (2002).

[Bas05] S. A. Basun. *private communication* (2005).

[Bea00] R. J. Beach, E. C. Honea, S. B. Sutton, C. M. Bibeau, J. A. Skidmore, M. A. Emanuel, S. A. Payne, P. V. Avizonis, R. S. Monroe and D. G. Harris. *High-Average-Power Diode-Pumped Yb:YAG Lasers*. In: *Proceedings of SPIE*, volume 3889, 246 (2000).

[Bei08] K. Beil. *Yb-Dotiertes $Lu_3Al_5O_{12}$ als Scheibenlasermaterial*. Diplomarbeit, Institut für Laser-Physik, Universität Hamburg (2008).

[Bei09] K. Beil, S. T. Fredrich-Thornton, R. Peters, K. Petermann and G. Huber. *Yb-Doped Thin-Disk Laser Materials: A Comparison between Yb:LuAG and Yb:YAG*. In: *Advanced Solid-State Photonics (Optical Society of America, Washington, DC, 2009), WB28* (2009).

[Bel95] A. Beltrán, J. Andrés, J. A. Igualada and J. Carda. *Garnet Crystal Structures. An ab Initio Perturbed Ion Study*. The Journal of Physical Chemistry **99** (17), 6493 (1995).

[Ber86] F. J. Bergin, J. F. Donegan, T. J. Glynn and G. F. Imbusch. *The Optical Spectroscopy of Chromium in ED-2 Silicate Glass*. Journal of Luminescence **34** (6), 307 (1986).

[Bik90] I. F. Bikmetov, A. B. Sobolev, V. A. Lobach, A. I. Mit'kovets, A. A. Stavrov and A. P. Shkadarevich. *Electronic Structure of Cr^{4+} Ions in Yttrium-Aluminum Garnet in the Embedded Cluster Approximation*. Journal of Applied Spectroscopy **53** (6), 983 (1990).

[Bis03] J.-F. Bisson, Y. Feng, A. Shirakawa, H. Yoneda, J. Lu, H. Yagi, T. Yanagitani and K. Ueda. *Laser Damage Threshold of Ceramic YAG*. Japanese Journal of Applied Physics **42** (8b), L 1025 (2003).

[Bis07a] J.-F. Bisson, D. Kouznetsov, K.-I. Ueda, S. T. Fredrich-Thornton, K. Petermann and G. Huber. *Switching of Emissivity and Photoconductivity in Highly Doped Yb^{3+}:Y_2O_3 and Lu_2O_3 Ceramics*. Applied Physics Letters **90**, 201901 (2007).

[Bis07b] J.-F. Bisson, H. Yagi, T. Yanagitani, A. Kaminskii, Y. N. Barabanenkov and K. Ueda. *Influence of the Grain Boundaries on the Heat Transfer in Laser Ceramics*. Optical Review **14** (1), 1 (2007).

[Bla92] G. Blasse. *Vibronic Transitions in Rare Earth Spectroscopy*. International Reviews in Physical Chemistry **11** (1), 71 (1992).

[Blo66] J. Blok and D. A. Shirley. *Systematic Variation of Quadrupole Crystal-Field Shielding in Rare-Earth Ethyl Sulfates*. Physical Review **143** (1), 278 (1966).

[Bod09] J. Bodzenta, A. Kaźmiercak-Bałata, K. B. Wokulska, J. Kucytowski, T. Łukasiewicz and W. Hofman. *Influence of Doping on Thermal Diffusivity of Single Crystals used in Photonics: Measurements based on Thermal Wave Methods*. Applied Optics **48** (7), C46 (2009).

[Bog76] G. A. Bogomolova, D. N. Vylegzhanin and A. A. Kaminskii. *Spectral and Lasing Investigations of Garnets with Yb^{3+}*. Soviet Physics JETP **42** (3), 440 (1976).

[Bog77] G. A. Bogomolova, L. A. Bumagina, A. A. Kaminskii and B. Z. Malkin. *Crystal Field in Laser Garnets with TR^{3+} Ions in the Exchange Charge Model*. Soviet Physics of the Solid State **19** (8), 1428 (1977).

[Bor27] M. Born and R. Oppenheimer. *Zur Quantentheorie der Molekeln*. Annalen der Physik **389** (20), 457 (1927).

[Bou90] D. P. Bour, D. B. Gilbert, K. B. Fabian, J. P. Bednarz and M. Ettenberg. *Low degradation rate in strained InGaAs/AlGaAs single quantum well lasers*. IEEE Photonics Technology Letters **2** (3), 173 (1990).

[Bri90] F. Bridges, G. Davies, J. RObertson and A. M. Stoneham. *The Spectroscopy of Crystal Defects: A Comparison of Defect Nomenclature*. Journal of Physics: Condensed Matter **2**, 2875 (1990).

[Bro05] D. C. Brown. *The Promise of Cryogenic Solid-State Lasers*. IEEE Journal of Selected Topics in Quantum Electronics **11** (3), 587 (2005).

[Bru97] H. W. Bruesselbach, D. S. Sumida, R. A. Reeder and R. W. Byren. *Low-Heat High-Power Scaling Using InGaAs-Diode-Pumped Yb:YAG Lasers*. IEEE Journal of Selected Topics in Quantum Electronics **3** (1), 105 (1997).

[Bru05] A. Bruesselbach and D. S. Sumida. *A 2.65-kW Yb:YAG Single-Rod Laser*. IEEE Journal of Selected Topics in Quantum Electronics **11** (3), 600 (2005).

[Bry65] B. W. Bryant. *Spectra of Doubly and Triply Ionized Ytterbium, Yb III and Yb IV*. Journal of the Optical Society of America **55** (7), 771 (1965).

[Bub54] R. H. Bube, F. Herman and A. W. Leverenz. *The Solid State*. Annual Review of Physical Chemistry **5**, 199 (1954).

[Bub58] R. H. Bube and W. L. Lind. *Photoconductivity of Zinc Selenide Crystals and a Correlation of Donor and Acceptor Levels in II-IV Photoconductors*. Physical Review **110** (5), 1040 (1958).

[Bub92] R. H. Bube. *Photoelectronic Properties of Semiconductors* (Cambridge University Press, 1992).

[Buc67] R. A. Buchanan, K. A. Wickersheim, J. J. Pearson and G. F. Herrmann. *Energy Levels of Yb^{3+} in Gallium and Aluminum Garnets I. Spectra*. Physical Review **159** (2), 245 (1967).

[Bur72] A. I. Burshtein. *Hopping Mechanism of Energy Transfer*. Soviet Journal of Experimental and Theoretical Physics **35**, 882 (1972).

[Bur85] A. I. Burshtein. *Energy Transfer Kinetics in Disordered Systems*. Journal of Luminescence **34**, 167 (1985).

[Bus97] K. Buse. *Light-Induced Charge Trasport Processes in Photorefractive Crystals I: Models and Experimental Methods*. Applied Physics B **64**, 273 (1997).

[Cai88] J. A. Caird, S. A. Payne, P. Randall Staver, A. J. Ramponi, L. L. Chase and W. F. Krupke. *Quantum Electronic Properties of the $Na_3Ga_2Li_3F_{12}$:Cr^{3+}*. IEEE Journal of Quantum Electronics **24** (6), 1077 (1988).

[Cam02] R. C. Campbell and S. E. Smith. *Flash Diffusivity Method: A Survey of Capabilities*. ElectronicsCooling Magazine **8** (2) (2002).

[Car89] W. T. Carnall, G. L. Goodman, K. Rajnak and R. S. Rana. *A Systematic Analysis of the Spectra of the Lanthanides Doped into Single Crystal LaF_3*. Journal of Chemical Physics **90** (7), 3443 (1989).

[Cas80] J. L. Caslavsky and Dennis J. Viechnicki. *Melting Behaviour and Metastability of Yttrium Aluminium Garnet (YAG) and $YAlO_3$ Determined by Optical Differential Thermal Analysis*. Journal of Materials Science **15**, 1709 (1980).

[Che88] C. Y. Chen, G. J. Pogatshnik, Y. Chen and M. R. Kokta. *Optical and Electron Paramagnetic Resonance Studies of Fe Impurities in Yttrium Aluminum Garnet Crystals*. Physical Review B **38** (13), 8555 (1988).

[Che94] J. K.-W. Chen. *The Electrical and Optical Properties of Doped Yttrium Aluminum Garnets*. Dissertation, Department of Electrical Engineering and Computer Science, Massachusetts Institute of Technology, Cambridge, Mass., USA (1994).

[Chi99] W. Y. Ching and Y. Xu. *Nonscalability and Nontransferability in the Electronic Properties of the Y-Al-O System*. Physical Review B **59** (20), 12815 (1999).

[Cho80] H. C. Chow and R. C. Powell. *Models for Energy Transfer in Solids*. Physical Review B **21** (9), 3785 (1980).

[Cho90] H. K. Choi and C. A. Wang. *InGaAs/AlGaAs Strained Single Quantum Well Diode Lasers with Extremely Low Threshold Current Density and High Efficiency*. Applied Physics Letters **57** (4), 321 (1990).

[Cho02] G. R. Choppin. *Covalency in f-Element Bonds*. Journal of Alloys and Compounds **344**, 55 (2002).

[Con26] E. Condon. *A Theory of Intensity Distribution in Band Systems*. Physical Review **28** (6), 1182 (1926).

[Con02] K. Contag. *Modellierung und numerische Auslegung des Yb:YAG Scheibenlasers*. Dissertation, Universität Stuttgart, Institut für Strahlwerkzeuge (2002).

[Cop96] T. B. Coplen, Members of the IUPAC Comission on Atomic Weights and Isotopic Abundances. *Atomic Weights of the Elements 1995*. Pure and Applied Chemistry **68** (12), 2339 (1996).

[Cro84] H. Crosswhite and D. J. Newman. *Spin-Correlated Crystal Field Parameters for Lanthanide Ions Substituted into $LaCl_3$*. The Journal of Chemical Physics **81** (11), 4959 (1984).

[Czo18] J. Czochralski. *Ein neues Verfahren zur Messung der Kristallisationsgeschwindigkeit der Metalle*. Zeitschrift für Physikalische Chemie **92**, 219 (1918).

[DeL93] L. D. DeLoach, S. A. Payne, L. L. Chase, L. K. Smith, W. L. Kway and W. F. Krupke. *Evaluation of Absorption and Emission Properties of Yb^{3+} Doped Crystals for Laser Applications*. IEEE Journal of Quantum Electronics **29** (4), 1179 (1993).

[Dex53] D. L. Dexter. *A Theory of Sensitized Luminescence in Solids*. The Journal of Chemical Physics **21** (5), 836 (1953).

[Dex62] D. L. Dexter. *Cooperative Optical Absorption in Solids*. Physical Review **126** (6), 1962 (1962).

[Dic01] B.-M. Dicks. *Optische Verstärker bei 1,06 µm für die Weltraumkommunikation*. Dissertation, Institut für Laser-Physik, Universität Hamburg (2001).

[Die63] G. H. Dieke and H. M. Crosswhite. *The Spectra of the Doubly and Triply Ionized Rare Earths*. Applied Optics **2** (7), 675 (1963).

[Dob04] L. Dobrzycki, E. Bulska, D. A. Pawlak, Z. Frukacz and K. Wozniak. *Structure of YAG Crystals Doped/Substituted with Erbium and Ytterbium*. Inorganic Chemistry **43** (24), 7656 (2004).

[Dol96] M. Dolg and H. Stoll. *Electronic Structure Calculations for Molecules Containing Lanthanide Atoms*. In: *Handbook on the Physics and Chemistry of Rare Earths*, editors K. A. Gschneider, Jr. and L. Eyring, volume 22, chapter 152, 1–116 (Elsevier Science B. V., 1996).

[Dor00] P. Dorenbos. *The 5d Level Positions of the Trivalent Lanthanides in Inorganic Compounds*. Journal of Luminescence **91**, 155 (2000).

[Dor03a] P. Dorenbos. *Energy of the First $4f^7 \rightarrow 4f^6 5d$ Transition of Eu^{2+} in Inorganic Compounds*. Journal of Luminescence **104**, 239 (2003).

[Dor03b] P. Dorenbos. *$f \rightarrow d$ Transition Energies of Divalent Lanthanides in Inorganic Compounds*. Journal of Physics: Condensed Matter **15**, 575 (2003).

[Dor03c] P. Dorenbos. *Systematic Behaviour in Trivalent Lanthanide Charge Transfer Energies*. Journal of Physics: Condensed Matter **15**, 8417 (2003).

[Dor05] P. Dorenbos. *The Eu^{3+} Charge Transfer Energy and the Relation with the Band Gap of Compounds*. Journal of Luminescence **111**, 89 (2005).

[Dor10] P. Dorenbos. *private communication* (2010).

[Eck30] C. Eckart. *The Application of Group Theory to the Quantum Dynamics of Monatomic Systems*. Reviews of Modern Physics **2** (3), 305 (1930).

[Ein16] A. Einstein. *Strahlungs-Emission und -Absorption nach der Quantentheorie*. Deutschen Physikalischen Gesellschaft. Verhandlungen **18**, 318 (1916).

[Ell96] A. Ellens, S. Schenker, A. Meijerink and G. Blasse. *Vibronic Transitions of Tm^{3+} in Various Lattices*. Journal of Luminescence **69** (1), 1 (1996).

[Ell97a] A. Ellens, H. Andres, M. L. H. ter Heerdt, R. T. Wegh, A. Meijerink and G. Blasse. *Spectral-Line-Broadening Study of the Trivalent Lanthanide-Ion Series. II. The Variation of the Electron-Phonon Coupling Strength through the Series*. Physical Review B **55** (1), 180 (1997).

[Ell97b] A. Ellens, H. Andres, A. Meijerink and G. Blasse. *Spectral-Line-Broadening Study of the Trivalent Lanthanide-Ion Series. I. Line Broadening as a Probe of the Electron-Phonon Coupling Strength*. Physical Review B **55** (1), 173 (1997).

[Eng09] M. Engholm, P. Jelger, F. Laurell and L. Norin. *Improved Photodarkening Resistivity in Ytterbium-Doped Fiber Lasers by Cerium Codoping*. Optics Letters **34** (8), 1285 (2009).

[Erg50] C. Erginsoy. *On the Mechanism of Impurity Band Conducion in Semiconductors*. Physical Review **80**, 1104 (1950).

[Erg52] C. Erginsoy. *Energy States of Overlapping Impurity Carriers in Semiconductors*. Physical Review **88** (4), 893 (1952).

[Fag04] D. Fagundes de Sousa, V. Peters, N. Martynyuk, K. Lünstedt, K. Petermann and S. Basun. *Quenching Studies of YAG Crystals Highly Doped with Rare-Earth Ions*. In: *13th International Laser Physics Workshop (LPHYS), Trieste* (2004).

[Fag07] D. Fagundes-Peters, N. Martynyuk, K. Lünstedt, V. Peters, K. Petermann, S. Basun, V. Laguta and A. Hofstätter. *High quantum efficiency YbAG-crystals*. Journal of Luminescence **125**, 238 (2007).

[Fan87] T. Y. Fan, G. Huber, R. L. Byer and P. Mitzscherlich. *Continuous-Wave Operation at 2.1 m of a Diode-Laser-Pumped, Tm-Sensitized Ho:$Y_3Al_5O_{12}$ Laser at 300K*. Optics Letters **12** (9), 678 (1987).

[Fan92] T. Y. Fan. *Optimizing the Efficiency and Stored Energy in Quasi-Three-Level Lasers*. IEEE Journal of Quantum Electronics **28** (12), 2692 (1992).

[Feo67] P. P. Feofilov and V. V. Ovsyankin. *Cooperative Luminescence of Solids*. Applied Optics **6** (11), 1828 (1967).

[Fin66] D. Findlay and R. Clay. *The Measurement of Internal Losses in 4-Level Lasers*. Physics Letters **20** (3), 277 (1966).

[För48] Th. Förster. *Zwischenmolekulare Energiewanderung und Fluoreszenz*. Annalen der Physik **437** (1-2), 55 (1948).

[Fra26] J. Franck. *Elementary Processes of Photochemical Reactions*. Transactions of the Faraday Society **21**, 536 (1926).

[Fra58] W. Franz. *Einfluß eines Elektrischen Feldes auf eine Optische Absorptionskante*. Zeitschrift für Naturforschung Teil A **13**, 484 (1958).

[Fre04] S. T. Fredrich. *Charakterisierung der Lasereigenschaften von Nd:YVO_4 und Nd:$GdVO_4$*. Diplomarbeit, Institut für Laser-Physik, Universität Hamburg (2004).

[Fre09] S. T. Fredrich-Thornton, R. Peters, K. Petermann and G. Huber. *Degradation of Laser Performance in Yb-Doped Oxide Thin-Disk Lasers at High Inversion Densities*. In: *Advanced Solid-State Photonics (Optical Society of America, Washington, DC, 2009), TuB18* (2009).

[Fre10] S. T. Fredrich-Thornton, H. Kühn, U. Wolters, K. Petermann and G. Huber. *Excitation Dependent Losses in Yb:YAG Thin-Disk Lasers*. In: *14th International Conference - Laser Optics 2010, ThR1-12* (2010).

[Füc20] C. Füchtbauer. *Absorption in Spectral Lines in Light of Quantum Theory*. Physikalische Zeitschrift **21**, 322 (1920).

[Gam00] D. R. Gamelin, S. R. Lüthi and H. U Güdel. *The Role of Laser Heating in the Intrinsic Optical Bistability of Yb-Doped Bromide Lattices*. Journal of Physical Chemistry B **104** (47), 11045 (2000).

[Gau03a] R. Gaume and B. Viana. *Optical and Thermo-Mechanical Properties of Solid-State Laser Materials*. Annales de Chimie - Science des Matériaux **28**, 89 (2003).

[Gau03b] R. Gaumé, B. Viana, D. Vivien, J.-P. Roger and D. Fournier. *A Simple Model for the Prediction of Thermal Conductivity in Pure and Doped Indulating Crystals*. Applied Physics Letters **83** (7), 1355 (2003).

[Gay86] S. K. Gayen, W. B. Wang, V. Petričevi´c and R. R. Alfano. *Nonradiative Transition Dynamics in Alexandrite*. Applied Physics Letters **49** (8), 437 (1986).

[Gaz73] G. E. Gazz and S. K. Dutta. *US Patent 3767745* (1973).

[Gel67] S. Geller. *Crystal Chemistry of the Garnets*. Zeitschrift für Kristallographie **125**, 1 (1967).

[Gie94] A. Giesen, H. Hügel, A. Voss, K. Wittig, U. Brauch and H. Opower. *Scalable concept for diode-pumped high-power solid-state lasers*. Applied Physics B **58** (5), 365 (1994).

[Gie07] A. Giesen and J. Speiser. *Fifteen Years of Work on Thin-Disk Lasers: Results and Scaling Laws*. IEEE Journal of Selected Topics in Quantum Electronics **13** (3), 598 (2007).

[Gol25] V. M. Goldschmidt, T. Barth and G. Lunde. *Geochemische Verteilungsgesetze der Elemente. V. Isomorphie und Polymorphie der Sesquioxyde. Die Lanthaniden-Kontraktion und Ihre Konsequenzen*.

Det Norske Videnskaps-Akademi Oslo: Skrifter Norske Videnskaps-Akademi i Oslo, I, Matematisk-Naturvidenskapelig Klasse (7) (1925).

[Gol95] E. V. Goldstein and P. Meystre. *Spontaneous Emission in Optical Cavities: A Tutorial Review*. In: *Spontaneous Emission and Laser Oscillation in Microcavities*, editors H. Yokoyama and K. Ujihara, chapter 1, 1–46 (CRC Press, 1995).

[Gol97] P. Goldner, F. Pellé, D. Meichenin and F. Auzel. *Cooperative Luminescence in Ytterbium-Doped $CsCdBr_3$*. Journal of Luminescence **71**, 137 (1997).

[Gol02] P. Goldner, B. Schaudel and M. Prassas. *Dependence of Cooperative Luminescence Intensity on Yb^{3+} Spatial Distribution in Crystals and Glasses*. Physical Review B **65**, 054103 (2002).

[Gör96] C. Görller-Warland and K. Binnemans. *Rationalization of Crystal-Field Parametrization*. In: *Handbook on the Physics and Chemistry of Rare Earths*, editors K. A. Gschneider, Jr. and L. Eyring, volume 23, chapter 155, 121–283 (Elsevier Science B. V., 1996).

[Gre73] C. Greskovich and J. P. Chernoch. *Polycrystalline Ceramic Lasers**. Journal of Applied Physics **44** (410), 4599 (1973).

[Gre74] C. Greskovich and J. P. Chernoch. *Improved Polycrystalline Ceramic Lasers*. Journal of Applied Physics **45** (10), 4495 (1974).

[Gue01] N. Guerassimova, N. Garnier, C. Dujardin, A. G. Petrosyan and C. Pédrini. *X-Ray-Excited Charge Transfer Luminescence in YAG:Yb and YbAG*. Journal of Luminescence **94-95**, 11 (2001).

[Gue02] N. Guerassimova, C. Dujardin, N. Garnier, C. Pédrini, A. G. Petrosyan, I. A. Kamenskikh, V. V. Mickhailin, I. N. Shpinkov, D. A. Spassky, K. L. Ovanesyan, G. O. Shirinyan, R. Chipaux, M. Cribier, J. Mallet and J.-P. Meyer. *Charge-Transfer Luminescence and Spectroscopic Properties of Yb^{3+} in Aluminium and Gallium Garnets*. Nuclear Instruments and Methods in Physics Research A **486** (1-2), 278 (2002).

[Gue05] N.V. Guerassimova, I.A. Kamenskikh, D.N. Krasikov, V.V. Mikhailin, S.N. Scherbinin, K. Petermann, D. F. de Sousa and G. Zimmerer. *Charge Transfer Luminescence of Yb^{3+} and Intrinsic Luminescence of Ytterbium-Containing Sesquioxides: Lu_2O_3-Yb, Y_2O_3-Yb, Sc_2O_3-Yb and Yb_2O_3*. In: *Proceedings of the Eighth International Conference on Inorganic Scintillators and their Use in Scientific and Industrial Applications (SCINT)*, 47–49 (2005).

[Gui01] O. Guillot-Noël, L. Binet and D. Gourier. *Toward Intrinsic Optical Bistability of Rare Earth Ion Pairs in Solids*. Chemical Physics Letters **344**, 612 (2001).

[Ham89] D. S. Hamilton, S. K. Gayen, G. J. Pogatshnik, R. D. Ghen and W. J. Miniscalo. *Optical-Absorption and Photoionization Measurements from the Excited States of Ce^{3+}:$Y_3Al_5O_{12}$*. Physical Review B **39** (13), 8807 (1989).

[Hap00] U. Happek, S. A. Basun, J. Choi, J. K. Krebs and M. Raukas. *Electron Transfer Processes in Rare Earth Doped Insulators*. Journal of Alloys and Compounds **303-304**, 198 (2000).

[Hat64] S. E. Hatch, W. F. Parsons and R. J. Weagley. *Hot-Pressed Polycrystalline CaF_2:Dy^{2+} Laser*. Applied Physics Letters **5** (8), 153 (1964).

[Heh93] M. P. Hehlen and H. U. Güdel. *Optical Spectroscopy of the Dimer System $Cs_3Yb_2Br_9$*. Journal of Chemical Physics **98** (3), 1768 (1993).

[Heh94] M. P. Hehlen, H. U. Güdel, Q. Shu, J. Rai and S. C. Rand. *Cooperative Bistability in Dense, Excited Atomic Systems*. Physical Review Letters **73** (8), 1103 (1994).

[Heh96] M. P. Hehlen, H. U. Güdel, Q. Shu and S. C. Rand. *Cooperative Optical Bistability in the Dimer System $Cs_3Y_2Br_9$:10% Yb^{3+}*. Journal of Chemical Physics **104** (4), 1232 (1996).

[Heh97] M. P. Hehlen. *Reabsorption Artifacts in Measured Excited-State Lifetimes of Solids*. Journal of the Optical Society of America B **14** (14), 1312 (1997).

[Heh99] M. P. Hehlen, A. Kuditcher, S. C. Rand and S. R. Lüthi. *Site-Selective, Intrinsically Bistable Luminescence of Yb^{3+} Ion Pairs in $CsCdBr_3$*. Physical Review Letters **82** (15), 3050 (1999).

[Hel41] K.-H. Hellwege. *Über die Fluoreszenz und die Kopplung zwischen Elektronentermen und Kristallgitter bei den Wasserhaltigen Salzen der Seltenen Erden*. Annalen der Physik **432** (7), 529 (1941).

[Hen89] B. Henderson and G. Imbusch. *Optical Spectroscopy of inorganic Solids* (Clarendon Press, Oxford, 1989).

[Hen00] B. Henderson and R. H. Bartram. *Crystal Field Engineering of Solid State Laser Materials* (Cambridge University Press, 2000).

[Hen01] M. Henke. *Interkonfigurale Übergänge Lanthanid-dotierter Kristalle*. Dissertation, Institut für Laser-Physik, Universität Hamburg (2001).

[Hip36] A. von Hippel. *Einige Prinzipielle Gesichtspunkte zur Spektroskopie der Ionenkristalle und Ihre Anwendung auf die Alkalihalogenide*. Zeitschrift für Physik **101** (11-12), 680 (1936).

[Hir07] C. Hirt. *Verlustprozesse in hoch Yb-dotierten Granat-und Sesquioxidkristallen*. Diplomarbeit, Institut für Laser-Physik, Universität Hamburg (2007).

[Hir08] C. Hirt, S. T. Fredrich-Thornton, F. Tellkamp, K. Petermann and G. Huber. *Photoconductivity Measurements Indicating a Nonlinear Loss Mechanism in Highly Doped Yb-Doped Oxides*. In: *Advanced Solid-State Photonics (Optical Society of America, Washington, DC, 2008), MF1* (2008).

[Hof06] A. M. Hofmeister. *Thermal Diffusivity of Garnets at High Temperature*. Physics and Chemistry of Minerals **33**, 45 (2006).

[Hou07] C. E. Housecroft and A. G. Sharpe. *Inorganic Chemistry* (Prentice Hall, 2007), 3rd revised (rv) edition.

[Hua50] K. Huang and A. Rhys. *Theory of Light Absorption and Non-Radiative Transitions in F-Centres*. Proceedings of the Royal Society of London. Series A **204**, 406 (1950).

[Hub80] G. Huber. *Miniature Neodymium Lasers*. In: *Current Topics in Materials Science*, editor E. Kaldis, volume 4, chapter 1, 1–45 (North-Holland, 1980).

[Ike92] A. Ikesue. *Japanese Patent 3463941* (1992).

[Ike95a] A. Ikesue, I. Furusato and K. Kamata. *Fabrication of Polycrystalline, Transparent YAG Ceramics by a Solid-State Reaction Method*. Journal of the American Ceramic Society **78** (1), 225 (1995).

[Ike95b] A. Ikesue, T. Kinoshita, K. Kamata and K. Yoshida. *Fabrication and Optical Properties of High-Performance Polycrystalline Nd:YAG Ceramics for Solid-State Lasers*. Journal of the American Ceramic Society **78** (4), 1033 (1995).

[Ino65] M. Inokuti and F. Hirayama. *Influence of Energy Transfer by the Exchange Mechanism on Donor Luminescence*. The Journal of Chemical Physics **6** (6), 1978 (1965).

[Ish05] T. Ishii. *First-Principle Calculations for the Cooperative Transitions of Yb^{3+} Dimer Clusters in $Y_3Al_5O_{12}$ and Y_2O_3 Crystals*. The Journal of Chemical Physics **122**, 024705 (2005).

[Iva85] S. N. Ivanov and E. N. Khazanov. *Propagation of Nonequilibrium Acoustic Phonons in Garnet Solid Solutions on an Aluminium Base*. Soviet Physics JETP **61** (1), 172 (1985).

[Jet09] S. Jetschke and U. Röpke. *Power-Law Dependence of the Photodarkening Rate Constant on the Inversion in Yb Doped Fibers*. Optics Letters **34** (1), 109 (2009).

[Jia02] D. Jia, R. S. Meltzer and W. M. Yen. *Location of the Ground State of Er^{3+} in Doped Y_2O_3 from Two-Step Photoconductivity*. Physical Review B **65**, 235116 (2002).

[Joh71] L. F. Johnson, J. E. Geusic and L. G. Van Uitert. *Coherent Oscillations from Tm^{3+}, Ho^{3+}, Yb^{3+} and Er^{3+} Ions in Yttrium Aluminum Garnets*. Applied Physics Letters **7** (5), 127 (1971).

[Jør62] C. K. Jørgensen. *Electron Transfer Spectra of Lanthanide Complexes*. Molecular Physics **5**, 271 (1962).

[Jør70] C. K. Jørgensen. *Electron Transfer Spectra*. Progress in Inorganic Chemistry **12**, 101 (1970).

[Jos90] N. V. Joshi. *Photoconductivity: Art, Science and Technology* (Marcel Dekker, Inc., 1990).

[Jou04] M.-F. Joubert, S. A. Kazanskii, Y. Guyot, J.-C. Gâcon and C. Pédrini. *Microwave Study of Photoconductivity Induced by Laser Pulses in Rare-Earth-Doped Dielectric Crystals*. Physical Review B **69**, 165217 (2004).

[Jud62] B. R. Judd. *Optical Absorption Intensities of Rare-Earth Ions*. Physical Review **127** (3), 750 (1962).

[Jud66] B. R. Judd. *Three-Particle Operators for Equivalent Electrons*. Physical Review **141** (1), 4 (1966).

[Jud68] B. R. Judd, H. M Crosswhite and H. Crosswhite. *Intra-Atomic Magnetic Interactions for f Electrons*. Physical Review **169** (1), 130 (1968).

[Kam90] A. A. Kaminskii. *Laser Crystals – Their Physics and Properties* (Springer-Verlag, 1990), 2nd edition.

[Kam05a] I. A. Kamenskikh, C. Dujardin, N. Garnier, N. Guerassimova, G. Ledoux, V. V. Mickhailin, C. Pedrini, A. G. Petrosyan and A. Vasil'ev. *Temperature Dependence of the Charge Transfer and f-f Luminescence of Yb^{3+} in Garnets and YAP*. Journal of Physics: Condensed Matter **17**, 5587 (2005).

[Kam05b] A. A. Kaminskii, M. Sh. Akchurin, R. Gainutdinov, K. Takaichi, A. Shirakava, H. Yagi, T. Yanagitani and K. Ueda. *Microhardness and Fracture Toughness of Y_2O_3- and $Y_3Al_5O_{12}$-Based Nanocrystalline Laser Ceramics*. Crystallography Reports **50** (5), 869 (2005).

[Kam09] I. Kamenskikh, M. Chugunova, S. T. Fredrich-Thornton, C. Pedrini, K. Petermann, A. Vasil'ev, U. Wolters and H. Yagi. *Potentiality of Ceramic Scintillators: General Considerations and YAG-Yb Optical Ceramics Performance*. In: *10th International Conference on Inorganic Scintillators and their Applications, Jeju, Korea, 8-12 June 2009* (2009).

[Kar85] L. G. Karaseva, N. Yu. Konstantinov and V. V. Gromov. *Nature of Radiation Colour Centres in SIngle Crystals of Yttrium Aluminum Garnet*. Radiation Physics and Chemistry **26** (5), 723 (1985).

[Kaz03] L. I. Kazakova, G. M. Kuz'micheva and E. M. Suchkova. *Growth of $Y_3Al_5O_{12}$ Crystals for Jewelry*. Inorganic Materials **39** (9), 959 (2003).

[Kek08] R. D. Kekatpure and M. L. Brongersma. *Quantification of Free-Carrier Absorption in Silicon Nanocrystals with an Optical Microcavity*. Nano Letters **8** (11), 3787 (2008).

[Kel58] L. V. Keldysh. *Behaviour of Non-Metallic Crystals in Strong Electric Fields*. Soviet Journal of Experimental and Theoretical Physics **6**, 763 (1958).

[Küh07] H. Kühn, S. T. Fredrich-Thornton, C. Kränkel, R. Peters and K. Petermann. *A Model for the Calculation of Radiation Trapping and Description of the Pinhole Method*. Optics Letters **32** (13), 1908 (2007).

[Kil08] A. Killi, I. Zawischa, . Sutter, J. Kleinbauer, S. Schad, J. Neuhaus and C. Schmitz. *Current Status and Development Trends of Disk Laser Technology*. In: *Solid State Lasers XVII: Technology and Devices, Proc. of SPIE Vol. 6871* (2008).

[Kim00] S. Kimura, F. Arai and M. Ikezawa. *Optical Study on Electronic Structure of Rare-Earth Sesquioxides*. Journal of the Physical Society of Japan **69** (10), 3451 (2000).

[Kis66] Z. J. Kiss and R. J. Pressley. *Crystalline Solid Lasers*. Applied Optics **5** (10), 1474 (1966).

[Kit99] Charles Kittel. *Einführung in die Festkörperphysik* (R. Oldenbourg Verlag, München Wien, 1999), 12th edition.

[Kle60] P. G. Klemens. *Thermal Resistance due to Point Defects at High Temperatures*. Physical Review **119** (2), 507 (1960).

[Kle67] P. H. Klein and W. J. Croft. *Thermal Conductivity, Diffusivity, and Expansion of Y_2O_3, $Y_3Al_5O_{12}$, and LaF_3 in the Range 77°-300°K*. Journal of Applied Physics **38** (4), 1603 (1967).

[Kle94] P. G. Klemens. *Phonon Scattering and Thermal Resistance Due to Grain Boundaries*. International Journal of Thermophysics **15** (6), 1345 (1994).

[Koe90] J. Koetke. *Kristallzucht und optische Charakterisierung von Nickel-dotierten Oxid-Kristallen*. Diplomarbeit, Institut für Laser-Physik, Universität Hamburg (1990).

[Kol88] R. M. Kolbas, N. G. Anderson, W. D. Laidig, Y. Sin, Y. C. Lo, K. Y. Hsieh and Y. L. Yang. *Strained-Layer InGaAs-GaAs-AlGaAs Photopumped and Current Injection Lasers*. IEEE Journal of Quantum Electronics **24**, 1605 (1988).

[Kon65] J. A. Koningstein. *Energy Levels and Crystal-Field Calculations of Trivalent Ytterbium in Yttrium Aluminum Garnet and Yttrium Gallium Garnet*. Theoretica Chimica Acta **3**, 271 (1965).

[Kop08] J. Koponen, M. Söderlund, H. J. Hoffman, D. A. V. Kliner, J. P. Koplow and M. Hotoleanu. *Photodarkening Rate in Yb-Doped Silica Fibers*. Applied Optics **47** (9), 1247 (2008).

[Kor96] M. V. Korzhik, G. Yu. Drobyshev, D. M. Kondratiev, A. E. Borisevich, V. B. Pavlenko and T. N. Timochenko. *Scintillation Quenching in Cerium-Doped Ytterbium-Based Crystals*. Physica Status Solidi (b) **197**, 495 (1996).

[Kot92] M. Kotzian, N. Rösch and M. C. Zerner. *Intermediate Neglect of Differential Overlap Spectroscopic Studies on Lanthanide Complexes I. Spectroscopic Parametrization and Application to Diatomic Lanthanide Oxides LnO (Ln=La, Ce, and Lu)*. Theoretica Chmica Acta **81**, 201 (1992).

[Krä08] C. Kränkel. *Ytterbium-dotierte Borate und Vanadate mit großer Verstärkungsbandbreite als aktive Materialien im Scheibenlaser*. Dissertation, Institut für Laser-Physik, Universität Hamburg (2008).

[Kra30] H. A. Kramers. *General Theory of Pramagnetic Rotation in Crystals*. Proceedings of the Koninklijke Nederlandse Akademie van Wetenschappen **33** (9), 959 (1930).

[Krä04] C. Kränkel, D. Fagundes-Peters, S. T. Fredrich, J. Johannsen, M. Mond, G. Huber, M. Bernhagen and R. Uecker. *Continuous Wave Laser Operation of Yb^{3+}:YVO_4*. Applied Physics B **79**, 543 (2004).

[Kre03] M. Kreye and K. D. Becker. *An Optical In-Situ Study of the Re-Oxidation Kinetics of Mixed Valent $Yb_3Al_{12}O_{12}$*. Physical Chemistry Chemical Physics **5**, 2283 (2003).

[Kru66] W. F. Krupke. *Optical Absorption and Fluorescence Intensities in Several Rare-Earth-Doped Y_2O_3 and LaF_3 Single Crystals*. Physical Review **145** (1), 325 (1966).

[Kru71] W. F. Krupke. *Radiative Transition Probabilities Within the $4f^3$ Ground Configuration of Nd:YAG*. IEEE Journal of Quantum Electronics **7** (4), 153 (1971).

[Kru74] W. F. Krupke. *Induced-Emission Cross Sections in Neodymium Laser Glasses*. IEEE Journal of Quantum Electronics **QE-10** (4), 450 (1974).

[Kru86] W. F. Krupke, M. D. Shinn, J. E. Marion, J. A. Caird and S. E. Stokowski. *Spectroscopic, Optical, and Thermomechanical Properties of Neodymium- and Chromium-Doped Gadolinium Scandium Gallium Garnet*. Journal of the Optical Society of America B **3** (1), 102 (1986).

[Kru90] W. F. Krupke and L. L. Chase. *Ground-State Depleted Solid-State Lasers: Principles, Characteristics and Scaling*. Optical and Quantum Electronics **22**, S1 (1990).

[Kru95] J. C. Krupa. *Optical Excitations in Lanthanide and Actinide Compounds*. Journal of Alloys and Compounds **225**, 1 (1995).

[Kru97] J. C. Krupa and M. Queffelec. *UV and VUV Optical Excitations in Wide Band Gap Materials Doped with Rare Earth Ions: 4f-5d Transitions*. Journal of Alloys and Compounds **250**, 287 (1997).

[Kru00] W. F. Krupke. *Ytterbium Solid-State Lasers - The First Decade*. IEEE Journal of Selected Topics in Quantum Electronics **6** (6), 1287 (2000).

[Küc95] S. Kück, K. Petermann, U. Pohlmann and G. Huber. *Near-Infrared Emission of Cr^{4+}-Doped Garnets: Lifetimes, QUantum Efficiencies, and Emission Cross Sections*. Physical Review B **51** (24), 17323 (1995).

[Kuk00] M. M. Kuklja. *Defects in Yttrium Aluminium Perovskite and Garnet Crystals: Atomistic Study*. Journal of Physics: Condensed Matter **12**, 2953 (2000).

[Kus69] T. Kushida. *Linewidths and Thermal Shifts of Spectral Lines in Neodymium-Doped Yttrium Aluminum Garnet and Calcium Fluorophosphate*. Physical Review **185** (2), 500 (1969).

[Kuw04] Y. Kuwano, K. Suda, N. Ishizawa and T. Yamada. *Crystal Growth and Properties of* $(Lu,Y)_3Al_5O_{12}$. Journal of Crystal Growth **260**, 159 (2004).

[Kya08] A. G. Kyazym-zade, A. A. Agaeva, V. M. Salmanov and A. G. Mokhtari. *Photoconductivity of of GaSe Single Crystals under High-Density Excitation*. Inorganic Materials **44** (4), 357 (2008).

[Lac91] P. Lacovara, H. K. Choi, C. A. Wang, R. I. Aggarwal and T. Y. Fan. *Room-temperature diode-pumped Yb:YAG laser*. Optics Letters **16** (14), 1089 (1991).

[Lad21] R. Ladenburg. *Die Quantentheoretische Deutung der Zahl der Dispersionselektronen*. Zeitschrift für Physik **4** (4), 451 (1921).

[Lap25] O. Laporte and W. F. Meggers. *Some Rules of Spectral Structure*. Journal of the Optical Society of America and Review of Scientific Instruments **11** (5), 459 (1925).

[Lar05] M. Larionov, K. Schuhmann, J. Speiser, C. Stolzenburg and A. Giesen. *Nonlinear Decay of the Excited State in Yb:YAG*. In: *Advanced Solid-State Photonics (TOPS), C. Denman and I. Sorokina, eds., Vol. 98 of OSA Trends in Optics and Photonics (Optical Society of America, 2005), paper 18* (2005).

[Lar08] M. Larionov. *Kontaktierung und Charakterisierung von Kristallen für Scheibenlaser*. Dissertation, Institut für Strahlwerkzeuge, Universität Stuttgart (2008).

[Law93] J. K. Lawson and S. A. Payne. *Excited-State Absorption of* Eu^{2+}*-Doped Materials*. Physical Review B **47** (21), 14003 (1993).

[Lin64] R. C. Linares. *Growth of Garnet Laser Crystals*. Solid State Communications **2**, 229 (1964).

[Liu05] G. Liu. *Electronic Energy Level Structure*. In: *Spectroscopic Properties of Rare Earths in Optical Materials*, editors G. Liu and B. Jacquier, chapter 1, 1–94 (Springer, 2005), illustrated edition.

[Liu06] Q. Liu, M. Gong, F. Lu, W. Gong, C. Li and D. Ma. *Corner-pumped Yb:Yttrium Aluminum Garnet Slab Laser Emitted up to 1 kW*. Applied Physics Letters **88**, 101113 (2006).

[Loh73] E. Loh. *Strong-Field Assignment on* $4f^{13}5d$ *Levels of* Yb^{2+} *in* $SrCl_2$. Physical Review B **7** (5), 1846 (1973).

[Lu02] J. Lu, K. Ueda, H. Yagi, T. Yanagitani, Y. Akiyama and A. A. Kaminskii. *Neodymium Doped Yttrium Aluminum Garnet* $(Y_3Al_5O_{12})$ *Nanocrystalline Ceramics - a New Generation of Solid State Laser and Optical Materials*. Journal of Alloys and Compounds **341**, 220 (2002).

[Lup95] V. Lupei, A. Lupei, C. Tiseanu, S. Georgescu, C. Stoicescu and P. M. Nanau. *High-Resolution Optical Spectroscopy of YAG:Nd: A Test for Structural and Distribution Models*. Physical Review B **51** (1), 8 (1995).

[Lup98] A. Lupei, V. Lupei and E. Osiac. *Spectral and Dynamical Effects of Octahedral Impurities on* RE^{3+} *in Garnets*. Journal of Physics: Condensed Matter **10** (43), 9701 (1998).

[Lup99a] A. Lupei, V. Lupei, V. N. Enaki, C. Presura and A. Petraru. *Electron-Phonon Coupling for Heavy* RE^{3+} *Ions in Crystals*. Spectrochimica Acta Part A **55**, 773 (1999).

[Lup99b] A. Lupei, V. Lupei, C. Presura, V. N. Enaki and A. Petraru. *Electron-Phonon Coupling Effects on* Yb^{3+} *Spectra in Several Laser Crystals*. Journal of Physics: Condensed Matter **11**, 3769 (1999).

[Lup03] A. Lupei and V. Lupei. RE^{3+} *Pairs in Garnets and Sesquioxides*. Optical Materials **24**, 181 (2003).

[Mad87] F. L. Madarasz and P. G. Klemens. *Reduction of Lattice Thermal Conductivity by Point Defects at Intermediate Temperatures*. International Journal of Thermophysics **8** (2), 257 (1987).

[Mai60] T. Maiman. *Stimulated Optical Radiation in Ruby*. Nature **187**, 493 (1960).

[Mak04] Y. Makino and S. Uchida. *Chemical Bonds and Calculation Approach to Rare Earth Oxides*. In: *Binary Rare Earth Oxides*, editor G. Adachi, chapter 4, 95–110 (Kluwer Academic Publishers, 2004).

[Mal01] M. Malinowski, M. Kaczkan, R. Piramidowicz, Z. Frukacz and J. Sarnecki. *Cooperative Emission in Yb^{3+}:YAG Planar Epitaxial Waveguides*. Journal of Luminescence **94-95**, 29 (2001).

[Mar99] I. R. Martín, V. D. Rodríguez, U. R. Rodríguez-Mendoza and V. Lavín. *Energy Transfer with Migration. Generalization of the Yokota-Tanimoto Model for Any Kind of Multipole Interaction*. Journal of Chemical Physics **4** (3), 1191 (1999).

[Mar02] N. Martynyuk. *Quenching Behaviour and Laser Operation of Highly Doped Yb:YAG Crystals*. Diplomarbeit, Institut für Laser-Physik, Universität Hamburg (2002).

[Mar04] N. V. Martynyuk, L. O. Vasylechko, S. V. Fadeev, A. O. Matkovskii and K. Petermann. *Crystal Structure of $Y_{3-x}Yb_xAl_5O_{12}$ Solid Solution*. Bulletin of National University "Lviv Polytechnic" **No. 513** (2004).

[Mar09] H. Marquardt, S. Ganschow and F. R. Schilling. *Thermal Diffusivity of Natural and Synthetic Garnet Solid Solution Series*. Physics and Chemistry of Minerals **36**, 107 (2009).

[McC64] D. E. McCumber. *Einstein Relations Connecting Broadband Emission and Absorption Spectra*. Physical Review **136** (4A), A954 (1964).

[McC85] D. S. McClure and C. Pedrini. *Excitons Trapped at Impurity Centers in HIghly Ionic Crystals*. Physical Review B **32** (12), 8465 (1985).

[Mei94] A. Meijerink, C. de Mello Donegá, A. Ellens, J. Sytsma and G. Blasse. *Vibronic Transitions of Rare Earth Ions*. Journal of Luminescence **58** (1-6), 26 (1994).

[Men25] G. Menzer. *Die Kristallstruktur von Granat*. Zentralblatt für Mineralogie, Geologie und Paläontologie A 344–345 (1925).

[Men09] J. Mende, E. Schmid, J. Speiser an G. Spindler and A. Giesen. *Thin-Disk Laser - Power Scaling to the kW Regime in Fundamental Mode Operation*. In: *Solid State Lasers XVII: Technology and Devices, Proc. of SPIE Vol. 7193* (2009).

[Mez06] L. Mezeix and D. J. Green. *Comparison of the Mechanical Properties of Single Crystal and Polycrystalline Yttrium Aluminum Garnet*. International Journal of Applied Ceramic Technology **3** (2), 166 (2006).

[Mir94] V. S. Mironov and A. A. Kaminskii. *The Role of Covalency and Bridging Ligands in Two-Ion Cooperative Optical Transitions in Lanthanide Ion-Coupled Systems*. physica status solidi (b) **183**, 481 (1994).

[Mir96] V. S. Mironov. *Superexchange Interaction Between Lanthanide f^1 Ions. Spin-Hamiltonian Calculations for the 90° and 180° f^1-f^1 Superexchange*. Journal of Physcis: Condensed Matter **8**, 10551 (1996).

[Mix95] E. Mix. *Spektroskopie und Lasereigenschaften Ytterbiumdotierter Kristalle und Fluorid-Phosphat-Gläser*. Diplomarbeit, Institut für Laser-Physik, Universität Hamburg (1995).

[Mix99] E. Mix. *Kristallzüchtung, Spektroskopie und Lasereigenschaften Yb-dotierter Sesquioxide*. Dissertation, Institut für Laser-Physik, Universität Hamburg (1999).

[Miy70] T. Miyakawa and D. L. Dexter. *Cooperative and Stepwise Excitation of Luminescence: Trivalent Rare-Earth Ions in Yb^{3+}-Sensitized Crystals*. Physical Review B **1** (1), 70 (1970).

[Moi89] B. Moine, B. Courtois and C. Pedrini. *Luminescence and Photoionization Processes of Yb^{2+} in CaF_2, SrF_2 and BaF_2*. Journal de Physique **50**, 2105 (1989).

[Mon01] E. Montoya, L. E. Bausá, B. Schaudel and P. Goldner. *Yb^{3+} Distribution in $LiNbO_3$:(MgO) Studied by Cooperative Luminescence*. Journal of Chemical Physics **114** (7), 3200 (2001).

[Mor98] J. Morikawa and T. Hashimoto. *Analysis of High-Order Harmonics of Temperature Wave for Fourier Transform Thermal Analysis*. Japanese Journal of Applied Phyiscs **37** (12A), L1484 (1998).

[Mor08] J. Morikawa, C. Leong, T. Hashimoto, T. Ogawa, Y. Urata, S. Wada, M. Higuchi and J. Takahashi. *Thermal Conductivity of Nd^{3+} Doped $GdVO_4$, YVO_4, $LuVO_4$, and $Y_3Al_5O_{12}$ by Temperature Wave Analysis*. Journal of Applied Physics **103** (2008).

[Mot61] N. F. Mott and W. D. Twose. *The Theory of Impurity Conduction*. Advances in Physics **10** (38), 107 (1961).

[Mül01] V. Müller. *Charakterisierung und Optimierung von hochdotierten Yb:YAG-Laserkristallen*. Diplomarbeit, Institut für Laser-Physik, Universität Hamburg (2001).

[Nak78] E. Nakazawa. *Charge-Transfer Type Luminescence of Yb^{3+} Ions in $LuPO_4$ and YPO_4*. Chemical Physics Letters **56** (1), 161 (1978).

[Nak79] E. Nakazawa. *Charge Transfer Type Luminescence of Yb^{3+} Ions in RPO_4 and R_2O_2S (R=Y, La, and Lu)*. Journal of Luminescence **18/19**, 272 (1979).

[Nak06] E. Nakazawa. *Fundamentals of Luminescence*. In: *Fundamentals of Phosphors*, editors W. M. Yen, S. Shionoya and H. Yamamoto, chapter 1, 25–38 (CRC Press, 2006).

[New71] D. J. Newman. *Theory of Lanthanide Crystal Fields*. Advances in Physics **20** (84), 197 (1971).

[Nik04] M. Nikl, A. Yoshikawa and T. Fukuda. *Charge Transfer Luminescence in Yb^{3+}-Containing Compounds*. Optical Materials **26**, 545 (2004).

[Nog02] M. A. Noginov, G. B. Loutts, C. S. Steward, B. D. Lucas, D. Fider, V. Peters, E. Mix and G. Huber. *Spectroscopic Study of Yb Doped Oxide Crystals for Intrinsic Optical Bistability*. Journal of Luminescence **96**, 129 (2002).

[Öbe07] K. J. Öberg and H. Lundberg. *Experimental Transition Probabilities and Improved Level Energies in Yb III*. The European Physical Journal D **42**, 15 (2007).

[Ofe62] G. S. Ofelt. *Intensities of Crystal Spectra of Rare-Earth Ions*. The Journal of Chemical Physics **37** (3), 511 (1962).

[Owe81] J. F. Owen, P. B. Dorain and T. Kobayasi. *Excited-State Absorption in Eu^{2+}:CaF_2 and Ce^{3+}:YAG Single Crystals at 298 and 77K*. Journal of Applied Physics **52** (3), 1216 (1981).

[Pad97] N. P. Padture and P. G. Klemens. *Low Thermal Conductivity in Garnets*. Journal of the American Ceramic Society **80** (4), 1018 (1997).

[Par59] L. G. Parratt. *Electronic Band Structure of Solids by X-Ray Spectroscopy*. Review of Modern Physics **31** (3), 616 (1959).

[Par61] W. Parker, R. Jenkins, C. Butler and G. Abbott. *Flash Method of Determining Thermanl Diffusivity, Heat Capacity, and Therman Conductivity*. Journal of Applied Physics **32** (9) (1961).

[Pat01] F. D. Patel, E. C. Honea, J. Speth, S. A. Payne, R. Hutcheson and R. Equall. *Laser Demonstration of $Yb_3Al_5O_{12}$ (YbAG) and Materials Properties of Highly Doped Yb:YAG*. IEEE Journal of Selected Topics in Quantum Electronics **37** (1), 135 (2001).

[Pau32] L. Pauling. *The Nature of the Chemical Bond. IV. The Energy of Single Bonds and the Ralative Electronegativity of Atoms*. Journal of the American Chemical Society **54**, 3570 (1932).

[Pay92] S. A. Payne, L. L. Chase, L. K. Smith, W. L. Kway and W. F. Krupke. *Infrared Cross-Section Measurements for Crystals Doped with Er^{3+}, Tm^{3+}, and Ho^{3+}*. IEEE Journal of Quantum Electronics **28** (11), 2619 (1992).

[Pea67] J. J. Pearson, G. F. Herrmann, K. A. Wickersheim and R. A. Buchanan. *Energy Levels of Yb^{3+} in Gallium and Aluminum Garnets. II. Calculations*. Physical Review **159** (2), 251 (1967).

[Ped79] C. Pedrini, D. S. McClure and C. H. Anderson. *Photoionization Thresholds of Divalent Rare Earth Ions in Alkaline Earth Fluorides*. Journal of Chemical Physics **70** (11), 4959 (1979).

[Ped86] C. Pedrini, R. Rogemond and D. S. McClure. *Photoionization Thresholds of Rare-Earth Impurity Ions. Eu^{2+}:CaF_2, Ce^{3+}:YAG, and Sm^{2+}:CaF_2*. Journal of Applied Physics **59** (4), 1196 (1986).

[Péd05] C. Pédrini. *Electronic Processes in Rare Earth Activated Wide Band Gap Materials*. physica status solidi (a) **202** (2), 185 (2005).

[Pei29] R. Peierls. *Zur kinetischen Theorie der Wärmeleitung in Kristallen*. Annalen der Physik **395** (8), 1055 (1929).

[Pet95] D. G. Pettifor. *Bonding and Structure of Molecules and Solids* (Oxford University Press, 1995).

[Pet01] V. Peters. *Growth and Spectroscopy of Ytterbium-Doped Sesquioxides*. Dissertation, Institut für Laser-Physik, Universität Hamburg (2001).

[Pet02] V. Peters, A. Bolz, K. Petermann and G. Huber. *Growth of High-Melting Sesquioxides by the Heat Exchanger Method*. Journal of Crystal Growth **237-239**, 879 (2002).

[Pet08] R. Peters, C. Kränkel, K. Petermann and G. Huber. *Power Scaling Potential of Yb:NGW in Thin Disk Laser Configuration*. Applied Physics B **91** (25), 25 (2008).

[Pet09] R. Peters. *Ytterbium-Dotierte Sesquioxide als Hocheffiziente Lasermaterialien*. Dissertation, Institut für Laser-Physik, Universität Hamburg (2009).

[Pie00] L. van Pieterson, M. Heeroma, E. de Heer and A. Meijerink. *Charge Transfer Luminescence of Yb^{3+}*. Journal of Luminescence **91**, 177 (2000).

[Pie02] L. van Pieterson, M. F. Reid, R. T. Wegh, S. Soverna and A. Meijerink. *$4f^n \rightarrow 4f^{n-1}5d$ Transitions of the Light Lanthanides: Experiment and Theory*. Physical Review B **65**, 0451113 (2002).

[Pip67] T. S. Piper, J. P. Brown and D. S. McClure. *fd and $f^{13}d$ Configurations in a Crystal Field, and the Spectrum of Yb++ in Cubic Crystals*. The Journal of Chemical Physics **46** (4), 1353 (1967).

[Puj01] A. Pujats and M. Springis. *The F-Type Centres in YAG Crystals*. Radiation Effects and Defects in Solids **155**, 65 (2001).

[Qiu02] H. Qiu, P. Yang, J. Dong, P. Deng, J. Xu and W. Chen. *The Influence of Yb Concentration on Laser Crystal Yb:YAG*. Materials Letters **55**, 1 (2002).

[Qua05] G. J. Quarles. *Comparison of Ceramics Lasers with Single Crystal Materials*. In: *Photonics West, San Jose, CA, USA, paper 5707-19* (2005).

[Qua07] G. J. Quarles. *Spectroscopy and Laser Evaluation and Caomparison of Rare-Earth Doped Ceramics for Direct Energy Applications*. In: *3rd Laser Ceramics Symposium: International Symposium on Transparent Ceramics for Photonic Applications, Tokyo, Japan, paper IO-C-11,* (2007).

[Qua08] G. J. Quarles. *Manufacturing and Applications of Next-Generation Laser Gain Materials*. In: *Advanced Solid State Photonics Topical Meeting, Nara, Japan, paper WC3* (2008).

[Rag97] R. S. Raghavan. *New Prospects for Real-Time Spectroscopy of Low Energy Electron Neutrinos from the Sun*. Physical Review Letters **78** (19), 3618 (1997).

[Raj64] K. Rajnak and B. G. Wybourne. *Configuration Interaction in Crystal Field Theory*. Journal of Chemical Physics **41** (2), 565 (1964).

[Rei71] A. R. Reinberg, L. A. Riseberg, R. W. Wacker R. M. Brown and W. C. Holton. *GaAs:Si LED Pumped Yb-Doped YAG Laser*. Applied Physics Letters **19** (1), 11 (1971).

[Rei00] M. F. Reid, L. van Pieterson, R. T. Wegh and A. Meijerink. *Spectroscopy and Calculation for $4f^N \rightarrow 4f^{N-1}5d$ Transitions of Lanthanide Ions in $LiYF_4$*. Physical Review B **62** (22), 14744 (2000).

[Rei02] M. F. Reid, L. van Pieterson and A. Meijerink. *Trends in Parameters for the $4f^N \leftrightarrow 4f^{N-1}5d$ Spectra of Lanthanide Ions in Crystals*. Journal of Alloys and Compounds **344**, 240 (2002).

[Rid99] B. K. Ridley. *Quantum Processes in Semiconductors Oxford Science Publications* (Oxford University Press Inc., New York, 1999).

[Rie96] E. Riedel and C. Janiak. *Anorganische Chemie* (de Gruyter, 1996), 7 edition.

[Ris67] L. A. Riseberg, W. B. Gandrud and H. W. Moos. *Multiphonon Relaxation of Near-Infrared Excited States of $LaCl_3$:Dy^{3+}*. Physical Review **159** (2), 262 (1967).

[Ris68] L. A. Riseberg and H. W. Moos. *Multiphonon Orbit-Lattice Relaxation of Excited States of Rare-Earth Ions in Crystals*. Physical Review **174** (2), 429 (1968).

[Ris88] W. P. Risk. *Modeling of Longitudinally Pumped Solid-State Lasers Exhibiting Reabsorption Losses*. Journal of the Optical Society of America B **5** (7), 1412 (1988).

[Rob78] D. J. Robbins and P. J. Dean. *The Effects of Core Structure on Radiative and Non-Radiative Recombinations at Metal Ion Substituents in Semiconductors and Phosphors*. Advances in Physics **27** (4), 499 (1978).

[Ros55] A. Rose. *Recombination Processes in Insulators and Semiconductors*. Physical Review **97** (2), 322 (1955).

[Rot85] S. R. Rotman. *Defect Structure of Luminescent Garnets*. Dissertation, Department of Electrical Engineering and Computer Science, Massachusetts Institute of Technology, Cambridge, Mass., USA (1985).

[Rot89a] S. R. Rotman, M. Roth, H. L. Tuller and C. Warde. *Defect-Property Correlations in Garnet Crystals. IV. The Optical Properties of Nickel-Doped Yttrium Aluminum Garnet*. Journal of Applied Physics **66** (3), 1366 (1989).

[Rot89b] S. R. Rotman, C. Warde, H. L. Tuller and J. Haggerty. *Defect-Property Correlations in Garnet Crystals. V. Energy Transfer in Luminescent Yttrium Aluminum-Yttrium Iron Garnet Solid Solutions*. Journal Applied Physics **66** (7), 3207 (1989).

[Rot90] S. R. Rotman and H. L. Tuller. *Ionic COnduction in Yttrium Aluminum Garnet*. Solid State Ionics **40/41**, 893 (1990).

[Rot98] S. R. Rotman and H. L. Tuller. *Defect-Property Correlations in Garnet Crystals. *VII: The Electrical Conductivity and Defect Structure of Yttrium Aluminum and Yttrium Iron Garnet Solid Solutions*. Journal of Electroceramics **2** (2), 95 (1998).

[Rus25] H. N. Russell and F. A. Saunders. *New Regularities in the Spectra of the Alkaline Earths*. Astrophysical Journal **61**, 38 (1925).

[Rut00] T. S. Rutherford, E. K. Gustafson W. M. Tulloch and R. L. Byer. *Edge-Pumped Quasi-Three-Level Slab Lasers: Design and Power Scaling*. IEEE Journal of Quantum Electronics **36** (2), 205 (2000).

[Sat76] S. Sato. *Optical Absorption and X-Ray Photoemission Spectra of Lanthanum and Cerium Halides*. Journal of the Physical Society of Japan **41** (3), 913 (1976).

[Sat06] Y. Sato and T. Taira. *The Studies of Thermal Conductivity in $GdVO_4$, YVO_4, and $Y_3Al_5O_{12}$ Measured by Quasi-One-Dimensional Flash Method*. Optics Express **14** (22), 10528 (2006).

[Sat09] Y. Sato, J. Akiyama and T. Taira. *Effects of Rare-Earth Doping on Thermal Conductivity in $Y_3Al_5O_{12}$ Crystals*. Optical Materials **31** (5), 720 (2009).

[Sau98] S. Sauvage, P. Boucaud, F. Glotin, R. Prazeres, J.-M. Ortega, A. Lemaître, J.-M. Gérard and V. Thierry-Flieg. *Saturation of Intrband Absorption and Electron Relaxation Time in N-Doped InAs/GaAs Self-Assembled Quantum Dots*. Applied Physics Letters **73** (26), 3818 (1998).

[Sch75] H. J. Schugar, E. I. Solomon and W. L. Cleveland an L. Goodman. *Simultaneous Pair Electronic Transitions in Ytterbium Oxide*. Journal of the American Chemical Society **97** (22), 6442 (1975).

[Sch98] T. Schweizer, P. E.-A. Möbert, J. R. Hector, D. W. Hewak, W. S. Brocklesby, D. N. Payne and G. Huber. *Optical Measurement of Narrow Band Rare-Earth 4f Levels with Energies Greater than the Band Gap of the Host*. Physical Review Letters **80** (7), 1537 (1998).

[Sch00] B. Schaudel, P. Goldner, M. Prassas and F. Auzel. *Cooperative Luminescence as a Probe of Clustering in Yb^{3+} Doped Glasses*. Journal of Alloys and Compounds **300-301**, 443 (2000).

[Sco74] G. B. Scott, D. E. Lacklinson and J. L. Page. *Absorption Spectra of $Y_3Fe_5O_{12}$ (YIG) and $Y_3Ga_5O_{12}$:Fe^{3+}*. Physical Review B **10** (3), 971 (1974).

[Sco77] G.B. Scott and J. L. Page. *The Absorption Spectra of $Y_3Fe_5O_{12}$ and $Y_3Ga_5O_{12}$:Fe^{3+} to 5.5 eV*. PhysicaStatus Solidi b **79**, 203 (1977).

[Sei39] F. Seitz. *An Interpretation of Crystal Luminescence*. Transaction of the Faraday Society **35**, 74 (1939).

[Sek89] M. Sekita, H. Haneda, T. Yanagitani and S. Shirasaki. *Induced Emission Cross Section of Nd:$Y_3Al_5O_{12}$ Ceramics*. Journal of Applied Physics **67** (1), 453 (1989).

[Sek91] M. Sekita, H. Haneda and S. Shirasaki. *Optical Spectra of Undoped and Rare-Earth-(=Pr, Nd, Eu, and Er) Doped Transparent Ceramic $Y_3Al_5O_{12}$*. Journal of Applied Physics **69** (6), 3709 (1991).

[Shu07] A. V. Shubin, M. V. Yashkov, M. A. Melkumov, S. A. Smirnow, I. A. Bufetov and E. M. Dianov. *Photodarkening of Aluminosilicate and Phosphosilicate Yb-Doped Fibers*. In: *Conference Digest of CLEO Europe-EQEC, CJ3-1-THU* (2007).

[Sla69] G. A. Slack, D. W. Oliver, R. M. Chrenko and S. Roberts. *Optical Absorption of $Y_3Al_5O_{12}$ from 10- to 55000-cm^{-1} Wave Numbers*. Physical Review **177** (3), 1308 (1969).

[Sla71] G. A. Slack and D. W. Oliver. *Thermal Conductivity of Garnets and Phonon Scattering by Rare-Earth Ions*. Physical Review B **4** (2), 592 (1971).

[Smi73] W. Smith. *The Action of Light on Selenium*. Journal of the Society of Telegraph Engineers **2** (4), 31 (1873).

[Sou02] D. F. de Sousa, R. Lebullenger, A. C. Hernandes and L. A. O. Nunes. *Evidence of Higher-Order Mechanisms than Dipole-Dipole Interaction in $Tm^{3+} \rightarrow Tm^{3+}$ Energy Transfer in Fluoroindogallate Glasses*. Physical Review B **65**, 094204 (2002).

[Sou03] D. F. De Sousa, V. Peters, G. Huber, A. Toncelli, D. Parisi and M. Tonelli. *Pump Modulation Frequency Resolved Excited State Absorption Spectra in Tm^{3+} Doped YLF*. Applied Physics B **77**, 817 (2003).

[Spr91] M. Springis, A. Pujats and J. Valbis. *Polarization of Luminescence of Colour Centres in YAG Crystals*. Journal of Physics: Condensed Matter **3**, 5457 (1991).

[Sta14] J. Stark. *Weitere Resultate über den Effekt des elektrischen Feldes auf Spektrallinien*. Die Naturwissenschaften **7**, 145 (1914).

[Ste00] C. Stewen, K. Contag, M. Larionov, A. Giesen and H. Hügel. *A 1-kW CW Thin Disk Laser*. IEEE Journal of Selected Topics in Quantum Electronics **6** (4), 650 (2000).

[Str99] P. Strange, A. Svane, W. M. Temmerman, Z. Szotek and H. Winters. *Understanding the Valency of Rare Earths from First-Priciple Theory*. Nature **399**, 756 (1999).

[Sum94] D. S. Sumida and T. Y. Fan. *Effect of Radiation Trapping on Fluorescence Lifetime and Emission Cross Section Measurements in Solid-State Laser Media*. Optics Letters **19** (17), 1343 (1994).

[Sun09] Y. Sun, S. E. Thompson and T. Nishida. *Strain Effect in Semiconductors* (Springer Science+Business Media, LLC, 2009).

[Sve93] O. Svelto. *Principles of Lasers* (Plenum Press, New York, 1993), 2nd edition.

[Tai97] T. Taira, W. M. Tulloch and R. L. Byer. *Modeling of Quasi-Three-Level Lasers and Operation of CW Yb:YAG Lasers*. Applied Optics **36** (9), 1867 (1997).

[Tak03] K. Takaichi, H. Yagi, J. Lu, A. Shirakawa, K. Ueda, T. Yanagitani and A. A. Kaminskii. *Yb^{3+}-Doped $Y_3Al_5O_{12}$ Ceramics - a New Solid-State Laser Material*. Physica Status Solidi (a) **200** (1), R5 (2003).

[Tem99] W. M. Temmerman, Z. Szotek, A. Svane, P. Strange, H. Winter, A. Delin, B. Johansson, O. Eriksson, L. Fast and J. M. Wills. *Electronic Configuration of Yb Compounds*. Physical Review Letters **83** (19), 3900 (1999).

[Thi01] C. W. Thiel, H. Cruguel, H. Wu, Y. Sun, G. J. Lapeyre, R. L. Cone, R. W. Equall and R. M. Macfarlane. *Systematics of $4f$ Electron Energies Relative to Host Bands by Resonant Photoemission of Rare-Earth Ions in Aluminum Garnets*. Physical Review B **64**, 085107 (2001).

[Thi03] C. W. Thiel. *Energies of Rare-Earth Ion States Relative to Host Bands in Optical Materials from Electron Photoemission Spectroscopy*. Dissertation, Department of Physics, Montana State University (2003).

[Tok06] M. Tokurakawa, K. Takaichi, A. Shirakawa, K. Ueda, H. Yagi, T. Yanagitani and A. A. Kaminskii. *Diode-Pumped Mode-Locked Yb^{3+}:Lu_2O_3 Ceramic Laser*. Optics Express **14** (26), 12832 (2006).

[Tok07] M. Tokurakawa, K. Takaichi, A. Shirakawa, K. Ueda, H. Yagi, T. Yanagitani and A. A. Kaminskii. *Diode-Pumped 188 fs Mode-Locked Yb^{3+}:Y_2O_3 Ceramic Laser*. Applied Physics Letters **90** (2007).

[Vog97] H. Vogel. *Gerthsen Physik* (Springer Verlag, Berlin, Heidelberg, New York, 1997), 19 edition.

[Vos02] A. Voss. *Der Scheibenlaser: Theoretische Grundlagen des Dauerstrichbetriebs und erste experimentelle Ergebnisse anhand von Yb:YAG*. Dissertation, Universität Stuttgart, Institut für Strahlwerkzeuge (2002).

[Wan08] X. Wang, S. Xiao, X. Yang and J. W. Ding. *Highly Efficient Cooperative Up-Conversion of Yb^{3+} in $NaYF_4$*. Journal of Material Science **43**, 1354 (2008).

[War59] I. Warshaw and R. Roy. *Stable and Metastable Equilibria in the Systems Y_2O_3-Al_2O_3 and Gd_2O_3-Fe_2O_3*. Journal of The American Ceramic Society **42** (9), 434 (1959).

[Web68] M. J. Weber. *Radiative and Multiphonon Relaxation of Rare-Earth Ions in Y_2O_3*. The Physical Review **171** (2), 283 (1968).

[Web71] M. J. Weber. *Luminescence Decay by Energy Migration and Transfer: Observation of Diffusion-Limited Relaxation*. Physical Review B **4** (9), 2932 (1971).

[Weg95] R. T. Wegh and A. Meijerink. *Cooperative Luminescence of Ytterbium(III) in La_2O_3*. Chemical Physics Letters **246**, 495 (1995).

[Wig27] E. Wigner. *Einige Folgerungen aus der Schrödingerschen Theorie für die Termstrukturen*. Zeitschrift für Physik **43** (9-10), 624 (1927).

[Wis08] D. J. Wisniewski, L. A. Boatner, J. S. Neal, G. E. Jellison, J. O. Ramey, A. North, M. Wisniewska, A. E. Payzant, J. Y. Howe, A. Lempicki, C. Brecher and J. Glodo. *Development of Novel Polycrystalline Ceramic Scintillators*. IEEE Transactions on Nuclear Science **55** (3), 1501 (2008).

[Wit84] G. de With and H. J. A. van Dijk. *Translucent $Y_3Al_5O_{12}$ ceramics*. Material Research Bulletin **19** (12), 1669 (1984).

[Woj96] A. J. Wojtowicz, A. Lempicki, D. Wisniewski, M. Balcerzyk and C. Brecher. *The Carrier Capture and Recombination Process in ln^{3+}-Activated Scintillators*. IEEE Transactions on Nuclear Science **43** (3), 2168 (1996).

[Wol09a] U. Wolters. *private communication* (2009).

[Wol09b] U. Wolters. *Spektroskopische Untersuchungen zur Photoleitfähigkeit hochdotierter Yb:YAG-Laserkristalle*. Diplomarbeit, Institut für Laser-Physik, Universität Hamburg (2009).

[Woo63] D. L. Wood. *Energy Levels of Yb^{3+} in Garnets*. The Journal of Chemical Physics **39** (7), 1671 (1963).

[Wu90] M. C. Wu, N. A. Olsson, D. Sivco and A. Y. Cho. *A 970 nm Strained-Layer InGaAs/GaAlAs Quantum Well Laser for Pumping an Erbium-Doped Optical Fiber Amplifier*. Applied Physics Letters **56** (3), 221 (1990).

[Wyn99] R. Wynne, J. L. Daneu and T. Y. Fan. *Thermal Coefficients of the Expansion and Refractive Index in YAG*. Applied Optics **38** (15), 3282 (1999).

[Xu99] Y. Xu and W. Y. Ching. *Electronic Structure of Yttrium Aluminum Garnet ($Y_3Al_5O_{12}$)*. Physical Review B **59** (16), 10530 (1999).

[Yac03] B. G. Yacobi. *Semiconductor Materials: An Introduction to Basic Principles* (Kluwer Academic/Plenum Publishers, New York, 2003).

[Yag04] H. Yagi and T. Yanagitani. *US Patent 6825144* (2004).

[Yag07a] H. Yagi. *Development of Polycrystalline Laser Ceramics*. Dissertation, Institute for Laser Science, University of Electro-Communications (2007).

[Yag07b] H. Yagi, T. Yanagitani, T. Numazawa and K. Ueda. *The Physical Properties of Transparent $Y_3Al_5O_{12}$ Elastic Modulus at High Temperature and Thermal Conductivity at Low Temperature*. Ceramics International **33**, 711 (2007).

[Yan98a] T. Yanagitani, H. Yagi and M. Ichikawa. *Japanese Patent 10-101333* (1998).

[Yan98b] T. Yanagitani, H. Yagi and Y. Yamasaki. *Japanese Patent 10-101411* (1998).

[Yan99] T. Yanagitani, S. Imagawa, H. Yagi and H. Kubo. *European Patent 0926106* (1999).

[Yen64] W. M. Yen, W. C. Scott and A. L. Schawlaw. *Phonon-Induced Relaxation in Excited Optical States of Trivalent Praseodymium in LaF_3*. Physical Review **136** (1A), A271 (1964).

[Yen99] W. M. Yen. *Photocnductivity and Luminescence Efficiency of Rare Earth Activated Insulating Materialss*. Material Research Society Symposium Proceedings **560**, 183 (1999).

[Yod51] H. S. Yoder and M. L. Keith. *Complete Substitution of Aluminum for Silicon: The System $3MnO{\cdot}Al_2O_3$ - $3Y_2O_3{\cdot}5Al_2O_3$*. The American Mineralogist **36** (7-8), 519 (1951).

[Yok67] M. Yokota and O. Tanimoto. *Effects of Diffusion on Energy Transfer by Resonance*. Journal of the Physical Society of Japan **22** (3), 779 (1967).

[Zel98] D. E. Zelmon, D. L. Small and R. Page. *Refractive-index Measurements of Undoped Yttrium Aluminum Garnet from 0.4 to 5 µm*. Applied Optics **37**, 4933 (1998).

[Zha97] B. L. Zhang and K. Raghavachari. *Photoabsorption and Photoluminescence of Divalent Defects in Silicate and Germanosilicate Glasses: First-Priciple Calculations*. Physical Review B **55** (24), R15 993 (1997).

[Zim07] G. Zimmerer. *SUPERLUMI: A Unique Setup for Luminescence Spectroscopy with Synchroton Radiation*. Radiation Measurements **42** (4-5), 859 (2007).

[Zor05] Y. Zorenko. *Luminescence of Isoelectric Impurities and Antisite Defects in Garnets*. physica status solidi (c) **2** (1), 375 (2005).

[Zor07] Y. Zorenko, A. Voloshinovskii, V. Savchyn, T. Voznyak, M. Nikl, K. Nejezchleb, V. Mikhailin, V. Kolobanov and D. Spassky. *Exciton and Antisite Defect-Related Luminescence in $Lu_3Al_5O_{12}$ Garnets*. Physica Status Solidi (b) **244** (6), 2180 (2007).

List of Publications

Scientific Journals

- C. Kränkel, D. Fagundes-Peters, S. T. Fredrich, J. Johannsen, M. Mond, G. Huber, M. Bernhagen, and R. Uecker
  Continuous wave laser operation of Yb^{3+}:YVO_4
  Appl. Phys. B **79**, 543-546 (2004)

- H. Kühn, S. T. Fredrich-Thornton, C. Kränkel, R. Peters, and K. Petermann
  Model for the calculation of radiation trapping and description of the pinhole method
  Opt. Lett **32** (13), 1908-1910, (2007)

- J.-F. Bisson, D. Kouznetsov, K.-I. Ueda, S. T. Fredrich-Thornton, K. Petermann, and G. Huber
  Switching of emissivity and photoconductivity in highly doped Yb^{3+}:Y_2O_3 and Lu_2O_3 ceramics
  Appl. Phys. Lett. **90**, 201901 (2007)

- M. Eichhorn, S. T. Fredrich-Thornton, E. Heumann, and G. Huber
  Spectroscopic properties of Er^{3+}:YAG at 300-550 K and their effects on the 1.6 µm laser transitions
  Appl. Phys. B **91**, 249- (2008)

- I. Kamenskikh, M. Chugunova, S. T. Fredrich-Thornton, C. Pedrini, K. Petermann, A. Vasil'ev, U. Wolters, and H. Yagi
  Potentiality of Ceramic Scintillators: General Considerations and YAG-Yb Optical Ceramics Performance
  IEEE Transactions on Nuclear Science **57** (3), 1211- (2010)

Other

- S. T. Fredrich
  Charakterisierung der Lasereigenschaften von Nd:YVO_4 und Nd:$GdVO_4$
  Universität Hamburg, Diplomarbeit (2004)

- S. T. Fredrich-Thornton
  Energy Transfer Processes in Highly Doped Yb:YAG Ceramics for Thin-Disk Laser Applications
  Japanese Society for the Promotion of Science (JSPS) Research Report (2007)

- M. Engholm, L. Norin, C. Hirt, S. T. Fredrich-Thornton, K. Petermann, and G. Huber
  Quenching processes in Yb lasers: correlation to the valence stability of the Yb ion (Proceedings Paper)
  Proceedings of SPIE Volume: 7193 Solid State Lasers XVIII: Technology and Devices, 71931U (2009)

Contributions to International Conferences

Talks

- K. Petermann, C. Kränkel, M. Mond. R. Peters, S. Fredrich, and G. Huber
  New Laser Materials for High Power Thin-Disc Lasers
  14^{th} International Conference on Luminescence and Optical Spectroscopy of Condensed Matter (ICL '05), Beijing, China (2005), paper

- S. T. Fredrich-Thornton, C. Kränkel, R. Peters, K. Petermann and G. Huber
  Yb-doped Oxides for High Power Thin-Disk Lasers
  2^{nd} Laser Ceramic Symposium (LCS '06), Tokio, Japan (2006), paper 10aAS6

- J. F. Bisson, S. T. Fredrich-Thornton, D. Kouznetsov, K. Ueda
  Efficient Broadband Luminescence in Highly Doped Yb:Y_2O_3 and Yb:YAG Pumped with Laser Diode
  the 5^{th} Asia Pacific Laser Symposium (APLS '06), Guilin, China (2006), paper I-16

- S. T. Fredrich-Thornton, J. F. Bisson, D. Kouznetsov, K. Ueda, K. Petermann, and G. Huber
  Upconversion to the Conduction Band in highly doped Yb:YAG and Yb:Y_2O_3
  Conference on Lasers and Electro-Optics (CLEO '07), Baltimore, USA (2007), paper CFJ6

- C. Hirt, S. T. Fredrich-Thornton, F. Tellkamp, K. Petermann, and G. Huber
  Photoconductivity Measurements Indicating a Nonlinear Loss Mechanism in Highly Yb-Doped Oxides
  Advanced Solid-State Photonics (ASSP '08), Nara, Japan (2008), paper MF1

- M. Eichhorn and S. T. Fredrich-Thornton
  Spectroscopic Properties of Er:YAG at Elevated Temperatures and Their Influence on the $^4I_{13/2}$ Laser Emission
  Conference on Lasers and Electro-Optics (CLEO '08), San Jose, USA (2008), paper CTuKK6

- R. Peters, S. T. Fredrich-Thornton, C. Hirt, K. Petermann, and G. Huber
  Thin-disc Lasers on the Basis of Highly Yb-doped Garnets and Sesquioxides
  International Laser Physics Workshop, Trondheim, Norway (2008), paper Mo 4.2.3

- S. T. Fredrich-Thornton, C. Hirt, F. Tellkamp, K. Petermann, and G. Huber
  Photoconductivity in Yb-doped Oxides
  15^{th} International Conference on Luminescence and Optical Spectroscopy of Condensed Matter (ICL '08), Lyon, France (2008), paper TuA2-O1

- R. Peters, C. Kränkel, S. T. Fredrich-Thornton, C. Hirt, K. Petermann, and G. Huber
  Novel Highly Yb-doped Thin-disc Lasers
  3^{rd} EPS-QEOD Europhoton Conference, Paris, Frankreich (2008), Invited Talk

- M. Engholm, L. Norin, C. Hirt, S. T. Fredrich-Thornton, K. Petermann, and G. Huber
  Quenching processes in Yb lasers: correlation to the valence stability of the Yb ion
  SPIE Photonics West 2009, San Jose, USA (2009)

- M. Tokurakawa, A. Shirakawa, K. Ueda, R. Peters, S. Fredrich-Thornton, K. Petermann, G. Huber, H. Yagi, T. Yanagitani, and A. A. Kaminskii
  Ultra-Short Pulses from Diode-Pumped Yb^{3+}-Doped Crystal and Ceramic Lasers with High Average Power,
  Advanced Solid-State Photonics (ASSP '09), Denver , USA (2009), paper MC3

- U. Wolters, S. T. Fredrich- Thornton, F. Tellkamp, K. Petermann, and G. Huber
  Photoconductivity in Yb-Doped Materials at High Excitation Densities and its Effect on Highly Yb-Doped Thin-Disk Lasers
  Conference on Lasers and Electro-Optics (CLEO/Europe-EQEC 2009), Munich, Germany (2009), paper CA9.2

- I. Kamenskikh, M. Chugunova, S. T. Fredrich-Thornton, C. Pedrini, K. Petermann, A. Vasil'ev, and H. Yagi
  Potentiality of Ceramic Scintillators: General Considerations and YAG-Yb Optical Ceramics Performance
  IEEE-10th International Conference on Inorganic Scintillators and their Applications (SCINT 2009), Jeju Island, Korea (2009)

- S. T. Fredrich-Thornton, H. Kühn, U. Wolters, K. Petermann, and G. Huber
  Excitation Dependent Losses in Yb:YAG Thin-Disk Lasers
  14^{th} International Conference on Laser Optics (LO '2010), St. Petersburg, Russia (2010), paper 387

Poster

- S. T. Fredrich, D. Fagundes-Peters, V. Peters, V. Laguta, K. Petermann, and G. Huber
  Investigation of quenching processes in Yb:YAG for thin disk laser applications
  10^{th} Europhysical Conference on Defects in Insulating Materials (EURODIM 2006), Milan, Italy (2006), paper PMo74

- S. T. Fredrich-Thornton, C. Hirt, F. Tellkamp, K. Petermann, G. Huber, K. Ueda, and H. Yagi
  Highly Doped Yb:YAG Thin-Disk Lasers: A Comparison between Single Crystal and Ceramic Active Media
  Advanced Solid-State Photonics (ASSP '08), Nara, Japan (2008), paper WB13

- C. Kränkel, H. Kühn, S. T. Fredrich-Thornton, C. Hirt, R. Peters, K. Petermann, and G. Huber
  Determination of Fluorecscence Lifetimes of Yb^{3+} in different Borate and Vanadate Hosts using the Pinhole Method
  Conference on Lasers and Electro-Optics (CLEO '08), San Jose, USA (2008), paper JTuA4

- H. Kühn, S. T. Fredrich-Thornton, C. Kränkel, R.Peters, K. Petermann, and G. Huber
  The pinhole method: lifetime measurements without radiation trapping
  15^{th} International Conference on Luminescence and Optical Spectroscopy of Condensed Matter (ICL '08), Lyon, France (2008), paper We-P-084

- L. Aarts, D. Amans, A. Belsky, B. Bezhanov, G. Burato, C. de Mello Donega, C. Dujardin, S. T. Fredrich-Thornton, C. Hirt, K. Horchani-Naifer, S. Ivanov, I. Kamenskikh, S. Kutovoi, C. Kränkel, D. Krasikov, G. Ledoux, A. Meijerink, V. Mikhailin, K. Ovanesyan, C. Pedrini, K. Petermann, R. Peters, A. Petrosyan, A. Scherbinin, G. Shapochkin, G. Shirinyan, D. Spassky, D. van der Linden, A. Vasil'ev, V. Vlasov, A. Zagumennyi, and Y. Zavartsev
  Search for Efficient Ytterbium-Doped Scintillators with Charge-Transfer Luminescence
  International Conference on Luminescence and Optical Spectroscopy of Condensed Matter (ICL '08), Lyon, Frankreich, (2008), paper MO-P-036

- S. T. Fredrich-Thornton, R. Peters, K. Petermann, and G. Huber
  Degradation of Laser Performance in Yb-Doped Oxide Thin-Disk Lasers at High Inversion Densities
  Advanced Solid-State Photonics (ASSP '09), Denver, USA (2009), paper TuB18

- K. Beil, S. T. Fredrich-Thornton, R. Peters, K. Petermann, and G. Huber
  Yb-Doped Thin-Disk Laser Materials: A Comparison between Yb:LuAG and Yb:YAG

Advanced Solid-State Photonics (ASSP '09), Denver, USA (2009), paper WB28

- U. Wolters, S. T. Fredrich-Thornton, F. Tellkamp, K. Petermann, G. Huber
  Photoconductivity in Yb-doped laser materials and its effect on laser operation at high excitation densities
  Russian-French-German Laser Symposium (RFGLS '09), Nizhny Novgorod, Russia (2009)

Contributions to National Conferences

Talks

- S. T. Fredrich, P. B. W. Burmester, K. Petermann, and G. Huber
  Vergleichsstudie zur Bestimmung kristallinterner Verluste
  Frühjahrstagung der Deutschen Physikalischen Gesellschaft (DPG '04), Munich (2004), paper Q4.5

- R. Peters, C. Kränkel, S. T. Fredrich, K. Petermann, and G. Huber
  Migration als Schlüsselparameter für Ytterbium-dotierte Scheibenlasermaterialien
  Frühjahrstagung der Deutschen Physikalischen Gesellschaft (DPG '06), Frankfurt (2006), paper Q11.4

- H. Kühn, S. T. Fredrich-Thornton, K. Petermann, and G. Huber
  Eine neue zerstörungsfreie Methode zur Bestimmung von Fluoreszenzlebensdauern in hochdotierten Kristallen
  Frühjahrstagung der Deutschen Physikalischen Gesellschaft (DPG '07), Düsseldorf (2007), paper Q68.7

- R. Peters, C. Kränkel, C. Hirt, S. T. Fredrich-Thornton, K. Petermann, and G. Huber
  Yb^{3+}:Lu_2O_3-Hochleistungslaser, Züchtung und Lasereigenschaften
  Arbeitskreistagung Kristalle für Laser und NLO der Deutschen Gesellschaft für Kristallwachstum und Kristallzüchtung (DGKK), Berlin (2007)

- C. Hirt, S. T. Fredrich-Thornton, F. Tellkamp, K. Petermann, and G. Huber
  Photoleitungsmessungen zur Identifizierung nicht-linearer Verluste in hoch-dotiertem Yb:YAG
  Frühjahrstagung der Deutschen Physikalischen Gesellschaft (DPG '08), Darmstadt (2008), paper Q11.3

- K. Beil, S. T. Fredrich-Thornton, C. Kränkel, R. Peters, K. Petermann, and G. Huber
  Yb:LuAG als Scheibenlasermaterial im hohen Leistungsbereich
  Frühjahrstagung der Deutschen Physikalischen Gesellschaft (DPG '09), Hamburg (2009), paper Q4.2

- U. Wolters, S. T. Fredrich-Thornton, C. Hirt, F. Tellkamp, K. Petermann, and G. Huber
  Photoleitungsexperimente zur Klärung nichtlinearer Verlustmechanismen in hoch Yb-dotierten oxidischen Lasermaterialien
  Frühjahrstagung der Deutschen Physikalischen Gesellschaft (DPG '09), Hamburg (2009), paper Q8.2

- U. Wolters, S. T. Fredrich-Thornton, K. Petermann, and G. Huber
  Photoleitfahigkeit Yb-dotierter Lasermaterialien bei hohen Inversionsdichten und ihr Einfluss auf hoch Yb-dotierte Scheibenlaser
  Frühjahrstagung der Deutschen Physikalischen Gesellschaft (DPG '10), Hannover (2010), paper Q18.4

Poster

- S. T. Fredrich, P. B. W. Burmester, K. Petermann, and G. Huber
  Vergleichsstudie: Bestimmung von kristallinternen Verlusten

14. Norddeutscher Lasertag, Braunschweig (2003)

- K. Beil, S. T. Fredrich-Thornton, C. Kränkel, R. Peters, K. Petermann, and G. Huber
  Yb:LuAG - a Potential Material for High Power Thin-Disk Lasers
  17. Norddeutscher Lasertag, Hannover (2008)

- U. Wolters, S. T. Fredrich-Thornton, C. Hirt, F. Tellkamp, K. Petermann, and G. Huber
  Photoconductivity in Yb-Doped Laser Crystals
  17. Norddeutscher Lasertag, Hannover (2008)

Presentations in Seminars, Workshops, Round Table Discussions

- S. T. Fredrich
  Vergleichstudie: Bestimmung von kristallinternen Verlusten
  Seminar über Festkörperlaser, Universität Hamburg (2004)

- S. T. Fredrich-Thornton
  The Thin Disk Laser Material Yb:YAG
  Ueda laboratory Group Seminar, Institute for Laser Science, University of Electro-Communications, Tokyo, Japan (2006)

- S. T. Fredrich-Thornton
  Fluorescence lifetime in Yb-doped materials
  Afternoon Tea Seminar, Institute for Laser Science, University of Electro-Communications, Tokyo, Japan (2006)

- S. T. Fredrich-Thornton
  Single Crystalline and Ceramic Yb:YAG Thin-Disk Lasers
  3^{rd} Laser Ceramic Symposium (LCS '07), Paris, France (2007), Round Table Discussion

- S. T. Fredrich-Thornton, U. Wolters, R. Peters, K. Petermann, and G. Huber
  Degradation of Laser Performance in Yb:YAG vs Yb:Lu_2O_3 at high inversion densities
  1^{st} Las-F Workshop (Las-F '09), Lintrup, Denmark (2009)

Acknowledgements

The work presented in this thesis was conducted from 2005 to 2010 under the supervision of Prof. Dr. Günter Huber in the Solid State Laser group, Institute of Laser-Physics, University of Hamburg, Germany. Investigations were also carried out in the research group of Prof. Dr. Ken-ichi Ueda at the Institute for Laser Science, University of Electro-Communications, Japan, during an 11 months research stay. This research was supported by the BMBF project "Scheibenlaser höchster Brillanz" under project number 13N8382 and the Japanese Society for the Promotion of Science.

I am indebted to my supervisor Prof. Dr. Günter Huber for his support and active interest in my research, and for always encouraging me to further explore my ideas. It was an honour to be part of the Group F for a total period of almost eight years. I am not exaggerating when I say that the lab and the office became a second home to me. The excellent facilities of Prof. Huber's group combined with the freedom and trust shown in allowing students to forge the direction of their research, with such a diverse range of topics to choose from, is probably unique. Furthermore, the time spent in Group F and the ILS, gave me plenty of opportunities to present my work at national and international conferences and symposia. The chance to meet researchers from all over the world and discuss each others' topics was a valuable experience and in some cases gave rise to real friendships being formed. Vielen lieben Dank für die wunderbare Zeit!

I thank Dr. Klaus Petermann for his enthusiasm, enduring optimism and for always sharing his time, not only for "our ytterbium problem" but also for all kinds of every day problems (inklusive des geblümten Sofas, usw.). Herzlichen Dank für so vieles!

I would also like to thank Prof. Dr. Ernst Heumann for sharing so many insights, especially into lab-related laser physics. In particular, I am deeply grateful for the one time at the CLEO, where I literally forced him to go through my slides with me just before my talk. Danke schön, auch für Little Italy!

A big thank you to the "Yb-thin disk laser"-team, Dr. Christian Kränkel and Dr. Rigo Peters. It was a great pleasure to work with you on the same project. Thank you for the countless discussions and all the valuable time we shared. Rigo, your persistent optimism was simply inspiring. Milano will never be forgotten (vor allem dieses Dinner auf dem Gehöft im Grünen)! Christian, thank you so much for all the time together. It is kind of hard to imagine that already more than 12 years have past since we first met. Who would have thought that we would have ended up in the same field of laser physics, at the same research group and even studying related PhD topics back then? I also have to thank you for proof reading this thesis and the last minute corrections all the way from Brazil. Always remember the Cola-Dose und das unglaubliche Buben-Blatt! Danke für alles und alles!

I would like to thank the former and the current members of Group F for being such a good team. The working atmosphere is truly exceptional. Especially, I would like to thank my office mates during my PhD years: Stefan Ehlert, Christina Braun, Christian "Hirti" Brandt, and Kolja Beil for all the fun and also the interdisciplinary discussions. Hirti and Kolja, thank you very much for your contributions during your Diplomas in the Yb-team und dass Ihr damals der Ameiseninvasion so tapfer und gelassen standgehalten habt!

Thank you also to the other members of the Yb-team: Ulrike Wolters, Dr. Henning Kühn and Uwe Kelling. The discussions on peculiar data, the various possible models and their representations, etc. were all interesting and also much fun. Thank you Ulrike, also for proof reading the photoconductivity part of this thesis. Ich bin sehr gespannt, wie es weiter geht!

Special thanks to Matthias "mawi" Fechner, Nils-Owe Hansen, Dr. René Hartke, Francesca Moglia and Dr. Jörg Siebenmorgen for all the "spam"-mails and great friendships. Danke Matthias, insbesondere für den Sommer 2008: Unvergessen die Mattengasse in Zürich und die unglaubliche ICL in Lyon (the '80s and the performance of the century, pool, cheese (!) and wine... just to name some keywords)! Danke Jörg for all the cultural activities,

Sushi-events, das Initiieren des Auswärtsessens und das Pflegen der Tradition (6. Dezember und so)! Never forget: Specs-Parties!!

I am also indebted to Friedjof Tellkamp for so many things, e.g. the "Schuhkristall" just to name one, Stephan Garbers for quick workshop help, Robert Fischer for being able to stay relaxed in almost any situation, Frau Frömmig for coffee, milk and picking up the ai-Phase mobile from the tax office with me, Teoman Gün for late night and weekend discussions at the ILP, Philipp Koopmann for driving me back to Rellingen (more than once), Sebastian Heinrich, Fabian Reichert, Thomas Calmano and all the others who helped clearing the great flood in der Großen Kristallzucht.

I owe a special debt of gratitude to Prof. Dr. Ken-ichi Ueda for welcoming me into his group and giving me the opportunity to work with Yb-doped laser ceramics. It was truly a great experience and a fruitful time. Thank you also for providing the second assessment for this thesis. I would also like to thank Dr. Akira Shirakawa, Dr. Mitsuru Musha, Dr. Masaki Tokurakawa, Dr. Jean-Francois Bisson, Dr. Dmitrii Kouznetsov, Mrs. Shoko Okudaira, and all the other members of the Ueda-laboratory for all the support and help. Special thanks to Tokurakawa-san, also for the ongoing German-Japanese collaborations!! In this context, I would like to extend my gratitude to Dr. Hideki Yagi of Konoshima Chemical Co., Ltd. Without his great support the investigations on the heavily doped Yb:YAG laser ceramics would not have been possible. Minasama, honto ni arigato gozaimashita.

This work was greatly motivated by the results of Dr. Mikhail Larionov obtained during his PhD research at the Institut für Strahlwerkzeuge in Stuttgart, Germany. Vielen Dank auch, dass Du als special guest bei meiner Dispu warst! I also thank Dr. Irina A. Kamenskikh of M.V. Lomonosov Moscow State University, Russia and Prof. Dr. Christian Pedrini of the Laboratoire de Physico-Chimie des Matériaux Luminescents, France for introducing me to the wonder world of scintillators and charge transfer, the numerous discussions as well as a wonderful time during and after the ICL conference in the summer of 2008. I also wish to thank Prof. Dr. Mauro Tonelli and Ms Daniela Parisi of the Pisa University, Italy for growing and providing the Yb-doped fluoride crystals. Thank you also to Dr. Gregory Stryganyuk for the CT measurements on the Ce-codoped sample during his time at HASYLAB and Dr. Heinz-Juergen Bernhardt of the Ruhr-Universität Bochum for the microprobe analysis. A big thank you goes to Priv. -Doz. Dr. Valery Baev for acting as the second referee of my disputation.

I would like to thank Dr. Philipp Burmester, Dr. Sebastian Bär, Dr. Christoph Czeranowsky, Dr. Dione Fagundes-Peters, Dr. Markus Henke, Kai Lünstedt, Dr. Bert Neubert and Dr. Volker Peters for being such great colleagues and postdocs when I entered the laser physics world, so that I always had somewhere to aim for. Bert, Christoph, Markus und Sebastian, danke vor allem auch für die jährlichen netten Runden um die Weihnachtszeit.

And a big thank you to Dr. Anika Vogel, who was there when I was studying for the laser physics diploma exam back in 2002 and who also (almost) stayed up with me the whole night printing, just before the submission of this thesis. Thank you so much for your friendship, all your support as well as the last-second corrections of the abstract and the publication list. Und wie ich Dich da um Deine Luftmatratze beneidet habe!

This work would not have been possible without the support of my closest friends and family. Many thanks to Ady, Annette, Antje, Britta, Chie, Donyo, Gila, Ha-chan, Hisayo-chan, Ine, Kana, Ken-san, Maichan, Maischo, Michiko-san, Milli, Minako, Naoko, Nao-chan, and Neinsen.

Above all I would like to express my gratitude to my parents for all their support throughout my life. I thank my father Günter Fredrich, for somehow laying the foundations for me to pursue this path, following his footsteps as a physicist. I thank my mother Kiyoko Fredrich, for teaching me her native language of Japanese, without her patience and persistence I would not have been able to take advantage of the time I spent conducting research in Japan. Finally, I thank Dr. Blair Thornton for English corrections, your great interest in my research, the inspiring discussions and most importantly thank you for all your support and patience over the period of this work. (Chinchai!)